CONTENTS

Revista Mexicana de Astronomía y Astrofísica, **47**, 197–209 (2011)

THE KINEMATICS AND VELOCITY ELLIPSOID OF THE G III STARS

Richard L. Branham, Jr.

Instituto Argentino de Nivología, Glaciología y Ciencias Ambientales, Argentina

Received 2010 October 27; accepted 2011 March 10

RESUMEN

Para estudiar la cinemática de las estrellas G gigante (clase de luminosidad III) se usan movimientos propios y paralajes de 3,075 estrellas, de las cuales 658 tienen velocidades radiales. Estas estrellas provienen de la reducción nueva hecha por van Leeuwen del catálogo Hipparcos. La solución da para la velocidad solar 16.72 ± 0.41 km s^{-1}; para las constantes de Oort, en unidades de km s^{-1} kpc^{-1}, $A = 14.05 \pm 3.28$ y $B = -9.30 \pm 2.87$, valores que representan una velocidad local de rotación de 198.48 ± 26.95 km s^{-1} si suponemos una distancia al centro Galáctico de 8.2 ± 1.1 kpc. Para las dispersiones de velocidades obtenemos, en unidades de km s^{-1}: $\sigma_x = 51.78 \pm 0.55$, $\sigma_y = 42.81 \pm 0.32$, $\sigma_z = 28.45 \pm 0.22$ con una desviación del vértice de $3.°88 \pm 6.°62$. Una comparasión de esta dispersión con las obtenidas de otras clases espectrales indica que la discontinuidad de Parengo existe también para las estrellas gigantes.

ABSTRACT

To study the kinematics of the G giant stars (luminosity class III) use is made of proper motions and parallaxes taken from van Leeuwen's new reduction of the Hipparcos catalog. 3,075 stars, of which 658 have radial velocities, were used in the final study. The solution gives: solar velocity of 16.72 ± 0.41 km s^{-1}; Oort's constant's, in units of km s^{-1} kpc^{-1}, $A = 14.05 \pm 3.28$ and $B = -9.30 \pm 2.87$, implying a rotational velocity of 198.48 ± 26.95 km s^{-1} if we take the distance to the Galactic center as 8.2 ± 1.1 kpc; velocity dispersions, in units of km s^{-1}, of: $\sigma_x = 51.78 \pm 0.55$, $\sigma_y = 42.81 \pm 0.32$, $\sigma_z = 28.45 \pm 0.22$ with a vertex deviation of $3.°88 \pm 6.°62$. A comparison of the velocity dispersions with those given by other spectral types shows that Parenago's discontinuity also exists for the giant stars.

Key Words: Galaxy: kinematics and dynamics — methods: numerical

1. INTRODUCTION

This paper continues a series on the kinematics and velocity ellipsoids of the giant stars (luminosity class III). Previously studied were the O-B5 giants (Branham 2006), the M giants (Branham 2008), the B6-9 and A giants (Branham 2009a), the K giants (Branham 2009b), and the F giants (Branham 2010). The G giants fill the remaining lacuna and complete the investigation of all of the giant stars. A search of the ADS data base[1] shows that the G giants as a group have not been studied since the research of Parenago in 1951 (Delhaye 1965), which adds impetus to this current study.

The methodology remains similar to that for the previous studies, so similar that I will eschew presentation of the mathematical development and refer the reader to the relevant previous publications where the necessary equations can be found. As in my investigation of the F giants the velocity ellipsoid calculation uses the singular value decomposition (SVD) to include stars for which only tangential velocities, but no radial velocities, are available. The section on the equations of condition briefly discusses this matter.

[1] `http://adswww.harvard.edu/`.

Little evidence exists to suggest that G stars form part of the Gould belt. There appears to be a clean break between the O-B stars and the later spectral types regarding participation in the Gould belt; O-B stars have definite Gould belt members whereas the others do not. Nevertheless, a plane will be fit to the G giants in a later section, but to examine the randomness of the data, not to infer that some G giants actually belong to the Gould belt.

To summarize briefly the mathematical procedure used, one solves for the kinematics and velocity ellipsoid of the G giants by use of semi-definite programming (SDP), which forces the solar motion calculated from the velocity ellipsoid to be the same as that calculated from the kinematical parameters. Nor is it necessary to use the same adjustment criterion for the two sets of calculations: the kinematical parameters may be reduced by use of a least squares criterion whereas the velocity ellipsoid may be calculated with the robust L_1 criterion (minimize the sum of the absolute values of the residuals), or with the same L_1 criterion for both. For a readable discussion of SDP see Vandenberge & Boyd (1996).

In their classical work *Statistical Astronomy*, Trumpler & Weaver (1962) refer to two incompleteness factors, K_1, which compensates for the deficiency of proper motions in a parallax catalog compared with a proper motion catalog, and K_2, which corrects for the absence of proper motions nearly in the line of sight and thus not detectable in either a proper motion or a parallax catalog. This study, however, shows that the calculation of incompleteness factors for the G giants is unnecessary or counterproductive.

2. THE OBSERVATIONAL DATA

The proper motions and parallaxes used in this study were taken from van Leeuwen's version of the Hipparcos catalog (van Leeuwen 2007), henceforth called simply the Hipparcos catalog, the radial velocities from the Wilson (Nagy 1991) and Strasbourg Data Centre (Barbier-Brossat & Figon 2000) catalogs. van Leeuwen's catalog (2007) omits a few stars contained in the original catalog (ESA 1997). For those few stars the relevant data were taken directly from the original catalog. The equinox of the Hipparcos catalog is J2000 and the catalog epoch is J1991.25. Stars listed as spectral class G, luminosity class III were extracted from the catalog. This resulted in a total of 3,075 G giants, of which 658 have radial velocities. The G giants are skewed towards the later giants; over 94% fall between G5 and G9, and the G8 stars alone account for 64.9% of the total.

The star's HD number determined if either of the two radial velocity catalogs contained an entry for that particular star. Not all of the data could be accepted. Negative parallaxes were excluded as were parallaxes smaller than 1 mas because the Ogorodnikov-Milne (OM) model was used for the equations of condition (Ogorodnikov 1965, pp. 61–63). This model, valid out to about 1 kpc, should be adequate because the minimum parallax used in this study, 1 mas, corresponds to a distance of 1 kpc. For a justification of this distance limit see Smart (1968, p. 285). Parallaxes smaller than 1 mas have such large mean errors that their inclusion seems unwarranted because of the uncertainty in their distances. Known multiple stars, flagged in the catalog, contaminate the proper motion by confusing orbital motion with genuine proper motion and were also excluded. And some of the solutions for the astrometric data in the catalog, also flagged, are substandard and were likewise excluded. Smith & Eichhorn (1996) have derived a procedure to correct the observed parallaxes, and this procedure was used to transform all of the parallaxes used in this study. In my study of the M giants (Branham 2008) I show that the Smith-Eichhorn correction seems to leave little residual parallax error.

What about the quality of the data? I have already commented on the high quality of the Hipparcos proper motions (Branham 2009b). Tangential velocities calculated from proper motions, therefore, should also be high quality. The radial velocities, however, come from disparate sources incorporated into the Wilson and the Strasbourg Data Center catalogs. My study of the F giants showed lower homogeneity in the radial velocities. One could perform a similar analysis with the G giants, but this seems otiose. The data are what they are and must be used as they are. The radial velocities, moreover, are not used alone but multiplied by the parallax in the equations of condition. A runs test shows that the radial velocities are of somewhat lower quality than the tangential velocities, but of acceptable quality. See the § 6. The runs test measures how often a variable, distributed about the mean, changes sign from plus to negative or negative to positive. The changes of sign, the runs, have a mean for n data points of $n/2 + 1$ and a variance of $n(n-2)/4(n-1)$. An advantage of the runs test over other tests for randomness resides in its being nonparametric, making no assumption about the normality of the data, although to actually calculate probabilities for the observed runs one does assume approximate normality. For a detailed description of the runs test see Wonnacott & Wonnacott (1972, pp. 409–411).

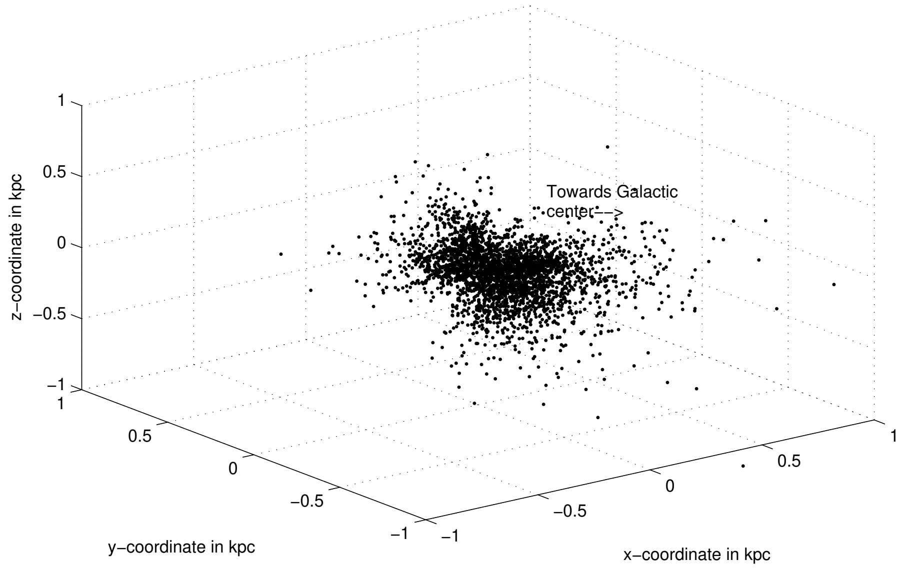

Fig. 1. Space distribution of G giants.

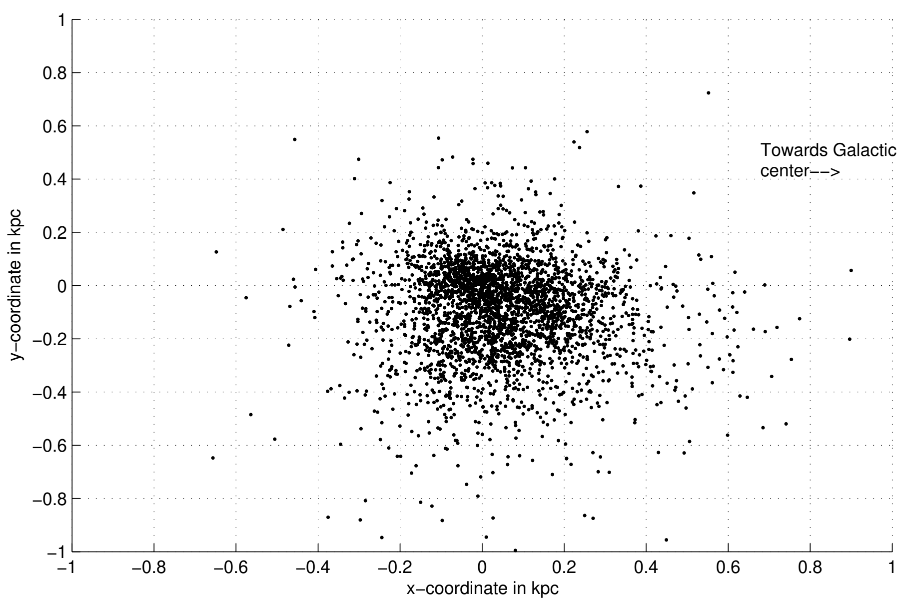

Fig. 2. Distribution in $x-y$ plane.

3. THE SPACE DISTRIBUTIONS

Let x, y, z be rectangular coordinates with origin at the Sun: x points towards the Galactic centre, y is perpendicular to x in the direction if increasing l, and z is positive for positive Galactic latitude. From ϖ, the star's parallax, l, its Galactic longitude, and b, its Galactic latitude, we calculate

$$\begin{pmatrix} x \\ y \\ z \end{pmatrix} = \frac{1}{\varpi} \begin{pmatrix} \cos l \cos b \\ \sin l \cos b \\ \sin b \end{pmatrix}. \tag{1}$$

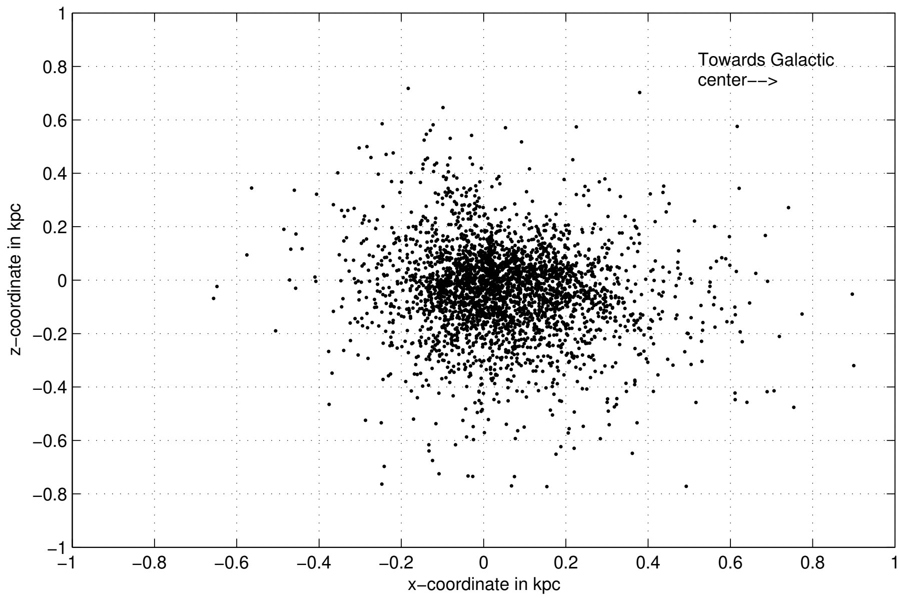

Fig. 3. Distribution in $x - z$ plane.

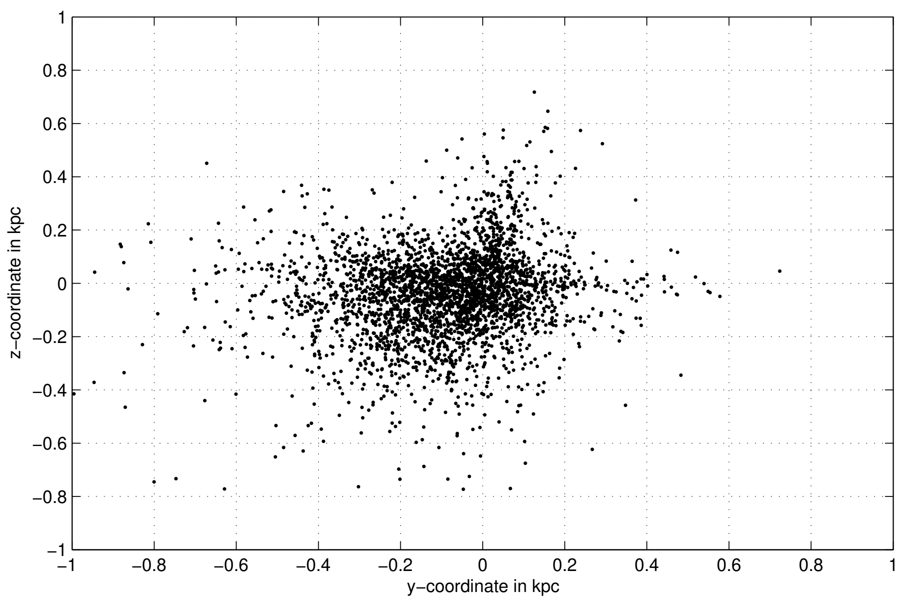

Fig. 4. Distribution in $y - z$ plane.

Figure 1 shows the distribution of the G giants in space, Figures 2, 3, and 4 the distributions in the $x - y$, $x - z$, and $y - z$ planes. Define a moment matrix, referred to the centroid of the distances, $\bar{x}, \bar{y}, \bar{z}$, from the x, y, z:

$$\begin{pmatrix} \sum_i (x_i - \bar{x})^2 & \sum_i (x_i - \bar{x})(y_i - \bar{y}) & \sum_i (x_i - \bar{x})(z_i - \bar{z}) \\ \sum_i (y_i - \bar{y})(x_i - \bar{x}) & \sum_i (y_i - \bar{y})^2 & \sum_i (y_i - \bar{y})(z_i - \bar{z}) \\ \sum_i (z_i - \bar{z})(x_i - \bar{x}) & \sum_i (z_i - \bar{z})(y_i - \bar{y}) & \sum_i (z_i - \bar{z})^2 \end{pmatrix}. \tag{2}$$

Before use of the moment matrix outliers should be eliminated from the distances. The criterion selected for the cutoff was five times the median of the distances to the stars. This cutoff results in only a sparse trim of the data. Stigler (1977) has shown that modest trimming works better than extreme trimming. Although the eigenvalues of the moment matrix indicate little concentration towards the Galactic plane, 129.7, 94.0, and 80.9 pc^2, the normalized eigenvector associated with the z-axis points towards $b_g = 55.^\circ671$, a significant tilt with respect to the Galactic plane. This tilt, however, seems to be a selection effect associated with the giants rather than a tilt associated with the Gould belt. Look at the G stars as a whole without discrimination as to luminosity class. There are 82 supergiants, 184 bright giants, 3,075 giants, 1,152 subgiants, 4,656 main sequence, and 9,332 unspecified luminosity class G stars. With this heterogeneous group the tilt becomes $79.^\circ494$. Further evidence that the tilt seems not associated with the Gould belt arises from an attempt to fit a plane to the G giants. Branham (2003) outlines the procedure for doing this. 1,389 stars are classified as "Gould belt", but the tilt of the plane of the remaining, supposedly "Galactic belt", stars becomes even worse, $35.^\circ58$, and with high correlations, up to 40%, among the x, y, z coordinates.. Thus, the procedure that works so well with the O-B5 stars to discriminate between Gould belt and Galactic belt stars fails completely for the G giants.

That the tilt should not unduly bias the solution can be inferred from a look at the randomness of the rectangular coordinates. The correlation between x and y is -10.1%, between x and z -12.9%, and between y and z 11.3%. Regarding the randomness in distance a runs test yields, after elimination of discordant distances, 1,487 runs out of an expected 1531 implying an 11.3% chance that the distances are random. The statistics for the G giants, therefore, indicate *relative* randomness.

4. EQUATION OF CONDITION FOR KINEMATICS AND THE VELOCITY ELLIPSOID

The equations of condition, given in detail in Branham (2009a) and which come from Ogordnikov (1965, pp. 74–75), involve twelve unknowns for the kinematical parameters: the components of the reflex solar motion X, Y, Z and the components of the displacement tensor $u_x, u_y, u_z, v_x, v_y, v_z, w_x, w_y, w_z$. All of these quantities are referred to Galactic latitude and longitude, l and b, rather than right ascension α and declination δ. Proper motions in α and δ are converted to proper motions in l and b expressed in milli-arc-seconds (mas) per year; radial velocity is expressed in km s^{-1}. Parallax ϖ is also expressed in mas. These kinematical parameters are calculated from the least squares criterion because there are fewer discordant observations, handled by a 2.5% trim of the data, than with the velocity ellipsoid calculation, for which the robust L_1 criterion is indicated. As with linear programming, one does this by minimization of an objective function. If r_i is one of m residuals from a solution for the kinematical parameters and r is the m-vector of the residuals, then we impose the condition $r^T \cdot r - \tau = 0$, where τ is an arbitrary parameter, and minimize τ in the objective function.

A sparse trim of the data seems indicated not only by what Stigler (1977) has found, light trimming or even no trimming works better than extreme trimming, but by what a General Colby reported to the Astronomer Royal, Sir George Airy (Airy 1854). In a geodetic adjustment for the determination of the scale of longitudes for England, inclusion of all data rather than just the most concordant data gave results that went from, to use Airy's words, "considerably in error" to "perfectly good."

The equations as derived by Ogorodnikov actually use the distance $1/\varpi$ rather than the parallax ϖ itself, but it is important to recast the equations to remove the parallax error from the denominator and thus ameliorate any possible Lutz-Kelker bias. The equations, therefore, are multiplied by ϖ, which places the parallax in the numerator.

To calculate the velocity ellipsoid use $\dot{x}, \dot{y}, \dot{z}$, the space velocities of a star, found from the proper motions and radial velocity and expressed in km s^{-1} are:

$$\begin{pmatrix} \dot{x} \\ \dot{y} \\ \dot{z} \end{pmatrix} = \begin{pmatrix} -\sin l & -\cos l \sin b & \cos l \cos b \\ \cos l & -\sin l \sin b & \sin l \cos b \\ 0 & \cos b & \sin b \end{pmatrix} \cdot \begin{pmatrix} \kappa \mu_l \cos b/\varpi \\ \kappa \mu_b/\varpi \\ \dot{r} \end{pmatrix}. \tag{3}$$

If radial velocities are unavailable, then we seem unable to calculate the space velocities. This, however, can be done if we use the SVD to employ only the tangential velocities. See Branham (2010) for details. There are other possibilities. Fuchs et al. (2009) use a deprojection formulation for the proper motions that assumes the lines of sight towards the stars are statistically uncorrelated with the velocities of the stars. The Section 7 shows that the SVD approach satisfies the assumption of statistical randomness and seems, therefore, satisfactory.

One fits a quadric surface with ten coefficients, $a, b, c, d, e, f, g, h, k, l$, to these velocities. To assure that the equation indeed corresponds to an ellipsoid one must impose the condition that the matrix of the a, b, c coefficients

$$A = \begin{pmatrix} a & c/2 & d/2 \\ c/2 & b & e/2 \\ d/2 & e/2 & c \end{pmatrix},$$

in fact be positive-definite and symmetric. To avoid the trivial solution $a = b = \cdots = q = 0$ another condition must be imposed. The one I use is that the volume of the ellipsoid must be a maximum. Because the volume is proportional to the determinant of A, the condition becomes $\det(A) = \max$. An eigenvalue-eigenvector decomposition of the matrix A yields the axes of the velocity ellipsoid and their orientation with respect to the Galactic coordinate system. Because of generally greater error in the data, the coefficients $a, \ldots, l$ are calculated by use of the robust L_1 criterion. SDP allows one to combine without difficulty the least squares criterion for the kinematical parameters and the L_1 criterion for the velocity ellipsoid. For the latter if there are n space velocities with n corresponding residuals $r_{sv,i}$, let $\gamma_i, i = 1, \ldots, n$, be n *positive* parameters. Then minimize the γ in the objective function subject to the conditions

$$\mathrm{diag}(\gamma + r_{sv}) > 0; \qquad \mathrm{diag}(\gamma - r_{sv}) > 0; \qquad \mathrm{diag}(\gamma) > 0.$$

The SDP formulation of the velocity ellipsoid calculation along with the L_1 criterion for the minimization of the residuals offers advantages over competing methods. The ellipsoid calculated is unique and represents a global minimum of the reduction criterion when that criterion is the L_1 (Calafiore 2002). Bochanski, Hawley, & West (2011) prefer a geometric simplex minimization with the least squares criterion. Although simplex minimization can be used with the L_1 criterion, thus making the procedure robust-see the algorithm in Branham (1990, pp. 191–197), the method can converge to a local rather than to a global minimum, particularly when many parameters are being fit, unless a good starting approximation is available. Pourbaix (1998) , using the simplex algorithm to calculate orbits of double stars, estimates that when n parameters are being fit there are $\approx \mathrm{O}(e^n)$ local minima. He implements a simulated annealing modification of the simplex algorithm to reject the local minima. With SDP and the L_1 criterion such a strategy becomes unnecessary because the minimum *is* global.

The solar velocity, $S_0 = \sqrt{X^2 + Y^2 + Z^2}$, calculated from both the solution for the kinematical parameters $X, Y, \ldots, w_y, w_z$ and the coefficients of the velocity ellipsoid must be the same. This condition can be imposed when one uses the SDP formulation of the problem.

5. SOME CORRECTIONS TO THE OBSERVATIONS AND COVARIANCE MATRICES

The total space motions needed in the velocity ellipsoid calculation should be corrected for the effects of Galactic rotation by modifying the proper motions and radial velocities used in the calculations to remove the rotation. This was done by the same procedure used in Branham (2009a).

In theory one should also apply a correction for the incompleteness of the sample of the G giant stars taken from the Hipparcos catalogue. Trumpler & Weaver (1962, p. 374) define a factor of incompleteness K_1 as

$$K_1 = \frac{N(m, \mu)}{N_\varpi(m, \mu)}, \tag{4}$$

where $N(m, \mu)$ is the number of stars in the sky for magnitude interval $m \pm \Delta m/2$ and proper motion interval $\mu \pm \Delta\mu/2$ and $N_\varpi(m, \mu)$ is the number of stars in the parallax catalogue for the same intervals. Equation (4) is difficult to apply if there is insufficient overlap between the proper motion catalog and the parallax catalog. For the Hipparcos parallaxes a logical proper motion catalog would be the Tycho II catalog (Høg et al. 2000). But for K_1 the sparse overlap between the two catalogs assures that the factor becomes large with large mean errors. One must question whether such corrections are realistic and should be applied. I feel they should not and that the randomness of the data is more important.

Trumpler & Weaver (1962, p. 375) also define a second incompleteness factor, K_2, to correct for the absence of proper motions in the parallax catalog nearly along the line of sight and hence undetectable. K_2 depends

TABLE 1

SOLUTION FOR KINEMATIC PARAMETERS FOR THE G III STARS

Quantity	Value	Mean Error
$\sigma(1)$ (mean error of unit weight in mas km s^{-1})	112.44	...
u_x (in mas km s^{-1})	−7.63	6.13
u_y (in mas km s^{-1})	23.35	4.06
u_z (in mas km s^{-1})	−3.59	5.23
v_x (in mas km s^{-1})	4.75	4.63
v_y (in mas km s^{-1})	−8.08	6.00
v_z (in mas km s^{-1})	−6.87	5.21
w_x (in mas km s^{-1})	1.57	4.15
w_y (in mas km s^{-1})	−7.68	3.74
w_z (in mas km s^{-1})	−11.39	5.86
S_0 (solar velocity in km s^{-1})	16.72	0.41
A (Oort constant in km s^{-1} kpc^{-1})	14.05	3.28
B (Oort constant in km s^{-1} kpc^{-1})	−9.30	2.87
$V0$ (Circular velocity in km s^{-1})	198.48	26.95
l_1 (longitude displacement)	$-26.^\circ45$	$7.^\circ05$
K (K term in km s^{-1})	−7.85	4.99

TABLE 2

VELOCITY DISPERSION AND VERTEX DEVIATION OF THE G III STARS

Quantity	Value	Mean Error
Mean absolute deviation of residuals in km s^{-1}	11.00	...
S_0 (solar velocity in km s^{-1})	16.72	1.05
σ_1 (velocity dispersion in x in km s^{-1})	51.78	0.55
σ_2 (velocity dispersion in y in km s^{-1})	42.81	0.32
σ_3 (velocity dispersion in z in km s^{-1})	28.45	0.22
l_1 (longitude of σ_1)	$3.^\circ88$	$6.^\circ62$
b_1 (latitude of σ_1)	$0.^\circ28$	$0.^\circ61$
l_2 (longitude of σ_2)	$93.^\circ93$	$1.^\circ90$
b_2 (latitude of σ_2)	$9.^\circ86$	$0.^\circ65$
l_3 (longitude of σ_3)	$-87.^\circ72$	$1.^\circ62$
b_3 (latitude of σ_3)	$80.^\circ14$	$0.^\circ49$

on the velocity ellipsoid. Branham (2009b) shows how this incompleteness factor can be evaluated. For the G giants this factor becomes an insignificant $5.6 \cdot 10^{-7}$. Therefore, neither the K_1 nor the K_2 incompleteness factor need be applied.

The covariance matrix to calculate mean errors is given in equation (25) of Branham (2006), and equation (26) of that publication shows how to calculate the errors for quantities, such as the Oort constants, derived from the displacement tensor.

6. RESULTS

After the equations of condition for the kinematical parameters had been formed, I applied two checks for the adequacy of the reduction model. The first check simply calculates the singular values of the matrix of

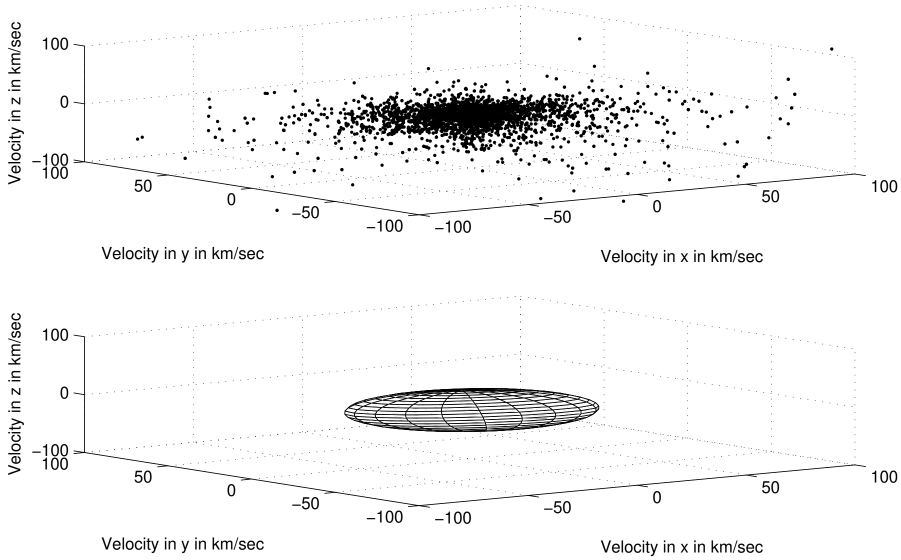

Fig. 5. '.'=rectangular velocity of star (upper); velocity ellipsoid (lower).

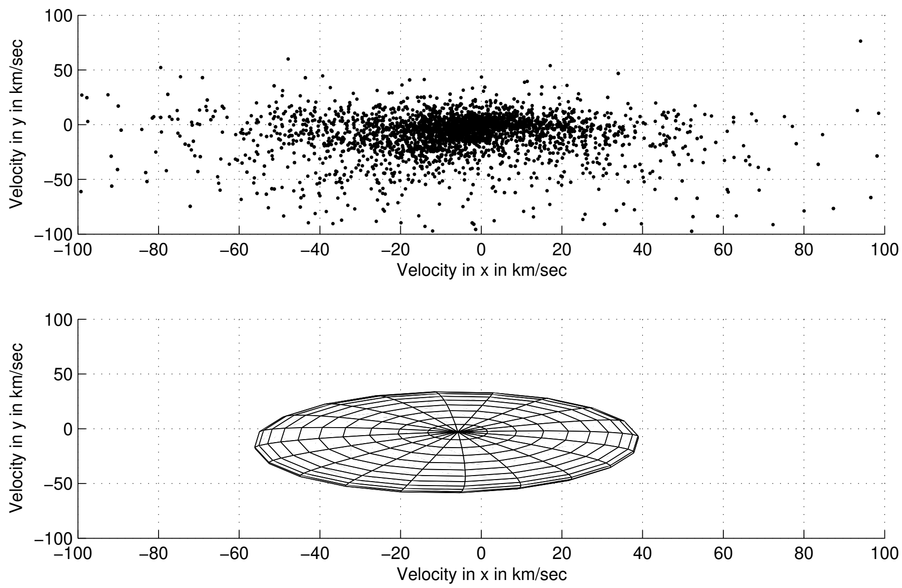

Fig. 6. Ellipsoid in $x - y$ plane.

the equations of condition. An inadequate reduction model, for example one in which some unknowns are strongly correlated, results in a high condition number for the matrix because of small singular values. The condition number of the matrix of the equations of condition for the G giants, however, is low, 22.8. The second check calculates Eichhorn's efficiency (Eichhorn 1990), a parameter that varies from 0 to 1 with 0 indicating redundancy in the parameters and 1 that all parameters are necessary. The efficiency of 0.94 indicates that *all* of the variables in the model are necessary and with little correlation among themselves.

The first solution for the G giants was calculated from all of the equations of condition. These solutions calculated residuals needed to find discordant data. For the G stars the criterion was five times the mean absolute deviation (MAD) of the residuals. This eliminated 168 of the 6,808 equations of condition, a 2.5%

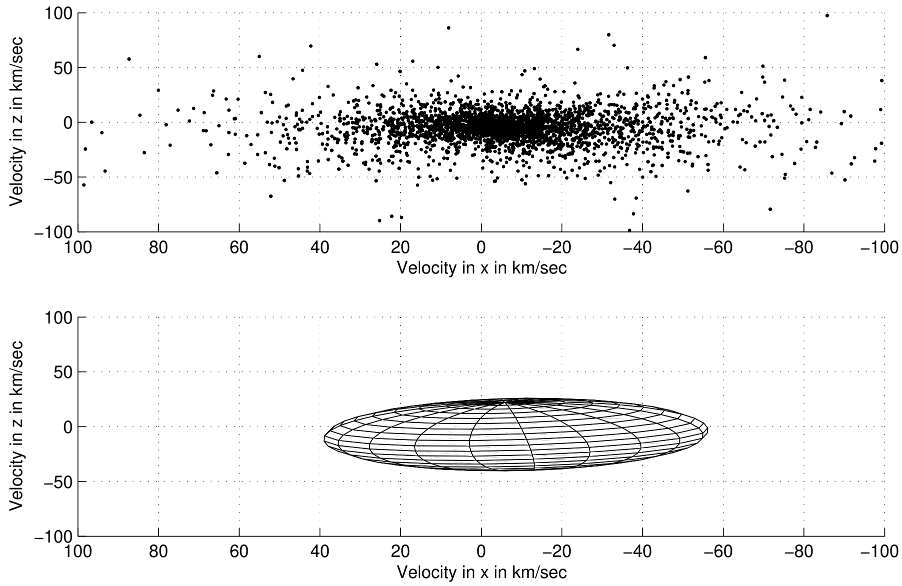

Fig. 7. Ellipsoid in $x - z$ plane.

trim. I have used this elimination criterion in the past, generally with good results, but a further reason exists to justify its use. For the G giants there is a 19.0% chance that the original residuals are random, as calculated by a runs test, but a 78.7% chance that the trimmed residuals are random. Eliminating some of the residuals, therefore, increases the randomness of the sample.

Table 1 shows the solution for the kinematical unknowns and Table 2 for the coefficients and orientation of the velocity ellipsoid for the G stars. For convenience the components for the displacement tensor are converted to the more familiar form of the solar motion, Oort constants, the deviation l_1 between the longitude of the geometric center and the kinematic center of the Galaxy, and K term. Also shown is the circular velocity V_0, found from the relation $V_0 = (A - B)R_0$, where R_0 is the distance to the centre of the Galaxy. Kerr & Lynden-Bell (1986) determine a value of 8.5 ± 1.1 kpc for R_0. Perryman (2008, App. A), however, after a survey of recent determinations feels that 8.2 kpc is a better determination. The mean error for V_0 comes from the procedure given in Branham (2008) and uses 8.2 kpc for R_0 with the same mean error as given by Kerr & Lynden-Bell (1986).

The orientation of the velocity ellipsoid in space and in the $x - y$, $x - z$, and $y - z$ planes is shown in Figures 5–8 for the G giants. (Because of the density of data points, it proved impossible to plot both the stars and the velocity ellipsoid on one graph because the stars blotted out the ellipsoid; therefore a subgraph was used for the stars and another for the ellipsoid.)

7. DISCUSSION

The distribution of the residuals from the kinematical solution, after eliminating discordant residuals, is seen in the histogram of Figure 9. As mentioned in the previous section, 168 of the residuals were eliminated, a 2.5% trim. The distribution is somewhat skewed, coefficient of skewness 0.09, more platykurtic, kurtosis of 1.42, than the normal distribution, kurtosis of 3, and more lighter tailed, Hogg's Q factor of 0.36, than a normal distribution, Q=2.58. The Q factor is defined as

$$Q = \frac{(U_{0.05} - L_{0.05})}{(U_{0.5} - L_{0.5})}, \tag{5}$$

where U_α and L_α are averages of the respective upper and lower 100α of the data (Stigler 1977). A runs test, however, reveals 3,350 runs out of an expected 3,404. The residuals, therefore, can be considered random. To be specific, there is a 19.0% chance that the residuals are taken randomly from a normal distribution.

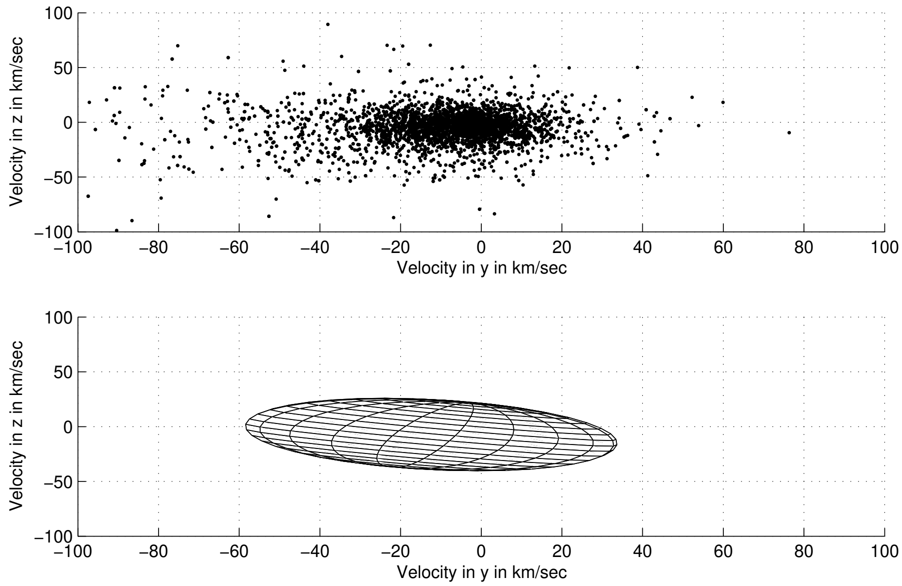

Fig. 8. Ellipsoid in $y - z$ plane.

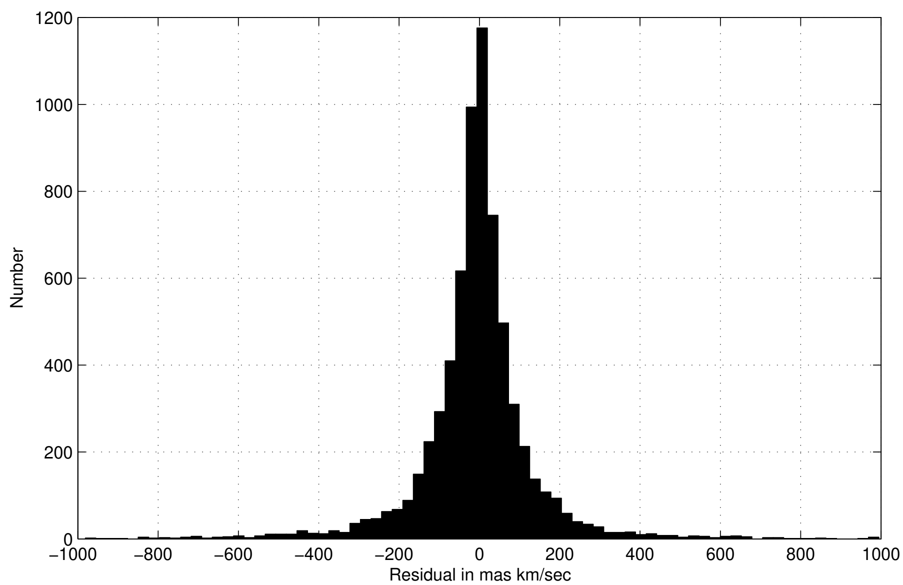

Fig. 9. Histogram of residuals from kinematical solution.

Because we generally use a 5% to 10% limit before rejecting the null hypothesis that a distribution is in fact not random, we infer that although the actual distribution deviates from normality the residuals conform to the null hypothesis of being random. If the runs test is applied separately to the equations of condition arising from the tangential velocities and those from the radial velocities, the former show 3,032 runs out of an expected 3,075 and the latter 303 runs out of an expected 329. This demonstrates that the tangential velocities seem of higher quality than the radial velocities, 31.2% probability of randomness versus 4.6%, but because they are used conjointly the residuals remain relatively random. All of this confirms, along with the singular values and Eichhorn's efficiency, that the reduction model suffers no serious defects and that inclusion of the K_1 incompleteness factor seems unnecessary.

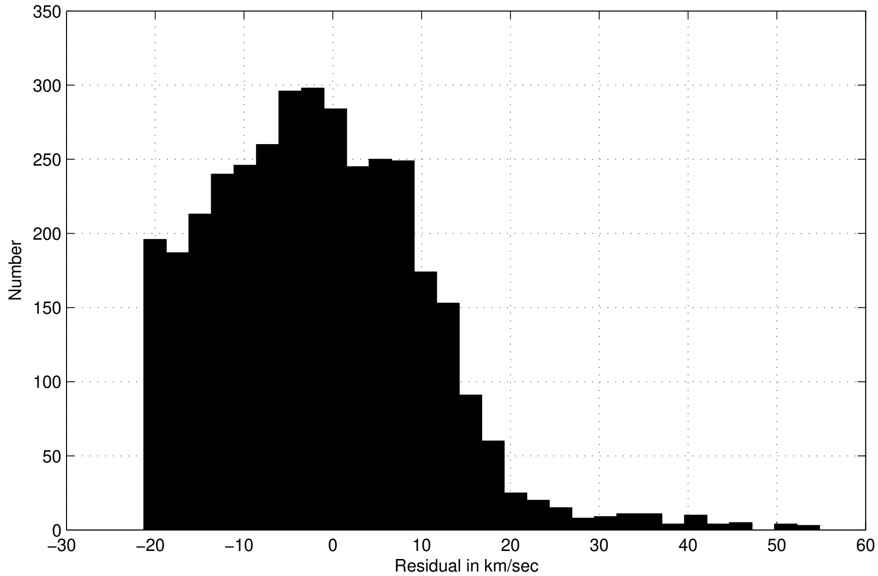

Fig. 10. Residuals in velocity for G giants.

TABLE 3

RECENT DETERMINATIONS OF THE SOLAR VELOCITY

Reference	Class	$-X$ (km s^{-1})	$-Y$ (km s^{-1})	$-Z$ (km s^{-1})	S_0 (km s^{-1})
Branham (2008)	M III	8.99 ± 0.42	20.40 ± 0.40	4.80 ± 0.39	24.20 ± 0.70[a]
Yuan et al. (2008)	O-B5	9.17 ± 0.40	8.66 ± 0.38	5.83 ± 0.34	13.90 ± 0.38[b]
Yuan et al. (2008)	K-M III	18.46 ± 0.32	17.70 ± 0.32	6.32 ± 0.32	20.61 ± 0.32[c]
Aumer & Binney (2009)	mixture IV, V	9.96 ± 0.33	5.25 ± 0.54	7.07 ± 0.34	13.29 ± 0.72
Branham (2009a)	B69 III	9.58 ± 0.39	11.94 ± 0.41	6.03 ± 0.33	16.40 ± 0.40[a]
Branham (2009a)	A III	9.85 ± 0.59	8.00 ± 0.58	5.80 ± 0.52	13.95 ± 0.58[a]
Branham (2009b)	K III	7.53 ± 0.26	19.11 ± 0.26	7.41 ± 0.22	21.83 ± 0.26[a]
Bobylev & Bajkova (2010)	Galactic masers	5.5 ± 2.2	11.0 ± 1.7	8.5 ± 1.2	15.0 ± 3.0
Branham (2010)	F III	10.84 ± 0.49	12.62 ± 0.49	8.14 ± 0.44	16.72 ± 0.41[a]
Schönrich et al. (2010)	F-G V	$11.1^{+0.69}_{-0.75}$	$12.24^{+0.47}_{-0.47}$	$7.25^{+0.37}_{-0.36}$	...
Shen & Zhang (2010)	Galactic Cepheids	12.58 ± 1.09	14.52 ± 1.06	8.98 ± 0.98	21.21 ± 1.81[d]

[a]Mean error calculated from equations (25) and (26) in Branham (2006).
[b]For heliocentric distance 0.2–3 kpc.
[c]For heliocentric distance 0.2–1 kpc.
[d]For heliocentric distance 0.2–3 kpc.

For the residuals from the velocity ellipsoid the situation becomes different, as Figure 10 shows. The residuals deviate even more from a normal distribution, coefficient of skewness 3.62, platykurtic, kurtosis 0.59, and light tailed, Q factor of 0.25. They are, however, even more random than the residuals from the kinematical solution, 1,784 runs out of an expected 1,813. There is thus a 33.7% probability that the residuals are random. This is the principal justification for use of the SVD to calculate the velocity ellipsoid.

Regarding recent determinations of the kinematical parameters Perryman (2008, p. 502) gives his Table 9.3 with pre-2007 results while Table 3 shows some post-2008 values. If we look at the 33 values for the solar velocity in both tables, without discriminating among spectrum-luminosity classes nor weighting by number of stars, there is a range from a minimum of 11.8 km s^{-1} to a maximum of 24.6 with mean 18.29 and standard deviation 3.74. The value in Table 1 falls well within this range. With respect to the Oort constants and

TABLE 4

RECENT DETERMINTIONS OF OORT CONSTANTS AND AUXILIARY QUANTITIES

Reference	Class	A (km s^{-1} kpc^{-1})	B (km s^{-1} kpc^{-1})	$A-B$	$-(A+B)$
Branham (2008)	M III	16.86 ± 2.78	-6.34 ± 2.56	23.20 ± 7.79[a]	-10.52 ± 8.82[a]
Yuan et al. (2008)	O-B5	15.33 ± 0.94	-15.12 ± 0.71	30.45 ± 1.18[b]	-0.21 ± 1.18[b]
Yuan et al. (2008)	K-M III	15.86 ± 1.30	-14.57 ± 1.01	30.44 ± 1.65[c]	1.29 ± 1.65[c]
Bobylev & Bajkova (2010)	Galactic masers	17.8 ± 0.8	-13.2 ± 1.5	31.1 ± 1.7	4.6 ± 1.7
Branham (2009a)	B69 III	11.77 ± 1.66	-9.05 ± 1.38	20.82 ± 3.83[a]	-2.72 ± 1.04[a]
Branham (2009a)	A III	11.48 ± 5.45	-8.29 ± 4.23	19.77 ± 12.09[a]	-3.19 ± 7.44[a]
Branham (2009b)	K III	13.08 ± 1.72	-10.21 ± 1.47	23.29 ± 2.20[a]	2.86 ± 0.82[a]
Branham (2010)	F III	14.85 ± 7.47	-10.85 ± 6.83	23.35 ± 4.07[a]	-4.75 ± 4.63[a]
Shen & Zhang (2010)	Galactic Cepheids	17.42 ± 1.17	-12.46 ± 0.86	29.88 ± 1.45	-4.96 ± 1.45[d]

[a]Mean error calculated from equations (25) and (26) in Branham (2006).
[b]For heliocentric distance 0.2–3 kpc.
[c]For heliocentric distance 0.2–1 kpc.
[d]For heliocentric distance 0.2–3 kpc.

TABLE 5

VELOCITY DISPERSIONS FOR THE GIANT STARS

Spectral type	σ_x (km s^{-1})	σ_y (km s^{-1})	σ_z (km s^{-1})	Number of stars
O-B5	32.44 ± 5.04	26.16 ± 2.75	18.71 ± 2.39	107 total space motion
B6-9	39.25 ± 3.29	10.83 ± 1.16	14.07 ± 0.85	147 total space motion
A	26.95 ± 4.26	23.08 ± 2.14	16.46 ± 0.55	144 total space motion
F	36.89 ± 1.90	24.66 ± 1.16	17.97 ± 0.81	222 total space motion 369 tangential velocity
G	51.78 ± 0.55	42.81 ± 0.32	28.45 ± 0.22	658 total space motion 2417 tangential velocity
K	50.58 ± 0.99	42.42 ± 1.13	32.92 ± 0.56	880 total space motion
M	57.40 ± 1.67	45.86 ± 1.63	33.84 ± 1.02	480 total space motion

associated quantities such as $A - B$ and $-(A + B)$, the former equal to V_0/R_0 and the latter to (dV/dR), Perryman's Table 9.3 shows determinations up to 2007 and Table 4 post-2008 determinations, a total of 28. We see that A ranges from a minimum of 9.6 km s^{-1} kpc^{-1} to a maximum of 19 with a mean of 14.52 and a standard deviation of 2.52, again without discriminating as to number of stars, spectrum or luminosity class, or other indicators. The value given in Table 1 coincides well with this mean. For B the corresponding values are minimum of -24 km s^{-1} kpc^{-1}, maximum of -6.34, mean -12.63, and standard deviation of 3.30. Once again, the value for B given in Table 1 shows no anomaly. The only quantity that shows a possibly discrepant value is the K term, putatively significant only for the early stars, with determinations falling near 5 km s^{-1}, and close to 0 for later spectral types. The value in Table 1, large and moreover negative, seems discrepant. Its mean error, however, is also large and furthermore Branham (2009a) has shown that this term is sensitive to errors in the data; little credence, therefore, should be placed on its value. In a recent paper McMillan & Binney (2010) find that the most probable range for V_0/R_0 falls between 29.9 km s^{-1} kpc^{-1} and 31.6 km s^{-1} kpc^{-1}. Many of the values in Perryman's Table 9.3 and Table 3 fall outside of this range which, however, merely shows that quantities such as the distance to the centre of the Galaxy and the Sun's circular velocity are difficult to determine.

About the velocity ellipsoid little can be said because the only previous study of all of the G giants is that of Parenago (Delhaye 1965, p. 64), which used fewer stars, 345, and a different reduction method, the method of moments (Trumpler & Weaver 1962, pp. 283–286). The dispersions of the velocity ellipsoid are higher than those Parenago found, but this is a consequence of use of the SDP method; see Branham (2004).

Some insight, however, can be gained if we take these results not in isolation but rather conjointly with my previous studies of the giant stars. Because all of these studies use the same reduction method, variations caused by differences in the calculation of the velocity ellipsoid, such as use of the method of moments, will be minimized. Table 5 shows the velocity dispersions for all of the giant stars from O to M.

Two conclusions follow from an examination of Table 5. There is a clear break in all of the velocity dispersions between the F and the G giants. Dehnen & Binney (1998) confirmed this break, known as Parenago's discontinuity, for the main sequence stars, but it appears as if the giant stars also show the discontinuity. Use of the SVD to include stars for which only tangential velocities are available, the second conclusion, seems justified on more than just a statistical basis. Neither the F giants compared with earlier spectral types that use only total space motions nor the G giants with later spectral types exhibit glaring discrepancies, indicating that the tangential velocities are integrated well with the total space motions.

8. CONCLUSIONS

Semi-definite programming proves itself once again a useful tool for problems of Galactic kinematics by allowing one to combine a solution for the kinematical parameters such as the Oort constants with one for the coefficients of the velocity ellipsoid. The singular value decomposition allows one to incorporate stars for which only tangential velocities but no radial velocities are available into the calculation of the velocity ellipsoid. When applied to the G III stars the calculated solutions appear concordant with what others have found. A comparison with giant stars of other spectral types confirms that Parenago's discontinuity exists for the giant stars as well as main sequence stars.

REFERENCES

Airy, G. 1854, AJ, 4, 24
Aumer, M., & Binney, J. J. 2009, MNRAS, 397, 1286
Bobylov, V. V., & Bajkova, A. T. 2010, MNRAS, 408, 1788
Barbier-Brossat, M., & Figon, P. 2000, A&AS, 142, 217
Bochanski, J. J., Hawley, S. L., & West, A. 2011, AJ, 141, 98
Branham, R. L., Jr. 1990, Scientific Data Analysis (New York: Springer)
__________. 2003, Ap&SS, 288, 417
__________. 2004, A&A, 421, 977
__________. 2006, MNRAS, 370, 1393
__________. 2008, RevMexAA, 44, 29
__________. 2009a, MNRAS, 396, 1473
__________. 2009b, RevMexAA, 45, 215
__________. 2010, MNRAS, 409, 1269
Calafiore, G. 2002, IEEE Trans. Sys., Man Cyber., Part A, 32, 269
Dehnen, W., & Binney, J. J. 1998, MNRAS, 298, 387
Delhaye, J. 1965, in Galactic Structure, ed. A. Blaauw & M. Schmidt (Chicago: Chicago Univ. Press), 61
Eichhorn, H. 1990, in Errors, Bias and Uncertainties in Astronomy, ed. C. Jaschek & F. Murtagh (Cambridge: Cambridge Univ. Press), 149
ESA 1997, The Hipparcos and Tycho Catalogues, ESA SP-1200 (Noordwijik: ESA)
Fuchs, B., et al. 2009, AJ, 137, 4149
Høg, E., et al. 2000, The Tycho-2 Catalogue of the 2.5 Million Brightest Stars, CD-Rom version (Washington, DC: U. S. Naval Observatory)
Kerr, F. J., & Lynden-Bell, D. 1986, MNRAS, 221, 1023
McMillan, P. J., & Binney, J. J. 2010, MNRAS, 402, 934
Nagy, T. A. 1991, Documentation for the Machine-Readable Version of the Wilson General Catalogue of Stellar Radial Velocities, CD-Rom version (Lanham, MD: ST Systems Corp.)
Ogorodnikov, K. F. 1965, Dynamics of Stellar Systems (Oxford: Pergamon)
Perryman, M. 2008, Astronomical Applications of Astrometry (Cambridge: Cambridge Univ. Press)
Pourbaix, D. 1998, A&AS, 131, 377
Shen, M., & Zhang, H. 2010, Chin. J. Astron. Astrophys., 34, 89
Smart, W. M. 1968, Stellar Kinematics (New York: Wiley)
Smith, H., Jr., & Eichhorn, H. 1996, MNRAS, 281, 211
Stigler, S. M. 1977, Annals of Statistics, 5, 1055
Schönrich, R., Binney, J. J., & Dehnen, W. 2010, MNRAS, 403, 1829
Trumpler, R. J., & Weaver, H. F. 1962, Statistical Astronomy (New York: Dover)
van Leeuwen, F. 2007, Hipparcos, the New Reduction of the Raw Data (New York: Springer)
Vandenberghe, L., & Boyd, S. 1996, SIAM Review, 38, 49
Wonnacott, T. H., & Wonnacott, R. J. 1972, Introductory Statistics (2nd ed., New York: Wiley)
Yuan, F.-T., Zhu, Z., & Kong, D.-L. 2008, Chin. J. Astron. Astrophys., 8, 714

Richard L. Branham, Jr.: Instituto Argentino de Nivología, Glaciología y Ciencias Ambientales, C.C. 330, 5500 Mendoza, Argentina (richardbranham_1943@yahoo.com).

Revista Mexicana de Astronomía y Astrofísica, **47**, 211–217 (2011)

SPECKLE INTERFEROMETRY AT THE OBSERVATORIO ASTRONÓMICO NACIONAL. III

V. G. Orlov, V. V. Voitsekhovich, C. A. Guerrero, F. Ángeles, A. Farah Simon, E. Luna, and R. Vázquez Robledo

Instituto de Astronomía
Universidad Nacional Autónoma de México, Mexico

Received 2011 March 10; accepted 2011 April 6

RESUMEN

Se presentan las mediciones interferométricas de motas de estrellas binarias realizadas durante agosto de 2010 con el telescopio 1.5 m y en noviembre de 2010 con el telescopio de 2.1 m del Observatorio Astronómico Nacional en SPM (Mexico). Los resultados reportados aquí son 238 mediciones de 225 pares con una magnitud límite de $V = 12.2$. De éstas, 211 parejas presentan separaciones de menos de $1''$. El error medio obtenido en la separación es de $0''.02$ y en el ángulo de posición de 1.5°. Algunos de los ángulos de posición se determinaron con los 180° usuales de ambigüedad.

ABSTRACT

We present speckle interferometric measurements of binary stars performed during August of 2010 with the 1.5 m telescope and during November of 2010 with the 2.1 m telescope of the Observatorio Astronómico Nacional at SPM (Mexico). We report here the results of 238 measurements of 225 pairs with a primary limiting magnitude of $V = 12.2$; 211 of them have separations less than $1''$. The mean error in separation is $0''.03$ and 1.5° in position angle. Some of the position angles were determined with the usual 180° ambiguity.

Key Words: binaries: visual — stars: fundamental parameters — techniques: high angular resolution — techniques: interferometric

1. INTRODUCTION

This is the third paper in the serie of publications presenting the results of speckle interferometric observations of binary stars performed with telescopes of the Observatorio Astronómico Nacional (OAN) of the Instituto de Astronomía Universidad Nacional Autónoma de México. Regular speckle interferometric measurements of binary stars have been made with telescopes of the OAN since 2008 (Orlov et al. 2009). This paper presents the results of double star observations carried out with the 1.5 m and the 2.1 m Telescopes of Sierra San Pedro Mártir National Astronomical Observatory (OAN-SPM) in August and November of 2010. For these observations we developed a new detector. This detector is a combination of the CCD camera Watec 120N with a third generation image intensifier. The third generation image intensifier also allows us to carry out near infrared speckle interferometric observations. The results reported here consist of 238 measures of 225 pairs with a primary limiting magnitude of $V = 12.2$; 211 of them have separations of less than $1''$. In these speckle observations we confirmed and measured 38 binaries first detected by Hipparcos. The paper concludes with a tabulation of the observational results. The analysis of specklegram has been performed using the technique described by Tokovinin, Mason, & Hartkopf (2010).

2. BRIEF DESCRIPTION OF THE EQUIPMENT

The observations were performed with the CCD camera Wat-120N which is optically connected with the 18 mm third-generation image intensifier. Because the Watec CCD device Wat-120N is primarily designed for amateur astronomers, its limiting sensitivity (0.00002 lx) is not enough for speckle interferometry, so we had to use the third-generation image intensifier. We describe some technical details

Fig. 1. Odd and even half frames taken with good seeing conditions.

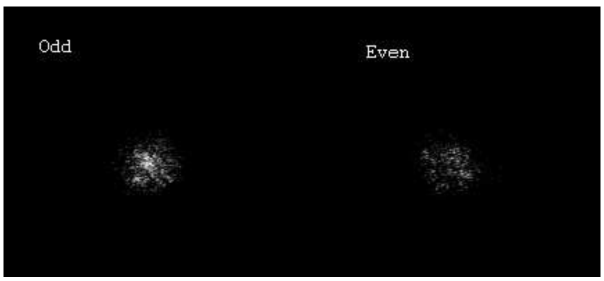

Fig. 2. Odd and even half frames taken with bad seeing conditions.

related to our CCD camera. The Wat-120N is an interline CCD camera where each single frame is a combination of two half-frames. One half-frame contains odd lines while the second one consists of the even lines. One half-frame is taken every 1/50th of a second. As one can see in Figure 1, in the case of good seeing conditions there are no difference between odd and even half frames. So, we can make the data processing for a complete frame 720×480. If the seeing conditions are not so good (Figure 2), the half-frames are very different. In this case we have to perform the data processing for the odd and even half-frames separately. Also we have to note that the Wat-120N does not have square pixels; this has to be taken into account during data processing.

The other disadvantage of Wat-120N is a manual control. We developed a simple Ethernet controller to resolve this problem. The set of our camera controls consists of three parts: gain control, gamma control, and on/off image intensifier switcher. The gain control has 8 values from 0 to 7 (Figure 3, the value 7 corresponds to the maximum gain). The gamma control allows three modes: linear (Off), low (Lo) and high (Hi). Two modes Lo and Hi are not linear and, if one needs measure accurate magnitude differences of components, they are not used during data recording. The last control is a switch on/off for the image intensifier.

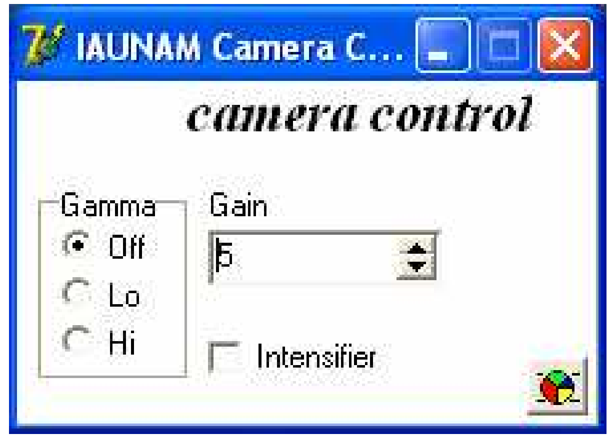

Fig. 3. Ethernet camera control.

3. OBSERVATIONS AND RESULTS

Data were recorded during the two observation campaigns carried out in August and November 2010. In August observations of 105 stars were performed at the OAN-SPM 1.5 m telescope. The atmospheric conditions (seeing and transparency) were excellent. For three nights in November 2010 we observed 120 stars with the 2.1 m telescope of OAN-SPM under poor atmospheric conditions. All the measurements were made through the R filter with a 640/130 nm bandpass window. In these speckle observations we measured 38 new binaries detected by Hipparcos (ESA 1997). For each star, a typical observing procedure involved the accumulation of one set of 998 frames (1996 half-frames). One frame consists of a two-dimensional 440×400 array of 8-bit numbers. After the calibration we determined that the pixel scales are equal to $0.039''$/px and $0.038''$/px for the 2.1 m telescope and for the 1.5 m telescope, respectively. Tables 1 and 2 contain the results of the measurements of binary stars performed at the 1.5 m and 2.1 m telescopes. The format for the presentation of these measurements is the same as in our previous publication (Orlov et al. 2010). The first column contains the epoch-2000 coordinates in the format used in the Washington Double Star (WDS) Catalog (Worley & Douglass 1997). The second column gives the name of the star or the discoverer designation. The third column gives the epoch of the observation in fractional Besselian years. The two following columns contain the measured position angles given in degrees and the angular distances in arcseconds. The last three columns show ephemerides calculated for the date of observation and references to publications in which orbital elements can be found (Hartkopf & Mason 2003).

TABLE 1

SPECKLE MEASUREMENTS ON THE 1.5 M TELESCOPE

WDS ($\alpha, \delta J2000.0$)	Disc. Name	Date Besselian	P.A. (deg)	Sep. (arcsec)	P.A. Orb. (deg)	Sep. Orb. (arcsec)	Reference
00008+1659	BAG 18	2010.6349	0.7	0.63			
00024+1047	A 1249	2010.6349	72.9	0.21	74.5	0.16	Zirm (2003)
00039+2759	A 429	2010.6349	331.4	0.53			
00039+2759 AC	A 429	2010.6349	289.4	5.26			
00061+0943	HDS 7	2010.6350	178.4	0.19			
00073+2058	HDS 12	2010.6350	191.3	1.35			
00074+2029	KU 3	2010.6350	76.2	0.92			
00090+2339	HU 402	2010.6350	68.7	0.56			
00095+1907	COU 247	2010.6350	249.9	0.30	258.0	0.37	Zirm (2003)
00260+1905	HDS 59	2010.6350	264.7	0.79			
00262+2827	COU 446	2010.6350	312.9	0.85			
00279+2334	BU 779	2010.6350	246.4	0.62			
00287+2134	HU 601	2010.6350	307.4	0.63			
00295+1501	HEI 200	2010.6350	62.9	0.76			
00307+1339	HDS 66	2010.6350	267.3	0.98			
00324+2147	HDS 72	2010.6351	39.4	0.22			
00445+1956	TDS1595	2010.6351	273.3	0.84			
00470+2315	HU 413	2010.6351	313.7	0.35	317.2	0.38	Olevic (2002)
00487+1841	BU 495	2010.6351	253.9	0.28	250.4	0.31	Scardia et al. (2000)
00511+2853	COU 447	2010.6351	39.4	0.84			
00536+1911	COU 252	2010.6351	96.9	0.31			
00557+1706	HEI 94	2010.6351	255.2	1.04			
01007+1659	HEI 96	2010.6351	68.2	0.38			
01024+0504	HDS 135	2010.6351	90.7	0.65	91.1	0.66	Balega et al. (2006)
01028+0214	A 2308	2010.6351	292.2	0.36	293.0	0.27	Baize (1984)
01041+2635	COU 351	2010.6351	245.9	0.77			
01055+2107	AG 14	2010.6351	315.2	0.76	263.5	0.55	Heintz (1998)
01093+2428	COU 78	2010.6351	358.2	0.76			
01166+1831	HDS 169	2010.6351	240.5	0.61			
17452+2107	COU 630	2010.6352	115.2	0.22			
17453+1750	TDT 488	2010.6352	9.7	0.74			
17470+2915	TDS 881	2010.6352	243.2	1.01			
17472+1502	HU 1288	2010.6352	163.2	0.40			
17502+2704	TDT 526	2010.6352	147.2	0.83			
17506+1517	FOX 22	2010.6352	339.2	0.95			
17513+1723	TDT 536	2010.6352	62.2	1.04			
17571+1547	MCT 10	2010.6352	281.2	1.07			
18031+2702	TDT 653	2010.6352	26.4	0.74			
18032+2603	HO 565	2010.6352	91.4	0.19			
18086+1700	HDS2555	2010.6352	111.7	0.48			
18086+1838	HU 314	2010.6352	79.2	0.27			
18088+1923	TDT 707	2010.6352	68.2	0.61			
18303+1907	COU 508	2010.6352	254.4	0.89			
18312+2516	A 248	2010.6352	34.2	0.48			
18382+1426	HU 675	2010.6352	61.2	0.25			
18389+2324	TDT 972	2010.6352	48.7	0.85			
18396+2356	TDT 980	2010.6352	101.9	0.25			
18406+2636	COU 641	2010.6352	54.2	0.57			
18421+2753	TDT1009	2010.6352	268.4	0.58			
18443+2720	TDS 941	2010.6352	92.4	0.85			
19073+2432	A 262	2010.6352	266.9	0.17			
19224+2517 Aa, Ab	TDT1405	2010.6353	159.9	0.61			
19266+2619	HDS2763	2010.6353	209.2	0.76			
19276+1806	TDT1471	2010.6353	105.2	0.59			
19282+1507	TDT1476	2010.6353	330.4	0.73			
19284+2734	TDT1480	2010.6353	167.4	0.66			
19409+1523	HEI 74	2010.6353	109.9	0.86			
19421+1533	HU 1305	2010.6353	102.2	0.42			
19464+2438	TDT1727	2010.6353	222.7	0.61			
19477+1913	TDT1759	2010.6344	354.2	0.65			

TABLE 1 (CONTINUED)

WDS ($\alpha, \delta J2000.0$)	Disc. Name	Date Besselian	P.A. (deg)	Sep. (arcsec)	P.A. Orb. (deg)	Sep. Orb. (arcsec)	Reference
20216+2346	STF2672	2010.6344	345.7	0.69			
20227+2837	COU1169	2010.6344	64.4	0.26			
20227+2930	TDT2218	2010.6344	292.4	0.41			
21067+2321	TDT2755	2010.6344	215.7	0.84			
21068+2306	HU 364	2010.6345	96.7	0.21			
21083+2913	COU1331	2010.6345	36.2	0.30			
21085+2332	TDT2781	2010.6345	317.9	0.75			
21091+1906	COU 329	2010.6345	99.9	0.64			
21091+2922	COU1332	2010.6345	21.2	0.23			
21096+2632	COU 529	2010.6345	218.7	0.36			
21106+1650	HU 367	2010.6345	339.2	0.30			
21107+1334	HEI 186	2010.6345	262.2	0.17			
21109+2925	BAG 29	2010.6345	279.7	0.24			
21115+2144	COU 227	2010.6345	112.9	0.51	213.0	0.13	Couteau (1995)
21125+2821	HO 152	2010.6345	135.4	0.22	132.8	0.27	Scardia et al. (2002)
21461+2448	TDT3149	2010.6345	218.4	0.65			
21466+1929	COU 431	2010.6345	183.2	0.46			
21468+2718	HO 608	2010.6346	127.4	0.57			
21481+2100	HU 378	2010.6346	297.4	0.18			
21488+2439	TDT3169	2010.6346	350.2	0.82			
21500+2157	TDT3184	2010.6346	170.7	2.56			
21521+2748	HO 171	2010.6346	341.7	0.73			
22196+2107	HU 383	2010.6346	29.9	0.36			
22202+2931	BU 1216	2010.6346	278.2	0.91			
22217+1125	TDT3484	2010.6346	256.7	0.26			
22392+2014	HU 393	2010.6347	226.4	0.87			
22396+2822	A 413	2010.6347	14.9	1.09			
22457+2924	HO 481	2010.6347	287.2	0.44			
22474+1749	WSI 91	2010.6347	113.7	0.26			
22479+1259	HU 985	2010.6347	136.4	0.70	139.6	0.67	Seymour et al. (2002)
23024+1837	HU 398	2010.6347	287.9	0.47	293.3	0.45	Baize (1981)
23038+2851	TDT3868	2010.6347	10.2	0.17			
23039+2512	COU 142	2010.6347	190.4	0.50			
23361+2027	TDT4118	2010.6347	1.9	0.58			
23368+2346	HU 498	2010.6348	298.2	0.67			
23379+2510	COU 441	2010.6348	10.7	0.69			
23380+1253	A 1241	2010.6348	9.9	0.62			
23401+1258	HU 1325	2010.6348	30.2	0.83	31.6	0.63	Olevic & Jovanovic (2001)
23401+1258	HU 1325				26.0	0.84	Scardia (2003)
23431+1150	A 1242	2010.6348	337.7	0.99	337.4	0.96	Ling (2004)
23435+1652	HEI 196	2010.6348	167.4	0.83			
23465+1705	EGB 8	2010.6348	86.4	1.07			
23470+1726	TDT4190	2010.6348	33.9	0.55			
23475+1729	TDT4195	2010.6348	315.2	0.70			
23486+1622	HEI 91	2010.6348	152.7	0.68			
23491+1915	COU 343	2010.6349	102.7	0.17			
23504+2620	COU 545	2010.6349	315.7	0.73			

4. CONCLUSION

We have presented the results of binary star observations focused on binaries from the WDS catalogue. In particular, we have been interested in new binaries discovered by Hipparcos. We confirmed 38 new binaries detected by Hipparcos. The main aim of this study was in the selection of binaries with a fast relative motion allowing to obtain candidates for determinations of new orbits. From our observation results we can also conclude that our new detector based on Wat-120N CCD is suitable for speckle observations with the OAN-based telescopes.

The speckle interferometry program at the OAN telescopes is supported by the Dirección General de Asuntos del Personal Académico (Universidad Nacional Autónoma de México, Mexico) under projects IN104910 and IN113308 (PAPIIT).

TABLE 2

SPECKLE MEASUREMENTS ON THE 2.1 M TELESCOPE

WDS ($\alpha, \delta J2000.0$)	Disc. Name	Date Besselian	P.A. (deg)	Sep. (arcsec)	P.A. Orb. (deg)	Sep. Orb. (arcsec)	Reference
00004+2749	TDS1238	2010.8836	87.9	0.85			
00008+1659	BAG 18	2010.8836	0.9	0.59			
00055+3406	HU 1201	2010.8919	304.2	0.21	307.19	0.192	Zirm (2003)
00085+3456	HDS 17	2010.8919	78.9	0.12	79.71	0.126	Cvetkovic (2010)
00260+1905	HDS 59	2010.8836	263.7	0.84			
00271+1852	TDS 19	2010.8836	137.4	0.90			
00295+1501	HEI 200	2010.8836	60.7	0.77			
00307+1339	HDS 66	2010.8836	266.9	0.93			
00312+0237	TDS1505	2010.8836	76.2	0.76			
00324+2147	HDS 72	2010.8836	38.9	0.21			
00344+2411	COU 350	2010.8837	140.9	0.94			
00353+2456	TDS1533	2010.8837	28.7	0.77			
00364+1213	A 807	2010.8837	233.9	0.86			
00374+0900	A 808	2010.8837	181.4	0.23			
00404+2504	COU 75	2010.8837	52.2	0.48			
00429+2047	A 2205	2010.8837	6.9	0.34	4.37	0.306	Baize (1989)
00487+1841	BU 495	2010.8837	247.7	0.28	249.789	0.314	Scardia et al. (2000)
01014+1155	BU 867	2010.8837	354.2	0.63	354.475	0.626	Hartkopf et al. (2008)
01046+2558	COU 253	2010.8837	95.9	0.95			
01055+2107	AG 14	2010.8837	314.7	0.76	263.073	0.549	Heintz (1998)
01072+3839	A 1516	2010.8920	4.7	0.22	355.60	0.145	Hartkopf et al. (2000)
01080+1204	A 2101	2010.8837	258.9	0.64			
01093+2428	COU 78	2010.8837	357.9	0.89			
01106+4917	COU2156	2010.8920	161.9	0.45			
01112+4113	A 655	2010.8920	353.9	0.33	349.24	0.317	Cvetkovic & Novakovic (2006)
01148+6056	BU 1100	2010.8920	353.4	0.33	351.21	0.268	Muller (1955)
01148+6056	BU 1100				153.72	0.199	Starikova (1977)
01178+4945	HU 520	2010.8920	167.4	0.33			
01251+4537	A 939	2010.8921	194.9	0.23	226.87	0.175	Starikova (1983)
01283+4247	AC 14	2010.8838	91.4	0.78			
01283+4247	AC 14	2010.8921	91.4	0.75			
01449+1951	A 2322	2010.8921	208.2	1.26			
01502+2702	BU 1313	2010.8921	153.7	0.53			
01510+2551	COU 452	2010.8921	179.2	0.23			
01513+6021	A 951	2010.8921	225.9	0.43			
01535+4437	STF3113	2010.8838	278.2	0.66			
01550+5817	A 954	2010.8921	198.7	0.63			
01551+5958	A 955	2010.8838	106.4	1.00			
01573+4812	A 818	2010.8838	204.7	0.28			
01584+5154	COU2559	2010.8838	65.4	0.40			
01586+3334	HDS 267	2010.8838	161.7	0.26			
01586+3334	HDS 267	2010.8922	165.7	0.23			
01588+3826	TDS2077	2010.8838	237.2	0.41			
02016+4107	COU1510	2010.8838	133.4	0.41			
02019+4831	COU2009	2010.8839	60.2	0.56			
02063+4936	COU2561	2010.8839	123.4	0.77			
02085+5852	HDS 284	2010.8839	77.7	0.22			
02085+5852	HDS 284	2010.8922	76.7	0.24			
02279+4523	COU2011	2010.8922	59.7	0.34			
02314+4234	A 660	2010.8922	311.4	0.52			
02323+3542	A 1927	2010.8922	192.2	0.81			
02382+4604	A 1278	2010.8922	311.7	0.22	286.29	0.231	Hartkopf & Mason (2001)
02417+5529	A 1280	2010.8923	12.7	0.33			
02454+5634 Aa, Ab	MLR 599	2010.8923	359.7	0.23			
03032+4121	COU1381	2010.8839	71.2	0.24			
03041+5040	COU2567	2010.8839	62.2	0.41			
03058+4818	COU2016	2010.8839	58.7	0.15			
03061+5144	COU2454	2010.8839	24.9	0.41			
03068+5813	TDS2446	2010.8839	351.4	0.77			

TABLE 2 (CONTINUED)

WDS ($\alpha, \delta J2000.0$)	Disc. Name	Date Besselian	P.A. (deg)	Sep. (arcsec)	P.A. Orb. (deg)	Sep. Orb. (arcsec)	Reference
03076+5230	MLR 658	2010.8839	80.2	0.40			
03081+4327	COU1679	2010.8839	1.9	0.50			
03084+4736	COU2017	2010.8839	9.4	0.28			
03129+5126	COU2568	2010.8839	309.4	0.40			
03138+3733 Aa, Ab	COU1075	2010.8839	40.4	0.89			
03141+5023	HU 543	2010.8840	106.9	0.29			
03150+3543	HO 502	2010.8840	15.2	0.84			
03250+4013	HU 1058	2010.8923	112.4	0.82			
03264+3520	HDS 430	2010.8923	278.2	0.23			
03279+4551	COU1687	2010.8840	290.4	0.77			
03279+4614	COU1686	2010.8840	262.7	0.53			
03354+3529	POP 83	2010.8923	265.9	0.51			
03484+5202	HU 546	2010.8840	26.2	0.30	28.527	0.358	Hartkopf & Mason (2009)
03499+4314	COU1691	2010.8840	318.4	0.38			
03503+4403	COU1692	2010.8840	37.9	0.53			
03522+5357	MLR 665	2010.8840	335.4	0.37			
03546+4554	TDS 121	2010.8840	113.4	0.97			
03586+4605	COU1696	2010.8840	139.2	0.86			
03594+4321	A 1708	2010.8840	338.2	0.82			
04016+5044	COU2458	2010.8841	141.2	0.65			
04017+5611	HDS 507	2010.8841	133.4	0.45			
04035+4211	A 1709	2010.8923	222.7	1.01			
04050+4936	COU2267	2010.8841	106.9	0.42			
04081+3407	COU1082	2010.8923	57.9	0.33			
04081+4535	COU2025	2010.8923	339.2	0.33			
04159+3142	STT 77	2010.8924	294.2	0.53	295.60	0.550	Starikova (1985)
04284+4914	HDS 575	2010.8924	315.7	0.45			
04302+5343	A 1300	2010.8841	148.2	0.85			
04306+5014	HU 550	2010.8841	298.4	0.53			
04308+4550	A 1007	2010.8841	161.9	0.27			
04310+4159	HDS 583	2010.8924	116.7	0.21			
04378+5249	MLR 696	2010.8841	66.2	1.05			
04381+5707	HDS 598	2010.8924	333.9	0.23			
04430+5712	A 1014	2010.8924	17.4	0.34	18.19	0.346	Brendley & Hartkopf (2007)
04477+4014	A 1545	2010.8924	95.7	0.45			
04542+4935 B	STF 603	2010.8925	105.9	1.13			
04542+4935 A	STF 603	2010.8925	99.4	2.18			
04599+4319	A 1551	2010.8841	273.4	0.23			
05038+3813	TDS3054	2010.8841	4.2	0.26			
05044+2139	COU 154	2010.8869	303.9	0.17			
05044+2938	A 1024	2010.8869	332.4	0.73			
05047+4458	A 1022	2010.8842	342.2	0.62			
05057+4516	COU2463	2010.8842	40.9	0.53			
05061+4222	COU2464	2010.8842	181.4	0.59			
05078+3723	COU1529	2010.8842	358.2	0.59			
05085+3755	COU1531	2010.8925	45.7	0.22			
05106+4924	HDS 684	2010.8925	57.2	0.46			
05119+4459	TDS3105	2010.8842	214.2	0.65			
05133+4940	COU2578	2010.8842	109.4	0.47			
05140+3655	POP 140	2010.8925	166.4	0.32			
05195+3809	COU1870	2010.8925	19.2	0.43			
05208+3329	COU1231	2010.8925	165.9	0.64			
05240+3238	COU1090	2010.8925	233.9	0.22			
05267+3857	HDS 714	2010.8925	262.4	0.45			
05310+2635	COU 574	2010.8869	136.2	0.32			
05319+2141	COU 268	2010.8869	164.2	0.72			
05326+4422	HDS 729	2010.8926	163.7	0.22			
05350+1838	A 2354	2010.8870	310.9	0.43			
05357+2054	COU 270	2010.8870	42.4	0.71			
06000+4643	A 1727	2010.8842	247.4	0.62			
06016+4111	COU2049	2010.8843	233.9	1.28			

TABLE 2 (CONTINUED)

WDS ($\alpha, \delta J2000.0$)	Disc. Name	Date Besselian	P.A. (deg)	Sep. (arcsec)	P.A. Orb. (deg)	Sep. Orb. (arcsec)	Reference
06025+3620	HU 1236	2010.8843	37.2	0.41			
06049+3211	HU 827	2010.8843	74.4	0.23			
06060+2331	HU 450	2010.8870	244.2	0.44			
06065+1832	A 2444	2010.8870	181.4	0.12			
06073+1848	COU 471	2010.8870	159.2	0.34			
06087+1724	STF 849	2010.8870	241.4	0.91			
06097+1630	A 2514	2010.8870	102.7	0.24			
06097+2914	A 54	2010.8870	332.4	0.55			
06117+2846	A 55	2010.8870	259.7	0.43			
06142+1217	TDS3652	2010.8870	17.9	0.43			
06150+1649	A 2044	2010.8871	34.9	0.34			
06152+2917	COU1103	2010.8871	51.9	0.23			
06185+2241	HDS 863	2010.8871	50.7	0.22			

REFERENCES

Baize, P. 1981, A&AS, 44, 199

_________. 1984, A&AS, 56, 103

_________. 1989, A&AS, 78, 125

Balega, I. I., Balega, Y. Y., Hofmann, K.-H., Malogolovets, E. V., Schertl, D., Shkhagosheva, Z. U., & Weigelt, G. 2006, A&A, 448, 703

Brendley, M., & Hartkopf, W. I. 2007, IAUDS Inf. Circ. 163

Couteau, P. 1995, VizieR Online Data Catalog 1209, http://cdsarc.u-strasbg.fr/viz-bin/Cat?I/209A

Cvetković, Z., & Novaković, B. 2006, Serb. Astron. J., 173, 73

Cvetkovic, Z. 2010, IAUDS Inf. Circ. 172

ESA 1997, The Hipparcos and Tycho Catalogues, ESA SP-1200 (Noordwijik: ESA)

Hartkopf, W. I., & Mason, B. D. 2001, IAUDS Inf. Circ. 145

_________. 2003, Sixth Catalog of Orbits of Visual Binary Stars (Washington: USNO), http://ad.usno.navy.mil/wds/orb6.html

_________. 2009, AJ, 138, 813

Hartkopf, W. I., Mason, B. D., & Rafferty, T. 2008, AJ, 135, 1334

Hartkopf, W. I., et al. 2000, AJ, 119, 3084

Heintz, W. D. 1998, ApJS, 117, 587

Ling, J. F. 2004, IAUDS Inf. Circ. 154

Muller, P. 1955, J. Obs., 38, 58

Olevic, D. 2002, IAUDS Inf. Circ. 147

Olevic, D., & Jovanovic, P. 2001, Serb. Astron. J., 163, 5

Orlov, V. G., Voitsekhovich, V. V., Mendoza-Valencia, G. A., Svyryd, A., Rivera, J. L., Ortiz, F., & Guerrero, C. A. 2009, RevMexAA, 45, 155

Orlov, V. G., Voitsekhovich, V. V., Rivera, J. L., Guerrero, C. A., & Ortiz, F. 2010, RevMexAA, 46, 245

Scardia, M. 2003, IAUDS Inf. Circ. 149

Scardia, M., Prieur, J.-L., Aristidi, E., & Koechlin, L. 2000, Astron. Nachr., 321, 255

Scardia, M., Prieur, J.-L., Koechlin, L., & Aristidi, E. 2002, IAUDS Inf. Circ. 146

Seymour, D., Mason, B. D., Hartkopf, W. I., & Wycoff, G. L. 2002, AJ, 123, 1023

Starikova, G. A. 1977, Astron. Tsirk. 961, 7

_________. 1983, Soviet Astron. Lett., 9, 189

_________. 1985, Trudy Gos. Astron. Inst. Sternberga, 57, 243

Tokovinin, A., Mason, B. D., & Hartkopf W. I. 2010, AJ, 139, 743

Worley, C. E., & Douglass, G. G. 1997, A&AS, 125, 523

Zirm, H. 2003, IAUDS Inf. Circ. 151

F. Ángeles, A. Farah Simon, C. A. Guerrero, E. Luna, V. G. Orlov, R. Vázquez Robledo, and V. V. Voitsekhovich: Instituto de Astronomía, Universidad Nacional Autónoma de México, Apdo. Postal 70-264, Cd. Universitaria, 04510 México D.F., México (fernando.angeles@gmail.com, farah, cguerrero@astro.unam.mx, eala@astrosen.unam.mx, orlov, rvazquez@astro.unam.mx, vvv.spm@gmail.com).

Revista Mexicana de Astronomía y Astrofísica, **47**, 219–234 (2011)

UPPER MAIN SEQUENCE STARS WITH ANOMALOUS ABUNDANCES. THE HGMN STARS HR 3273, HR 8118, HR 8567 AND HR 8937

C. Saffe, N. Núñez, and H. Levato

Instituto de Ciencias Astronómicas, de la Tierra y del Espacio (ICATE)
and Facultad de Ciencias Exactas, Físicas y Naturales
Universidad Nacional de San Juan, Argentina

Received 2010 December 13; accepted 2011 April 14

RESUMEN

Este trabajo es parte de un estudio para verificar posibles tendencias de las abundancias en estrellas HgMn con los parámetros estelares, rotación y edad. Presentamos un análisis de las estrellas HR 3273, HR 8118, HR 8567 y HR 8937. Utilizamos espectros echelle tomados con el telescopio de 2.1 m del CASLEO y modelos de atmósferas de ATLAS9. El He resultó por debajo del valor solar para las estrellas HgMn. El O resultó levemente sobreabundante en HR 3273 y HR 8567. MgII resultó por debajo excepto para HR 8118. El SiII resultó aproximadamente solar en HR 8118 y HR 8937, y por debajo en HR 3273 y HR 8567. El Fe resultó levemente sobreabundante en HR 8118 y HR 8937 y subabundante en HR 3273 y HR 8567. Las especies Sc, Ti, Cr, Mn, Sr, Y y Zr resultaron sobreabundantes mientras que el Ni resultó estar por debajo del valor solar.

ABSTRACT

This work is part of our current study for verifying a possible relation between abundances of HgMn stars with stellar parameters, rotation and age. We present an analysis of the stars HR 3273, HR 8118, HR 8567 and HR 8937. We used echelle spectra taken with the CASLEO 2.1 m telescope and ATLAS9 model atmospheres. HeI was underabundant for the HgMn stars. O was slightly underabundant in HR 3273 and HR 8567. MgII was underabundant except for HR 8118. SiII was close to solar in HR 8118 and HR 8937, and underabundant in HR 3273 and HR 8567. Fe was slightly underabundant in HR 3273 and HR 8567, and slightly overabundant in HR 8118 and HR 8937. The species Sc, Ti, Cr, Mn, Sr, Y and Zr were overabundant while Ni was underabundant.

Key Words: stars: chemically peculiar — stars: individual (HR 3273, HR 8118, HR 8567, HR 8937)

1. INTRODUCTION

The mercury-manganese (HgMn) stars belong to a group of chemically peculiar (CP) stars observed in the upper main sequence. Their hydrogen spectral types are usually B7-B9 with effective temperatures between 10000 K and 15000 K. HgMn stars show typically intensified lines of Hg (up to ∼5 dex), Mn (up to ∼3 dex) and a deficiency of He. This group shows an unusually high proportion of multiple systems: more than two thirds of them are spectroscopic binaries (SBs), many of which are double-lined systems (e.g., Hubrig & Mathys 1995). They are usually slow rotators (e.g., Abt, Chaffee, & Suffolk 1972) and they show no evidence of large-scale organized magnetic fields (e.g., Auriére et al. 2007, 2010; Makaganiuk et al. 2011).

The relation of the anomalous abundances and stellar parameters is not totally clear. Some authors found no correlation between the total HgII abundance and the effective temperature (e.g., Smith 1997; Woolf & Lambert 1999), while Dolk, Wahlgren, & Hubrig (2003) found a possible correlation for a sample of 31 HgMn stars. On the other hand, Smith & Dworetsky (1993) and later Jomaron, Dworetsky,

TABLE 1

OBSERVATIONAL DATA FOR THE SAMPLE OF HGMN STARS

Parameter	HR 3273	HR 8118	HR 8567	HR 8937	References
$B-V$	−0.08	−0.08	−0.04	−0.10	R1,R6,R8
$U-B$	−0.38	−0.32	−0.37	−0.37	R1,R6
V	6.42	6.76	6.36	4.37	R1,R6,R9
$b-y$	−0.020	−0.028	−0.018	−0.046	R2
m_1	0.090	0.117	0.101	0.125	R2
c_1	0.710	0.801	0.678	0.677	R2
β	2.704	2.780	2.737	2.776	R2
J	6.515	6.848	6.410	4.477	R7
H	6.607	6.925	6.493	4.669	R7
K	6.585	6.907	6.467	4.611	R7
Sp. Type	B9p (HgMn)	B9p Hg(Mn?)	B8(Mn), HgMn	B9.5 IVp (HgMn)	R3,R4,R5 R10, R11

References: R1: Cousins & Stoy (1962), R2: Hauck & Mermilliod (1998), R3: Andersen & Nordström (1977), R4: Renson & Manfroid (2009), R5: Wolff & Wolff (1974), R6: Corben & Stoy (1968) , R7: Cutri et al. (2003), R8: Crawford (1963), R9: Corben (1971), R10: Cowley et al. (1969), R11: Houk (1982).

& Allen (1999) found a dependence between MnI and MnII abundances and temperature. The authors suggest that difussion takes place in the atmospheres of these stars, but probably affected by other factors such as rotation and evolutionary state. This research is part of our current program for deriving elemental abundances among field CP stars and members of open clusters. The motivation of our work is to derive abundances for a sample of HgMn stars to determine possible relations with their fundamental parameters and other factors such as rotation, evolutionary state and age. In particular in this paper we report the results of four CP stars of the HgMn class, HR 3273, HR 8118, HR 8567 and HR 8937.

The star HR 3273 was classified as an HgMn star by Andersen & Nordström (1977). They studied ∼70 bright southern stars using coudé spectrograms of 20 Å/mm, taken with the ESO 1.5 m telescope at La Silla, Chile. The authors identified HR 3273 as a B9p (HgMn) star, with no definite variation in their spectra. UBV photoelectric photometry was published by Cousins & Stoy (1962). $uvby-\beta$ photometry was provided by Hauck & Mermilliod (1998), Eggen (1977) and Gronbech & Olsen (1976). JHK infrared photometry was presented by Cutri et al. (2003).

The star HR 8118 was classified as Hg(Mn?) star in the spectroscopic study of the Bright Star Catalogue by Cowley et al. (1968). They identified the line HgII $\lambda\lambda$3984 in the spectra taken at the Yerkes observatory with a dispersion of 125 Å/mm. Then the star was listed and classified as B9p Hg(Mn?) in the study of A bright stars (Cowley et al. 1969). UBV photometry was obtained by Crawford (1963) and Corben (1971). $uvby-\beta$ photometry was published by Gronbech & Olsen (1977) and Hauck & Mermilliod (1998).

The star HR 8567 was classified as HgMn star by Wolff & Wolff (1974). They studied 194 stars of types B4-B9 and identified in their sample 24 HgMn stars. The authors used UV spectrograms with a dispersion of 50 Å/mm in the region 3440–3500 Å. In this spectral range there are several strong lines of MnII. HR 8567 was classified as B8(Mn) star in the catalog of Renson & Manfroid (2009) and listed as HgMn star in the catalog of Schneider (1981). UBV photoelectric photometry was published by Rybka (1969) and Corben & Stoy (1968). $uvby-\beta$ photometry was obtained by Hauck & Mermilliod (1998), Gronbech & Olsen (1976) and Eggen (1977), and JHK infrared photometry was presented by Cutri et al. (2003).

The star HR 8937 was classified as B9p by Bertaud (1958) and then listed as B9.5 IVp (HgMn) in the Michigan Catalogue of Two Dimensional Spectral Types (Houk 1982). UBV photoelectric photometry have been provided by Abt & Golson (1962) and Irwin (1961). $uvby$ photometry was published by Crawford, Barnes, & Golson (1970) and Hauck & Mermilliod (1998), and their β photometric index were determined by Strauss & Ducati (1981).

Table 1 presents some relevant observational data for the sample of HgMn stars, HR 3273, HR 8118, HR 8567 and HR 8937.

2. OBSERVATIONAL MATERIAL AND LINE IDENTIFICATIONS

The stellar spectra of the stars were obtained at Complejo Astrónomico El Leoncito (CASLEO) between April 21 and 23, 2004. We used the *Jorge Sahade* 2.15 m telescope that fed the EBASIM echelle spectrograph through an optical fiber. The spectra were recorded on a TEK1024 (1024×1024 pixels) CCD detector. The EBASIM spectrograph uses gratings as cross dispersers. We have used one grating with 226 lines mm^{-1} centered at $\sim$5000 Å. Three spectra of each star were obtained, covering the visual range $\sim\lambda\lambda$3800–5900 Å. The S/N ratio of the spectra is around 250 and the resolving power of the spectrograph is approximately 40000. Table 2 gives the spectral coverage of the 55 orders of the EBASIM spectrograph[1]. It contain echelle orders overlapping in $\sim\lambda\lambda$3762–5644 Å and increasing gaps of 1–4 Å for $\lambda \gtrsim 5645$ Å.

The spectra were reduced using IRAF[2] standard procedures for echelle spectra. We applied bias and flat corrections and then normalized order by order with the *continuum* task, using 7–9 order Chebyshev polynomials. We also corrected the scattered light in the spectrograph (*apscatter* task). We fitted the background with a linear function on both sides of the echelle apertures, using the task *apall.* Extensive description of the characteristics of the reduction technique and some results obtained with the observational material, have been previously published (e.g., Saffe & Levato 2009). The equivalent widths were measured by integrating the profiles across the stellar metallic lines using the *splot* task. There are no differences among the equivalent width measurements of the same lines in different spectra.

We used Gaussian profiles to fit the stellar lines. This is an interactive process in which the IRAF user marks two continuum points in the spectra and then the program fits a single line profile (splot task). IRAF uses a fixed linear continuum through the stellar line. The fitting uses an interactive algorithm based on the Levenberg-Marquardt method. The successive iterations tend to improve the fit by varying the parameters along the gradient of improvement in the χ^2 function. The final fit is overplotted on the spectrum of the star and the user decides if the fit is satisfactory or not. The center, continuum at the center, core intensity, integrated flux, equivalent width and FWHMs are printed and saved in a log file. All the parameters except the continuum are based on the fitted analytic profiles.

Pintado & Adelman (2003) compared EBASIM and DAO (Dominion Astrophysical Observatory) equivalent widths corresponding to echelle and coudé spectra, respectively. The scattered light is usually easier to measure in the latter case. They used Gaussian profiles for the EBASIM spectra and rotational profiles for the DAO spectra, due to the lower res-

TABLE 2

SPECTRAL COVERAGE FOR THE EBASIM ECHELLE SPECTROGRAPH USING THE GRATING OF 226 LINES mm^{-1}

Order	Range [Å]	Order	Range [Å]
1	3762–3798	29	4625–4670
2	3787–3823	30	4663–4708
3	3813–3849	31	4702–4748
4	3839–3875	32	4741–4788
5	3865–3902	33	4781–4828
6	3891–3929	34	4822–4869
7	3918–3956	35	4864–4911
8	3946–3984	36	4906–4954
9	3973–4012	37	4949–4998
10	4002–4041	38	4993–5042
11	4030–4070	39	5037–5087
12	4059–4099	40	5083–5133
13	4088–4129	41	5129–5180
14	4118–4159	42	5176–5227
15	4149–4190	43	5224–5276
16	4179–4221	44	5273–5325
17	4210–4252	45	5323–5375
18	4242–4284	46	5374–5426
19	4274–4317	47	5425–5478
20	4307–4350	48	5478–5533
21	4340–4383	49	5533–5588
22	4373–4417	50	5588–5644
23	4407–4451	51	5645–5701
24	4442–4486	52	5703–5760
25	4478–4522	53	5762–5820
26	4514–4558	54	5822–5881
27	4550–4594	55	5884–5943
28	4587–4632		

[1]Due to modifications in the configuration of the EBASIM spectrograph, the spectral coverage could slightly vary in different observing runs.

[2]IRAF is distributed by the National Optical Astronomical Observatories which is operated by the Association of Universities for Research in Astronomy, Inc., under a cooperative agreement with the National Science Foundation.

olution of the EBASIM data. For 170 unblended lines of the star α Sex in the region 3840–4930 Å, they obtained nearly the same scale for the equivalent widths. Then, they did not apply any additional correction to the equivalent widths of the EBASIM spectra. However, we caution that the comparison done in Pintado & Adelman (2003) needs to be extended and made more robust. The authors plan to extend it with high S/N (> 500) spectra of sharp-lined stars.

The stellar lines of the HgMn stars were identified using the same procedure of previous papers (Saffe, Levato, & López-García 2004, 2005; Saffe & Levato 2009). We used the general references of *A Multiplet Table of Astrophysical Interest* (Moore 1945) and *Wavelengths and Transition Probabilities for Atoms and Atomic Ions*, Part 1 (Reader et al. 1980) as well as the more specialized references for P II (Svendenius, Magnusson, & Zetterberg 1983), Mn II (Iglesias & Velasco 1964), Fe II (Dworetsky 1971; Johansson 1978; Guthrie 1985) and Y II (Nilsson, Johansson, & Kurucz 1991). The final line list is similar to those used in recent papers of HgMn stars (Zavala et al. 2007; Adelman & Yüce 2010).

3. ATMOSPHERIC PARAMETERS

An estimate of the effective temperature and gravity was done by Woolf & Lambert (1999), who used the Strömgren $uvby-\beta$ photometry and the calibration of Moon & Dworetsky (1985). For HR 3273, the authors derived 12350 K and 3.28 dex for $T_{\rm eff}$ and $\log g$, respectively. Glagolevskij (1994) used the Shallis-Blackwell method and derived two temperatures from the parameters Q and X (reddening free index and multicolor photometry parameter). For HR 8118 they obtained 11900 K and 11500 K, while for HR 8937 they obtained 12400 and 12300 K, using the Q and X parameters, respectively. Dolk et al. (2003) derived a temperature and gravity using *uvby* photometric data but with the calibration of Napiwotzki, Shonberner, & Wenske (1993). For HR 8567, they obtained 11977 K and 4.06 dex, while for HR 8937 they derived 12476 K and 4.13 dex for $T_{\rm eff}$ and $\log g$, respectively.

We compared the observed Hγ profiles with synthetic spectra of the Hγ region calculated with SYNTHE (Kurucz & Avrett 1981) using Kurucz ATLAS9 (Kurucz 1995, private communication) model atmospheres with [M/H]=0.0, i.e. solar abundance, which seems to be adequate for these stars. However it is difficult to obtain accurate Balmer line profiles in this region from echelle spectra covering several orders. Thus, we estimated $T_{\rm eff}$ and $\log g$ using the $uvby-\beta$ mean colors of Hauck & Mermilliod (1998) with the calibration of Napiwotzki et al. (1993), and then we corrected the $T_{\rm eff}$ values according to Adelman & Rayle (2000). These values are presented in the first two columns of Table 3. Next we adjusted the surface gravity to get ionization equilibrium from FeI and FeII. A similar strategy was applied by Adelman & Yüce (2010) in the derivation of the fundamental parameters. The final adopted values of the fundamental parameters are shown in Table 3.

TABLE 3

TEMPERATURE AND GRAVITY DERIVED FOR THE HGMN STARS

Star	$uvby-\beta$ $T_{\rm eff}$	$uvby-\beta$ $\log g$	Adopted $T_{\rm eff}$	Adopted $\log g$
HR 3273	12253	3.32	12253	3.42
HR 8118	11381	4.01	11381	4.11
HR 8567	12315	3.78	12315	3.68
HR 8937	12088	4.28	12088	4.28

We fitted a synthetic spectrum to $\sim$20 Fe lines in order to derive an estimation of the rotational velocities of the HgMn stars. We used the program SYNTHE (Kurucz & Avrett 1981) and the command *broaden* to reproduce the instrumental broadening of the EBASIM spectrograph, adopting a resolving power of $R \sim 40000$. The value of R is approximate, and thus the derived rotational velocities should be taken with caution. The final $v \sin i$ values are obtained using the average and standard deviation of the lines. We derived rotational velocities of 20 ± 2 km s^{-1}, 30 ± 1 km s^{-1}, 22 ± 1 km s^{-1} and 24 ± 2 km s^{-1} for the stars HR 3273, HR 8118, HR 8567 and HR 8937, respectively. The HgMn stars of our sample are not extremely slow rotators.

4. ABUNDANCE ANALYSES

To derive the abundances of the chemical species we used the WIDTH9 code (Kurucz 1995, private communication) and equivalent widths measured in the spectra of the stars. The program also requires the selection of a model atmosphere and the atomic data for the lines (oscillator strength, excitation potentials, damping constants, etc.). The code calculates a theoretical equivalent width for an initial input abundance (taken from the model atmosphere) and compares this value with the measured EW. WIDTH9 computes basically the line profile and the curve of growth. Then it modifies the abundance iteratively to achieve a difference between theoretical and measured equivalent width < 0.01 mÅ. The process is repeated for each measured spectral line.

TABLE 4

DETERMINATION OF MICROTURBULENT VELOCITY FROM FEII LINES

Star	Species	n	ξ_1 km s^{-1}	$\log N/N_T$	ξ_2 km s^{-1}	$\log N/N_T$	gf-values
HR 3273	FeII	64	0.3	-4.75 ± 0.22	0.0	-4.74 ± 0.27	N4+KX+MF
		37	0.9	-4.87 ± 0.24	0.0	-4.80 ± 0.28	N4+MF
	adopted ξ:	0.3 km s^{-1}					
HR 8118	FeII	63	1.0	-4.36 ± 0.21	0.0	-4.28 ± 0.28	N4+KX+MF
		37	1.2	-4.41 ± 0.24	0.0	-4.27 ± 0.26	N4+MF
	adopted ξ:	0.5 km s^{-1}					
HR 8567	FeII	56	0.0	-4.91 ± 0.21	0.0	-4.91 ± 0.28	N4+KX+MF
		33	0.5	-4.99 ± 0.24	0.0	-4.98 ± 0.26	N4+MF
	adopted ξ:	0.1 km s^{-1}					
HR 8937	FeII	80	0.9	-4.32 ± 0.21	0.0	-4.27 ± 0.28	N4+KX+MF
		39	1.1	-4.40 ± 0.24	0.0	-4.29 ± 0.26	N4+MF
	adopted ξ:	0.5 km s^{-1}					

Note: the source of gf values are KX (Kurucz & Bell 1995), MF (Fuhr, Martin, & Wiese 1988) and N4 (Fuhr & Wiese 2006).

The adopted metal line damping constants were the default semi-classical approximations except for those of neutral and singly-ionized Ca-Ni lines, whose values are based on the data of Kurucz & Bell (1995). For the lines of CII, multiplet 6, and MgII, multiplet 4, the adopted values for Stark broadening were based on data of Sahal-Brechot (1969), and for SiII and CaII, the damping constants are those of Lanz, Dimitrijevic, & Artru (1988), and Chapelle & Sahal-Brechot (1970) respectively. We prefer this choice of gf values to the VALD database (Piskunov 1996) to ensure homogeneity with our previous work.

To determine the abundances we need an initial estimation of the microturbulent velocity (ξ). For this estimation we have used the standard method. We computed abundances from the FeII lines for a range of possible microturbulent velocities (ξ). For determining the final values (Table 4), we looked for the conditions that the abundances of FeII were not dependent on the equivalent widths (ξ_1) or that they minimize the rms scatter of the abundances (ξ_2). Values for each species were derived using lines with gf values from 3 different sources: KX values (Kurucz & Bell 1995), MF values (Fuhr et al. 1988) and N4 values (Fuhr & Wiese 2006). The sources of gf values shown in the last column of Table 4 determine the number of lines, n. The values derived for the microturbulence using the FeII lines are 0.32 km s^{-1}, 0.55 km s^{-1}, 0.13 km s^{-1} and 0.52 km s^{-1}, for the HgMn stars HR 3273, HR 8118, HR 8567 and HR 8937, respectively. Once a ξ value has been fixed the abundances corresponding to all chemical species measured are determined using the WIDTH9 code.

In our abundance determination we did not include seriously blended lines. To give an idea of the sensitivity of our results, raising the temperature of HR 3273 by $\sim$4% (500 K) increases the average abundance by $\sim$2%, and raising the surface gravity by $\sim$15% (0.5 dex) increases the average abundance by $\sim$0.5%. Table 5 shows the sensivity of the results for the abundances to these changes.

We present in the Table 6 the He/H ratios derived comparing the observed HeI line profiles with synthetized spectra. We used the program SYNTHE under the LTE condition; the results were convolved with the rotational velocity of the star and the instrumental broadening of the spectrograph. The mean derived He/H values are 0.07, 0.09, 0.08 and 0.03, for the stars HR 3273, HR 8118, HR 8567 and HR 8937, respectively.

Previous works in literature derived the Hg abundance taking into account the isotopic and hyperfine structure, using higher resolution spectra and S/N than ours (Woolf & Lambert 1999; Dolk et al. 2003). They determined the isotopic mixture for the line HgII $\lambda\lambda$3984 using similar values of $T_{\rm eff}$ and $\log g$. We adopted the Hg abundance derived by these authors for HR 3273 (-5.25 ± 0.32 dex), HR 8567 (-5.58 ± 0.37 dex) and HR 8937 (-4.23 ± 0.43 dex). These values are comparable to those derived using the equivalent width of $\lambda\lambda$ 3984, and LTE model atmosphere, i.e. -4.83 dex, -5.39 dex and -4.06 dex,

TABLE 5

SENSITIVITY OF THE DERIVED ABUNDANCES OF HR 3273 TO CHANGES IN EFFECTIVE TEMPERATURE AND SURFACE GRAVITY

HR 3273 Element	$\log N/H$ for adopted model	$\log N/H$ for 500 K hotter model	$\log N/H$ for 0.5 dex greater model
CII	−3.61	−3.96	−3.57
OI	−3.23	−3.15	−3.27
MgI	−5.17	−4.68	−5.26
MgII	−5.11	−5.02	−5.08
AlII	−6.80	−6.83	−6.70
SiII	−4.92	−4.95	−4.89
PII	−5.97	−6.13	−5.89
SII	−4.99	−5.28	−4.91
CaII	−5.57	−5.31	−5.70
ScII	−8.03	−7.72	−8.00
TiII	−6.35	−6.06	−6.30
CrII	−5.53	−5.32	−5.45
MnI	−4.63	−4.13	−4.68
MnII	−4.68	−4.52	−4.59
FeI	−4.34	−3.93	−4.37
FeII	−4.75	−4.67	−4.65
FeIII	−4.56	−4.81	−4.38
NiII	−6.74	−6.66	−6.57
YII	−7.68	−7.37	−7.64
ZrII	−7.79	−7.46	−7.72

TABLE 6

HE/H DETERMINATION FOR THE SAMPLE OF HGMN STARS

Line	HR 3273	HR 8118	HR 8567	HR 8937
3867	0.08	—	—	—
4026	0.07	0.09	0.09	0.03
4121	0.08	—	0.09	—
4471	0.06	0.09	0.07	0.03
4713	0.06	0.09	0.08	0.03
4921	—	—	0.09	—
Average	0.07±0.01	0.09	0.08±0.01	0.03

for HR 3273, HR 8567 and HR 8937, respectively, with a mean offset of −0.23 dex. For HR 8118 we used our estimation based on the equivalent width of $\lambda\lambda$ 3984 (−5.03 dex) and then we added the mean offset (−0.23 dex), obtaining finally −5.26 dex for the Hg abundance of this star. This is not a perfect solution as some very sharp-lined HgMn stars have $\lambda\lambda$ 3984 lines with a unique distribution of Hg isotopes.

5. DISCUSSION

HR 3273, HR 8118, HR 8567 and HR 8937 are main sequence stars with anomalous abundances, i.e. different from solar values. The comparison of derived and solar abundances for the HgMn stars is presented in the Table 7. We included the rms of the average abundance for each species and the number of lines n involved in the average. Solar abundances have been taken from Grevesse, Noels, & Sauval

TABLE 7

COMPARISON OF DERIVED AND SOLAR ABUNDANCES

Species	HR 3273 $\log N/N_H$	n	HR 8118 $\log N/N_H$	n	HR 8567 $\log N/N_H$	n	HR 8937 $\log N/N_H$	n	Sun $\log N/N_H$
HeI	-1.12 ± 0.06	5	-1.01 ± 0.01	3	-1.04 ± 0.05	5	-1.47 ± 0.04	3	-1.01
CII	-3.61 ± 0.11	2	-3.10 ± 0.02	2	-3.82 ± 0.27	3	-3.24 ± 0.03	2	-3.45
OI	-3.23	1	-3.71	1	-3.09	1			-3.13
MgI	-5.17	1	-4.96 ± 0.02	2	-5.14	1	-5.01 ± 0.01	2	-4.42
MgII	-5.11 ± 0.03	2	-4.54 ± 0.10	3	-4.91 ± 0.03	2	-4.73 ± 0.15	3	-4.42
AlII	-6.80	1	-5.47	1	-6.52	1			-5.53
SiII	-4.92 ± 0.22	8	-4.61 ± 0.17	6	-4.78 ± 0.20	7	-4.52 ± 0.18	8	-4.45
PII	-5.97	1					-5.37	1	-6.55
SII	-4.99 ± 0.14	7	-4.45 ± 0.19	5	-4.73 ± 0.18	7	-5.09 ± 0.09	3	-4.67
CaII	-5.57	1	-6.18	1	-5.35	1	-5.93	1	-5.64
ScII	-8.03	1	-7.02	1	-7.62	1			-8.83
TiII	-6.35 ± 0.24	34	-6.11 ± 0.22	34	-5.97 ± 0.23	32	-6.60 ± 0.23	26	-6.98
CrI			-5.20	1					-6.33
CrII	-5.53 ± 0.23	37	-5.19 ± 0.19	23	-5.34 ± 0.21	32	-5.73 ± 0.25	30	-6.33
MnI	-4.63 ± 0.22	7	-5.54 ± 0.18	3	-4.20 ± 0.26	14	-4.67 ± 0.19	11	-6.61
MnII	-4.68 ± 0.21	39	-5.26 ± 0.32	12	-4.25 ± 0.23	41	-4.46 ± 0.21	39	-6.61
FeI	-4.34 ± 0.02	2	-4.27 ± 0.35	19	-4.78 ± 0.24	3	-4.30 ± 0.40	18	-4.50
FeII	-4.75 ± 0.21	64	-4.31 ± 0.19	63	-4.91 ± 0.21	56	-4.29 ± 0.20	80	-4.50
FeIII	-4.56	1					-4.35	1	-4.50
NiII	-6.74 ± 0.30	2	-6.06 ± 0.21	2	-6.79 ± 0.25	2			-5.75
SrII			-8.43	1	-8.35	1	-6.30	1	-9.03
YII	-7.68 ± 0.26	5	-6.32 ± 0.24	9	-7.40 ± 0.16	8	-6.37 ± 0.20	11	-9.76
ZrII	-7.79 ± 0.05	2	-7.06 ± 0.16	13	-7.59 ± 0.32	2	-7.72 ± 0.14	6	-9.40
BaII			-9.17	1					-9.87
HgII	-5.25	1	-5.03	1	-5.58	1	-4.23	1	-10.83
$T_{\rm eff}$	12253		11381		12315		12088		
$\log g$	3.42		4.11		3.68		4.28		

(1996). We also present in Tables 8–11 the line by line abundance values derived for the sample of HgMn stars. The columns shown are the code of the species, the name of the element, multiplet number, wavelength of the line, $\log gf$ value, reference for the $\log gf$ value, equivalent width and abundance of the line. In Figure 1 we show the abundance anomalies relative to solar as a function of the atomic number. The HgMn stars are presented as crosses (HR 3273), empty triangles (HR 8118), empty circles (HR 8567) and empty squares (HR 8937). For comparison purposes we show the abundances of four other HgMn stars, depicted as filled circles (HR 4817), filled triangles (π Boo), filled hexagons (μ Lep) and filled squares (28 Her). These data are taken from Adelman & Pintado (1997). From the values presented in Table 7 and Figure 1, our sample of HgMn stars shows an abundance pattern similar to other HgMn stars. However there are some differences in particular cases.

The star HR 3273 shows a relatively low abundance of SiII (8 lines) compared to other HgMn stars. In the star HR 8567, the abundance of CrII (32 lines) is relatively high compared to other HgMn stars. The CrII lines $\lambda\lambda$4588, 4634 and 5237, for instance, are intense in the spectra. The Mn and Hg abundances are similar to other HgMn stars. The abundance of CII in HR 8118 and HR 8937 is also relatively high. However, this value is based on few lines, and assumes the LTE approximation. For star HR 8937, the abundance of SrII is high compared to other HgMn stars. However, this value is derived

TABLE 8

LINE ABUNDANCES OF HR 3273

Code	Species	Mult.	λ(Å)	$\log gf$	Ref.	$W_{\rm eq}$	$\log(N/N_T)$	Code	Species	Mult.	λ(Å)	$\log gf$	Ref.	$W_{\rm eq}$	$\log(N/N_T)$
6.01	C II	4	3918.97	−0.53	WF	19	−3.72	24.01	Cr II	31	4261.91	−1.53	KX	46	−5.40
6.01	C II	4	3920.68	−0.23	WF	30	−3.49	24.01	Cr II	31	4275.57	−1.70	KX	42	−5.36
8.00	O I	12	5330.73	−0.87	WF	22	−3.22	24.01	Cr II	44	4554.99	−1.38	MF	47	−5.42
12.00	Mg I	2	5183.60	−0.16	WS	6	−5.17	24.01	Cr II	39	4565.74	−2.11	MF	25	−5.36
12.01	Mg II	10	4390.57	−0.53	WS	23	−5.14	24.01	Cr II	44	4588.20	−0.63	MF	79	−5.05
12.01	Mg II	9	4427.99	−1.21	WS	6	−5.07	24.01	Cr II	44	4592.05	−1.22	MF	42	−5.72
13.01	Al II	2	4663.05	−0.28	FW	5	−6.80	24.01	Cr II	44	4616.63	−1.29	MF	43	−5.64
14.01	Si II	1	3853.66	−1.44	LA	50	−5.18	24.01	Cr II	44	4618.80	−1.11	MF	60	−5.22
14.01	Si II	1	3856.02	−0.49	LA	96	−5.10	24.01	Cr II	44	4634.07	−1.24	MF	55	−5.27
14.01	Si II	1	3862.59	−0.74	LA	90	−4.97	24.01	Cr II	30	4836.23	−2.25	MF	24	−5.31
14.01	Si II	3.01	4075.45	−1.40	SG	14	−4.85	24.01	Cr II	30	4848.23	−1.14	MF	51	−5.63
14.01	Si II	3.01	4076.78	−1.67	SG	13	−4.61	24.01	Cr II	30	4884.61	−2.08	MF	19	−5.63
14.01	Si II	3	4128.05	0.38	LA	120	−4.54	24.01	Cr II	190	4912.46	−0.95	KX	17	−5.53
14.01	Si II	3	4130.89	0.53	LA	91	−5.06	24.01	Cr II	43	5232.50	−2.09	KX	15	−5.67
14.01	Si II	5	5041.02	0.29	SG	60	−5.07	24.01	Cr II	43	5237.33	−1.16	MF	52	−5.42
15.01	P II	15	4602.07	0.74	WS	8	−5.97	24.01	Cr II	23	5246.77	−2.45	MF	20	−5.31
16.01	S II	44	4153.07	0.62	WS	11	−4.94	24.01	Cr II	23	5249.44	−2.43	KX	13	−5.54
16.01	S II	44	4162.66	0.78	WS	12	−4.99	24.01	Cr II	43	5274.96	−1.29	KX	48	−5.43
16.01	S II	9	4815.55	0.18	WM	9	−5.26	24.01	Cr II	43	5279.88	−2.10	MF	34	−5.05
16.01	S II	7	4925.34	−0.47	WS	7	−4.77	24.01	Cr II	43	5280.05	−2.01	KX	36	−5.08
16.01	S II	15	5014.04	0.03	KX	8	−4.99	24.01	Cr II	43	5308.44	−1.81	MF	25	−5.61
16.01	S II	39	5212.62	0.24	WS	6	−4.91	24.01	Cr II	43	5310.70	−2.28	MF	17	−5.39
16.01	S II	38	5320.72	0.46	WS	6	−5.08	24.01	Cr II	43	5313.59	−1.65	MF	33	−5.54
20.01	Ca II	1	3933.66	0.13	WM	212	−5.57	24.01	Cr II	43	5334.87	−1.56	KX	34	−5.59
21.01	Sc II	7	4246.82	0.24	LD	40	−8.03	25.00	Mn I	2	4030.75	−0.47	MF	15	−4.91
22.01	Ti II	34	3900.54	−0.45	MF	55	−6.38	25.00	Mn I	2	4033.06	−0.62	MF	19	−4.62
22.01	Ti II	34	3913.46	−0.53	MF	50	−6.50	25.00	Mn I	2	4034.48	−0.81	MF	9	−4.84
22.01	Ti II	31	3932.02	−1.78	MF	10	−6.49	25.00	Mn I	5	4041.35	0.29	MF	13	−4.69
22.01	Ti II	11	4012.38	−1.61	MF	35	−6.11	25.00	Mn I	28	4462.03	0.32	MF	9	−4.47
22.01	Ti II	87	4028.34	−1.00	MF	14	−6.69	25.00	Mn I	21	4762.37	0.42	MF	21	−4.19
22.01	Ti II	87	4053.82	−1.21	MF	22	−6.22	25.00	Mn I	16	4783.43	0.04	MF	7	−4.69
22.01	Ti II	105	4163.64	−0.40	MF	35	−6.34	25.01	Mn II	I	3859.21	−2.56	KX	11	−4.91
22.01	Ti II	20	4287.87	−2.02	MF	19	−5.91	25.01	Mn II	I	3878.99	−1.71	KX	40	−4.73
22.01	Ti II	19	4294.09	−1.11	MF	37	−6.33	25.01	Mn II	I	3917.32	−1.15	KX	29	−4.97
22.01	Ti II	41	4300.04	−0.77	MF	58	−5.97	25.01	Mn II	I	3930.95	−2.15	KX	13	−4.68
22.01	Ti II	41	4301.92	−1.16	MF	20	−6.70	25.01	Mn II	I	3952.42	−1.50	KX	12	−4.78
22.01	Ti II	41	4312.86	−1.16	MF	27	−6.49	25.01	Mn II	I	3986.58	−2.60	KX	14	−4.70
22.01	Ti II	41	4320.95	−1.87	MF	17	−6.07	25.01	Mn II	I	4000.05	−1.21	KX	26	−4.58
22.01	Ti II	51	4394.06	−1.59	MF	6	−6.86	25.01	Mn II	I	4081.44	−2.24	KX	28	−4.27
22.01	Ti II	19	4395.03	−0.66	MF	49	−6.41	25.01	Mn II	I	4087.91	−2.91	KX	7	−4.81
22.01	Ti II	61	4395.84	−2.17	MF	8	−6.14	25.01	Mn II	I	4136.90	−1.29	KX	59	−4.21
22.01	Ti II	61	4409.24	−2.64	KX	5	−5.90	25.01	Mn II	I	4140.44	−2.46	KX	17	−4.67
22.01	Ti II	115	4411.07	−1.06	MF	10	−6.25	25.01	Mn II	2	4174.32	−3.55	KX	44	−4.62
22.01	Ti II	40	4417.71	−1.43	MF	21	−6.39	25.01	Mn II	I	4184.45	−1.95	KX	22	−4.72
22.01	Ti II	19	4443.80	−0.70	MF	45	−6.50	25.01	Mn II	I	4200.27	−1.74	KX	32	−4.64
22.01	Ti II	19	4450.48	−1.45	MF	16	−6.58	25.01	Mn II	2	4205.38	−3.38	KX	51	−4.54
22.01	Ti II	31	4468.49	−0.60	MF	44	−6.60	25.01	Mn II	I	4240.39	−2.07	KX	25	−4.51
22.01	Ti II	115	4488.32	−0.82	MF	17	−6.18	25.01	Mn II	7	4244.25	−2.39	KX	33	−4.34
22.01	Ti II	31	4501.27	−0.75	MF	41	−6.56	25.01	Mn II	I	4251.73	−1.06	KX	52	−4.68
22.01	Ti II	50	4533.96	−0.77	MF	57	−5.97	25.01	Mn II	2	4260.46	−4.25	KX	15	−4.77
22.01	Ti II	41	4563.76	−0.96	MF	35	−6.46	25.01	Mn II	I	4377.74	−2.14	KX	20	−4.95
22.01	Ti II	82	4571.97	−0.53	MF	53	−6.19	25.01	Mn II	I	4393.38	−2.32	KX	15	−4.94
22.01	Ti II	59	4657.20	−2.15	MF	7	−6.23	25.01	Mn II	I	4403.51	−1.80	KX	11	−5.08
22.01	Ti II	92	4779.98	−1.37	MF	13	−6.28	25.01	Mn II	I	4478.64	−0.95	KX	40	−4.92
22.01	Ti II	82	4805.09	−1.10	MF	17	−6.39	25.01	Mn II	I	4497.94	−2.59	KX	9	−4.98
22.01	Ti II	14	4911.20	−0.34	MF	17	−6.65	25.01	Mn II	I	4503.20	−2.16	KX	15	−4.82
22.01	Ti II	86	5129.16	−1.39	MF	9	−6.53	25.01	Mn II	I	4689.55	−2.54	KX	11	−4.56
22.01	Ti II	86	5185.90	−1.35	MF	17	−6.24	25.01	Mn II	I	4702.73	−2.34	KX	10	−4.78
22.01	Ti II	7	5188.69	−1.21	MF	17	−6.52	25.01	Mn II	I	4717.26	−1.86	KX	15	−4.86
24.01	Cr II	167	3865.60	−0.78	KX	32	−5.84	25.01	Mn II	I	4730.40	−2.15	KX	40	−4.33
24.01	Cr II	130	3866.52	−2.07	KX	4	−5.86	25.01	Mn II	I	4749.11	−2.00	KX	16	−4.85
24.01	Cr II	129	3911.32	−2.06	KX	9	−5.56	25.01	Mn II	I	4764.73	−1.35	KX	62	−4.37
24.01	Cr II	183	3979.50	−0.73	KX	30	−5.79	25.01	Mn II	I	4791.78	−1.72	KX	29	−4.69
24.01	Cr II	183	4012.50	−0.89	KX	37	−5.44	25.01	Mn II	I	4806.82	−1.56	KX	46	−4.72
24.01	Cr II	19	4051.93	−2.19	KX	22	−5.80	25.01	Mn II	I	4830.06	−1.85	KX	25	−4.70
24.01	Cr II	19	4054.08	−2.48	KX	24	−5.46	25.01	Mn II	I	4839.74	−1.86	KX	19	−4.87
24.01	Cr II	26	4072.56	−2.41	KX	10	−5.76	25.01	Mn II	I	4842.32	−2.01	KX	25	−4.53
24.01	Cr II	165	4082.28	−1.23	KX	13	−5.99	25.01	Mn II	I	5102.52	−1.93	KX	27	−4.63
24.01	Cr II	26	4086.13	−2.42	KX	8	−5.83	25.01	Mn II	I	5177.65	−1.77	KX	44	−4.24
24.01	Cr II	26	4132.42	−2.35	KX	11	−5.73	25.01	Mn II	I	3902.36	−2.72	KX	13	−4.57
24.01	Cr II	162	4145.78	−1.16	KX	25	−5.66	26.00	Fe I	43	4132.06	−0.68	N4	4	−4.31
24.01	Cr II	26	4179.42	−1.77	KX	23	−5.84	26.00	Fe I	1146	5383.37	0.65	N4	3	−4.36

TABLE 8 (CONTINUED)

Code	Species	Mult.	λ(Å)	$\log gf$	Ref.	$W_{\rm eq}$	$\log(N/N_T)$
26.01	Fe II	38	3935.96	−1.86	N4	18	−4.78
26.01	Fe II	3	3938.29	−4.07	N4	11	−4.72
26.01	Fe II	190	3938.97	−1.85	N4	16	−4.71
26.01	Fe II	127	4024.55	−2.44	N4	11	−4.99
26.01	Fe II	172	4048.83	−2.14	N4	23	−4.34
26.01	Fe II	28	4122.67	−3.38	N4	15	−4.82
26.01	Fe II	27	4233.17	−1.81	N4	77	−4.36
26.01	Fe II	27	4273.33	−3.34	N4	11	−4.95
26.01	Fe II	28	4296.57	−3.01	N4	24	−4.81
26.01	Fe II	27	4303.18	−2.61	N4	51	−4.38
26.01	Fe II	27	4351.77	−2.08	N4	44	−5.16
26.01	Fe II	J	4357.58	−2.10	KX	11	−4.59
26.01	Fe II	27	4385.39	−2.57	N4	34	−4.92
26.01	Fe II	27	4416.83	−2.60	N4	33	−4.92
26.01	Fe II	37	4489.18	−2.97	N4	23	−4.83
26.01	Fe II	37	4491.40	−2.70	N4	24	−5.04
26.01	Fe II	38	4508.29	−2.21	N4	42	−4.99
26.01	Fe II	37	4515.34	−2.48	N4	34	−4.99
26.01	Fe II	37	4520.22	−2.60	N4	33	−4.91
26.01	Fe II	38	4522.63	−2.03	N4	47	−5.03
26.01	Fe II	38	4541.52	−3.05	N4	17	−4.92
26.01	Fe II	37	4555.89	−2.29	N4	42	−4.94
26.01	Fe II	38	4576.34	−3.04	N4	17	−4.93
26.01	Fe II	37	4582.84	−3.10	N4	15	−4.94
26.01	Fe II	38	4583.84	−2.02	N4	60	−4.62
26.01	Fe II	D	4596.02	−1.84	N4	12	−4.69
26.01	Fe II	38	4620.52	−3.28	N4	15	−4.76
26.01	Fe II	37	4629.34	−2.37	N4	38	−4.98
26.01	Fe II	186	4635.32	−1.65	N4	22	−4.65
26.01	Fe II	28	4666.76	−3.33	N4	11	−4.90
26.01	Fe II	43	4731.45	−3.13	N4	17	−4.82
26.01	Fe II	J	4913.29	0.01	KX	11	−4.69
26.01	Fe II	J	4951.58	0.18	KX	14	−4.69
26.01	Fe II	J	4977.04	0.04	KX	11	−4.65
26.01	Fe II	J	4990.51	0.18	KX	13	−4.72
26.01	Fe II	J	4993.36	−3.65	MF	6	−4.88
26.01	Fe II	J	5001.96	0.90	KX	30	−4.86
26.01	Fe II	J	5004.20	0.50	KX	18	−4.85
26.01	Fe II	J	5018.44	−1.22	MF	88	−4.44
26.01	Fe II	J	5021.59	−0.30	KX	11	−4.37
26.01	Fe II	J	5022.79	−0.02	KX	12	−4.60
26.01	Fe II	J	5035.71	0.61	KX	27	−4.63
26.01	Fe II	J	5061.72	0.22	KX	11	−4.88
26.01	Fe II	J	5070.90	0.24	KX	11	−4.88
26.01	Fe II	J	5075.76	0.28	KX	12	−4.78
26.01	Fe II	J	5093.58	0.11	KX	12	−4.65
26.01	Fe II	J	5097.27	0.31	KX	25	−4.37
26.01	Fe II	J	5106.11	−0.28	KX	10	−4.38
26.01	Fe II	J	5145.77	−0.40	KX	8	−4.33
26.01	Fe II	J	5150.49	−0.12	KX	11	−4.46
26.01	Fe II	J	5169.03	−0.87	MF	90	−4.72
26.01	Fe II	J	5199.12	0.10	KX	7	−4.92
26.01	Fe II	J	5216.85	0.81	KX	19	−5.01
26.01	Fe II	J	5228.90	−0.30	KX	7	−4.49
26.01	Fe II	J	5232.79	−0.06	KX	14	−4.37
26.01	Fe II	J	5234.62	−2.05	MF	45	−4.84
26.01	Fe II	J	5247.95	0.55	N4	18	−4.74
26.01	Fe II	J	5254.93	−3.23	KX	11	−4.79
26.01	Fe II	J	5257.12	0.03	KX	9	−4.66
26.01	Fe II	J	5260.25	1.07	KX	33	−4.82
26.01	Fe II	J	5272.40	−2.03	MF	16	−4.44
26.01	Fe II	J	5276.00	−1.94	MF	45	−4.96
26.01	Fe II	J	5291.67	0.58	KX	17	−4.86
26.01	Fe II	J	5339.59	0.54	KX	17	−4.80
26.02	Fe III	4	4419.60	−2.22	KX	7	−4.56
28.01	Ni II	12	4015.47	−2.42	KX	4	−6.44
28.01	Ni II	11	4067.03	−1.29	KX	12	−7.03
39.01	Y II	6	3950.35	−0.49	HL	12	−7.90
39.01	Y II	6	3982.59	−0.49	HL	11	−7.96
39.01	Y II	14	4124.90	−1.50	HL	4	−7.25
39.01	Y II	22	4900.12	−0.09	HL	14	−7.74
39.01	Y II	20	5205.72	−0.34	HL	12	−7.57
40.01	Zr II	16	3998.95	−0.67	GB	6	−7.84
40.01	Zr II	30	4045.64	−0.60	KX	8	−7.74
80.01	Hg II	–	3983.94	−1.73	DW	83	−4.83

from one line and should be taken with caution. For HR 8937 we adopted the Hg abundance derived by Dolk et al. (2003). They found an abundance of -4.23 ± 0.43 dex, i.e., a relatively high value. We compared this value with an estimation using the equivalent width of $\lambda\lambda$3984 and derived -4.06 dex, i.e. also a high abundance for HgII in this star.

For star HR 8118, the abundances of CII, AlII and ScII seem to be relatively high compared to other HgMn stars. However, these values are based on the measurement of few lines (2, 1 and 1, respectively) and should be taken with caution. On the other hand, the abundances of CrII, YII and ZrII are also relatively high, from a greater number of lines (23, 9 and 13, respectively). We caution that this star has the highest $v \sin i$ in our sample (30 ± 1 km s^{-1}) which suggest that high abundance values in different species might be due to blends with another lines. However this effect is not clearly seen in the FeII abundances (63 lines), and thus the CrII abundance could be real. A comparison of higher resolution spectra with synthetic spectra is needed to verify the abundance of Cr, Y and Zr in this star.

HeI was slightly underabundant for the sample of HgMn stars and underabundantin HR 8937. O was slightly underabundant in the stars HR 3273 and HR 8567. MgII was underabundant, except for HR 8118 (which is close to the solar value). SiII was close to solar in HR 8118 and HR 8937, and underabundant in HR 3273 and HR 8567. Fe was slightly underabundant in HR 3273 and HR 8567, and slightly overabundant in HR 8118 and HR 8937. The species Sc, Ti, Cr, Mn, Sr, Y and Zr were overabundant while Ni was underabundant.

As we said in the Introduction, our purpose is to discuss the possible trend of the abundances of the critical elements in HgMn stars with stellar parameters. Papers in the literature show that the abundances of some elements seem to correlate with the effective temperature (e.g., Smith & Dworetsky 1993; Smith 1997; Woolf & Lambert 1999; Jomaron et al. 1999; Dolk et al. 2003). However, it is not clear (for instance) how the abundances are corre-

TABLE 9

LINE ABUNDANCES OF HR 8118

Code	Species	Mult.	λ(Å)	$\log gf$	Ref.	W_{eq}	$\log(N/N_T)$	Code	Species	Mult.	λ(Å)	$\log gf$	Ref.	W_{eq}	$\log(N/N_T)$
6.01	C II	4	3918.97	−0.53	WF	16	−3.12	24.01	Cr II	30	4884.61	−2.08	MF	35	−5.20
6.01	C II	4	3920.68	−0.23	WF	23	−3.09	24.01	Cr II	190	4901.62	−0.83	KX	28	−5.28
12.00	Mg I	2	5172.68	−0.38	WS	28	−4.98	24.01	Cr II	43	5232.50	−2.09	KX	34	−5.08
12.00	Mg I	2	5183.60	−0.16	WS	41	−4.93	24.01	Cr II	23	5246.77	−2.45	MF	25	−5.14
12.01	Mg II	5	3848.21	−1.59	WS	31	−4.42	24.01	Cr II	23	5249.44	−2.43	KX	25	−5.16
12.01	Mg II	10	4390.57	−0.53	WS	50	−4.65	24.01	Cr II	43	5308.44	−1.81	MF	46	−5.02
12.01	Mg II	9	4427.99	−1.21	WS	18	−4.55	24.01	Cr II	43	5310.70	−2.28	MF	29	−5.03
13.01	Al II	2	4663.05	−0.28	FW	25	−5.47	25.00	Mn I	2	4033.06	−0.62	MF	24	−5.29
14.01	Si II	1	3853.66	−1.44	LA	64	−4.66	25.00	Mn I	2	4034.48	−0.81	MF	9	−5.63
14.01	Si II	1	3856.02	−0.49	LA	120	−4.78	25.00	Mn I	16	4754.04	−0.09	MF	3	−5.69
14.01	Si II	1	3862.59	−0.74	LA	95	−4.85	25.01	Mn II	I	4136.90	−1.29	KX	17	−5.49
14.01	Si II	3.01	4075.45	−1.40	SG	19	−4.38	25.01	Mn II	I	4184.45	−1.95	KX	12	−5.01
14.01	Si II	3	4130.89	0.53	LA	123	−4.54	25.01	Mn II	7	4244.25	−2.39	KX	9	−5.11
14.01	Si II	5	5041.02	0.29	SG	81	−4.47	25.01	Mn II	I	4251.73	−1.06	KX	17	−5.69
16.01	S II	44	4145.06	0.23	KX	6	−4.33	25.01	Mn II	2	4260.46	−4.25	KX	11	−4.94
16.01	S II	44	4153.07	0.62	WS	8	−4.51	25.01	Mn II	I	4478.64	−0.95	KX	14	−5.69
16.01	S II	44	4162.66	0.78	WS	13	−4.31	25.01	Mn II	I	4702.73	−2.34	KX	9	−4.72
16.01	S II	9	4815.55	0.18	WM	6	−4.78	25.01	Mn II	I	4730.40	−2.15	KX	13	−5.13
16.01	S II	7	5032.43	0.18	WS	12	−4.30	25.01	Mn II	I	4755.72	−1.24	KX	37	−5.27
20.01	Ca II	1	3933.66	0.13	WM	249	−6.18	25.01	Mn II	I	4806.82	−1.56	KX	13	−5.69
21.01	Sc II	7	4246.82	0.24	LD	89	−7.03	25.01	Mn II	I	5177.65	−1.77	KX	18	−4.97
22.01	Ti II	34	3900.54	−0.45	MF	75	−6.13	25.01	Mn II	I	4238.79	−3.63	KX	14	−5.43
22.01	Ti II	34	3913.46	−0.53	MF	75	−6.07	26.00	Fe I	45	3815.84	0.23	N4	31	−4.79
22.01	Ti II	31	3932.02	−1.78	MF	33	−6.08	26.00	Fe I	4	3859.91	−0.71	N4	27	−4.73
22.01	Ti II	87	4028.34	−1.00	MF	42	−6.25	26.00	Fe I	43	4132.06	−0.68	N4	26	−3.96
22.01	Ti II	105	4163.64	−0.40	MF	57	−6.05	26.00	Fe I	152	4187.04	−0.55	N4	19	−3.87
22.01	Ti II	33	4227.33	−2.36	KX	11	−6.20	26.00	Fe I	152	4187.80	−0.55	N4	12	−4.13
22.01	Ti II	20	4287.87	−2.02	MF	26	−6.05	26.00	Fe I	152	4198.30	−0.72	N4	7	−4.21
22.01	Ti II	41	4290.22	−1.12	MF	72	−5.62	26.00	Fe I	522	4199.10	0.16	N4	29	−3.97
22.01	Ti II	19	4294.09	−1.11	MF	66	−5.85	26.00	Fe I	152	4222.21	−0.97	N4	9	−3.85
22.01	Ti II	41	4300.04	−0.77	MF	78	−5.77	26.00	Fe I	693	4227.43	0.27	N4	12	−4.50
22.01	Ti II	41	4301.92	−1.16	MF	51	−6.24	26.00	Fe I	152	4250.12	−0.41	N4	17	−4.07
22.01	Ti II	41	4307.87	−1.29	MF	57	−5.92	26.00	Fe I	42	4250.79	−0.71	N4	15	−4.28
22.01	Ti II	41	4312.86	−1.16	MF	50	−6.25	26.00	Fe I	42	4271.76	−0.16	N4	17	−4.80
22.01	Ti II	104	4386.85	−1.26	MF	28	−5.95	26.00	Fe I	41	4383.54	0.20	N4	30	−4.79
22.01	Ti II	51	4394.06	−1.59	MF	20	−6.58	26.00	Fe I	41	4404.75	−0.14	N4	22	−4.64
22.01	Ti II	19	4395.03	−0.66	MF	73	−6.07	26.00	Fe I	554	4736.77	−0.75	N4	6	−3.84
22.01	Ti II	61	4395.84	−2.17	MF	14	−6.19	26.00	Fe I	318	4920.50	0.07	N4	13	−4.47
22.01	Ti II	61	4409.52	−2.57	KX	12	−5.89	26.00	Fe I	383	5232.94	−0.06	N4	24	−3.93
22.01	Ti II	115	4411.07	−1.06	MF	20	−6.11	26.00	Fe I	1146	5383.37	0.65	N4	11	−4.39
22.01	Ti II	40	4417.71	−1.43	MF	46	−6.10	26.00	Fe I	686	5586.76	−0.14	N4	15	−3.89
22.01	Ti II	19	4450.48	−1.45	MF	32	−6.46	26.01	Fe II	127	3845.18	−2.29	KX	17	−4.73
22.01	Ti II	31	4468.49	−0.60	MF	68	−6.28	26.01	Fe II	29	3872.77	−3.32	KX	31	−4.18
22.01	Ti II	31	4501.27	−0.75	MF	65	−6.25	26.01	Fe II	173	3906.04	−1.83	N4	32	−4.22
22.01	Ti II	50	4533.96	−0.77	MF	80	−5.63	26.01	Fe II	38	3935.96	−1.86	N4	36	−4.05
22.01	Ti II	41	4563.76	−0.96	MF	64	−6.02	26.01	Fe II	3	3938.29	−4.07	N4	21	−4.24
22.01	Ti II	82	4571.97	−0.53	MF	73	−5.95	26.01	Fe II	190	3938.97	−1.85	N4	24	−4.26
22.01	Ti II	59	4657.20	−2.15	MF	18	−6.07	26.01	Fe II	28	4122.67	−3.38	N4	25	−4.36
22.01	Ti II	92	4779.98	−1.37	MF	26	−6.20	26.01	Fe II	27	4233.17	−1.81	N4	87	−4.05
22.01	Ti II	82	4805.09	−1.10	MF	40	−6.11	26.01	Fe II	27	4273.33	−3.34	N4	37	−3.98
22.01	Ti II	114	4874.01	−0.79	MF	18	−6.45	26.01	Fe II	28	4296.57	−3.01	N4	46	−4.06
22.01	Ti II	114	4911.20	−0.34	MF	29	−6.57	26.01	Fe II	27	4303.18	−2.61	N4	53	−4.27
22.01	Ti II	86	5129.16	−1.39	MF	26	−6.25	26.01	Fe II	27	4351.77	−2.08	N4	58	−4.64
22.01	Ti II	86	5185.90	−1.35	MF	36	−6.04	26.01	Fe II	J	4357.58	−2.10	KX	8	−4.52
22.01	Ti II	7	5188.69	−1.21	MF	43	−6.16	26.01	Fe II	27	4385.39	−2.57	N4	52	−4.28
24.00	Cr I	7	5208.43	0.16	MF	21	−5.20	26.01	Fe II	27	4416.83	−2.60	N4	43	−4.52
24.01	Cr II	129	3911.32	−2.06	KX	17	−5.18	26.01	Fe II	37	4489.18	−2.97	N4	40	−4.20
24.01	Cr II	183	3979.50	−0.73	KX	44	−5.40	26.01	Fe II	37	4491.40	−2.70	N4	39	−4.49
24.01	Cr II	19	4051.93	−2.19	KX	41	−5.34	26.01	Fe II	38	4508.29	−2.21	N4	52	−4.60
24.01	Cr II	26	4072.56	−2.41	KX	36	−4.94	26.01	Fe II	37	4515.34	−2.48	N4	55	−4.23
24.01	Cr II	165	4082.28	−1.23	KX	25	−5.60	26.01	Fe II	37	4520.22	−2.60	N4	41	−4.55
24.01	Cr II	26	4132.42	−2.35	KX	13	−5.64	26.01	Fe II	38	4522.63	−2.03	N4	58	−4.60
24.01	Cr II	162	4145.78	−1.16	KX	45	−5.09	26.01	Fe II	38	4541.52	−3.05	N4	29	−4.41
24.01	Cr II	26	4179.42	−1.77	KX	39	−5.44	26.01	Fe II	37	4555.89	−2.29	N4	52	−4.52
24.01	Cr II	31	4275.57	−1.70	KX	56	−4.98	26.01	Fe II	38	4576.34	−3.04	N4	30	−4.41
24.01	Cr II	44	4554.99	−1.38	MF	62	−5.01	26.01	Fe II	37	4582.84	−3.10	N4	22	−4.56
24.01	Cr II	44	4588.20	−0.63	MF	87	−4.97	26.01	Fe II	38	4583.84	−2.02	N4	75	−4.11
24.01	Cr II	44	4592.05	−1.22	MF	63	−5.14	26.01	Fe II	D	4596.02	−1.84	N4	18	−4.25
24.01	Cr II	44	4616.63	−1.29	MF	63	−5.08	26.01	Fe II	38	4620.52	−3.28	N4	22	−4.38
24.01	Cr II	178	4697.60	−1.88	MF	15	−5.07	26.01	Fe II	37	4629.34	−2.37	N4	66	−4.01
24.01	Cr II	30	4812.34	−1.80	MF	42	−5.29	26.01	Fe II	186	4635.32	−1.65	N4	32	−4.12
24.01	Cr II	30	4848.23	−1.14	MF	65	−5.26	26.01	Fe II	28	4666.76	−3.33	N4	18	−4.47

TABLE 9 (CONTINUED)

Code	Species	Mult.	λ(Å)	$\log gf$	Ref.	$W_{\rm eq}$	$\log(N/N_T)$	Code	Species	Mult.	λ(Å)	$\log gf$	Ref.	$W_{\rm eq}$	$\log(N/N_T)$
26.01	Fe II	43	4731.45	−3.13	N4	27	−4.37	26.01	Fe II	J	5291.67	0.58	KX	22	−4.37
26.01	Fe II	J	4826.68	−0.44	KX	5	−4.40	26.01	Fe II	J	5339.59	0.54	KX	25	−4.22
26.01	Fe II	J	4951.58	0.18	KX	14	−4.44	28.01	Ni II	11	3849.55	−1.88	KX	21	−5.85
26.01	Fe II	J	4984.47	0.01	KX	12	−4.32	28.01	Ni II	11	4067.03	−1.29	KX	26	−6.27
26.01	Fe II	J	4990.51	0.18	KX	15	−4.35	38.01	Sr II	1	4215.52	−0.17	WM	35	−8.43
26.01	Fe II	J	4993.36	−3.65	MF	10	−4.49	39.01	Y II	6	3950.35	−0.49	HL	65	−6.35
26.01	Fe II	J	5001.96	0.90	KX	39	−4.34	39.01	Y II	6	3982.59	−0.49	HL	62	−6.47
26.01	Fe II	J	5004.20	0.50	KX	22	−4.43	39.01	Y II	14	4124.90	−1.50	HL	42	−6.20
26.01	Fe II	J	5018.44	−1.22	MF	106	−4.04	39.01	Y II	5	4422.58	−1.27	HL	53	−6.13
26.01	Fe II	J	5035.71	0.61	KX	28	−4.34	39.01	Y II	22	4854.86	−0.38	HL	48	−6.80
26.01	Fe II	J	5045.11	−0.13	KX	8	−4.40	39.01	Y II	22	4900.12	−0.09	HL	74	−5.99
26.01	Fe II	J	5061.72	0.22	KX	12	−4.52	39.01	Y II	20	4982.13	−1.29	HL	30	−6.51
26.01	Fe II	J	5070.90	0.24	KX	13	−4.50	39.01	Y II	20	5200.41	−0.57	HL	59	−6.10
26.01	Fe II	J	5075.76	0.28	KX	17	−4.29	39.01	Y II	20	5289.82	−1.85	HL	20	−6.30
26.01	Fe II	J	5082.23	−0.10	KX	9	−4.33	40.01	Zr II	17	3915.96	−0.82	KX	28	−7.22
26.01	Fe II	J	5093.58	0.11	KX	21	−4.00	40.01	Zr II	16	3958.23	−0.31	KX	44	−7.14
26.01	Fe II	J	5097.27	0.31	KX	32	−3.85	40.01	Zr II	30	3991.15	−0.25	KX	45	−7.07
26.01	Fe II	J	5145.77	−0.40	KX	10	−3.93	40.01	Zr II	16	3998.95	−0.67	GB	41	−6.90
26.01	Fe II	J	5149.46	0.40	KX	25	−4.12	40.01	Zr II	54	4018.37	−0.99	KX	12	−7.41
26.01	Fe II	J	5160.84	−2.64	KX	10	−4.05	40.01	Zr II	42	4034.10	−1.55	BG	8	−7.17
26.01	Fe II	J	5169.03	−0.87	MF	111	−4.31	40.01	Zr II	29	4090.53	−1.10	GB	18	−7.15
26.01	Fe II	J	5216.85	0.81	KX	22	−4.57	40.01	Zr II	41	4149.22	−0.03	BG	52	−6.94
26.01	Fe II	J	5234.62	−2.05	MF	58	−4.34	40.01	Zr II	29	4156.28	−0.71	GB	32	−7.13
26.01	Fe II	J	5247.95	0.55	N4	18	−4.44	40.01	Zr II	97	4186.67	−0.58	KX	20	−7.10
26.01	Fe II	J	5251.23	0.42	N4	21	−4.22	40.01	Zr II	99	4231.67	−1.02	KX	13	−6.91
26.01	Fe II	J	5254.93	−3.23	KX	19	−4.28	40.01	Zr II	130	4494.42	−0.48	KX	20	−6.85
26.01	Fe II	J	5257.12	0.03	KX	12	−4.20	40.01	Zr II	129	4661.78	−0.80	KX	12	−6.83
26.01	Fe II	J	5260.25	1.07	KX	39	−4.38	56.01	Ba II	1	4934.07	0.00	WM	10	−9.17
26.01	Fe II	J	5272.40	−2.03	MF	14	−4.27	80.01	Hg II	–	3983.94	−1.73	DW	59	−5.03
26.01	Fe II	J	5276.00	−1.94	MF	58	−4.45								

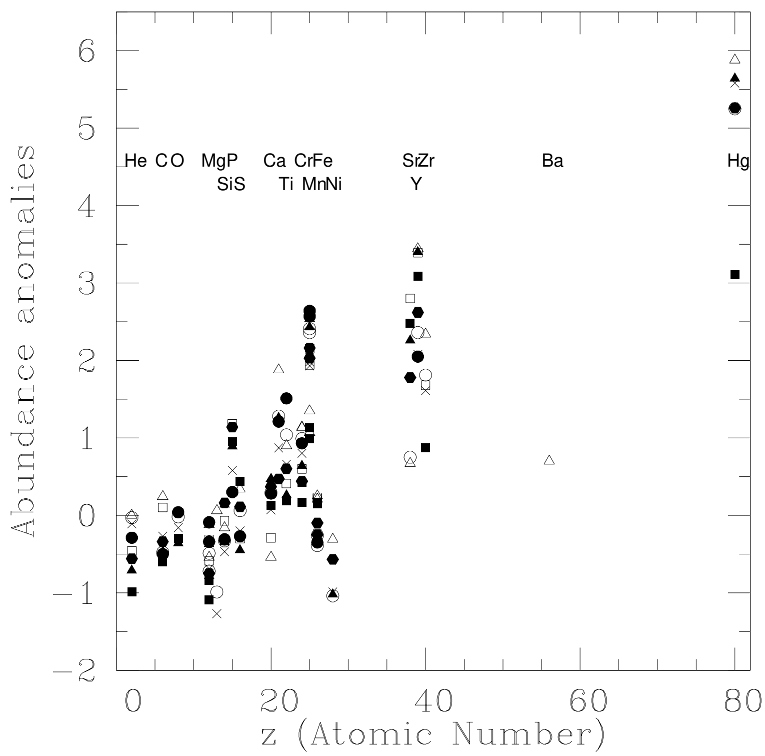

Fig. 1. Abundance anomalies relative to solar as a function of the atomic number. The HgMn stars are presented as crosses (HR 3273), empty triangles (HR 8118), empty circles (HR 8567) and empty squares (HR 8937). For comparison purposes we show the abundances of four other HgMn stars, depicted as filled circles (HR 4817), filled triangles (π Boo), filled hexagons (μ Lep) and filled squares (28 Her). Data taken from Adelman & Pintado (1997).

TABLE 10

LINE ABUNDANCES OF HR 8567

Code	Species	Mult.	λ(Å)	$\log gf$	Ref.	$W_{\rm eq}$	$\log(N/N_T)$	Code	Species	Mult.	λ(Å)	$\log gf$	Ref.	$W_{\rm eq}$	$\log(N/N_T)$
6.01	C II	4	3918.97	−0.53	WF	15	−3.76	24.01	Cr II	44	4616.63	−1.29	MF	50	−5.34
6.01	C II	4	3920.68	−0.23	WF	26	−3.53	24.01	Cr II	44	4634.07	−1.24	MF	62	−4.96
6.01	C II	6	4267.26	0.72	WF	15	−4.19	24.01	Cr II	178	4697.60	−1.88	MF	9	−5.31
8.00	O I	12	5330.73	−0.87	WF	28	−3.09	24.01	Cr II	30	4812.34	−1.80	MF	30	−5.53
12.00	Mg I	2	5183.60	−0.16	WS	8	−5.14	24.01	Cr II	30	4836.23	−2.25	MF	31	−5.06
12.01	Mg II	10	4390.57	−0.53	WS	31	−4.95	24.01	Cr II	30	4848.23	−1.14	MF	54	−5.46
12.01	Mg II	9	4427.99	−1.21	WS	10	−4.88	24.01	Cr II	30	4884.61	−2.08	MF	24	−5.43
13.01	Al II	2	4663.05	−0.28	FW	8	−6.52	24.01	Cr II	190	4912.46	−0.95	KX	19	−5.43
14.01	Si II	1	3853.66	−1.44	LA	56	−4.99	24.01	Cr II	43	5232.50	−2.09	KX	21	−5.42
14.01	Si II	1	3856.02	−0.49	LA	107	−4.89	24.01	Cr II	43	5237.33	−1.16	MF	59	−5.11
14.01	Si II	1	3862.59	−0.74	LA	88	−4.98	24.01	Cr II	23	5249.44	−2.43	KX	16	−5.40
14.01	Si II	3.01	4075.45	−1.40	SG	16	−4.72	24.01	Cr II	43	5274.96	−1.29	KX	49	−5.35
14.01	Si II	3.01	4076.78	−1.67	SG	19	−4.35	24.01	Cr II	43	5308.44	−1.81	MF	37	−5.19
14.01	Si II	3	4130.89	0.53	LA	114	−4.73	24.01	Cr II	43	5310.70	−2.28	MF	20	−5.25
14.01	Si II	5	5041.02	0.29	SG	73	−4.77	24.01	Cr II	43	5313.59	−1.65	MF	43	−5.18
16.01	S II	44	4153.07	0.62	WS	12	−4.79	24.01	Cr II	43	5334.87	−1.56	KX	40	−5.37
16.01	S II	44	4162.66	0.78	WS	14	−4.82	25.00	Mn I	2	4030.75	−0.47	MF	31	−4.50
16.01	S II	9	4815.55	0.18	WM	13	−4.93	25.00	Mn I	2	4033.06	−0.62	MF	49	−3.76
16.01	S II	1	4991.97	−0.65	WS	7	−4.45	25.00	Mn I	2	4034.48	−0.81	MF	16	−4.63
16.01	S II	15	5014.04	0.03	KX	14	−4.47	25.00	Mn I	5	4035.72	−0.19	KX	12	−4.33
16.01	S II	7	5032.43	0.18	WS	15	−4.71	25.00	Mn I	5	4041.35	0.29	MF	30	−4.25
16.01	S II	39	5212.62	0.24	WS	4	−4.93	25.00	Mn I	5	4058.93	−0.45	MF	8	−4.25
20.01	Ca II	1	3933.66	0.13	WM	280	−5.35	25.00	Mn I	23	4235.14	−0.26	KX	14	−3.81
21.01	Sc II	7	4246.82	0.24	LD	54	−7.61	25.00	Mn I	28	4455.01	−0.39	KX	11	−3.76
22.01	Ti II	34	3900.54	−0.45	MF	66	−5.97	25.00	Mn I	28	4462.03	0.32	MF	11	−4.46
22.01	Ti II	34	3913.46	−0.53	MF	70	−5.78	25.00	Mn I	22	4470.14	−0.44	MF	5	−4.16
22.01	Ti II	31	3932.02	−1.78	MF	23	−5.99	25.00	Mn I	21	4709.71	−0.34	MF	6	−4.14
22.01	Ti II	87	4028.34	−1.00	MF	31	−6.19	25.00	Mn I	16	4754.04	−0.09	MF	14	−4.32
22.01	Ti II	105	4163.64	−0.40	MF	48	−5.96	25.00	Mn I	21	4761.51	−0.14	MF	8	−4.20
22.01	Ti II	41	4290.22	−1.12	MF	54	−5.74	25.00	Mn I	16	4783.43	0.04	MF	17	−4.30
22.01	Ti II	19	4294.09	−1.11	MF	61	−5.55	25.01	Mn II	I	3878.99	−1.71	KX	55	−4.16
22.01	Ti II	41	4301.92	−1.16	MF	35	−6.28	25.01	Mn II	I	3917.32	−1.15	KX	43	−4.47
22.01	Ti II	41	4312.86	−1.16	MF	43	−6.04	25.01	Mn II	I	3930.95	−2.15	KX	23	−4.29
22.01	Ti II	94	4316.79	−1.42	MF	11	−6.31	25.01	Mn II	I	3952.42	−1.50	KX	23	−4.35
22.01	Ti II	41	4320.95	−1.87	MF	38	−5.49	25.01	Mn II	I	3986.58	−2.60	KX	28	−4.20
22.01	Ti II	104	4386.85	−1.26	MF	29	−5.62	25.01	Mn II	I	3995.31	−2.44	KX	24	−4.52
22.01	Ti II	19	4395.03	−0.66	MF	65	−5.83	25.01	Mn II	I	4000.05	−1.21	KX	40	−4.11
22.01	Ti II	61	4395.84	−2.17	MF	14	−5.86	25.01	Mn II	I	4081.44	−2.24	KX	41	−3.83
22.01	Ti II	115	4411.07	−1.06	MF	20	−5.84	25.01	Mn II	I	4087.91	−2.91	KX	12	−4.47
22.01	Ti II	40	4417.71	−1.43	MF	40	−5.88	25.01	Mn II	I	4140.44	−2.46	KX	26	−4.35
22.01	Ti II	19	4443.80	−0.70	MF	58	−6.06	25.01	Mn II	2	4174.32	−3.55	KX	58	−4.08
22.01	Ti II	19	4450.48	−1.45	MF	25	−6.29	25.01	Mn II	I	4180.06	−2.83	KX	13	−4.46
22.01	Ti II	31	4468.49	−0.60	MF	61	−6.04	25.01	Mn II	I	4184.45	−1.95	KX	38	−4.18
22.01	Ti II	115	4488.32	−0.82	MF	24	−5.94	25.01	Mn II	I	4200.27	−1.74	KX	48	−4.06
22.01	Ti II	50	4533.96	−0.77	MF	65	−5.67	25.01	Mn II	2	4205.38	−3.38	KX	66	−3.92
22.01	Ti II	41	4563.76	−0.96	MF	54	−5.86	25.01	Mn II	I	4240.39	−2.07	KX	40	−4.01
22.01	Ti II	59	4657.20	−2.15	MF	11	−5.98	25.01	Mn II	7	4244.25	−2.39	KX	44	−3.95
22.01	Ti II	92	4779.98	−1.37	MF	27	−5.84	25.01	Mn II	I	4251.73	−1.06	KX	61	−4.29
22.01	Ti II	82	4805.09	−1.10	MF	32	−5.97	25.01	Mn II	2	4260.46	−4.25	KX	25	−4.41
22.01	Ti II	114	4874.01	−0.79	MF	12	−6.38	25.01	Mn II	I	4377.74	−2.14	KX	29	−4.64
22.01	Ti II	114	4911.20	−0.34	MF	27	−6.32	25.01	Mn II	I	4391.96	−2.89	KX	12	−4.45
22.01	Ti II	113	5072.29	−0.75	MF	11	−6.44	25.01	Mn II	I	4393.38	−2.32	KX	31	−4.36
22.01	Ti II	86	5129.16	−1.39	MF	21	−6.06	25.01	Mn II	I	4403.51	−1.80	KX	23	−4.59
22.01	Ti II	86	5185.90	−1.35	MF	30	−5.84	25.01	Mn II	I	4478.64	−0.95	KX	56	−4.34
22.01	Ti II	7	5188.69	−1.21	MF	35	−5.99	25.01	Mn II	I	4497.94	−2.59	KX	16	−4.59
22.01	Ti II	70	5226.54	−1.30	MF	26	−6.15	25.01	Mn II	I	4503.20	−2.16	KX	26	−4.43
24.01	Cr II	167	3865.60	−0.78	KX	50	−5.26	25.01	Mn II	I	4509.22	−3.60	KX	8	−3.97
24.01	Cr II	129	3911.32	−2.06	KX	13	−5.32	25.01	Mn II	17	4510.21	−0.72	KX	17	−3.98
24.01	Cr II	183	3979.50	−0.73	KX	36	−5.58	25.01	Mn II	I	4689.55	−2.54	KX	24	−4.02
24.01	Cr II	19	4051.93	−2.19	KX	30	−5.55	25.01	Mn II	I	4702.73	−2.34	KX	15	−4.50
24.01	Cr II	26	4072.56	−2.41	KX	25	−5.16	25.01	Mn II	I	4717.26	−1.86	KX	27	−4.43
24.01	Cr II	165	4082.28	−1.23	KX	16	−5.83	25.01	Mn II	I	4730.40	−2.15	KX	52	−3.90
24.01	Cr II	26	4086.13	−2.42	KX	15	−5.48	25.01	Mn II	I	4749.11	−2.00	KX	23	−4.57
24.01	Cr II	181	4127.06	−1.77	KX	10	−5.40	25.01	Mn II	I	4791.78	−1.72	KX	41	−4.28
24.01	Cr II	26	4132.42	−2.35	KX	15	−5.54	25.01	Mn II	I	4806.82	−1.56	KX	66	−3.93
24.01	Cr II	26	4179.42	−1.77	KX	29	−5.63	25.01	Mn II	I	4830.06	−1.85	KX	39	−4.23
24.01	Cr II	31	4275.57	−1.70	KX	51	−5.02	25.01	Mn II	I	4839.74	−1.86	KX	32	−4.43
24.01	Cr II	191	4465.73	−1.18	KX	9	−5.65	25.01	Mn II	I	4842.32	−2.01	KX	39	−4.05
24.01	Cr II	44	4554.99	−1.38	MF	50	−5.25	25.01	Mn II	I	5102.52	−1.93	KX	48	−3.91
24.01	Cr II	39	4565.74	−2.11	MF	33	−5.08	25.01	Mn II	I	5307.35	−2.07	KX	17	−4.25
24.01	Cr II	44	4588.20	−0.63	MF	80	−4.96	25.01	Mn II	I	3902.36	−2.72	KX	13	−4.53
24.01	Cr II	44	4592.05	−1.22	MF	54	−5.28	26.00	Fe I	4	3859.91	−0.71	N4	10	−4.68

TABLE 10 (CONTINUED)

Code	Species	Mult.	λ(Å)	$\log gf$	Ref.	W_{eq}	$\log(N/N_T)$
26.00	Fe I	20	3872.50	−0.93	N4	3	−4.54
26.00	Fe I	41	4383.54	0.20	N4	6	−5.10
26.01	Fe II	127	3845.18	−2.29	KX	8	−5.24
26.01	Fe II	38	3935.96	−1.86	N4	12	−4.96
26.01	Fe II	190	3938.97	−1.85	N4	11	−4.88
26.01	Fe II	28	4122.67	−3.38	N4	9	−4.99
26.01	Fe II	27	4273.33	−3.34	N4	8	−5.02
26.01	Fe II	28	4296.57	−3.01	N4	15	−5.03
26.01	Fe II	27	4303.18	−2.61	N4	46	−4.47
26.01	Fe II	27	4351.77	−2.08	N4	35	−5.35
26.01	Fe II	27	4385.39	−2.57	N4	28	−5.03
26.01	Fe II	27	4416.83	−2.60	N4	26	−5.05
26.01	Fe II	37	4489.18	−2.97	N4	18	−4.89
26.01	Fe II	37	4491.40	−2.70	N4	18	−5.16
26.01	Fe II	38	4508.29	−2.21	N4	32	−5.23
26.01	Fe II	37	4515.34	−2.48	N4	26	−5.14
26.01	Fe II	37	4520.22	−2.60	N4	22	−5.15
26.01	Fe II	38	4522.63	−2.03	N4	40	−5.17
26.01	Fe II	38	4541.52	−3.05	N4	13	−4.98
26.01	Fe II	37	4555.89	−2.29	N4	34	−5.10
26.01	Fe II	38	4576.34	−3.04	N4	13	−5.00
26.01	Fe II	37	4582.84	−3.10	N4	11	−5.07
26.01	Fe II	38	4583.84	−2.02	N4	51	−4.83
26.01	Fe II	D	4596.02	−1.84	N4	8	−4.84
26.01	Fe II	38	4620.52	−3.28	N4	8	−5.03
26.01	Fe II	37	4629.34	−2.37	N4	31	−5.10
26.01	Fe II	186	4635.32	−1.65	N4	17	−4.77
26.01	Fe II	28	4666.76	−3.33	N4	10	−4.90
26.01	Fe II	43	4731.45	−3.13	N4	10	−5.05
26.01	Fe II	J	4908.15	−0.30	KX	8	−4.50
26.01	Fe II	J	4951.58	0.18	KX	12	−4.76
26.01	Fe II	J	4984.47	0.01	KX	6	−4.92
26.01	Fe II	J	4990.51	0.18	KX	8	−4.94
26.01	Fe II	J	4993.36	−3.65	MF	4	−4.95
26.01	Fe II	J	5001.96	0.90	KX	28	−4.85
26.01	Fe II	J	5004.20	0.50	KX	14	−4.96
26.01	Fe II	J	5018.44	−1.22	MF	77	−4.68
26.01	Fe II	J	5022.79	−0.02	KX	8	−4.78
26.01	Fe II	J	5032.71	0.11	KX	14	−4.52
26.01	Fe II	J	5035.71	0.61	KX	21	−4.79
26.01	Fe II	J	5061.72	0.22	KX	7	−5.06
26.01	Fe II	J	5070.90	0.24	KX	6	−5.16
26.01	Fe II	J	5075.76	0.28	KX	8	−4.95
26.01	Fe II	J	5082.23	−0.10	KX	5	−4.80
26.01	Fe II	J	5093.58	0.11	KX	11	−4.64
26.01	Fe II	J	5145.77	−0.40	KX	5	−4.49
26.01	Fe II	J	5149.46	0.40	KX	14	−4.76
26.01	Fe II	J	5150.49	−0.12	KX	9	−4.50
26.01	Fe II	J	5169.03	−0.87	MF	81	−4.89
26.01	Fe II	J	5199.12	0.10	KX	5	−5.08
26.01	Fe II	J	5203.64	−0.05	KX	6	−4.81
26.01	Fe II	J	5216.85	0.81	KX	17	−5.00
26.01	Fe II	J	5234.62	−2.05	MF	37	−5.02
26.01	Fe II	J	5247.95	0.55	N4	22	−4.55
26.01	Fe II	J	5260.25	1.07	KX	30	−4.84
26.01	Fe II	J	5272.40	−2.03	MF	14	−4.46
26.01	Fe II	J	5276.00	−1.94	MF	34	−5.21
26.01	Fe II	J	5291.67	0.58	KX	13	−4.94
28.01	Ni II	11	3849.55	−1.88	KX	9	−6.54
28.01	Ni II	11	4067.03	−1.29	KX	11	−7.03
38.01	Sr II	1	4215.52	−0.17	WM	21	−8.35
39.01	Y II	6	3950.35	−0.49	HL	21	−7.55
39.01	Y II	6	3982.59	−0.49	HL	19	−7.62
39.01	Y II	5	4422.58	−1.27	HL	7	−7.43
39.01	Y II	22	4854.86	−0.38	HL	12	−7.59
39.01	Y II	22	4900.12	−0.09	HL	24	−7.38
39.01	Y II	20	5119.11	−1.36	HL	4	−7.14
39.01	Y II	20	5200.41	−0.57	HL	14	−7.28
39.01	Y II	20	5205.72	−0.34	HL	20	−7.24
40.01	Zr II	16	3998.95	−0.67	GB	5	−7.91
40.01	Zr II	42	4161.21	−0.72	BG	15	−7.26
80.01	Hg II	–	3983.94	−1.73	DW	50	−5.39

lated with stellar rotation. If difussion is operating in the atmospheres, probably one should expect that abundance anomalies should decrease with increasing rotational velocity. In fact, CP stars are rarely found having rotational velocities larger than $\sim$120 km s^{-1}. Finding a trend or its absence will be important in the context of the diffusion theory, which is the best explanation today for the spectroscopic characteristics of CP stars.

The authors acknowledge the use of the CCD and data reduction acquisition system supported by US NSF Grant AST 90-15827 to R. M. Rich. The authors thank Drs. R.L. Kurucz and I. Hubeny for making their codes available to them. This work was partially supported by a grant PICT 20269 from Agencia Nacional de Promoción Científica y Tecnológica.

REFERENCES

Abt, H., & Golson, J. 1962, ApJ, 136, 35

Abt, H., Chaffee, F. H., & Suffolk, G. 1972, ApJ, 175, 779

Adelman, S. J., & Pintado, O. 1997, A&AS, 125, 219

Adelman, S. J., & Rayle, K. E. 2000, A&A, 355, 308

Adelman, S. J., & Yüce, K. 2010, Astron. Nachr., 331, 785

Andersen, J., & Nordström, B. 1977, A&AS, 29, 309

Auriére, M., et al. 2007, A&A, 475, 1053

Auriére, M., et al. 2010, A&A, 523, 40

Bertaud, C. 1958, J. Obs., 42, 45

Corben, P. M. 1971, Mon. Not. Astron. Soc. S. Afr., 30, 37

Corben, P. M., & Stoy, R. H. 1968, Mon. Not. Astron. Soc. S. Afr., 27, 11

Cousins, A., & Stoy, R. 1962, Royal Greenwich Obs. Bull., 64, 103

Cowley, A. P., Cowley, C. R., Hiltner, W., Jaschek, M., & Jaschek, C. 1968, PASP, 80, 746

Cowley, A. P., Cowley, C. R., Jaschek, M., & Jaschek, C. 1969, AJ, 74, 375

Crawford, D. L. 1963, ApJ, 137, 530

Crawford, D. L., Barnes, J. V., & Golson, C. 1970, AJ, 75, 624

Cutri, R., et al. 2003, he IRSA 2MASS All-Sky Point Source Catalog, NASA/IPAC Infrared Science Archive `http://irsa.ipac.caltech.edu/applications/Gator/`

Chapelle, J., & Sahal-Brechot, S. 1970, A&A, 6, 415

TABLE 11

LINE ABUNDANCES OF HR 8937

Code	Species	Mult.	λ(Å)	$\log gf$	Ref.	W_{eq}	$\log(N/N_T)$
6.01	C II	4	3918.97	−0.53	WF	19	−3.21
6.01	C II	4	3920.68	−0.23	WF	24	−3.27
12.00	Mg I	2	5172.68	−0.38	WS	15	−5.01
12.00	Mg I	2	5183.60	−0.16	WS	22	−5.02
12.01	Mg II	5	3848.21	−1.59	WS	25	−4.51
12.01	Mg II	10	4390.57	−0.53	WS	35	−4.88
12.01	Mg II	9	4427.99	−1.21	WS	11	−4.80
14.01	Si II	1	3853.66	−1.44	LA	69	−4.59
14.01	Si II	1	3856.02	−0.49	LA	122	−4.76
14.01	Si II	1	3862.59	−0.74	LA	103	−4.76
14.01	Si II	3.01	4075.45	−1.40	SG	17	−4.52
14.01	Si II	3.01	4076.78	−1.67	SG	17	−4.23
14.01	Si II	3	4128.05	0.38	LA	145	−4.27
14.01	Si II	3	4130.89	0.53	LA	128	−4.56
14.01	Si II	5	5041.02	0.29	SG	90	−4.44
15.01	P II	15	4602.07	0.74	WS	11	−5.37
16.01	S II	44	4153.07	0.62	WS	4	−5.13
16.01	S II	44	4162.66	0.78	WS	7	−4.96
16.01	S II	9	4815.55	0.18	WM	5	−5.17
20.01	Ca II	1	3933.66	0.13	WM	232	−5.93
22.01	Ti II	34	3900.54	−0.45	MF	47	−6.76
22.01	Ti II	34	3913.46	−0.53	MF	49	−6.65
22.01	Ti II	87	4028.34	−1.00	MF	16	−6.70
22.01	Ti II	105	4163.64	−0.40	MF	30	−6.55
22.01	Ti II	19	4294.09	−1.11	MF	36	−6.44
22.01	Ti II	41	4300.04	−0.77	MF	54	−6.22
22.01	Ti II	41	4301.92	−1.16	MF	16	−6.90
22.01	Ti II	41	4312.86	−1.16	MF	26	−6.58
22.01	Ti II	19	4395.03	−0.66	MF	47	−6.58
22.01	Ti II	61	4395.84	−2.17	MF	6	−6.34
22.01	Ti II	51	4399.77	−1.27	MF	16	−6.75
22.01	Ti II	40	4417.71	−1.43	MF	16	−6.62
22.01	Ti II	19	4443.80	−0.70	MF	37	−6.81
22.01	Ti II	19	4450.48	−1.45	MF	13	−6.76
22.01	Ti II	31	4468.49	−0.60	MF	37	−6.89
22.01	Ti II	115	4488.32	−0.82	MF	11	−6.48
22.01	Ti II	31	4501.27	−0.75	MF	33	−6.85
22.01	Ti II	50	4533.96	−0.77	MF	51	−6.28
22.01	Ti II	41	4563.76	−0.96	MF	31	−6.63
22.01	Ti II	82	4571.97	−0.53	MF	47	−6.47
22.01	Ti II	59	4657.20	−2.15	MF	9	−6.17
22.01	Ti II	92	4779.98	−1.37	MF	9	−6.53
22.01	Ti II	82	4805.09	−1.10	MF	13	−6.61
22.01	Ti II	114	4911.20	−0.34	MF	9	−7.05
22.01	Ti II	86	5185.90	−1.35	MF	22	−6.14
22.01	Ti II	7	5188.69	−1.21	MF	14	−6.72
24.01	Cr II	167	3865.60	−0.78	KX	25	−5.92
24.01	Cr II	167	3905.64	−0.90	KX	43	−5.30
24.01	Cr II	129	3911.32	−2.06	KX	9	−5.43
24.01	Cr II	183	3979.50	−0.73	KX	15	−6.15
24.01	Cr II	19	4051.93	−2.19	KX	9	−6.16
24.01	Cr II	26	4072.56	−2.41	KX	11	−5.57
24.01	Cr II	162	4145.78	−1.16	KX	16	−5.85
24.01	Cr II	31	4261.91	−1.53	KX	46	−5.31
24.01	Cr II	31	4275.57	−1.70	KX	28	−5.64
24.01	Cr II	44	4554.99	−1.38	MF	31	−5.76
24.01	Cr II	44	4558.65	−0.66	MF	64	−5.51
24.01	Cr II	39	4565.74	−2.11	MF	13	−5.63
24.01	Cr II	44	4588.20	−0.63	MF	65	−5.50
24.01	Cr II	44	4592.05	−1.22	MF	30	−5.94
24.01	Cr II	44	4616.63	−1.29	MF	24	−6.06
24.01	Cr II	44	4618.80	−1.11	MF	45	−5.65
24.01	Cr II	44	4634.07	−1.24	MF	39	−5.68
24.01	Cr II	30	4812.34	−1.80	MF	11	−6.11
24.01	Cr II	30	4824.13	−1.22	MF	48	−5.55
24.01	Cr II	30	4836.23	−2.25	MF	12	−5.61
24.01	Cr II	30	4848.23	−1.14	MF	31	−6.11
24.01	Cr II	105	4876.40	−1.46	KX	35	−5.68
24.01	Cr II	30	4884.61	−2.08	MF	8	−5.94
24.01	Cr II	43	5232.50	−2.09	KX	15	−5.50
24.01	Cr II	23	5246.77	−2.45	MF	16	−5.29
24.01	Cr II	43	5274.96	−1.29	KX	24	−6.01
24.01	Cr II	43	5308.44	−1.81	MF	20	−5.61
24.01	Cr II	43	5310.70	−2.28	MF	8	−5.63
24.01	Cr II	43	5313.59	−1.65	MF	19	−5.82
24.01	Cr II	43	5334.87	−1.56	KX	19	−5.90
25.00	Mn I	2	4030.75	−0.47	MF	27	−4.98
25.00	Mn I	2	4033.06	−0.62	MF	47	−4.26
25.00	Mn I	2	4034.48	−0.81	MF	19	−4.86
25.00	Mn I	5	4035.72	−0.19	KX	10	−4.80
25.00	Mn I	5	4041.35	0.29	MF	26	−4.71
25.00	Mn I	22	4414.89	−0.29	MF	7	−4.51
25.00	Mn I	16	4754.04	−0.09	MF	12	−4.72
25.00	Mn I	21	4761.51	−0.14	MF	5	−4.74
25.00	Mn I	21	4765.85	−0.08	MF	11	−4.45
25.00	Mn I	21	4766.42	0.10	MF	11	−4.62
25.00	Mn I	16	4783.43	0.04	MF	15	−4.72
25.01	Mn II	I	3859.21	−2.56	KX	10	−4.80
25.01	Mn II	I	3878.99	−1.71	KX	40	−4.61
25.01	Mn II	I	3917.32	−1.15	KX	35	−4.65
25.01	Mn II	I	3952.42	−1.50	KX	15	−4.53
25.01	Mn II	I	3986.58	−2.60	KX	18	−4.41
25.01	Mn II	I	3995.31	−2.44	KX	17	−4.65
25.01	Mn II	I	4000.05	−1.21	KX	31	−4.31
25.01	Mn II	I	4081.44	−2.24	KX	32	−4.02
25.01	Mn II	I	4087.91	−2.91	KX	9	−4.51
25.01	Mn II	I	4110.62	−1.51	KX	34	−4.68
25.01	Mn II	I	4140.44	−2.46	KX	18	−4.50
25.01	Mn II	I	4184.45	−1.95	KX	28	−4.38
25.01	Mn II	I	4200.27	−1.74	KX	39	−4.28
25.01	Mn II	2	4205.38	−3.38	KX	57	−4.25
25.01	Mn II	I	4240.39	−2.07	KX	29	−4.25
25.01	Mn II	7	4244.25	−2.39	KX	37	−4.10
25.01	Mn II	2	4260.46	−4.25	KX	19	−4.49
25.01	Mn II	I	4377.74	−2.14	KX	22	−4.73
25.01	Mn II	I	4391.96	−2.89	KX	7	−4.58
25.01	Mn II	I	4393.38	−2.32	KX	20	−4.61
25.01	Mn II	I	4403.51	−1.80	KX	20	−4.58
25.01	Mn II	I	4478.64	−0.95	KX	49	−4.51
25.01	Mn II	I	4497.94	−2.59	KX	10	−4.74
25.01	Mn II	I	4500.54	−2.07	KX	15	−4.77
25.01	Mn II	I	4503.20	−2.16	KX	19	−4.55
25.01	Mn II	I	4689.55	−2.54	KX	15	−4.22
25.01	Mn II	I	4702.73	−2.34	KX	13	−4.49
25.01	Mn II	I	4717.26	−1.86	KX	19	−4.56
25.01	Mn II	I	4730.40	−2.15	KX	46	−4.03
25.01	Mn II	I	4749.11	−2.00	KX	17	−4.64
25.01	Mn II	I	4791.78	−1.72	KX	29	−4.56
25.01	Mn II	I	4806.82	−1.56	KX	55	−4.30
25.01	Mn II	I	4830.06	−1.85	KX	30	−4.41
25.01	Mn II	I	4839.74	−1.86	KX	21	−4.65
25.01	Mn II	I	4842.32	−2.01	KX	25	−4.38
25.01	Mn II	I	5102.52	−1.93	KX	40	−4.08
25.01	Mn II	I	5307.35	−2.07	KX	11	−4.39
25.01	Mn II	I	3902.36	−2.72	KX	10	−4.59
25.01	Mn II	I	3926.11	−2.42	KX	26	−4.08
26.00	Fe I	45	3815.84	0.23	N4	19	−4.80
26.00	Fe I	20	3825.88	−0.04	N4	20	−4.80
26.00	Fe I	4	3859.91	−0.71	N4	14	−4.79
26.00	Fe I	20	3865.52	−0.98	N4	18	−3.88
26.00	Fe I	20	3872.50	−0.93	N4	12	−4.17
26.00	Fe I	43	4071.74	−0.02	N4	12	−4.78
26.00	Fe I	152	4198.30	−0.72	N4	8	−3.89
26.00	Fe I	522	4199.10	0.16	N4	18	−4.01
26.00	Fe I	42	4271.76	−0.16	N4	11	−4.74
26.00	Fe I	41	4383.54	0.20	N4	19	−4.79
26.00	Fe I	41	4404.75	−0.14	N4	16	−4.51
26.00	Fe I	318	4920.50	0.07	N4	22	−3.90
26.00	Fe I	289	4957.30	−0.41	N4	9	−3.90
26.00	Fe I	318	4957.60	0.23	N4	9	−4.58
26.00	Fe I	325	5192.34	−0.42	N4	8	−3.86
26.00	Fe I	383	5232.94	−0.06	N4	17	−3.86
26.00	Fe I	1146	5383.37	0.65	N4	12	−4.10
26.00	Fe I	686	5586.76	−0.14	N4	8	−3.96

TABLE 11 (CONTINUED)

Code	Species	Mult.	λ(Å)	log gf	Ref.	W_{eq}	log(N/N_T)	Code	Species	Mult.	λ(Å)	log gf	Ref.	W_{eq}	log(N/N_T)
26.01	Fe II	127	3845.18	−2.29	KX	13	−4.82	26.01	Fe II	J	5070.90	0.24	KX	18	−4.36
26.01	Fe II	173	3906.04	−1.83	N4	28	−4.29	26.01	Fe II	J	5075.76	0.28	KX	15	−4.44
26.01	Fe II	38	3935.96	−1.86	N4	24	−4.37	26.01	Fe II	J	5082.23	−0.10	KX	9	−4.39
26.01	Fe II	3	3938.29	−4.07	N4	13	−4.39	26.01	Fe II	J	5093.58	0.11	KX	22	−4.01
26.01	Fe II	90	3938.97	−1.85	N4	20	−4.34	26.01	Fe II	J	5097.27	0.31	KX	31	−3.95
26.01	Fe II	28	4122.67	−3.38	N4	20	−4.41	26.01	Fe II	J	5106.11	−0.28	KX	13	−4.02
26.01	Fe II	27	4233.17	−1.81	N4	83	−4.02	26.01	Fe II	J	5117.03	−0.13	KX	8	−4.41
26.01	Fe II	27	4273.33	−3.34	N4	20	−4.36	26.01	Fe II	J	5145.77	−0.40	KX	12	−3.92
26.01	Fe II	28	4296.57	−3.01	N4	33	−4.32	26.01	Fe II	J	5149.46	0.40	KX	28	−4.09
26.01	Fe II	27	4303.18	−2.61	N4	57	−4.01	26.01	Fe II	J	5150.49	−0.12	KX	12	−4.18
26.01	Fe II	27	4351.77	−2.08	N4	50	−4.74	26.01	Fe II	J	5160.84	−2.64	KX	10	−4.03
26.01	Fe II	J	4357.58	−2.10	KX	9	−4.45	26.01	Fe II	J	5169.03	−0.87	MF	106	−4.26
26.01	Fe II	27	4385.39	−2.57	N4	45	−4.37	26.01	Fe II	J	5180.31	0.04	KX	5	−4.77
26.01	Fe II	27	4416.83	−2.60	N4	40	−4.49	26.01	Fe II	J	5199.12	0.10	KX	21	−4.03
26.01	Fe II	37	4472.93	−3.53	N4	13	−4.38	26.01	Fe II	J	5203.64	−0.05	KX	16	−4.07
26.01	Fe II	37	4489.18	−2.97	N4	31	−4.34	26.01	Fe II	J	5216.85	0.81	KX	28	−4.45
26.01	Fe II	37	4491.40	−2.70	N4	36	−4.46	26.01	Fe II	J	5223.26	−0.41	KX	7	−4.17
26.01	Fe II	38	4508.29	−2.21	N4	50	−4.53	26.01	Fe II	J	5228.90	−0.30	KX	12	−3.99
26.01	Fe II	37	4515.34	−2.48	N4	42	−4.51	26.01	Fe II	J	5232.79	−0.06	KX	16	−4.07
26.01	Fe II	37	4520.22	−2.60	N4	38	−4.54	26.01	Fe II	J	5234.62	−2.05	MF	57	−4.22
26.01	Fe II	38	4522.63	−2.03	N4	56	−4.55	26.01	Fe II	J	5247.95	0.55	N4	31	−4.08
26.01	Fe II	38	4541.52	−3.05	N4	28	−4.35	26.01	Fe II	J	5251.23	0.42	N4	30	−3.98
26.01	Fe II	37	4555.89	−2.29	N4	51	−4.44	26.01	Fe II	J	5254.93	−3.23	KX	13	−4.44
26.01	Fe II	38	4576.34	−3.04	N4	26	−4.40	26.01	Fe II	J	5257.12	0.03	KX	12	−4.30
26.01	Fe II	37	4582.84	−3.10	N4	22	−4.48	26.01	Fe II	J	5260.25	1.07	KX	46	−4.25
26.01	Fe II	38	4583.84	−2.02	N4	69	−4.15	26.01	Fe II	J	5272.40	−2.03	MF	18	−4.09
26.01	Fe II	D	4596.02	−1.84	N4	18	−4.24	26.01	Fe II	J	5276.00	−1.94	MF	52	−4.51
26.01	Fe II	38	4620.52	−3.28	N4	20	−4.35	26.01	Fe II	J	5291.67	0.58	KX	37	−3.95
26.01	Fe II	37	4629.34	−2.37	N4	50	−4.39	26.01	Fe II	J	5306.18	0.09	N4	23	−3.87
26.01	Fe II	186	4635.32	−1.65	N4	29	−4.20	26.01	Fe II	J	5339.59	0.54	KX	30	−4.11
26.01	Fe II	28	4666.76	−3.33	N4	18	−4.37	26.02	Fe III	4	4419.60	−2.22	KX	3	−4.35
26.01	Fe II	43	4731.45	−3.13	N4	22	−4.41	38.01	Sr II	1	4215.52	−0.17	WM	81	−6.30
26.01	Fe II	J	4908.15	−0.30	KX	10	−4.17	39.01	Y II	6	3950.35	−0.49	HL	52	−6.51
26.01	Fe II	J	4913.29	0.01	KX	14	−4.32	39.01	Y II	6	3982.59	−0.49	HL	54	−6.45
26.01	Fe II	J	4951.58	0.18	KX	18	−4.32	39.01	Y II	14	4124.90	−1.50	HL	29	−6.29
26.01	Fe II	J	4977.04	0.04	KX	17	−4.16	39.01	Y II	5	4235.73	−1.50	HL	34	−6.26
26.01	Fe II	J	4984.47	0.01	KX	12	−4.33	39.01	Y II	5	4422.58	−1.27	HL	35	−6.49
26.01	Fe II	J	4990.51	0.18	KX	15	−4.41	39.01	Y II	22	4854.86	−0.38	HL	37	−6.81
26.01	Fe II	J	4993.36	−3.65	MF	7	−4.55	39.01	Y II	22	4900.12	−0.09	HL	59	−6.18
26.01	Fe II	J	5001.96	0.90	KX	44	−4.25	39.01	Y II	20	4982.13	−1.29	HL	19	−6.53
26.01	Fe II	J	5004.20	0.50	KX	24	−4.43	39.01	Y II	20	5200.41	−0.57	HL	48	−6.15
26.01	Fe II	J	5015.75	−0.05	KX	24	−3.86	39.01	Y II	20	5205.72	−0.34	HL	54	−6.10
26.01	Fe II	J	5018.44	−1.22	MF	102	−3.99	39.01	Y II	20	5289.82	−1.85	HL	10	−6.35
26.01	Fe II	J	5021.59	−0.30	KX	6	−4.44	40.01	Zr II	17	3915.96	−0.82	KX	6	−7.86
26.01	Fe II	J	5022.79	−0.02	KX	19	−4.17	40.01	Zr II	16	3958.23	−0.31	KX	15	−7.85
26.01	Fe II	J	5030.63	0.40	KX	21	−4.44	40.01	Zr II	30	3991.15	−0.25	KX	16	−7.77
26.01	Fe II	J	5035.71	0.61	KX	31	−4.32	40.01	Zr II	16	3998.95	−0.67	GB	16	−7.45
26.01	Fe II	J	5045.11	−0.13	KX	9	−4.38	40.01	Zr II	41	4149.22	−0.03	BG	24	−7.69
26.01	Fe II	J	5061.72	0.22	KX	16	−4.41	40.01	Zr II	41	4208.98	−0.46	BG	13	−7.70
26.01	Fe II	J	5067.89	−0.20	KX	8	−4.35	80.01	Hg II	–	3983.94	−1.73	DW	128	−4.06

Dolk, L., Wahlgren, G. M., & Hubrig, S. 2003, A&A, 402, 299

Dworetsky, M. M. 1971, PhD Thesis, University of California, USA

Eggen, O. 1977, PASP, 89, 205

Fuhr, J. R., Martin, G. A., & Wiese, W. L. 1988, J. Phys. Chem. Ref. Data, 17, Suppl. 4

Fuhr, J. R., & Wiese, W. L. 2006, J. Phys. Chem. Ref. Data, 35, 1669

Glagolevskij, Yu. V. 1994, Bull. Spec. Astrophys. Obs., 38, 152

Grevesse, N., Noels, A., & Sauval, A. 1996, in ASP Conf. Ser. 99, Cosmic Abundances, ed. S. Holt & G. Sonneborn (San Francisco: ASP), 117

Gronbech, B., & Olsen, E. H. 1976, A&AS, 25, 213

_________. 1977, A&AS, 27, 443

Guthrie, B. N. 1985, MNRAS, 216, 1

Hauck, B., & Mermilliod, M. 1998, A&AS, 129, 431

Houk, N. 1982, Michigan Catalogue of Two-Dimensional Spectral Types for the HD Stars, Vol. 3 (Ann Arbor: Univ. Michigan Dept. Astron.)

Hubrig, S., & Mathys, G. 1995, in ASP Conf. Ser. 81, Laboratory and Astronomical High Resolution Spectra, ed. A. J. Sauval, R. Blomme, & N. Grevesse (San Francisco: ASP), 555

Iglesias, L., & Velasco, R. 1964, Publ. Inst. Opt. Madrid, No. 23

Irwin, J. B. 1961, ApJS, 6, 253

Johansson, S. 1978, Phys. Scr., 18, 217

Jomaron, C. M., Dworetsky, M. M., & Allen, C. S. 1999,

MNRAS, 303, 555
Kurucz, R. L., & Avrett, E. H. 1981, SAO Spec. Rep., 391
Kurucz, R. L., & Bell, B. 1995, Atomic Line Data, Kurucz CD-ROM No. 23 (Cambridge: SAO)
Lanz, T., Dimitrijevic, M. S., & Artru, M. C. 1988, A&A, 192, 249
Makaganiuk, V., et al. 2011, A&A, 525, 97
Moon, T. T., & Dworetsky, M. 1985, MNRAS, 217, 305
Moore, C. E. 1945, A Multiplet Table of Astrophysical Interest (Princeton: Princeton Univ. Obs.)
Napiwotzki, R., Shonberner, D., & Wenske, V. 1993, A&A, 268, 653
Nilsson, A., Johansson, S., & Kurucz, R. L. 1991, Phys. Scr., 44, 226
Pintado, O. I., & Adelman, S. J. 2003, A&A, 406, 987
Piskunov, N. E. 1996, in ASP Conf. Ser. 108, Model Atmosphere and Spectrum Synthesis, ed. S. J. Adelman, F. Kupka, & W. W. Weiss (San Francisco: ASP), 307
Reader, J., Corliss, C. H., Wiese, W. L., & Martin, G. A. 1980, Wavelengths and Transition Probabilities for Atoms and Atomic Ions, Part 1 (NSRDS-NBS 68; Washington: NBS)
Renson, P., & Manfroid, J. 2009, A&A 498, 961
Rybka, E. 1969, Acta Astron., 19, 229
Saffe, C., & Levato, H. 2009, RevMexAA, 45, 171
Saffe, C., Levato, H., & López-García, Z., 2004, RevMexAA, 40, 231
_________. 2005, RevMexAA, 41, 415
Sahal-Brechot, S. 1969, A&A, 2, 322
Schneider, H. 1981, A&AS, 44, 137
Smith, K. C. 1997, A&A, 319, 928
Smith, K. C., & Dworetsky, M. M. 1993, A&A, 274, 335
Strauss, F. M., & Ducati, J. R. 1981, A&AS, 44, 337
Svendenius, N., Magnusson, C. E., & Zetterberg, P. O. 1983, Phys. Scr., 27, 339
Woolf, V. M., & Lambert, D. L. 1999, ApJ, 521, 414
Wolff, S., & Wolff, R. 1974, ApJ, 194, 65
Zavala, R. T., et al. 2007, ApJ, 655, 1046

C. Saffe, N. Núñez and H. Levato: Instituto de Ciencias Astronómicas, de la Tierra y del Espacio, C.C 467, 5400, San Juan, Argentina. CS and HL are members of the Carrera del Investigador Científico, Consejo Nacional de Investigaciones Científicas y Técnicas de la República Argentina (csaffe, nnunez, hlevato@icate-conicet.gob.ar).

Revista Mexicana de Astronomía y Astrofísica, **47**, 235–253 (2011)

ON THE STELLAR AND BARYONIC MASS FRACTIONS OF CENTRAL BLUE AND RED GALAXIES

A. Rodríguez-Puebla,[1] V. Avila-Reese,[1] C. Firmani,[1,2] and P. Colín[3]

Received 2011 January 21; accepted 2011 April 14

RESUMEN

Con la técnica del empate de abundancias, las relaciones locales masa estelar y bariónica-masa de halo ($M_{\rm s}$–$M_{\rm h}$ y $M_{\rm b}$–$M_{\rm h}$) para galaxias *centrales* azules y rojas (GAs y GRs) se infieren por separado. Se hace uso de las funciones de masa estelar galáctica observadas de GAs y GRs y las respectivas relaciones masa de gas-$M_{\rm s}$. Las funciones de masa de halos asociados a las GAs y GRs centrales se toman de una descomposición adecuadamente obtenida de la función de halos distinguibles ΛCDM. Para $M_{\rm h} \gtrsim 10^{11.5}$ $M_\odot$, la $M_{\rm s}$ de GRs tiende a ser mayor que la de GAs a una dada $M_{\rm h}$, pero no más que un factor $\sim$1.7. Para $M_{\rm h} \lesssim 10^{11.5}$ $M_\odot$, esta tendencia se invierte. Para GAs (GRs): (a) el máximo de $f_{\rm s}$=$M_{\rm s}/M_{\rm h}$ es $0.021^{+0.016}_{-0.009}$ ($0.034^{+0.026}_{-0.015}$) y se alcanza a $\log(M_{\rm h}/M_\odot) = 12.0$ (= 11.9); (b) $f_{\rm s} \propto M_{\rm h}$ ($f_{\rm s} \propto {M_{\rm h}}^3$) hacia el lado de bajas masas, mientras que en el otro extremo $f_{\rm s} \propto {M_{\rm h}}^{-0.4}$ ($f_{\rm s} \propto {M_{\rm h}}^{-0.6}$). Las $f_{\rm b}$=$M_{\rm b}/M_{\rm h}$ de GAs y GRs son cercanas para $M_{\rm h} \gtrsim 10^{11.7}$ $M_\odot$, y alcanzan valores máximos de $f_{\rm b} = 0.028^{+0.018}_{-0.011}$ y $f_{\rm b} = 0.034^{+0.025}_{-0.014}$. Hacia masas menores la dependencia de $f_{\rm b}$ sobre $M_{\rm h}$ es mucho más empinada para GRs que para GAs. Discutimos las diferencias encontradas para las relaciones $f_{\rm s}$–$M_{\rm h}$ y $f_{\rm b}$–$M_{\rm h}$ entre GAs y GRs a la luz de inferencias semi-empíricas de evolución galáctica.

ABSTRACT

Using the abundance matching technique, we infer the local stellar and baryonic mass-halo mass ($M_{\rm s}$–$M_{\rm h}$ and $M_{\rm b}$–$M_{\rm h}$) relations separately for *central* blue and red galaxies (BGs and RGs). The observational inputs are the SDSS central BG and RG stellar mass functions and the measured gas mass-$M_{\rm s}$ relations. For halos associated to central BGs, the distinct ΛCDM halo mass function is used and set up to exclude: (i) the observed group/cluster mass function and (ii) halos with a central major merger at resdshifts $z \leq 0.8$. For central RGs, the complement of this mass function to the total one is used. At $M_{\rm h} > 10^{11.5}$ $M_\odot$, the $M_{\rm s}$ of RGs tend to be higher than those of BGs for a given $M_{\rm h}$, the difference not being larger than 1.7. At $M_{\rm h} < 10^{11.5}$ $M_\odot$, this trend is inverted. For BGs (RGs): (a) the maximum value of $f_{\rm s} = M_{\rm s}/M_{\rm h}$ is $0.021^{+0.016}_{-0.009}$ ($0.034^{+0.026}_{-0.015}$) and it is attained at $\log(M_{\rm h}/M_\odot) = 12.0$ (= 11.9); (b) $f_{\rm s} \propto M_{\rm h}$ ($f_{\rm s} \propto {M_{\rm h}}^3$) at the low-mass end while at the high-mass end, $f_{\rm s} \propto {M_{\rm h}}^{-0.4}$ ($f_{\rm s} \propto {M_{\rm h}}^{-0.6}$). The baryon mass fractions, $f_{\rm b}$=$M_{\rm b}/M_{\rm h}$, of BGs and RGs reach maximum values of $f_{\rm b} = 0.028^{+0.018}_{-0.011}$ and $f_{\rm b} = 0.034^{+0.025}_{-0.014}$, respectively. At $M_{\rm h} < 10^{11.3}$ $M_\odot$, the dependence of $f_{\rm b}$ on $M_{\rm h}$ is much steeper for RGs than for BGs. We discuss the differences found in the $f_{\rm s}$–$M_{\rm h}$ and $f_{\rm b}$–$M_{\rm h}$ relations between BGs and RGs in the light of semi-empirical galaxy evolution inferences.

Key Words: dark matter — galaxies: luminosity function, mass function

1. INTRODUCTION

The galaxy stellar and baryonic mass functions (*GSMF* and *GBMF*, respectively), inferred from the observed luminosity function and gas fraction-stellar mass ($f_{\rm g}$–$M_{\rm s}$) relation, contain key statistical in-

[1]Instituto de Astronomía, Universidad Nacional Autónoma de México, Mexico.

[2]Osservatorio Astronomico di Brera, Italy.

[3]Centro de Radioastronomía y Astrofísica, Universidad Nacional Autónoma de México, Mexico.

formation to understand the physical processes of galaxy formation and evolution. Within the context of the popular Λ Cold Dark Matter (ΛCDM) hierarchical scenario, dark matter halos are the sites where galaxies form and evolve (White & Rees 1978; White & Frenk 1991). Hence, a connection between *GBMF* or *GSMF* and the halo mass function (*HMF*) is expected. The result of such a connection is the galaxy stellar and baryonic mass-halo mass relations, $M_{\rm s}$–$M_{\rm h}$ and $M_{\rm b}$–$M_{\rm h}$, and their intrinsic scatters, both set by complex dynamical and astrophysical processes intervening in galaxy formation and evolution (see for recent reviews Baugh 2006; Avila-Reese 2007; Benson 2010). In this sense, the $M_{\rm b}/M_{\rm h}$ and $M_{\rm s}/M_{\rm h}$ ratios quantify the efficiency at which galaxy and star formation proceeds within a halo of mass $M_{\rm h}$. Therefore, the empirical or semi-empirical inference of the $M_{\rm b}$–$M_{\rm h}$ and $M_{\rm s}$–$M_{\rm h}$ relations and their scatters (locally and at other epochs) is nowadays a challenge of great relevance in astronomy.

For simplicity, in statistical studies like those related to the *GSMF*, galaxies are labelled by their mass alone. However, according to their observed properties, correlations, and evolution, galaxies show a very different nature, at least for the two major groups in which they are classified: the rotationally-supported disk star-forming (late-type) and the pressure-supported spheroid quiescent (early-type) galaxies. In the same way, the evolution of galaxies is expected to differ if they are centrals or satellites. The main intrinsic processes of galaxy evolution are associated to central galaxies, while satellite galaxies undergo several *extra* astrophysical processes because of the influence of the environment of the central galaxy/halo system in which they were accreted. Hence, if the $M_{\rm b}$–$M_{\rm h}$ or $M_{\rm s}$–$M_{\rm h}$ relations are used for constraining galaxy formation and evolution processes, these relations are separately required for at least the two main families of late- and early-type galaxies and should take into account whether the galaxy is central or satellite. Fortunately, in the last years there appeared several studies in which a decomposition of complete *GSMF*s by color, concentration or other easily measurable indicators of the galaxy type was carried out (e.g., Bell et al. 2003; Shao et al. 2007; Bernardi et al. 2010). Furthermore, in a recent work Yang, Mo, & van den Bosch (2009, hereafter YMB09) used the Sloan Digital Sky Survey (SDSS) data to obtain the *GSMF*s of both central and central + satellite galaxies separated in each case into blue and red objects.

With the advent of large galaxy surveys, a big effort has been made to constrain the $z \sim 0$ *total* $M_{\rm s}$–$M_{\rm h}$ relation (i) *directly* by estimating halo masses with galaxy-galaxy weak lensing, with kinematics of satellite galaxies or with X-ray studies; and (ii) *indirectly* by linking observed statistical galaxy properties (e.g., the galaxy stellar mass function *GSMF*, the two-point correlation function, galaxy group catalogs) to the theoretical *HMF* (for recent reviews and additional references see Moster et al. 2010; Behroozi, Conroy, & Wechsler 2010, hereafter BCW10; More et al. 2011). While the latter approach does not imply a measure-based determination of halo masses, it is simpler from a practical point of view, as it allows to cover larger mass ranges, and can be extended to higher redshifts than the former approach (see recent results in Conroy & Wechsler 2009; Moster et al. 2010; Wang & Jing 2010; BCW10). Besides, both the weak lensing and satellite kinematics methods in practice are (still) statistical in the sense that one needs to stack large number of galaxies in order to get sufficient signal-to-noise. This introduces a significant statistical uncertainty in the inferred halo masses.

The indirect approach for linking galaxy and halo masses spans a large variety of methods, among which the halo occupation distribution (Peacock & Smith 2000; Berlind & Weinberg 2002; Kravtsov et al. 2004) and the conditional luminosity function formalisms (Yang, Mo, & van den Bosch 2003; Yang et al. 2004) can be mentioned. These formalisms introduce *a priori* functional forms with several parameters that should be constrained by the observations. Therefore, the final inferred $M_{\rm s}$–$M_{\rm h}$ relation is actually model-dependent and yet sometimes poorly constrained due to degeneracies in the large number of parameters. A simpler and more empirical method –in the sense that it uses only the *GSMF* (or luminosity function) as input and does not require to introduce any model– has been found to give reasonable results. This indirect method, called the abundance matching technique (hereafter AMT; e.g., Marinoni & Hudson 2002; Vale & Ostriker 2004; Conroy, Wechsler, & Kravtsov 2006; Shankar et al. 2006; Conroy & Wechsler 2009; Baldry, Glazebrook, & Driver 2008; Guo et al. 2010; Moster et al. 2010; BCW10), is based on the assumption of a monotonic correspondence between $M_{\rm s}$ and $M_{\rm h}$; in the limit of zero scatter in the $M_{\rm s}$–$M_{\rm h}$ relation, the halo mass $M_{\rm h}$ corresponding to a galaxy of stellar mass $M_{\rm s}$, is found by matching the observed cumulative *GSMF* to the theoretical cumulative *HMF*.

In this paper we apply the AMT in order to infer the local $M_{\rm s}$–$M_{\rm h}$ relation for *central blue and red* galaxies separately, which requires as input *both* the observed central blue and red *GSMF*s, taken here from YMB09. Note that in order to infer the $M_{\rm s}$–$M_{\rm h}$ relation of galaxy subpopulations (e.g., blue/red or central/satellite ones) solely from the overall *GSMF*, models for each subpopulation should be introduced, which greatly increases the uncertainty of the result. Regarding the *HMF*s to be matched with the corresponding observed central *GSMF*s, the theoretical *HMF* is decomposed into two functions –associated to halos hosting blue and red galaxies– based on empirical facts: blue galaxies are rare as central objects in groups/clusters of galaxies, and they should not have undergone late major mergers because of the dynamical fragility of disk (blue) galaxies. Nowadays, it is not clear whether or not the $M_{\rm s}$–$M_{\rm h}$ relation varies significantly with galaxy color or type. Previous studies that discussed this question were based on direct methods: the weak lensing (Mandelbaum et al. 2006) and satellite kinematics (More et al. 2011) techniques. The uncertainties in the results of these studies are still large, and can be subject to biases intrinsic to the sample selection and to effects of environment.

We also estimate here the galaxy baryon mass-halo mass relations, $M_{\rm b}$–$M_{\rm h}$[4], where $M_{\rm b}= M_{\rm s}+ M_{\rm g}$, by using the *GSMF*s combined with average observational determinations of the galaxy gas mass, $M_{\rm g}$, as a function of $M_{\rm s}$. The galaxy baryonic mass fraction, $f_{\rm b}= M_{\rm b}/M_{\rm h}$, and its dependence on mass is important for constraining models and simulations of galaxy evolution, and is also a key input for some approaches, implemented to model the most generic population of galaxies, namely *isolated (central) disk galaxies* (e.g., Mo, Mao, & White 1998; Firmani & Avila-Reese 2000; van den Bosch 2000; Stringer & Benson 2007; Dutton et al. 2007; Gnedin et al. 2007; Dutton & van den Bosch 2009). In these and other studies, it was shown that several disk galaxy properties, correlations, and their scatters depend (or are constrained) by $f_{\rm b}$. In a similar way, the $f_{\rm b}$–$M_{\rm h}$ dependence is expected to play some role in the results of structural and dynamical models of spheroid-dominated galaxies.

In § 2 we describe the method and the data input. The stellar/baryon mass-halo mass relations for the total, blue and red (sub)samples are presented in § 3. In § 4 we compare our results with other observational works, and discuss whether they are consistent or not with expectations of semi-empirical inferences. The summary and our conclusions are given in § 5.

[4]We assume that the galaxy baryonic mass is included in the halo (virial) mass $M_{\rm h}$.

2. THE METHOD

The AM statistical technique is based on the hypothesis of a one-to-one monotonic increasing relationship between $M_{\rm s}$ (or $M_{\rm b}$) and $M_{\rm h}$. Therefore, by matching the *cumulative* galaxy stellar and halo mass functions, for a given $M_{\rm s}$ a unique $M_{\rm h}$ is assigned:

$$\int_{M_{\rm h}}^{\infty} \phi_h(M_h')dM_h' = \int_{M_{\rm s}}^{\infty} \phi_s(M_s')dM_s', \qquad (1)$$

where ϕ_h is the overall *HMF* (distinct + subhalos) and ϕ_s is the overall *GSMF*; *distinct* halos are those not contained inside more massive halos. It is reasonable to link central galaxies with distinct halos. Therefore, in the case of using the *GSMF* for only central galaxies, the distinct *HMF* should be used for the matching. Since the main purpose of this paper is the inference of the $M_{\rm s}$–$M_{\rm h}$ (and the corresponding $M_{\rm b}$–$M_{\rm h}$) relation for blue (red) galaxies, (i) a *GSMF* that separates galaxies by color is necessary (the data to be used here are discussed in § 2.1), and (ii) a criterion to select the halos that will likely host blue (red) galaxies shall be introduced (see § 2.2.1).

In this paper we will not carry out an exhaustive analysis of uncertainties in the inference of the $M_{\rm s}$–$M_{\rm h}$ relation with the AMT. This was extensively done in BCW10 (see also Moster et al. 2010). In BCW10 the uncertainty sources are separated into three classes: uncertainties (i) in the observational inference of *GSMF*, (ii) in the dark matter HMF, which includes uncertainties in the cosmological parameters, and (iii) in the matching process arising primarily from the intrinsic scatter between $M_{\rm s}$ and $M_{\rm h}$.

2.1. *Galaxy and Baryonic Stellar Mass Functions*

In the last years, complete galaxy luminosity functions (and therefore, *GSMF*s) were determined for local samples covering a large range of luminosities (masses). The stellar mass is inferred from (multi) photometric and/or spectral data (i) by using average stellar mass-to-light ratios, depending only on color (inferred from application of stellar population synthesis –SPS– models to galaxy samples with independent mass estimates, e.g., Bell et al. 2003), or (ii) by applying directly the SPS technique to each sample galaxy, when extensive multiwavelength and/or spectral information is available.

In both cases, a large uncertainty is introduced in the inference of $M_{\rm s}$ due to the uncertainties in the IMF, stellar evolution, stellar spectral libraries, dust extinction, metallicity, etc. Bell et al. (2003) estimated a scatter of ≈0.1 dex in their $M_{\rm s}/L$ ratios

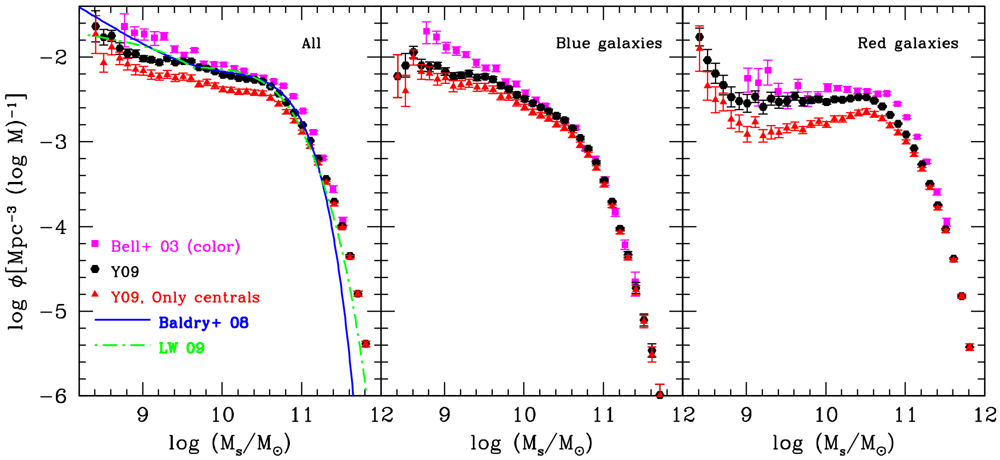

Fig. 1. Left panel: Different local *GSMF*s for *all* galaxies. The reported data in Bell et al. (2003, pink squares) and YMB09 (black hexagons) are plotted directly, while for Baldry et al. (2008, blue solid line) and Li & White (2009, dot-dashed green line), the best fits these authors find to their samples are plotted. Red triangles show the data from YMB09 corresponding to the *GSMF* of central-only galaxies. Middle and right panels: Data corresponding to the decomposition of the *GSMF* into blue and red galaxies, respectively, from Bell et al. (2003) and for the all and central-only galaxies from YMB09. The color figure can be viewed online.

in infrared bands. Conroy, Gunn, & White (2009) carried out a deep analysis of propagation of uncertainties in SPS modelling and concluded that $M_{\rm s}$ at $z\sim0$ carry errors up to ∼0.3 dex (but see Gallazzi & Bell 2009). Here, we will consider an overall systematic uncertainty of 0.25 dex in the $M_{\rm s}$ determination (see BCW10).

Most of the current local *GSMF*s were inferred from 2dF Galaxy Redshift Survey, Two Micron All-Sky Survey (2MASS) and SDSS (e.g., Cole et al. 2001; Bell et al. 2003; Baldry et al. 2006). The low-mass completeness limit due to missing low surface brightness galaxies occurs at $\sim10^{8.5}$ $M_{\rm s}$ (Baldry et al. 2008). An upturn of the *GSMF* close to this end (below $M_{\rm s}\sim10^9$ $M_\odot$) was confirmed in several recent works (Baldry et al. 2008; YMB09; Li & White 2009). Due to this upturn, a better fit to the *GSMF*s is obtained by using a double or even triple Schechter function. Since the low-mass end of the *GSMF* is dominated by late-type galaxies, this upturn plays an important role in the $M_{\rm s}$–$M_{\rm h}$ relation of late-type galaxies at low masses.

For our purposes, observational works where the *GSMF* is decomposed into late- and early-types galaxies are required. Such a decomposition has been done, for example, in Bell et al. (2003), who combined 22679 SDSS Early Data Release and 2MASS galaxies, and used two different criteria, color and concentration, to split the sample into two types of galaxies. A much larger sample taken from the NYU-VAGC based on the SDSS DR4 has been used by YMB09 (see also Yang, Mo, & van den Bosch 2008), who split the sample into *blue and red* sub-samples according to a criterion in the $^{0.1}(g-r)-M_r$ diagram. In both works, $M_{\rm s}$ is calculated from the $r-$band magnitude by using the corresponding color-dependent $M_{\rm s}/L_r$ ratio given in Bell et al. (2003). In YMB09 each color subsample is in turn separated into central and satellite galaxies according to their memberships in the constructed groups, where the central galaxy is defined as the most massive one in the group and the rest as satellite galaxies.

In Figure 1, the Bell et al. (2003) and YMB09 *GSMF*s are reproduced by using the data sets reported in these papers. In the left panel, the full samples from each work (solid squares and solid hexagons, respectively) are plotted, as well as the case of central-only galaxies from YMB09 (solid triangles); both *GSMF*s and the other ones plotted in this figure are normalised to $h=0.7$ and to a Chabrier (2003) IMF. In the central and right panels, the corresponding blue (late-type) and red (early-type) sub-samples are plotted with the same symbols as in the left panel. For the Bell et al. (2003) sub-samples, only those separated by their color criterion are plotted. Both *GSMF*s corresponding to the full and blue sub-samples are in good agreement for $M_{\rm s}\gtrsim10^{9.5}$ $M_\odot$. For lower masses, the Bell et al. (2003) *GSMF*'s are higher. On one hand, the Bell et al. (2003) sample is much smaller than the

YMB09 one (therefore its cosmic variance is more significant). On the other hand, the redshift completeness and M_s limit in YMB09 are treated with updated criteria.

In Figure 1 we also plot fits to the overall *GSMF* presented in Baldry et al. (2008, double Schechter function, solid blue line) and in Li & White (2009, triple Schechter function, dashed green line) for new SDSS releases and by using directly SPS models to estimate M_s for each galaxy. These fits agree well with the YMB09 data in the mass range $9.2 \lesssim \log(M_s/M_\odot) \lesssim 11.2$. For smaller masses, the Baldry et al. (2008) fit tends to be steeper while the Li & White (2009) fit tends to be shallower than the YMB09 data. For larger masses, both fits decrease faster with M_s than the YMB09 data. All these (small) differences are due to the different methods used to estimate M_s, as well as the different volumes and limit corrections of the samples (see Baldry et al. 2008, YMB09, and Li & White 2009 for discussions).

The split into two colors of the sample used by YMB09 is a rough approximation to the two main families of disk- and spheroid-dominated galaxies. It is well known that the morphological type correlates with the galaxy color, though with a large scatter. There is for example a non-negligible fraction of galaxies (mostly highly inclined) that are red but of disk-like type (e.g., Bernardi et al. 2010). However, given that here we consider a partition of the overall sample just in two groups, we believe that it is reasonable to assume as a first approximation that the color criterion for the partition will provide at this level a result similar to that of a morphological criterion.

For the YMB09 sample, the blue and red galaxies are ≈55% and ≈45%, respectively, for $M_s \gtrsim 3 \times 10^8\ M_\odot$. Red galaxies dominate the total *GSMF* at large masses. At $M_s \approx 2 \times 10^{10}\ M_\odot$ the abundances of red and blue galaxies are similar and at lower masses the latter are increasingly more abundant than the former as M_s is smaller. For $M_s \lesssim 10^9\ M_\odot$, the abundance of red galaxies, mainly central ones, steeply increases towards smaller masses. The existence of this peculiar population of faint central red galaxies is discussed in YMB09. Wang et al. (2009) suggested that these galaxies are hosted by small halos that have passed through their massive neighbors, and the same environmental effects that cause satellite galaxies to become red are also responsible for the red colors of such galaxies. However, as these authors showed, even if the environmental effects work, there are in any case over 30% of small halos that

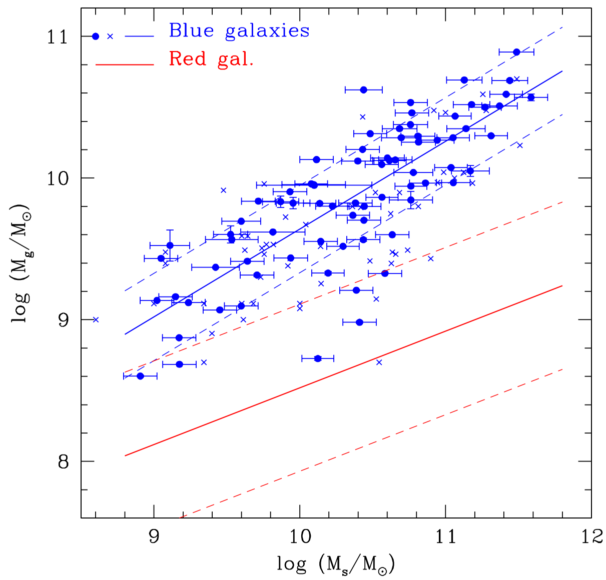

Fig. 2. Gas mass vs stellar mass for a sample of disk high and low surface brightness galaxies collected and homogenised by Avila-Reese et al. (2008, blue dots with error bars) and for a sample of disk galaxies presented by McGaugh (2005, blue crosses). The solid blue line is the orthogonal linear doubly-weighted regression to the data from the former authors and the dashed lines show an estimate of the intrinsic scatter around the fit. The solid red line is an estimate of the M_g–M_s correlation for red galaxies using our fit to blue galaxies and the ratio of blue-to-red atomic gas fraction determined in Wei et al. (2010), see text. The color figure can be viewed online.

are completely isolated, so that these effects cannot be invoked for them.

In the YMB09 sample, around 70% of the galaxies are central. As mentioned in the § 1, the inference of the M_s–M_h relation for central-only galaxies is important for studies aimed to constrain galaxy formation and evolution in general; satellite galaxies are interesting on its own but they lack generality because their evolution and properties are affected by extra environmental processes.

In what follows, the YMB09 *GSMF* provided in tabular form and split into blue/red and central/satellite galaxies will be used for applying the AMT. Our main goal is to infer the M_s–M_h relation for central blue (late-type) and red (early-type) galaxies.

We will infer also the corresponding M_b–M_h (baryonic) relations. The blue and red *GBMF*s are estimated from the blue and red *GSMF*s, respectively, where in order to pass from M_s to M_b, the cool (atomic and molecular) gas mass, M_g, corresponding on average to a given M_s is taken from the empirical blue and red M_g–M_s relations. In Figure 2 a compilation of observational estimates is plotted in the M_s–M_g plane for a sample of disk galaxies that includes low surface brightness galaxies from Avila-Reese et al. (2008; blue dots with error bars; they added H_2 mass contribution by using an estimate for the H_2-to-HI mass ratio as a function of galaxy type), and for another galaxy sample from McGaugh (2005; blue crosses; no H_2 contribution is considered and their dwarf galaxies were excluded). An orthogonal linear doubly-weighted regression to the data from Avila-Reese et al. (2008) gives:

$$\frac{M_g}{10^{10}M_\odot} = 0.43 \times \left(\frac{M_s}{10^{10}M_\odot}\right)^{0.62}. \quad (2)$$

This fit is plotted in Figure 2 with its corresponding estimated scatter (≈0.3 dex; blue solid and dashed lines). This is the relation and its scatter used to calculate M_b and the blue *GBMF*. A similar relation has been inferred by Stewart et al. (2009). The gas fractions in red galaxies are much smaller than in blue galaxies. For sub-samples of blue and red galaxies, Wei et al. (2010) reported for each one the atomic gas fractions versus M_s (molecular gas was not included). The ratio of their fits to these data as a function of M_s is used here to estimate from equation 2 (blue galaxies) the corresponding average M_g for red galaxies as a function of M_s. The red solid line shows the obtained relationship. As an approximation to the scatter (short-dashed lines), the average scatter reported for red galaxies in Wei et al. (2010) is adopted here.

2.2. *Halo and sub-halo mass functions*

A great effort has been made in the last decade to determine the *HMF* at $z = 0$ and at higher redshifts by means of N-body cosmological simulations. A good fit to the results, at least for low redshifts, is the universal function derived from a Press-Schechter formalism (Press & Schechter 1974) generalized to the elliptical gravitational collapse (Sheth & Tormen 1999, hereafter S-T). In fact, Tinker et al. (2008) have shown that at a high precision level, the *HMF* may change for different cosmological models and halo mass definitions as well as a function of z. For our purposes and for the cosmology used here, the S-T approximation provides a good description of the $z = 0$ *HMF* of distinct halos:

$$\phi_h(M_h)dM_h = A\left(1+\frac{1}{\nu^{2q}}\right)\sqrt{\frac{2}{\pi}}\frac{\bar{\rho}_M\nu}{M_h^2}\left|\frac{d\ln\sigma}{d\ln M_h}\right|\exp\left[-\frac{\nu^2}{2}\right]dM_h, \quad (3)$$

where $A = 0.322$, $q = 0.3$, $\nu^2 = a(\delta_c/D(z)\sigma(M_h))$ with $a = 0.707$; $\delta_c = 1.686\Omega_m^{0.0055}$ is the linear threshold in the case for spherical collapse in a flat universe with cosmological constant, $D(z)$ is the growth factor and $\sigma(M_h)$ is the mass power spectrum variance of fluctuations linearly extrapolated to $z = 0$. The halo (virial) mass, M_h is defined in this paper as the mass enclosed within the radius where the overdensity is $\bar{\rho}_{vir} = \Delta$ times the *mean matter* density, $\bar{\rho}_M$; $\Delta \approx 340$ according to the spherical collapse model for the cosmology used here. The cosmological parameters assumed here are close to those of WMAP5 (Komatsu et al. 2009): $\Omega_M = 0.27, \Omega_\Lambda = 1 - \Omega_m = 0.73, h = 0.70, \sigma_8 = 0.8$.

The distinct *HMF* should be corrected when a *GSMF* corresponding to *all* galaxies is used in the AMT. In this case, satellite galaxies are included in the *GSMF*. Therefore, subhalos should be taken into account in the *HMF*. The subhalo fraction is no more than ≈20% of all the halos at $z = 0$ (e.g., Shankar et al. 2006; Conroy et al. 2006; Giocoli et al. 2010; BCW10). When necessary, we correct the S-T *HMF* for (present-day) subhalo population by using the fitting formula to numerical results given in Giocoli et al. (2010):

$$\frac{dn(m_{sub})}{d\ln m_{sub}} = A_0 m_{sub}^{\eta-1}\exp\left[-\left(\frac{m_{sub}}{m_0}\right)^\gamma\right], \quad (4)$$

with $\eta = 0.07930$, $\log A_0 = 7.812$, $\log(m_0/M_\odot) = 13.10$ and $\gamma = 0.407$.

The upper panel of Figure 3 shows the (distinct) S-T *HMF* (solid line), the sub-halo *HMF* (short-long-dashed line), and the distinct+subhalo *HMF* (dash-dotted line). The correction by sub-halos in the abundance is small at low masses and negligible at high masses. When the *GSMF* refers only to central galaxies –which is the case in this paper– then it is adequate to use the distinct *HMF* for the AMT, i.e. *the subhalo abundance correction is not necessary.*

2.2.1. *Halos hosting blue and red galaxies*

In the AMT, the cumulative *GSMF* and *HMF* are matched in order to link a given M_s to M_h. When a subsample of the total *GSMF* is used –as is the case for inferring the M_s–M_h relation of only late- or early-type galaxies– it would not be correct to use the total *HMF* for the matching. This function, in the ignorance of which is the mass function of halos hosting blue (red) galaxies, at least should be re-normalised (decreased uniformly) by the same fraction corresponding to the decrease of the subsample *GSMF* with respect to the total *GSMF*. In

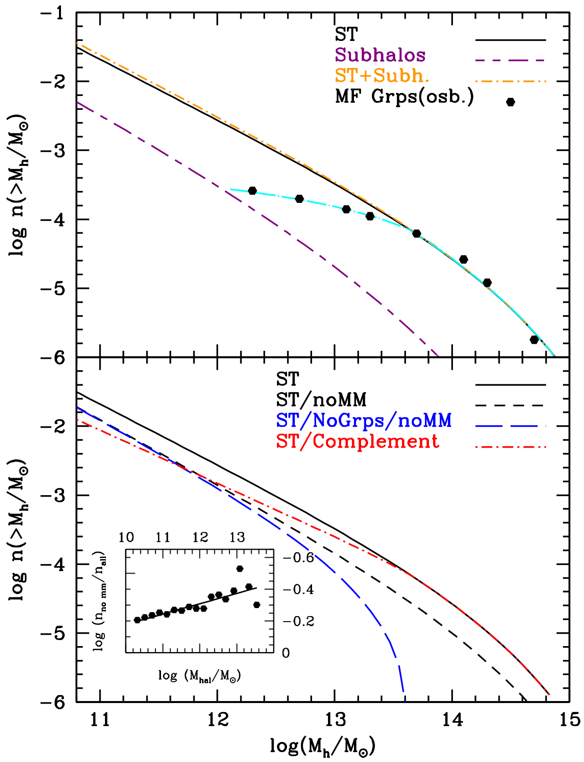

Fig. 3. Upper panel: Distinct S-T *HMF* for the cosmology adopted in this paper (solid black line), sub-halo mass function at $z = 0$ according to Giocoli et al. (2010, short-long-dashed purple line), and the sum of both (dot-dashed orange line). The solid dots are measures of the group/cluster mass function according to Heinämäki et al. (2003) and adequately corrected to our definition of virial halo mass; the dot-long-dashed cyan line is a eye-fit to the data. Lower panel: The same distinct S-T *HMF* (solid black line) shown in the upper panel but (i) excluding the halos that suffered late major mergers –since $z = 0.8$– (short-dashed black line) and (ii) excluding these halos and those of observed groups/clusters (long-dashed blue line). The latter is the *HMF* to be assigned to the sub-sample of central blue galaxies. The complement of this function to the total (S-T) one (dot-dashed red line) is the *HMF* to be assigned to the sub-sample of central red galaxies. The inset shows the ratio of number densities of halos that did not suffer major mergers since $z = 0.8$ to all the (distinct) halos according to measures in a cosmological N-body simulation (Colín et al. 2011, in preparation, see text). The fit to this ratio (solid line in the inset) is what has been used to correct the S-T *HMF* for halos thad did not suffer late major mergers. The color figure can be viewed online.

YMB09, ≈55% (≈45%) of the galaxies are in the blue (red) sub-samples for $M_s \gtrsim 3 \times 10^8\ M_\odot$. We may go one step further by proposing general observational/physical conditions for halos to be the hosts of blue (late-type) or red (early-type) galaxies. Note that the division of galaxies we do here is quite broad –just into two groups– and therefore very general conditions are enough.

Halos that host central blue and red galaxies are expected to have (i) a different environment, and (ii) a different merger history. We take into account these two factors in order to roughly estimate the *HMF* of those halos that will host today central blue and red galaxies.

Environment.- Blue (late-type) galaxies are rare in the centers of groups and clusters of galaxies (high-density environments; e.g., Norberg et al. 2001; Zehavi et al. 2005; Li et al. 2006; de Lapparent & Slezak 2007; Padilla, Lambas, & González 2010; Blanton & Moustakas 2009, and references therein). For example, in the SDSS YMB09 sample that we use here (see also Weinmann et al. 2006), among the groups with 3 or more members, the fraction of those with a central blue galaxy is only ≈20%, and most of these central galaxies have actually low masses. Therefore, cluster- and group-sized halos (more massive than a given mass) cannot be associated to central blue galaxies when using the AMT. This means that the halo mass function of groups/clusters of galaxies should be excluded from the theoretical *HMF* (Shankar et al. 2006).

Heinämäki et al. (2003) determined the *HMF* of groups with 3 or more members and with a number density enhancement $\delta n/n \geq 80$ from the Las Campanas Redshift Survey. The authors estimated the corresponding group virial mass on the basis of the line-of-sight velocity and harmonic radius of the group, in such a way that this mass was defined at the radius where $\delta n/n = 80$. The observational galaxy overdensity $\delta n/n$ is related to the mass overdensity $\delta\rho/\rho$ roughly through the bias parameter b: $\delta\rho/\rho = (1/b)\times\delta N/N$, where $b \approx 1/\sigma_8$ (Martínez et al. 2002). Hence, for $\sigma_8 = 0.8$, $\delta\rho/\rho \approx 64$; since the group selection was carried out in Tucker et al. (2000), where an Einstein-de Sitter cosmology was used, then $\rho = \rho_{\rm crit}$ in this case. In our case, the halo virial mass is defined at the radius where $\delta\rho/\rho \approx 340$ (see § 2.2); in terms of $\rho_{\rm crit}$, our overdensity is $340 \times \Omega_M = 92$. Therefore, the halo virial masses in Heinämäki et al. (2003) should be slightly larger than those used here. For the NFW halos of masses larger than $\sim 10^{13}\ M_\odot$, the differences are estimated to be factors of 1.10–1.20. We correct the group masses of Heinämäki et al. (2003) by 15%. In the upper panel of Figure 3, the corrected group (halo) mass function is reproduced (solid dots) and a eye-fit to them is plotted (dot-dashed cyan line).

Merger history.- Disk (blue, late-type) galaxies are dynamically fragile systems and thus they are not expected to survive strong perturbations such as those produced in major mergers or close interactions. However, as several theoretical studies have shown (e.g., Robertson et al. 2004; Governato, Mayer, & Brook 2008), when the mergers are gas-rich ('wet') and/or occur at early epochs (in fact, both facts are expected to be correlated), it is highly probable that a gaseous disk is regenerated or formed again with the late accreted gas. Therefore, a reasonable restriction for halos that will host disk galaxies is that they did not undergo *central* major mergers since a given epoch (at earlier epochs, while the central major merger may destroy the disk, a new gaseous disk can be formed later on). Based on numerical simulations, Governato et al. (2008) suggested that a 'wet' major merger of disk galaxies at $z \sim 0.8$ has still a non-negligible probability of rebuilding a significant disk by $z \sim 0$. We will assume here that halos whose *centers* have a major merger at $z < 0.8$ will not host a disk galaxy.

In Colín et al. (2011, in preparation) the present-day abundance fraction of halos with no *central* major merger since $z = 0.8$ was measured as a function of $M_{\rm h}$ from an N-body ΛCDM cosmological high-resolution simulation with $\Omega_m = 0.24$, $\Omega_\Lambda = 0.76$, and $\sigma_8 = 0.75$ (box size and mass per particle of 64 h^{-1} Mpc and $1.64 \times 10^7 h^{-1}\, M_\odot$, respectively). The friends-of-friends (FOF) method with a linking-length parameter of 0.17 was applied for identifying halos. The mass ratio to define a major merger was $q = M_{\rm h,2}/M_{\rm h,1} > 0.2$ and the merger epoch was estimated as the time when the center of the accreted halo arrived at the center of the larger halo by dynamical friction; this epoch is calculated as the cosmic time when both FOF halos have "touched" plus the respective dynamical friction (merging) time as given by the approximation of Boylan-Kolchin, Ma, & Quataert (2008). The fraction of halos that did not suffer a major merger since $z = 0.8$ with respect to all the halos as a function of $M_{\rm h}$ measured in Colín et al. (2011, in preparation) is used here to correct our distinct S-T *HMF*. This measured fraction is shown in the inset in the lower panel of Figure 3; the solid line is a linear fit by eye in the log-log plot: $\log(n_{\rm noMM}/n_{\rm all}) = 0.472 - 0.065 \log(M_{\rm h}/M_\odot)$. As it is seen, the fraction slightly decreases with mass, which is consistent with the idea that larger mass halos are assembling later with a significant fraction of their masses being acquired in late major mergers. After the correction mentioned above, we get the mass function of halos that did not suffer a central major merger ($q > 0.2$) since $z = 0.8$ (short-dashed black line in the lower panel of Figure 3).

The final corrected HMFs.- The function obtained after (i) subtracting from the distinct S-T *HMF* the group mass function and (ii) excluding halos that did not suffer a late central major merger is plotted in Figure 3 (blue long-dashed line). This mass function is proposed here to correspond to halos that today host blue galaxies. The overall number fraction of these halos with respect to the distinct ones (described by the S-T *HMF*) is $\sim$58%, which is roughly consistent with the fraction of blue galaxies in the YMB09 sample. The *HMF* corresponding to the complement is plotted in Figure 3 as the red dot-dashed curve. By exclusion, this *HMF* will be associated with the *GSMF* of the red central galaxy sub-sample for deriving the $M_{\rm s}$–$M_{\rm h}$ relation of red galaxies.

3. RESULTS

3.1. *The overall, central, and satellite stellar-halo mass relations*

In Figure 4, the $M_{\rm s}$–$M_{\rm h}$ relation obtained by using the Li & White (2009) *GSMF* (see § 2.1 and Figure 1) and the S-T *HMF* corrected to include sub-halos is plotted (long-dashed blue line). The relation given by BCW10, who also used as input the Li & White (2009) *GSMF*, is shown (short-dashed red line). Both curves are almost indistinguishable, showing an excellent consistency of our results with those of BCW10, in spite of the differences in some of the methodological aspects.

Further, we plot in Figure 4 the $M_{\rm s}$–$M_{\rm h}$ relation as above but using now the total YMB09 *GSMF* (dot-dashed pink line). This relation is similar to the one inferred using the Li & White (2009) *GSMF*. For $\log(M_{\rm h}/M_\odot) \gtrsim 12$, the former slightly shifts with mass to higher values of $M_{\rm s}$ for a given $M_{\rm h}$ than the latter (at $\log(M_{\rm h}/M_\odot) = 13.5$ the difference is no larger than 0.08 dex in $\log M_{\rm s}$). Such a shift is explained by the (small) systematical difference between the YMB09 and Li & White (2009). *GSMF*s at masses larger than $\log(M_{\rm s}/M_\odot) \sim 11$ (see § 2.1 and Figure 1).

In Figure 4, the $M_{\rm s}$–$M_{\rm h}$ relations given in Baldry et al. (2008, dot-dashed orange line), Moster et al. (2010, short-long-dashed line) and Guo et al. (2010, dotted green line) are also plotted. When necessary, we have corrected the stellar masses to the Chabrier IMF, and the halo masses to the definition of virial mass used here (see § 2.2). As mentioned above, Baldry et al. (2008) corrected their *HMF* to exclude groups/clusters of galaxies (something that we do

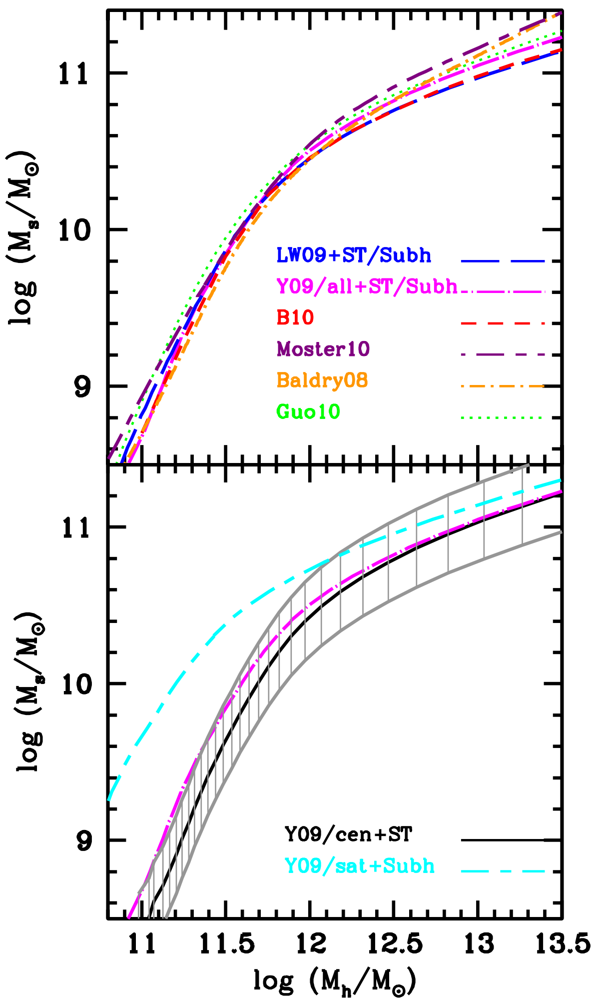

Fig. 4. Upper panel: Stellar mass vs halo mass as inferred here by using the Li & White (2009) overall *GSMF* and the S-T *HMF* increased by the subhalo population (long-dashed blue line) to be compared with the BCW10 inference, who used the same *GSMF* (short-dashed red line). The dot-dashed pink line shows the same $M_{\rm s}$ vs $M_{\rm h}$ inference but using the overall YMB09 *GSMF*. Different determinations of the overall $M_{\rm s}$–$M_{\rm h}$ relation by other authors (indicated in the panel), who took into account in different ways the issue of group/cluster masses (see text) are also plotted. Lower panel: Same $M_{\rm s}$–$M_{\rm h}$ relation as in the upper panel (dot-dashed pink line) but for the central-only YMB09 *GSMF* and the S-T (distinct) *HMF* (solid line). The grey curves connected by vertical lines show the estimated 1σ uncertainty for the latter case. The $M_{\rm s}$–$M_{\rm h}$ relation inferred for the only satellite YMB09 *GSMF* and the Giocoli et al. (2010) $z = 0$ subhalo mass function is plotted as a short-long-dashed cyan line. The color figure can be viewed online.

but only for the central blue galaxies, see § 2.2.1 and the result below). As seen in Figure 4, their correction produces a steeper $M_{\rm s}$–$M_{\rm h}$ relation at the high-mass side than in our case. Moster et al. (2010) and Guo et al. (2010) constrained the $M_{\rm s}$–$M_{\rm h}$ relation by assigning stellar masses to the halos and subhalos of an N-body cosmological simulation in such a way that the total *GSMF* was reproduced. Therefore, by construction, their $M_{\rm s}$–$M_{\rm h}$ relations take into account the group/cluster halo masses issue. The $M_{\rm s}$–$M_{\rm h}$ relations in both works are also slightly steeper than ours at high masses but shallower on average than that of Baldry et al. (2008). Note that in BCW10 the scatter in $M_{\rm s}$ at fixed $M_{\rm h}$ was taken into account but the group/cluster halo masses issue was not.

The $M_{\rm s}$–$M_{\rm h}$ relation using the YMB09 *GSMF* only for central galaxies and the distinct (S-T) *HMF* is plotted in the lower panel of Figure 4 (solid black line). At large masses, this relation is quite similar to that for all galaxies/satellites and halos/subhalos (dot-dashed pink line). This is because at large masses the great majority of galaxies are centrals and the correction for sub-halos is negligible (see Figures 1 and 3). At lower masses, the exclusion of satellites and sub-halos implies a lower $M_{\rm s}$ for a given $M_{\rm h}$. This is because the *GSMF* decreases more than the *HMF* as the mass is smaller when passing from the total (galaxy and halo) samples to the central-only galaxy/distinct halo samples. The physical interpretation of this result could be that satellite galaxies of a given $M_{\rm s}$ have less massive halos than central galaxies, due to tidal stripping. The $M_{\rm s}$–$M_{\rm h}$ relation derived only for the satellites YMB09 *GSMF* and the Giocoli et al. (2010) $z = 0$ sub-halo *HMF* is plotted in the lower panel of Figure 4 (short-long-dashed cyan line).

3.1.1. *Uncertainties*

The uncertainty (standard deviation) in the $M_{\rm s}$–$M_{\rm h}$ relation obtained using the YMB09 central *GSMF* and the distinct S-T *HMF* (solid line), is plotted in Figure 4 (grey curves connected by vertical lines). As remarked in § 2, we did not take into account all possible uncertainty sources in the $M_{\rm s}$–$M_{\rm h}$ relation but have just considered the two following ones:

(i) The systematic uncertainty in stellar mass estimates, which is an uncertainty in the *GSMF*. We assume for this uncertainty a scatter of 0.25 dex (Gaussian-distributed) independent of mass, and propagate it to the $M_{\rm s}$–$M_{\rm h}$ relation (it is by far the dominant source of error in the relation obtained with the AMT, see below and BCW10).

(ii) The intrinsic scatter in stellar mass at a fixed halo mass, which is an uncertainty in the process of matching abundances. To take into account this scatter in M_s at fixed M_h a probability density distribution should be assumed. The convolution of this distribution with the true or intrinsic *GSMF* gives the measured *GSMF*. The cumulative true *GSMF* is then the one used for the AM (BCW10). The observational data allow to estimate the scatter in luminosity (or M_s) and to date it appears to be independent of M_h (More et al. 2009; YMB09). In BCW10 a log-normal mass-independent scatter in M_s of 0.16 ± 0.04 is assumed. Here, we follow the overall procedure of BCW10 for taking into account this scatter.

We also explored the effect of (iii) the statistical uncertainty in the number density of the *GSMF* (as given in YMB09), but we found that the effect is negligible as compared to the one produced by item (i) (see also BCW10, their § 4.3.1). The effect of the intrinsic scatter in M_s for a given M_h is also very small in the overall scatter of the M_s–M_h relation but it affects the high mass end of the calculated M_s–M_h relation, where both the *GSMF* and *HMF* decay exponentially, since there are more low mass galaxies that are scattered upward than high mass galaxies that are scattered downward (BCW10). For instance, at $M_\mathrm{h} = 10^{13.5}\ M_\odot$, the stellar mass after including this scatter is 1.2 times smaller. The contribution from all other sources of error, including uncertainties in the cosmological model, is much smaller, ranging from 0.02 to 0.12 dex at $z = 0$.

From Figure 4 we see that the 1σ uncertainty in the M_s–M_h relation is approximately 0.25 dex in $\log M_\mathrm{s}$ without any systematic dependence on M_h, in good agreement with previous results (BCW10; Moster et al. 2010). This uncertainty is larger than the differences between the M_s–M_h average relations found by different authors, including those that use the indirect AMT but with different *GSMF*s, methodologies, and corrections, and those who use more sophisticated formalisms (see for comparisons and discussions BCW10 and More et al. 2011). On one hand, this shows that most methods and recent studies aimed at relating halo masses to observed galaxies as a function of their stellar masses are converging to a relatively robust determination. On the other hand, this result suggests that attaining a higher precision in estimating M_s from observations is the crucial task for lowering the uncertainty in the inference of the M_s–M_h relation.

3.2. *The stellar-halo mass relations for central blue and red galaxies*

The upper and lower left panels of Figure 5 show the mean M_s–M_h and f_s–M_h relations for: all central galaxies (solid line, as in Figure 4), central blue (short-dashed line), and central red (long dashed line) galaxies. In order to infer these relations for blue galaxies, the central blue YMB09 *GSMF* and the distinct (S-T) *HMF* corrected for excluding halos (i) associated to observed groups/clusters of galaxies and (ii) that suffered central major mergers since $z = 0.8$ (see § 2.2.2) were used. In the case of red galaxies, the central red YMB09 *GSMF* and the *HMF* complementary to the one associated to blue galaxies were used.

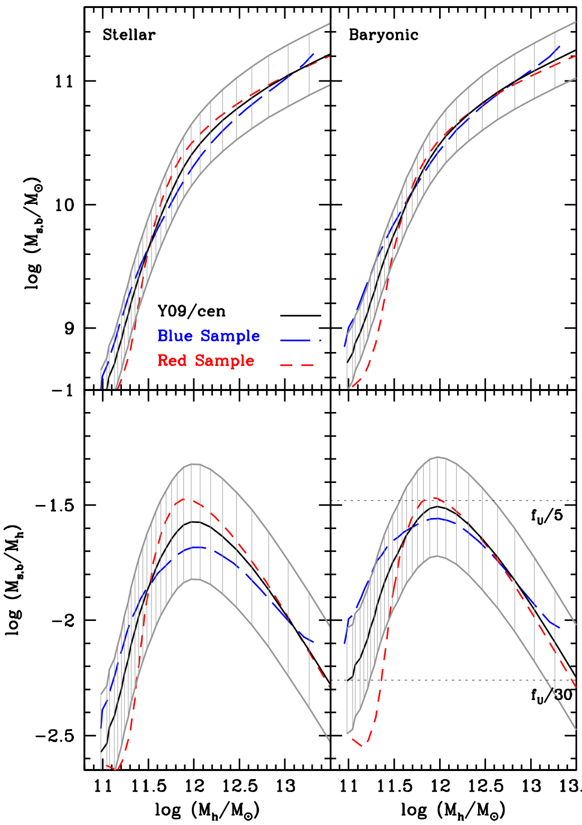

Fig. 5. Left panels: Mean M_s–M_h (top) and f_s–M_h (bottom) relations of all central (solid black line), blue central (long-dashed blue line), and red central (short-dashed red line) galaxies as inferred here using the YMB09 data. The grey curves connected by vertical lines show the 1σ uncertainty for the all-galaxies case; similar uncertainty regions around the main relations are found for the blue and red sub-samples (see Figure 8). Right panels: Same as in left panels but for M_b instead of M_s. Dotted lines: $f_\mathrm{b} = f_U/5$ and $f_U/30$, where $f_U = 0.167$ is the universal baryon fraction. The color figure can be viewed online.

The shaded area in Figure 5 is the same 1σ uncertainty shown in Figure 4 for the overall central sample. The uncertainties corresponding to the M_s–

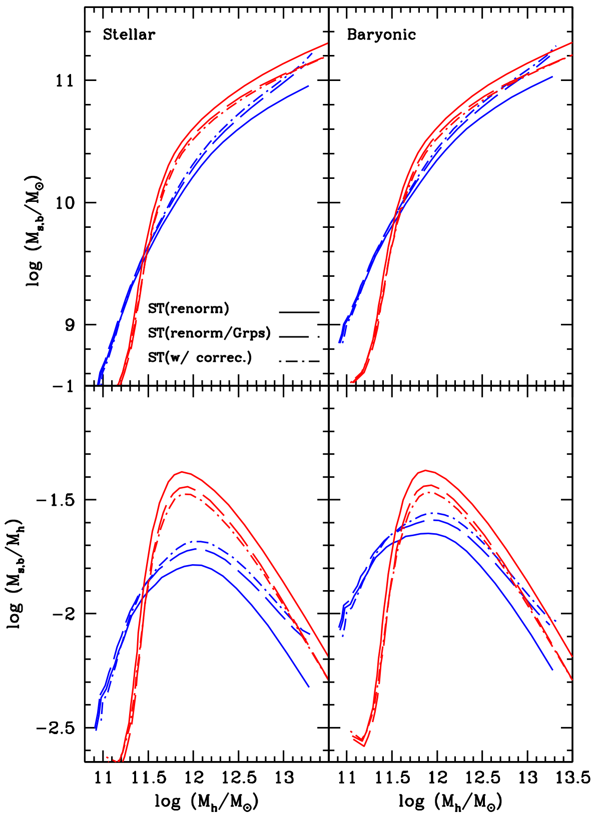

Fig. 6. Left panels: Mean $M_{\rm s}$–$M_{\rm h}$ (top) and $f_{\rm s}$–$M_{\rm h}$ (bottom) relations of central blue (blue lines) and red (red lines) galaxies when (i) no systematical corrections to the corresponding "blue" and "red" *HMF*s were applied apart from re-normalisations in the global abundance (see text, solid lines), (ii) the *HMF*s were corrected by group/cluster abundances and re-normalised (long-dashed lines), and (iii) the *HMF*s were corrected both by group/cluster abundances and late major mergers (as in Figure 4, dot-dashed lines). Right panels: Same as in left panels but for $M_{\rm b}$ instead of $M_{\rm s}$. The color figure can be viewed online.

$M_{\rm h}$ and $f_{\rm s}$–$M_{\rm h}$ relations for the blue and red galaxy sub-samples would be close to the one of the total sample if the corrections made to the *HMF* did not introduce an extra uncertainty. In fact this is not true, in particular for the group/cluster mass function introduced to correct the *HMF* associated to blue galaxies. Unfortunately, the work used for this correction does not report uncertainties. Hence, the uncertainties calculated here for the blue and red samples (shown explicitly in Figure 8 below) could be underestimated, specially at large masses.

In the mass range $11.5 \lesssim \log(M_{\rm h}/M_\odot) \lesssim 13.0$, the $M_{\rm s}$–$M_{\rm h}$ and $f_{\rm s}$–$M_{\rm h}$ relations for central blue (red) galaxies lie slightly below (above) the relations corresponding to the overall sample. For masses below these ranges, the trends invert. The $f_{\rm s}$–$M_{\rm h}$ curves for blue and red sub-samples peak at $\log(M_{\rm h}/M_\odot) = 11.98$ and 11.87, with values of $f_{\rm s} = 0.021^{+0.016}_{-0.009}$ and $f_{\rm s} = 0.034^{+0.026}_{-0.015}$, respectively. The corresponding stellar masses at these peaks are $\log(M_{\rm s}/M_\odot) = 10.30 \pm 0.25$ for blue galaxies and $\log(M_{\rm s}/M_\odot) = 10.40 \pm 0.25$ for red galaxies. These masses are around 0.23 and 0.30 times the characteristic stellar mass $M^\star \approx 10^{10.93}\ M_\odot$ of the overall YMB09 *GSMF*, respectively. The maximum difference between the blue and red mean $M_{\rm s}$–$M_{\rm h}$ relations is attained at $\log(M_{\rm h}/M_\odot) \approx 11.9$; at this mass, the $f_{\rm s}$ value of the former is 1.7 times smaller than the $f_{\rm s}$ of the latter. For larger masses this difference decreases.

At the low-mass end, roughly $f_{\rm s} \propto M_h$ ($\propto M_s^{0.5}$) and $f_{\rm s} \propto M_h^{3.0}$ ($\propto M_s^{0.8}$) for the blue and red samples, respectively, while at the high-mass end, $f_{\rm s} \propto M_h^{-0.4}$ ($\propto M_s^{-0.7}$) and $f_{\rm s} \propto M_h^{-0.6}$ ($\propto M_s^{-1.5}$), respectively.

It is important to note that the differences between blue and red $M_{\rm s}$–$M_{\rm h}$ relations at almost all masses are within the 1σ uncertainty of our inferences. We conclude that the $M_{\rm s}$–$M_{\rm h}$ ($f_{\rm s}$–$M_{\rm h}$) relation does not depend significantly on galaxy color (type). If anything, the mean $f_{\rm s}$–$M_{\rm h}$ relation of red galaxies is narrower and more peaked than the one of blue galaxies. In the mass range where the abundances of blue and red galaxies are closer ($10.0 < \log(M_{\rm s}/M_\odot) < 10.7$), the intrinsic scatter around the $M_{\rm s}$–$M_{\rm h}$ relation would slightly correlate with color in the sense that the redder (bluer) the galaxy, the larger (smaller) its $M_{\rm s}$ for a fixed $M_{\rm h}$, with a maximum average deviation from the mean due to color no larger than $\sim$0.1 dex. For masses smaller than $M_{\rm s} \approx 10^{9.7}\ M_\odot$, the correlation of the scatter with color would invert.

The (slight) differences between blue and red $M_{\rm s}$–$M_{\rm h}$ ($f_{\rm s}$–$M_{\rm h}$) relations can be understood basically by the differences in the respective cumulative *GSMF*s and, at a minor level, by the differences of the corresponding *HMF*s for each case. The sharp peak in the red $f_{\rm s}$–$M_{\rm h}$ relation is associated to the turn-over at $M_{\rm s} \sim 10^{10.5}\ M_\odot$ in the *GSMF* of red galaxies (see Figure 1).

In order to estimate the influence of the corrections introduced to the *HMF* for blue (red) galaxies, we have redone the analysis using the original distinct (S-T) *HMF* without any correction but renormalised to obtain the same fraction of halos as the fraction implied by the *GSMF* of blue (red) galaxies with respect to the total *GSMF*. The results

TABLE 1

FIT PARAMETERS

Parameter	All	Blue	Red
$\log M_{0,h}$	11.97	11.99	11.87
$\log M_s^*$	10.40	10.30	10.40
β	0.34	0.37	0.18
α	1.45	0.90	1.50
γ	0.90	0.90	0.90
a ($M_s < M_s^*$)	0.000	0.125	0.000
a ($M_s > M_s^*$)	0.095	0.125	0.093

are shown in Figure 6, with solid curves of blue color (blue galaxies) and red color (red galaxies). For comparison, the corresponding relations plotted in Figure 5 are reproduced here (dot-dashed blue and red lines, respectively). One sees that the corrections to the *HMF* we have introduced for associating halos to the blue and red galaxy sub-samples act in the direction of reducing the differences among them in the M_s–M_h (f_s–M_h) relations, specially for larger masses. The group/cluster mass function correction to the *HMF* hosting central blue galaxies is the dominant one. The dashed blue and red curves show such a case, where only this correction (and a small re-normalisation) is applied.

3.2.1. *Analytical fits to the stellar-halo mass relations*

From the comparison of the *GSMF* and *HMF* it is easy to deduce that high- and low-mass galaxies have significantly different M_s–M_h scalings, a fact attributed to the different feedback/gas accretion mechanisms dominating in large and small systems (see e.g., Benson et al. 2003). The transition point between the low- and high-mass scalings defines a characteristic halo mass $M_{0,h}$ and an associated stellar mass M_s^*. Therefore, it was common to describe the M_s–M_h relation as a double-power law with the turnover point at $M_{0,h}$. However, BCW10 have argued recently that a power-law at the high-mass side is conceptually a bad description for the M_s–M_h relation and proposed a modification to it. Our results show indeed that a power-law is not sufficient to describe the high-mass side of the M_s–M_h relations.

We have found that a good analytical description to the overall, blue, and red mean M_s–M_h relations inferred here can be obtained for the inverse of the relations (M_h as a function of M_s, as in BCW10), by proposing a power-law dependence for low masses and a sub-exponential law for high masses (see BCW10). The functional form that fits

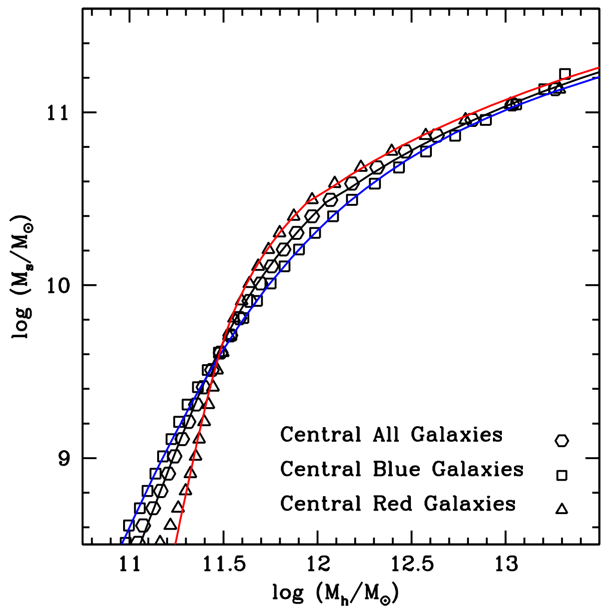

Fig. 7. Analytical fits given by equation (5) and Table 1 compared to the mean M_s–M_h relation obtained here for all central galaxies (black solid line) and the central blue (blue solid line) and red (red solid line) galaxy subsamples. The color figure can be viewed online.

well the three M_h–M_s relations is:

$$M_h = \frac{M_{0,h}}{2^\gamma}\left[\left(\frac{M_s}{M_s^*}\right)^{\beta/\gamma} + \left(\frac{M_s}{M_s^*}\right)^{\alpha/\gamma}\right]^\gamma 10^{a(M_s/M_s^*-1)}, \tag{5}$$

where β regulates the behavior of the relation at masses $M_\mathrm{s} < M_s^*$, α together with the sub-exponential term ($a < 1$) regulate the behavior at masses $M_\mathrm{s} > M_s^*$, and γ regulates the transition of the relation around M_s^*. In Table 1 are given the values of all the parameters that best fit our results for the (central) overall, blue, and red M_s-M_h relations. Note that a assumes two different values depending on whether the mass is smaller or larger than M_s^*.

Figure 7 shows the three mean M_s–M_h relations obtained here and the functional form given in equation (5) with the corresponding parameters reported in Table 1. The functional form is an excellent fit to the overall and blue M_s–M_h relations at all masses and to the red M_s–M_h relation for masses larger than $M_\mathrm{h} \approx 10^{11.3}\ M_\odot$.

3.3. *The baryonic-halo mass relations for central blue and red galaxies*

The right upper and lower panels of Figure 5 show the mean M_b–M_h and f_b–M_h relations, as in the left panels, for all central galaxies (solid line), central blue (long-dashed blue line), and central red (short-dashed red line) galaxies. The blue and red *GBMF*s were calculated from the corresponding *GSMF*s and adding to $M_{\rm s}$ the respective gas mass, $M_{\rm g}$ (see § 2.1). The total *GBMF* is the sum of both of them. The error in $M_{\rm b}$ was calculated as the sum in quadrature of the errors in $M_{\rm s}$ and $M_{\rm g}$. This error, together with the intrinsic scatter in $M_{\rm s}$ (see § 2.2), both propagated to the $M_{\rm b}$–$M_{\rm h}$ relation, account for an uncertainty (standard deviation) of $\sim$0.23 dex in $\log M_{\rm b}$ at all masses (grey curves connected by vertical lines in Figure 5).

The baryonic mass fraction, $f_{\rm b}$, for blue galaxies is larger than the corresponding stellar one, $f_{\rm s}$, in particular at smaller halo masses. At $M_{\rm h} \approx 10^{11}\ M_\odot$, $f_{\rm b}$ is a factor 2.4 times higher than $f_{\rm s}$, while the peak of $f_{\rm b} = 0.028^{+0.018}_{-0.011}$ (at $M_{\rm h} = 10^{12.0}\ M_\odot$) is only 1.3 times larger than the peak of $f_{\rm s}$ (at $M_{\rm h} = 10^{12.0}\ M_\odot$). For larger masses, the difference between $f_{\rm b}$ and $f_{\rm s}$ decreases, while for smaller masses, the lower is $M_{\rm h}$, the larger is $f_{\rm b}$ compared to $f_{\rm s}$. For red galaxies, $f_{\rm s}$ and $f_{\rm b}$ are very similar, some differences being observed only at the lowest masses.

For masses larger (smaller) than $M_{\rm h} \approx 10^{11.6}\ M_\odot$, the differences between the $M_{\rm b}$–$M_{\rm h}$ ($f_{\rm b}$–$M_{\rm h}$) relation of blue and red galaxies become smaller (larger) than in the case of stellar masses (see § 3.2 and left panels of Figure 5). In general, the $f_{\rm b}$ bell-shaped curve for red galaxies is more peaked and narrower than the one for blue galaxies.

For blue galaxies, roughly $f_{\rm b} \propto {M_{\rm h}}^{0.7}$ (${M_{\rm b}}^{0.4}$) at the low-mass end, and $f_{\rm b} \propto {M_{\rm h}}^{-0.5}$ (${M_{\rm b}}^{-0.8}$) at the high-mass end. For red galaxies, roughly $f_{\rm b} \propto {M_{\rm h}}^{2.9}$ (${M_{\rm b}}^{0.8}$) at the low-mass end, and $f_{\rm b} \propto {M_{\rm h}}^{-0.6}$ (${M_{\rm b}}^{-1.5}$) at the high-mass end. For halos of masses $M_{\rm h} \approx 10^{11.0}\ M_\odot$ and $M_{\rm h} \approx 10^{13.2}\ M_\odot$, the baryon fraction for blue (red) galaxies decreases to values $f_{\rm b} \approx 0.004$ and 0.0085 ($f_{\rm b} \approx 0.0031$ and 0.0071), respectively. Therefore, for all masses, $f_{\rm b} \ll f_U$, where $f_U \equiv \Omega_b/\Omega_M$ is the universal baryon mass fraction; for the cosmology used here, $f_U = 0.167$.

4. DISCUSSION

4.1. *Comparison with other work*

As discussed in § 3.1 (see Figure 4), our inference of the local overall $M_{\rm s}$–$M_{\rm h}$ relation is in general in good agreement with several recent works that make use of the AMT (e.g., Baldry et al. 2008; Guo et al. 2010; Moster et al. 2010; BCW10). The aim in this paper is to estimate the $M_{\rm s}$–$M_{\rm h}$ and $M_{\rm b}$–$M_{\rm h}$ relations for blue (late-type) and red (early-type) central galaxies separately. We found that the differences between the means of the obtained relations for blue and red galaxies are within the 1σ uncertainty (see Figure 5). In more detail, the mean stellar and baryonic mass fractions ($f_{\rm s}$ and $f_{\rm b}$) as a function of $M_{\rm h}$ for red galaxies are narrower and more peaked than those for blue galaxies in such a way that for a given mass range (11.5–13.0 and 11.5–12.5 in $\log(M_{\rm h}/M_\odot)$ for the stellar and baryonic cases, respectively) the former are higher than the latter, and outside these ranges the trend is inverted, especially at the low-mass side.

There are only a few previous attempts to infer the halo masses of central galaxies as a function of mass (luminosity) *and* galaxy type (Mandelbaum et al. 2006; More et al. 2011). These works use direct techniques (see Introduction), which are, however, limited by low signal-to-noise ratios, especially for less massive systems, so that the halo mass determinations are reliable only for galaxies with $M_{\rm s} \gtrsim 10^{10}\ M_\odot$. These techniques are galaxy-galaxy weak lensing and kinematics of satellite galaxies around central galaxies. In order to overcome the issue of low signal-to-noise ratios in the current measures, large samples of galaxies are stacked together in bins of similar properties (e.g., luminosity, $M_{\rm s}$, galaxy type) obtaining in this way higher (statistically averaged) signals of the corresponding measures (the tangential shear in the case of lensing and the weighted satellite velocity dispersion in the case of satellite kinematics). Besides, estimates of $M_{\rm h}$ with these sophisticated techniques are subject to several assumptions, among them, those related to the internal halo mass distribution. It is usual to assume the Navarro, Frenk, & White (1997) density profile with the mean concentration for a given mass as measured in N-body cosmological simulations.

It is not easy to achieve a fair comparison of the results obtained with the AM formalism and those with the direct methods. We have inferred the mean (and scatter) of $\log M_{\rm s}$ as a function of $M_{\rm h}$, while the weak lensing and satellite kinematics techniques constrain $M_{\rm h}$ as a function of $M_{\rm s}$ (see e.g., More et al. 2011); besides, the former calculates the mean of $M_{\rm h}$ (and its scatter) in a linear scale instead of a logarithmic one. These different ways of defining the relationship between stellar and halo masses, depending on the shapes and scatters of the corresponding relations, diverge less or more among them. In BCW10 (see their Figure 10), it was shown that at low masses ($\log(M_{\rm h}/M_\odot \lesssim 12$, $\log(M_{\rm s}/M_\odot) \lesssim 10.5$), averaging $\log M_{\rm s}$ as a function of $M_{\rm h}$ or $\log M_{\rm h}$ as a function of $M_{\rm s}$ give equivalent results for the AMT, but at high masses, where the $M_{\rm s}$–$M_{\rm h}$ relation becomes much

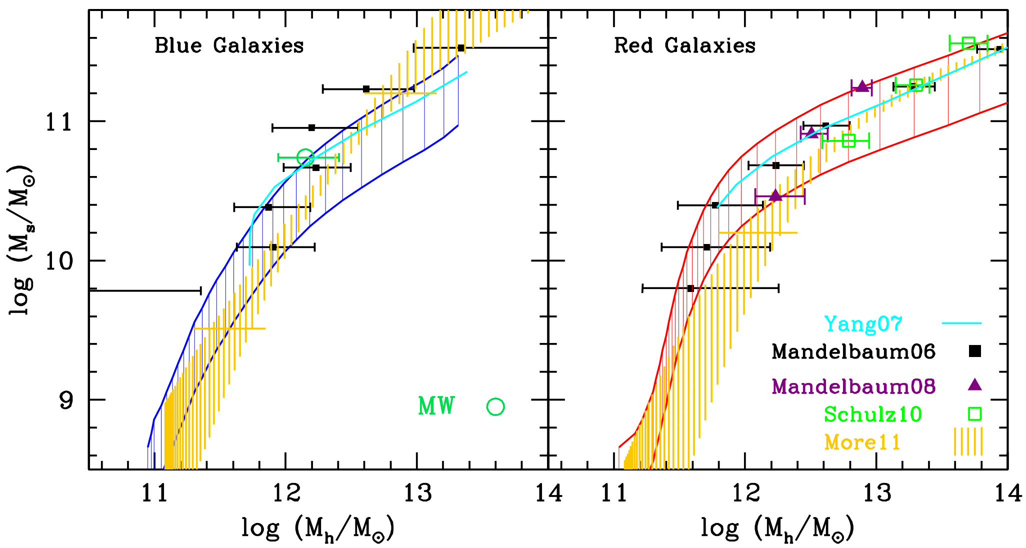

Fig. 8. Comparison with other observational inferences. Left panel: $M_\mathrm{s} - M_\mathrm{h}$ relation for blue (late-type) galaxies. The blue curves connected by vertical lines encompass the $\pm1\sigma$ interval inferred here. We also reproduce the inferences using galaxy-galaxy weak lensing by Mandelbaum et al. (2006, black squares), galaxy groups (Yang et al. 2007, cyan solid line), and satellite kinematics (More et al. 2011, orange vertical lines). Estimates for the Milky Way are plotted (open circle with error bar). Right panel: $M_\mathrm{s} - M_\mathrm{h}$ relation for red (early-type) galaxies. The red curves connected by vertical lines encompass the $\pm1\sigma$ interval inferred here. Other determinations as in the left panel but for early-type galaxies are plotted. More recent inferences with the weak lensing technique by Mandelbaum et al. (2008, filled violet triangles) and by Schulz et al. (2010, open green squares) are also plotted. The color figure can be viewed online.

shallower, this relation becomes steeper (higher stellar mass at a fixed halo mass) for the latter case with respect to the former one.

In Figure 8, the results from Mandelbaum et al. (2006) are reproduced, left panel for central late-type galaxies and right panel for central early-type galaxies (solid squares with error bars). The error bars are 95 percent confidence intervals (statistical). Mandelbaum et al. (2006) have used the (de Vaucouleours/exponential) bulge-to-total ratio, frac_deV, given in the SDSS PHOTO pipeline as a criterion for late- (frac_deV<0.5) and early-type (frac_dV≥ 0.5) separation. This criterion of course is not the same as the color used in YMB09, but there is a correlation between both of them in such a way that a comparison between our results and those of Mandelbaum et al. (2006) is qualitatively possible. Note that we have decreased the halo masses of Mandelbaum et al. (2006) by $\approx$15% on going from their to our definition of halo virial mass. In more recent works, Mandelbaum, Seljak, & Hirata (2008) and Schulz, Mandelbaum, & Padmanabhan (2010) reported a new weak lensing analysis for the massive central early-type galaxies using the seventh SDSS data release (DR7) and a more sophisticated criteria for selecting the early-type lens population. Their results are plotted in the right panel of Figure 8 with solid triangles and open squares, respectively.

In the case of the satellite kinematics determinations of M_h by More et al. (2011), the same SDSS sample and similar recipes as in YMB09 for calculating M_s, classifying galaxies into blue and red, and finding central and satellites galaxies were used. More et al. (2011) applied their analysis to constrain the mean $\log M_\mathrm{h}$ as a function of M_s, but also presented the constraints of their model for the mean of $\log M_\mathrm{s}$ as a function of M_h. Their results for the latter case, kindly made available to us in electronic form by Dr. S. More, are reproduced in Figure 8 as the shaded (orange) regions which represent the 68% confidence intervals. On going from their to our definitions of halo mass and IMF, their M_h and M_s were decreased by $\approx$15% and $\approx$25%, respectively. The dotted horizontal lines in each panel show the approximate range in M_s where the determinations are reliable according to More et al. (2011, see their Figure 11).

In More et al. (2011) are also reported results for the average M_h as a function of M_s split into central blue and red galaxies corresponding to the galaxy group analysis by Yang et al. (2007). The solid (cyan) curves in Figure 8 reproduce these results.

Finally, the standard $\pm 1\sigma$ deviation intervals that we have obtained from the AMT are reproduced in Figure 8 for central blue and red galaxies (solid blue and red curves connected by vertical lines, respectively). Note that in the determinations with direct methods, the systematic uncertainty in $M_{\rm s}$, which is the main source of error in the AMT, was not taken into account.

Our inference for early-type (red) galaxies is consistent (within the uncertainties, errors, and different ways of presenting the constraints) with the weak lensing results of Mandelbaum et al. (2006) and Schulz et al. (2010), and with the galaxy group analysis of Yang et al. (2007) as reported in More et al. (2011), for all the masses reported in each one of these papers. With respect to the satellite kinematics analysis by More et al. (2011), their mean halo masses for $M_{\rm s} \sim 5 \times 10^9 - 10^{11}\ M_\odot$ (for smaller masses their uncertainties are very large) are larger than ours (and those of Mandelbaum et al. 2006) by factors around 2. For larger masses, all determinations agree roughly with our results. In fact, there is some indication that satellite kinematics yields halo masses around low mass central galaxies that are systematically larger than most other methods, specially for red central galaxies (Skibba et al. 2011; but see More et al. 2011 for a discussion).

For late-type (blue) galaxies, our results are in reasonable agreement with those of Mandelbaum et al. (2006) for masses $M_{\rm s} \lesssim 10^{10.8}\ M_\odot$. At higher masses, their results imply halo masses for a given $M_{\rm s}$ smaller than ours, with the difference increasing with increasing stellar mass. The discrepancy would be weaker taking into account that the mean $M_{\rm s}$–$M_{\rm h}$ relation in our case becomes steeper when calculating $M_{\rm h}$ as a function of $M_{\rm s}$. On the other hand, it must be said that the number statistics becomes poor for massive late-type galaxies, resulting in a stacked weak lensing analysis with large error bars. For example, in the two most massive bins in the Mandelbaum et al. (2006) sample (the two uppermost points in Figure 8), only 5 and 11 percent of the galaxies are classified as late types. Future weak lensing work should confirm whether high-mass late-type galaxies do or do not have such relatively small halos as found in Mandelbaum et al. (2006). Regarding the comparison with the satellite kinematics inferences of More et al. (2011), the agreement is reasonable at least up to $M_{\rm s} \approx 10^{11}\ M_\odot$, though the relation inferred by these authors is less curved than ours. For larger masses, these authors caution that their results become very uncertain, as in the weak lensing case, because of poor statistics of massive blue galaxies. The galaxy groups inference (Yang et al. 2007), in the mass range allowed by this technique, gives halo masses slightly smaller than the means of our inference for a given $M_{\rm s}$.

In general, most techniques for inferring the relationship between stellar and halo masses of galaxies agree among them within factors up to 2–3 in $M_{\rm h}$ (BCW10; More et al. 2011; Dutton et al. 2010). This seems to be also the case for samples partitioned into late- and early-type galaxies, as shown here. However, beyond the detailed comparison between our results and those obtained with direct techniques, it seems that there is a systematic qualitative difference: in our case, at a given halo mass (for $10^{11.5}\ M_\odot \lesssim M_{\rm h} \lesssim 10^{13.0}\ M_\odot$), blue centrals, on average, have lower stellar masses than red centrals, while in the case of determinations with direct techniques, the opposite occurs, at least for masses larger than $M_{\rm h} \sim 10^{12}\ M_\odot$ (Mandelbaum et al. 2006; More et al. 2011; see also Figures 5 and 8).

A partial source of bias contributing to this difference could be that in the weak lensing and satellite kinematics techniques the same concentration for halos hosting late- and early-type galaxies is assumed. If halos of late- (early-)type galaxies are less (more) concentrated than the corresponding average, then for the same measure (shear or satellite velocity dispersion), the halo masses are expected to be higher (lower) than the obtained ones. Therefore, the differences found (Mandelbaum et al. 2006 and More et al. 2011) in the mass halos of late- and early-type galaxies of a given $M_{\rm s}$ would decrease or even invert their sense.

While it is difficult to make any robust statement about possible systematics in each technique regarding late and early types, we ask ourselves what should be modified in our assumptions in order to invert the behavior of the $M_{\rm s}$–$M_{\rm h}$ relations with galaxy type (color) obtained here. We have shown in Figure 6 that our corrections to the *HMF* had the effect of bringing the $M_{\rm s}$–$M_{\rm h}$ relations of blue and red galaxies into closer agreement at large masses. One possibility in order not only to bring the relations into closer agreement but to invert them is to make even steeper (shallower) the *HMF* corresponding to blue (red) galaxies, mainly at the high-mass end (see Figure 3, lower panel). This would imply, for instance, a larger correction to the *HMF* due to groups than that made by us. The group/cluster mass function used by us (Heinämäki et al. 2003) is one of the most general ones found in the literature; it includes all kinds of groups/clusters with 3 or more members and $\delta N/N \geq 80$. The authors note that their sample is complete down to a dynamical mass roughly equivalent to $M_{\rm h} = 5\times10^{13}\ M_\odot$. It could be that the abundance of groups of lower masses is larger than that given in Heinämäki et al. (2003), though it is difficult to accept that blue galaxies are completely absent in the centers of small and loose groups of a few (>2) members.

Last but not least, in Figure 8 we include observational estimates for our Galaxy (open circle). The uncertainties in the estimates of $M_{\rm h}$ for the Milky Way are still large but better than most of the determinations for other individual galaxies. For recent reviews on different results see Guo et al. (2010) and Dutton et al. (2010). In Figure 8 we plot a recent estimate of $M_{\rm h}$ based on observations of 16 high velocity stars (Smith et al. 2007). These authors find $M_{\rm h} = 1.42^{+1.14}_{-0.54} \times 10^{12}\ M_\odot$, which is in good agreement with several previous works (e.g., Wilkinson & Evans 1999; Sakamoto, Chiba, & Beers 2003; Li & White 2008), though results from Xue et al. (2008) suggest lower values (but see a recent revision by Przybilla et al. 2010). For its $M_{\rm h}$, the $M_{\rm s}$ of the Milky Way seems to be at the high extremum of blue galaxies, close to values typical of red galaxies. It should be said that it is an open question whether the Milky Way is an average galaxy or not. In the stellar Tully-Fisher and radius–$M_{\rm s}$ relations (e.g., Avila-Reese et al. 2008), the Milky Way is shifted from the average to the high-velocity and low-radius sides, respectively.

4.2. *Interpretations and consistency of the results*

Although our main result is that the differences between the $M_{\rm s}$–$M_{\rm h}$ and $M_{\rm b}$–$M_{\rm h}$ relations for central blue and red galaxies are marginal (within the uncertainties of our determinations), we will explore whether such differences are expected or not. For this it is important to approach the problem from an evolutionary point of view.

In Firmani & Avila-Reese (2010, hereafter FA10), the determinations of the $M_{\rm s}$–$M_{\rm h}$ relation for all galaxies at different redshifts, out to $z = 4$ (BCW10), and the average ΛCDM individual halo mass aggregation histories (MAHs) were used to determine the individual *average* $M_{\rm s}$ growth of galaxies in general as a function of mass (called in that paper as Galaxian Hybrid Evolutionary Tracks, GHETs). It was found that the more massive the galaxies, the earlier transit from their active (star-forming, blue) regime of $M_{\rm s}$ growth to a passive (red) phase (population 'downsizing'), while their corresponding halos continue growing, more efficiently at later epochs the more massive they are ('upsizing'). The inferred trend for the transition stellar mass is $\log(M_{\rm tran}/M_\odot) \approx 10.30 + 0.55z$. Therefore, galaxies of mass $M_{\rm s} \approx 10^{10.3}\ M_\odot$ are on average becoming passive (red) today. For $M_{\rm s} \gtrsim M_{\rm tran}$, the larger the mass, the redder will be the galaxy on average. The opposite applies for $M_{\rm s} \lesssim M_{\rm tran}$, the smaller the mass, the bluer will be the galaxy. Interestingly enough, $M_{\rm s} \approx 10^{10.3}\ M_\odot$ is roughly the mass where the overall YMB09 blue and red *GSMF*s cross: for masses larger than this crossing mass, $M_{\rm cross}$, redder galaxies become more and more abundant than bluer ones and the inverse happens at smaller masses (see Figure 1).

Galaxies that are transiting from active to passive at $z \sim 0$ (those around $M_{\rm tran} \approx 10^{10.3}\ M_\odot$) have probably been subject recently to a process that induced an *efficient* transformation of the available gas into stars in such a way that their stellar populations started to redden passively. Hence, for a given $M_{\rm h}$, they are expected to have a higher $M_{\rm s}$ (or $f_{\rm s}$) than those galaxies of similar mass that did not suffer (yet?) the above process (bluer ones). The relatively small difference in $f_{\rm s}$ for blue and red galaxies we have found here (whose maximum is attained around $M_{\rm tran} \sim M_{\rm cross}$, Figure 5) would imply that the scatter around $M_{\rm tran}$ is moderate.

Galaxies more massive than $M_{\rm tran}$ (or $M_{\rm cross}$), according to the evolutionary analysis by FA10, underwent the process of efficient gas consumption into stars (and the further cessation of $M_{\rm s}$ growth) earlier on average than more massive galaxies, while their halos continue growing. Therefore, one expects that the more massive the galaxy, the redder and the lower its stellar (and baryonic) mass fraction $f_{\rm s}$ will be on average. The few blue massive galaxies may have slightly smaller stellar masses (lower $f_{\rm s}$) than the corresponding red ones because they should have transformed gas into stars less efficiently in the past. Therefore, by including gas, i.e. when passing to $f_{\rm b}$ the difference between blue and red massive galaxies at large masses should become negligible. This is indeed what happens (see Figure 5).

Galaxies less massive than $M_{\rm tran}$ (or $M_{\rm cross}$) at $z \sim 0$, according to FA10, are in general the more actively assembling their stellar masses the smaller they are ('downsizing' in specific SFR), while their dark halo mass growth is already very slow. This implies the existence in the galaxies of relatively larger reservoirs of cold gas the smaller they are (gas not related to the halo-driven infall) because the SF has been delayed in the disk and/or cold gas is being lately (re)accreted into the galaxy. However, if for some reason the gas reservoir in these galaxies is lost, then the galaxy will redden and its baryonic and stellar mass fractions will be smaller than those of the galaxies that were able to keep their gas reservoir (the majority), in agreement with our inferences here (Figure 5).

5. SUMMARY AND CONCLUSIONS

By means of the AM technique and using the central blue and red *GSMF*s, constructed from the local SDSS sample by YMB09, we have inferred the local M_s–M_h (or f_s–M_h) relations for *central* galaxies and for the sub-samples of blue and red galaxies. To derive the relations for the sample of blue galaxies, (i) the mass function of observed groups/clusters of galaxies is subtracted from the distinct (S-T) *HMF* (blue, late-type galaxies are not observed in the centers of groups and clusters), and (ii) halos that suffered a major merger since $z = 0.8$ are excluded. For red galaxies, the *HMF* is assumed to be the complement of the "blue" one, with respect to the overall (distinct) *HMF*. We consider as sources of uncertainty in our analysis only the systematical error in assigning stellar masses to galaxies (0.25 dex) and the intrinsic statistical scatter in stellar mass at a fixed halo mass (0.16 dex). By using the observational M_g–M_s relation and its scatter, we transited from M_s to M_b ($= M_s + M_g$) in the *GSMF* and estimated the overall blue and red *GBMF*s, which were used to obtain the corresponding baryonic M_b–M_h (or f_b–M_h) relations using the AM technique.

The M_s–M_h relation obtained here agrees rather well with previous studies (see Figure 4). The small differences found in this work can be explained mainly in terms of the different *GSMF*s used in each study, and to a lesser extent by variations in the methodology. The 1σ uncertainty in the obtained M_s–M_h relation is ≈ 0.25 dex in log M_s. The M_s–M_h relation of central galaxies lies below (lower M_s for a given M_h) the overall one by a factor ~ 1.6 at $M_h = 10^{11}\ M_\odot$ and by less than 5% for $M_h > 10^{13}\ M_\odot$.

Our main result refers to the calculation of the *central* M_s–M_h and M_b–M_h relations for the two broad populations into which the galaxy sample can be divided: blue (late-type) and red (early-type) galaxies. We highlight the following results from our analysis:

- At $M_h \gtrsim 10^{11.3}\ M_\odot$ the mean stellar mass fraction f_s of blue galaxies is smaller than that of red galaxies, the maximum difference being attained at $M_h \approx 10^{11.7}\ M_\odot$; at this mass, the f_s of red galaxies is 1.7 times that of blue galaxies (see Figure 5). At larger masses, the difference decreases until it disappears. At $M_h \lesssim 10^{11.3}\ M_\odot$ the trend is reversed as blue galaxies tend to have higher values of f_s than red ones. In the case of the baryonic mass fractions, f_b, the same trends of the stellar relations remain but at $M_h \gtrsim 10^{11.3}\ M_\odot$ the difference in f_b between blue and red galaxies is small, while for smaller masses, the difference increases.

- The M_s–M_h and M_b–M_h (or f_s–M_h and f_b–M_h) relations of central blue and red sub-samples do not differ significantly from the respective relations of the overall central sample, and these differences are within the 1σ uncertainty of the inferences (Figure 5). For blue (red) galaxies, the maximum value of f_s is $0.021^{+0.016}_{-0.009}$ ($0.034^{+0.026}_{-0.015}$) and is attained for halos of mass $M_h = 10^{11.98}\ M_\odot$ ($M_h = 10^{11.87}\ M_\odot$); the corresponding stellar mass is $M_s = 10^{10.30\pm0.25}\ M_\odot$ ($M_s = 10^{10.40\pm0.25}\ M_\odot$), which is around 0.23 (0.30) times $M^\star$, the Schechter fit characteristic mass of the overall *GSMF* of YMB09. For smaller and larger masses, f_s significantly decreases.

- We have compared our results with the few observational inferences of the M_s–M_h relation for blue (late-type) and red (early-type) galaxies that exist in the literature. Although these studies estimate halo masses using direct techniques (weak lensing and galaxy satellite kinematics), they are still limited by the stacking approach they need to apply (due to the low signal-to-noise ratio of individual galaxies) and by the large uncertainties owing to the unknown systematics. The overall differences among the different studies (including ours) amount to factors of up to 2–4 at a given mass (these factors being much smaller at other masses) for most methods (Figure 8). For blue galaxies, all methods agree reasonably well for low masses ($M_h \lesssim 3 \times 10^{12}\ M_\odot$), but for higher masses, our inference implies larger halos for a given M_s than the results from direct techniques. For red galaxies, at high masses ($M_h \gtrsim 3 \times 10^{12}\ M_\odot$), all methods agree reasonably well, but at lower masses, the satellite kinematics technique produces halo masses, for a given M_s, larger than those obtained by other methods.

- According to our results, for $M_h \lesssim 10^{11.3}\ M_\odot$, the intrinsic scatter of the M_s–M_h relation should slightly anti-correlate with galaxy color (for a fixed M_h, the bluer the galaxy, the higher its M_s), while for more massive systems, the correlation should be direct (for a fixed M_h, the redder the galaxy, the higher its M_s). For massive blue galaxies to have had higher higher f_s values than red ones as the results from direct techniques suggest, the *HMF* halos hosting blue (red) galaxies should have been even steeper (shallower) than what we have proposed here; this seems too extreme.

• The maximum baryon mass fraction of blue and red galaxies are $f_\mathrm{b} = 0.028^{+0.018}_{-0.011}$ and $f_\mathrm{b} = 0.034^{+0.025}_{-0.014}$, respectively, much smaller than $f_U = 0.167$ in both cases, and these maxima are attained at $M_\mathrm{h} \approx 10^{12}\ M_\odot$. At large masses f_b decreases approximately as $f_\mathrm{b} \propto {M_\mathrm{h}}^{-0.5}({M_\mathrm{b}}^{-0.8})$ for blue galaxies and as $f_\mathrm{b} \propto {M_\mathrm{h}}^{-0.6}({M_\mathrm{b}}^{-1.5})$ for red galaxies, in such a way that from $M_\mathrm{h} \approx 5 \times 10^{12}\ M_\odot$ on, blue galaxies have on average slightly larger values of f_b than red ones. At low masses, the f_b of red galaxies strongly decreases as the mass decreases $f_\mathrm{b} \propto {M_\mathrm{h}}^{2.9}({M_\mathrm{b}}^{0.8})$, while for blue galaxies, due to the increasing gas fractions the smaller the mass, f_b decreases more slowly than f_s, as $f_\mathrm{b} \propto {M_\mathrm{h}}^{0.7}$ ($\propto {M_\mathrm{b}}^{0.4}$).

The AM technique has been revealed as a relatively simple but powerful method for connecting empirically galaxies to dark halos. Here we extended this technique towards inferences for the blue and red galaxy sub-populations separately. By introducing a minimum of assumptions –otherwise the method becomes close to a semi-analytical model– we have found that the stellar and baryon mass-halo mass relations of blue and red galaxies do not differ significantly among them and from the overall ones. The maximum differences occur around the peak of these relations, $M_\mathrm{h} \approx 10^{12}\ M_\odot$, and are consistent qualitatively with the inference that the galaxies in these halos are transiting from an active to a quiescent regime of M_s growth (FA10). Those that transited recently did so because they had an efficient process of gas consumption into stars and further cessation of M_s growth; therefore, they should be redder and have higher f_s values than those that have not transited. For larger and smaller masses than $M_\mathrm{h} \approx 10^{12}\ M_\odot$, the differences decrease and even invert, something that is also consistent with the inferences by FA10, based on the semi-empirical determinations of the evolution of the overall M_s–M_h relation.

We thank the referee for his/her useful comments and suggestions. We are grateful to Dr. S. More for sending us in electronic form the data plotted in Figure 8. A.R-P. acknowledges a graduate student fellowship provided by Conacyt. We thank PAPIIT-Universidad Nacional Autónoma de México grant IN114509 and Conacyt grant 60354 for partial funding, as well as a bilateral DFG-Conacyt grant through which we got access to results from N-body numerical simulations performed by Dr. S. Gottloeber.

REFERENCES

Avila-Reese, V. 2007, in Ap&SS Proc., Stellar and Galactic Connections Between Particle Physics and Astrophysics, ed. A. Carramiñana et al. (Berlin: Springer), 115 (arXiv:astro-ph/0605212v1)
Avila-Reese, V., Zavala, J., Firmani, C., & Hernández-Toledo, H. M. 2008, AJ, 136, 1340
Baldry, I. K., Balogh, M. L., Bower, R. G., Glazebrook, K., Nichol, R. C., Bamford, S. P., & Budavari, T. 2006, MNRAS, 373, 469
Baldry, I. K., Glazebrook, K., & Driver, S. P. 2008, MNRAS, 388, 945
Baugh, C. M. 2006, Rep. Prog. Phys., 69, 3101
Behroozi, P. S., Conroy, C., & Wechsler, R. H. 2010, ApJ, 717, 379 (BCW10)
Bell, E. F., McIntosh, D. H., Katz, N., & Weinberg, M. D. 2003, ApJS, 149, 289
Benson, A. J. 2010, Phys. Rep., 495, 33
Benson, A. J., Bower, R. G., Frenk, C. S., Lacey, C. G., Baugh, C. M., & Cole, S. 2003, ApJ, 599, 38
Berlind, A. A., & Weinberg, D. H. 2002, ApJ, 575, 587
Bernardi, M., Shankar, F., Hyde, J. B., Mei, S., Marulli, F., & Sheth, R. K. 2010, MNRAS, 404, 2087
Blanton, M. R., & Moustakas, J. 2009, ARA&A, 47, 159
Boylan-Kolchin, M., Ma, C.-P., & Quataert, E. 2008, MNRAS, 383, 93
Chabrier, G. 2003, PASP, 115, 763
Cole, S., et al. 2001, MNRAS, 326, 255
Conroy, C., Gunn, J. E., & White, M. 2009, ApJ, 699, 486
Conroy, C., & Wechsler, R. H. 2009, ApJ, 696, 620
Conroy, C., Wechsler, R. H., & Kravtsov, A. V. 2006, ApJ, 647, 201
de Lapparent, V., & Slezak, E. 2007, A&A, 472, 29
Dutton, A. A., Conroy, C., van den Bosch, F. C., Prada, F., & More, S. 2010, MNRAS, 407, 2
Dutton, A. A., & van den Bosch, F. C. 2009, MNRAS, 396, 14
Dutton, A. A., van den Bosch, F. C., Dekel, A., & Courteau, S. 2007, ApJ, 654, 27
Firmani, C., & Avila-Reese, V. 2000, MNRAS, 315, 457
_________. 2010, ApJ, 723, 755 (FA10)
Gallazzi, A., & Bell, E. F. 2009, ApJS, 185, 253
Giocoli, C., Tormen, G., Sheth, R. K., & van den Bosch, F. C. 2010, MNRAS, 404, 502
Gnedin, O. Y., Weinberg, D. H., Pizagno, J., Prada, F., & Rix, H.-W. 2007, ApJ, 671, 1115
Governato, F., Mayer, L., & Brook, C. 2008, in ASP Conf. Ser. 396, Formation and Evolution of Galaxy Disks, ed. J. G. Funes, S. J., & E. M. Corsini (San Francisco: ASP), 453
Guo, Q., White, S., Li, C., & Boylan-Kolchin, M. 2010, MNRAS, 367
Heinämäki, P., Einasto, J., Einasto, M., Saar, E., Tucker, D. L., & Müller, V. 2003, A&A, 397, 63

Komatsu, E., et al. 2009, ApJS, 180, 330
Kravtsov, A. V., Berlind, A. A., Wechsler, R. H., Klypin, A. A., Gottlöber, S., Allgood, B., & Primack, J. R. 2004, ApJ, 609, 35
Li, C., Kauffmann, G., Jing, Y. P., White, S. D. M., Börner, G., & Cheng, F. Z. 2006, MNRAS, 368, 21
Li, C., & White, S. D. M. 2009, MNRAS, 398, 2177
Li, Y.-S., & White, S. D. M. 2008, MNRAS, 384, 1459
Mandelbaum, R., Seljak, U., & Hirata, C. M. 2008, JCAP, 8, 6
Mandelbaum, R., Seljak, U., Kauffmann, G., Hirata, C. M., & Brinkmann, J. 2006, MNRAS, 368, 715
Marinoni, C., & Hudson, M. J. 2002, ApJ, 569, 101
Martínez, H. J., Zandivarez, A., Merchán, M. E., & Domínguez, M. J. L. 2002, MNRAS, 337, 1441
McGaugh, S. S. 2005, ApJ, 632, 859
Mo, H.J., Mao, S., & White, S.D.M. 1998, MNRAS, 295,319
More, S., van den Bosch, F. C., Cacciato, M., Mo, H. J., Yang, X., & Li, R. 2009, MNRAS, 392, 801
More, S., van den Bosch, F. C., Cacciato, M., Skibba, R., Mo, H. J., & Yang, X. 2011, MNRAS, 410, 210
Moster, B. P., Somerville, R. S., Maulbetsch, C., van den Bosch, F. C., Macciò, A. V., Naab, T., & Oser, L. 2010, ApJ, 710, 903
Navarro, J. F., Frenk, C. S., & White, S. D. M. 1997, ApJ, 490, 493
Norberg, P., et al. 2001, MNRAS, 328, 64
Padilla, N., Lambas, D. G., & González, R. 2010, MNRAS, 409, 936
Peacock, J. A., & Smith, R. E. 2000, MNRAS, 318, 1144
Press, W. H., & Schechter, P. 1974, ApJ, 187, 425
Przybilla, N., Tillich, A., Heber, U., & Scholz, R.-D. 2010, ApJ, 718, 37
Robertson, B., Yoshida, N., Springel, V., & Hernquist, L. 2004, ApJ, 606, 32
Sakamoto, T., Chiba, M., & Beers, T. C. 2003, A&A, 397, 899
Schulz, A. E., Mandelbaum, R., & Padmanabhan, N. 2010, MNRAS, 408, 1463
Shankar, F., Lapi, A., Salucci, P., De Zotti, G., & Danese, L. 2006, ApJ, 643, 14
Shao, Z., Xiao, Q., Shen, S., Mo, H. J., Xia, X., & Deng, Z. 2007, ApJ, 659, 1159
Sheth, R. K., & Tormen, G. 1999, MNRAS, 308, 119 (S-T)
Skibba, R. A., van den Bosch, F. C., Yang, X., More, S., Mo, H., & Fontanot, F. 2011, MNRAS, 410, 417
Smith, M. C., et al. 2007, MNRAS, 379, 755
Stewart, K. R., Bullock, J. S., Barton, E. J., & Wechsler, R. H. 2009, ApJ, 702, 1005
Stringer, M. J., & Benson, A. J. 2007, MNRAS, 382, 641
Tinker, J., et al. 2008, ApJ, 688, 709
Tucker, D. L., et al. 2000, ApJS, 130, 237
Vale, A., & Ostriker, J. P. 2004, MNRAS, 353, 189
van den Bosch, F. C. 2000, ApJ, 530, 177
Wang, L., & Jing, Y. P. 2010, MNRAS, 402, 1796
Wang, Y., et al. 2009, ApJ, 697, 247
Wei, L. H., Kannappan, S. J., Vogel, S. N., & Baker, A. J. 2010, ApJ, 708, 841
Weinmann, S. M., van den Bosch, F. C., Yang, X., & Mo, H. J. 2006, MNRAS, 366, 2
Wilkinson, M. I., & Evans, N. W. 1999, MNRAS, 310, 645
White, S. D. M., & Frenk, C. S. 1991, ApJ, 379, 52
White, S. D. M., & Rees, M. J. 1978, MNRAS, 183, 341
Xue, X. X., et al. 2008, ApJ, 684, 1143
Yang, X., Mo, H. J., Jing, Y. P., van den Bosch, F. C., & Chu, Y. 2004, MNRAS, 350, 1153
Yang, X., Mo, H. J., & van den Bosch, F. C. 2003, MNRAS, 339, 1057
———. 2008, ApJ, 676, 248
———. 2009, ApJ, 695, 900 (YMB09)
Yang, X., Mo, H. J., van den Bosch, F. C., Pasquali, A., Li, C., & Barden, M. 2007, ApJ, 671, 153
Zehavi, I., et al. 2005, ApJ, 630, 1

A. Rodríguez-Puebla & V. Avila-Reese: Instituto de Astronomía, Universidad Nacional Autónoma de México, Apdo. Postal 70-264, 04510, México, D.F., Mexico (apuebla@astroscu.unam.mx).
C. Firmani: Osservatorio Astronomico di Brera, via E.Bianchi 46, I-23807 Merate, Italy.
P. Colín: Centro de Radioastronomía y Astrofísica, Universidad Nacional Autónoma de México, Apdo. Postal 72-3 (Xangari), Morelia, Michoacán 58089, Mexico.

Revista Mexicana de Astronomía y Astrofísica, **47**, 255–259 (2011)

SPECTRAL MORPHOLOGY AND ROTATION IN THE OPEN CLUSTER NGC 6025

Mónica Grosso and Hugo Levato

Instituto de Ciencias Astronómicas, de la Tierra y del Espacio (ICATE)
Consejo Nacional de Investigaciones Científicas y Técnicas, CONICET
Universidad Nacional de San Juan, Argentina

Received 2011 January 19; accepted 2011 April 19

RESUMEN

Hemos clasificado espectralmente a los probables miembros más brillantes del cúmulo abierto NGC 6025 y hemos calculado sus velocidades de rotación. Encontramos un módulo de distancia de 9.80 ± 0.06 (error probable) y derivamos una edad de 84 millones de años para este cúmulo. La estrella más brillante de NGC 6025, HD 143448 fue clasificada como B1Ve y es una estrella azul desubicada (*blue straggler*) tal como fue propuesto por otros autores (ver Mermilliod 1982). Hemos encontrado tres estrellas peculiares (dos de Si y una de Hg-Mn?) y dos binarias de dos espectros, una de ellas previamente estudiada pero probablemente no miembro del cúmulo. Otra estrella del campo tiene emisión, pero probablemente tampoco es miembro del cúmulo. El promedio de la rotación axial para los miembros de este cúmulo es 73% del promedio de rotación de las estrellas de campo de igual temperatura.

ABSTRACT

We have performed spectral classification and measurements of the axial rotation velocity for the brightest stars in the region of the open cluster NGC 6025. A distance modulus of 9.80 ± 0.06 (pe) and an age of 84 million years were derived. The brightest star of the cluster, HD 143448 was classified as B1Ve and it is a blue straggler as proposed by other authors (see Mermilliod 1982). We found three peculiar stars (two Si and one Hg-Mn?). Another star in the field shows emission but is probably a non-member. We also found two SB2 binaries. The average axial rotation for the cluster members seems to be 73% of the average rotation of the field stars with the same temperature.

Key Words: Hertzsprung-Russell and C-M diagrams — open clusters and associations: individual (NGC 6025) — stars: rotation

1. INTRODUCTION

The galactic cluster NGC 6025 was studied several decades ago in two papers. Feinstein (1971) provided for the first time, UBV photoelectric measurements and derived a distance modulus of 9.4 ± 0.1 and an age of 10^8 years. Four years later Kilambi (1975) published *ubvy* photoelectric and UBV photographic data and obtained 9.7 ± 0.1 for the distance modulus and an age of 9×10^7 years. This author also derived the luminosity function and showed that this cluster has fractionally more bright members than does the Pleiades cluster. There is no spectroscopic study on NGC 6025 even as basic as an MK spectral classification of its members. Paunzen et al. (2001) classified star number 20 in a paper devoted to spectral classification of candidates for λ Bootis stars. There are also some papers in the literature that include NGC 6025 in statistical studies of open clusters (see Kharchenko et al. 2009).

In this paper we classify in the MK system the stars that have been considered to be members in previous papers although we use the new SPM4 Catalogue (van Altena et al. 2010, private communication) to confirm membership. We include other stars in the field of the cluster and we estimate the spectral types of 33 stars and the rotational velocities for 27.

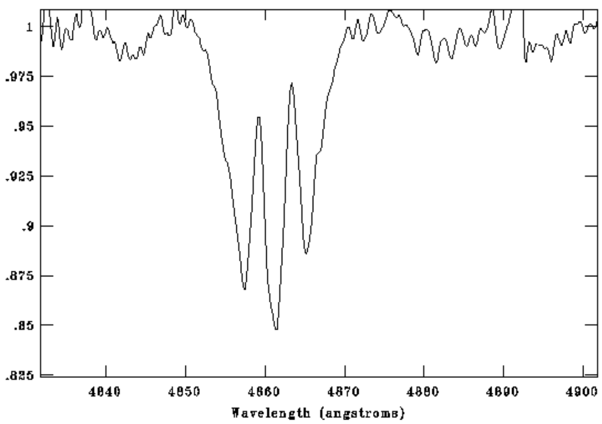

Fig. 1. Hβ profile in the spectrum of HD 143448.

2. OBSERVATIONS AND REDUCTION

The sample contains stars brighter than 11.3 magnitude in the V band. The observations were collected with the Jorge Sahade 2.15 m telescope at Complejo Astronómico El Leoncito, San Juan, Argentina. We used a REOSC spectrograph in simple and cross dispersion mode. The spectra cover the range 3600–6000 Å with a resolution around 3.6 Å/2px for simple dispersion and 0.28 Å/2px and a spectral range between 3700–5700 Å for cross dispersion. The detector was a CCD TEK of 1024 × 1024 pixels, of size 0.024 mm, thinned and back illuminated. Data reduction was carried out using IRAF tasks. The S/N for spectra in cross dispersion was about 100 and 200 for the classification spectra.

2.1. *MK classification*

The spectral classification in the MK system was derived using the WINMK code version 2.4 developed by Richard Gray at the Appalachian State University, USA[1]. The classification was carried out by comparison with MK standard stars taken with the same equipment and conditions and using the MK technique (Gray & Corbally 2009).

2.2. *Comments about some stars*

Star number 1 is a blue straggler with emission in Hβ and we have classified its spectrum as B1Ve. This star was previously classified by Morris (1961) as B3 IV and by Garrison, Hiltner, & Schild (1977) as B1.5 V. The profile of Hβ is similar in all 5 echelle spectra of star number 1 that we have taken and it is shown in Figure 1.

Star 6 shows emission in Hβ but it is probably a non-member of the cluster according to its absolute proper motion, although its position in the HR diagram fits well (see below). The classification spectrum of Star 11 shows Hg II λ 3984 and probably but less clear Mn II λ 4206. Star 25 is a Bp star of the Silicon type with λ 4200 well seen at the classification dispersion. Star 59 is also a Bp star of the Silicon type but with lower excitation level. Star 10 is an SB2 and eclipsing binary (González & Levato 2010, private communication). Star 26, HD 143511, was extensively studied by González & Levato (2006) and it is an SB2 and also an eclipsing binary with a period of 5.53546 days. It is probably a non-member of the cluster according to its absolute proper motion. Kilambi found stars 4, 6, 10 and 60 to have the Stromgreen m_1 index larger than normal. Additional features for each star are included in the notes to Table 1.

2.3. *Proper motions*

We have included in Table 1 the absolute proper motions in RA and DEC in mas yr^{-1}, taken from the SPM4 (van Altena et al. 2010, private communication) which contains 100 million stars. This catalogue is an excellent tool, among other purposes to decide about membership to open clusters. From the proper motion point diagram shown in Figure 2, it is clear that stars 6, 11, 15, 21 and 26 are probable non-members of the cluster. All of them have proper motions differing by more than 3σ from the average absolute proper motion of the cluster. We have used this criterion to decide about membership from the proper motion data.

3. RESULTS

3.1. *Reddening and distance*

The spectral types and the projected rotational velocities derived in this paper are listed in Table 1. The first column shows Feinstein's identification, the second is the HD number when available, or the CPD number. Columns 3 and 4 list the proper motions taken from van Altena et al. (2010, private communication), Column 5 lists the V magnitude taken from Feinstein (1971), Column 6 the MK types derived in the present paper, and Column 7 the projected axial rotation velocity also derived in this paper (see below). Comments have been included at the end of the table. They include conclusions about membership and the Hipparcos parallaxes available for five stars of the sample. Using the intrinsic $B-V$ for each MK type taken from the calibration published by Allen (2001) and using the observed $B-V$ taken from Feinstein (1971) we derived and interstellar extinction of 0.55 mag. adopting $A_v =$

[1] www1.appstate.edu/dept/physics/MK/xmk22.htm.

TABLE 1

RESULTS FOR THE OPEN CLUSTER NGC 6025

N	HD/CPD	μ_α [mas yr^{-1}]	μ_δ [mas yr^1]	V [mag]	ST	$v \sin\ i$ [km s^{-1}]
1[a]	143448	−1.49	−4.53	7.3	B1Ve	195
2[b]	143449	−2.34	−3.93	8.11	B5IV	65
3[c]	143413	−1.59	−7.00	8.42	B7 IV	240
4[d]	−60 6332	−5.46	−8.19	9.73	B8 V	60
5	−60 6316	0.98	0.33	10.23	B9 V	60
6[e]	143288	−0.65	27.21	8.96	B6 Ve	215
7[f]	143340	−2.30	−4.50	8.05	B5 IV	60
8	−60 6325	−6.07	−6.10	8.86	B6 V	200
10[g]	−60 6335	0.89	−3.46	10.8	A2:+A2:	20;20
11[h]	143287	−25.52	−12.15	8.34	B9 IVp(Hg−Mn?)	70
12[j]	143309	5.65	0.26	9.3	B6 V	10
13	−60 6319	−3.30	−4.96	9.62	B8 V	185
14[k]	−60 6322	1.85	0.68	9.85	B8.5 V	15
15[l]	−60 6327	−12.39	−29.72	9.63	F0 V	120
16	−60 6339	2.30	−3.99	9.88	B8 V	270
17[m]	−60 6343	−2.84	−11.15	11.17	B6/B7 V::	70
20	−60 6340	1.35	−7.86	11.25	A1V	···
21[n]	−60 6341	−16.76	−9.01	9.98	F5::	20
22[o]	143388	−1.44	5.89	9.15	B5 V	15
23	−60 6336	−3.66	−3.88	10.59	A0 V	60
24	−59 6562	−0.99	−3.76	10.06	B9 V	···
25	143412	−0.44	−3.56	9.7	B8 IIIpSiλ 4200	···
26[p]	143511	−8.02	−20.66	8.31	A0 V+A0 V:	25;25
29	−60 6313	−8.20	−6.75	10.69	B9 V	125
30	−60 6321	−5.77	−6.17	10.88	B9.5 V	···
34	−60 6362	−6.23	−0.69	10.51	B9 V	···
35	−60 6329	−1.35	4.31	10.97	A0 V	···
37	143220	−1.33	1.54	10.15	A3 III	15
38	−60 6311	−2.09	−4.61	10.68	A0 V	···
39[q]	−60 6342	−5.39	1.39	11.24	F0 V	···
43	143123	0.59	−5.43	9.34	B5 V	10
47	−60 6352	−3.74	−6.30	11.01	A1 V	···
59	143447	−1.67	−6.37	10.69	B9.5 p Si	···
60	−59 6578	−3.27	−3.97	10.48	B9.5 V	85
64	−60 6297	−7.91	−1.94	11.71	···	50
65	−60 6298	−4.98	−8.12	10.86	A0V	80
66	−60 6296	−4.29	−3.33	10.87	B9.5 V	80

Additional comments on individual stars:

[a]Variable (MQ TrA) between 7.2 and 7.3 mag in V. Blue struggler (see Mermilliod 1982). Parallax from Hipparcos (HIP 78682): 0.79 mas.
[b]Parallax from Hipparcos (HIP 78683): 0.64 mas.
[c]Parallax from Hipparcos (HIP 78659): 0.86 mas.
[d]m1 large as measured by Kilambi (1975). SB1.
[e]Probably a non-member due to its p.m. Emmission in Hβ.
[f]HIP 78643. Parallax 2.42 mas in new reduction (van Leeuwen 2007).
[g]SB2 (González & Levato 2010, private communication). $\delta V = 45$ km s^{-1} - m1 large.
[h]HIP 78604. parallax 3.58 mas. non-member according to its pm.
[j]Is it a variable (V350 Nor) between 9.2 and 9.310 V magnitude. It was classified by Houk & Cowley (1975) B9/B9 Ib/II.
[k]Radial velocity variable (González & Levato 2010, private communication).
[l]Probably non-member. Source proper motion.
[m]Spectral type not in the MK system. Only high resolution spectrum available.
[n]Probably non-member due to its proper motion.
[o]Radial velocity variable (González & Levato 2010, private communication).
[p]SB2, eclipsing binary, $P = 5.5354$ days. Probably non-member due to its pm.
[q]Probably non-member due to its spectroscopic parallax.

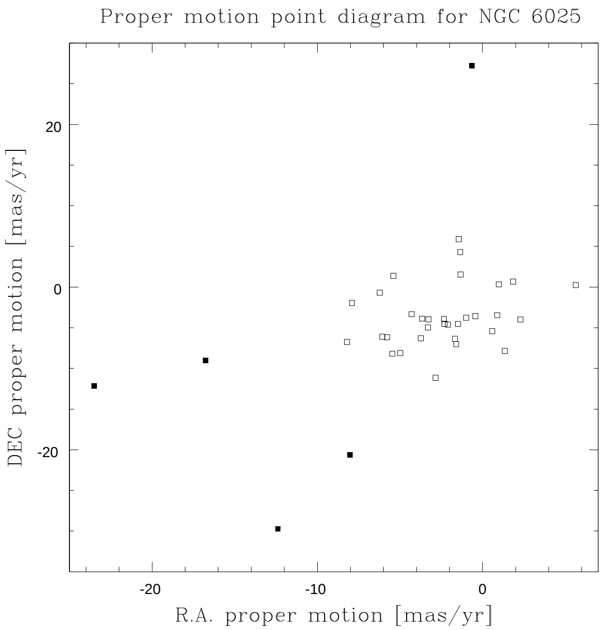

Fig. 2. Proper Motion point diagram for the stars in NGC 6025. Filled squares are non-members according with the 3σ criterium.

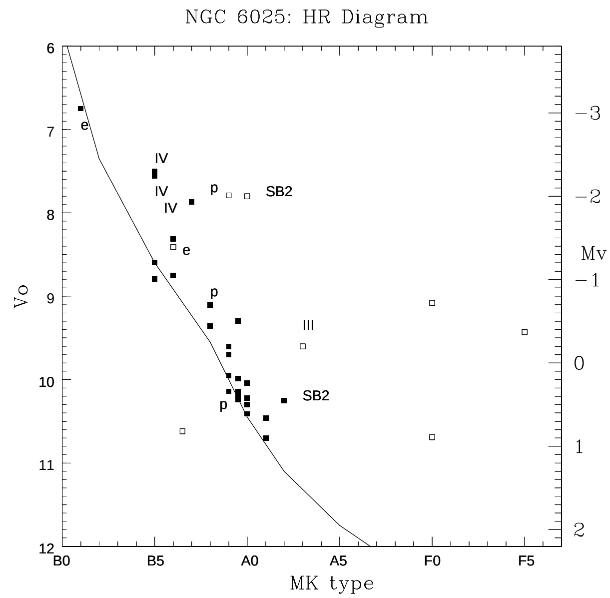

Fig. 3. Observed HR diagram for NGC 6025. Filled squares are probable members while open squares are non-members.

$3.3E(B-V)+0.28(B-V)E(B-V)+0.04E(B-V)^2$ from Allen (2001). Using the calibration between M_v and MK spectral types published by Allen (2001) we derived a true distance modulus for each star and obtained an average true distance modulus for the cluster $(m_v - M_v) = 9.80 \pm 0.06$ (pe of the mean which corresponds to 912 pc) using only the probable members as indicated in Table 1. We have not included neither CP, Be, giants nor binaries in the calculation. It is interesting to note the uncertainties in the Hipparcos parallaxes for stars 1, 2, and 3 that imply distances larger than 1 kpc. The errors in their parallaxes quoted in the Hipparcos catalogue are as large as the parallaxes themselves. We also want to point out a significant difference in the absolute visual magnitude vs MK type calibration between Allen (2001) and Gray & Corbally (2009) for the range B8-A2, which is an important range in this cluster. The visual absolute magnitude difference for the A0 V reaches 0.75 magnitudes, but it is 0.6 magnitudes for A2 V, in the sense that Allen's calibration is brighter than Gray & Corbally's. For late A stars the calibrations agree. To choose one or the other calibration to derive the spectroscopic distance of NGC 6025 is important, because the distance may increase or decrease by almost 50%. We have used Allen (2001) in order to keep consistency with our previous results on open cluster classification. The HR diagram for NGC 6025 is presented in Figure 3 where the absolute magnitude scale was drawn for a distance modulus of 9.8 mag. The main sequence has been taken from Allen (2001). Emission line stars, evolved stars, binaries and Bp-Ap stars were labeled. Probable non-members as indicated in Table 1 were plotted as open squares in Figure 3.

3.2. *Age*

We checked the age, taking into account that the earliest type on the main sequence of the cluster is B6 V. This implies a mass of 5.2 solar masses according to the calibration by Allen (2001). In such a case, the maximum age of the cluster should be 88 million years old using Schaller et al.'s (1992) results. This agrees quite well with the old determination by Kilambi (1975) (90 million years). We also checked the age using the isochrone grids calculated by Girardi et al. (2000). We plotted isochrones for solar composition on a $B-V$ vs Mv HR diagram and the best fit corresponds to log(age) = 7.9 (80 million years). So we have adopted 84 ± 4 million years as the most probable age determined in this paper (log(age) = 7.92).

3.3. *Axial Rotational velocities*

For the determination of the projected rotation velocities we have used as standards those from the Slettebak's system (Slettebak 1975). Calibration curves were constructed between the *fwhm* of the lines λ 4471 of HeI and λ 4481 of MgII against the $v \sin i$ for the selected standards. Linear regression lines were obtained for the spectral ranges B2–B5, B5–B7, B8–A2, A2–A5, A7–F2 for λ 4471 for the first two ranges and λ 4481 for all ranges except the first one. We have calculated the mean percentage of projected rotation velocities for the members of NGC 6025 with respect to field stars of the same types. These mean values were adopted from Abt & Morrell (1995) and Abt, Levato, & Grosso (2002). The extreme values of $v \sin\ i$ observed for cluster members are 10 km s^{-1} and 270 km s^{-1} for the minimum and maximum respectively. The cluster members seem to rotate with $73\% \pm 9\%$ of the rotation of field stars of same temperatures.

4. CONCLUSIONS

We have derived a distance of 912 pc for NGC 6025, somewhat larger than previous determinations. We have found two peculiar stars of the silicon type among its members. We found a Hg-Mn? peculiar object in the region but it is probably a non-member. We found that the average axial rotation of the main sequence cluster members of NGC 6025 is less than 75% of that of the field stars of the same temperatures. This may be due to the presence of spectroscopic binaries in a larger proportion than among field stars (see Abt 2009). A thorough spectroscopic study to determine the spectroscopic binaries among the upper main sequence of NGC 6025 is under way.

The CCD and data acquisition system at CASLEO has been partly financed by R. M. Rich through U.S. NSF grant AST-90-15827. This research was partially supported by a grant PIP1113 from the National Research Council (CONICET). We thank Richard Gray who provided the WINMK version 2.4 code. Our appreciation also to W. van Altena for making available to us the SPM4 Catalogue before publication. This research has made use of the WEBDA database, operated at the Institute for Astronomy of the University of Vienna. We appreciate very much the support of CASLEO personnel in the observing process.

REFERENCES

Abt, H. 2009, PASP, 121, 1307
Abt, H., Levato, H., & Grosso, M. 2002, ApJ, 573, 359
Abt, H., & Morrell, N. 1995, ApJS, 99, 135
Allen, C. W. 2001, in Allen's Astrophysical Quantities, ed. A. N. Cox (4th ed.; New York: Spring-Verlag), 387
Feinstein, A. 1971, PASP, 83, 800
Garrison, R. F., Hiltner, W. A., & Schild, R. E. 1977, ApJS, 35, 111
Girardi, L. O., Bressan, A., Bertelli, G., & Chiosi, C. 2000, A&A, 141, 371
González, J. F., & Levato, H. 2006, A&A, 448, 283
Gray, R., & Corbally, C. 2009, Stellar Spectral Classification (Princeton: Princeton Univ. Press)
Houk, N., & Cowley, A. P. 1975, Michigan Catalogue of Two Dimensional Spectral Types for HD Stars, Vol. 1 (Ann Arbor: University of Michigan)
Kharchenko, N. V., Berczik, P., Petrov, M. I., Piskunov, A. E., Rser, S., Schilbach, E., & Scholz, R.-D. 2009, A&A, 495, 807
Kilambi, G. 1975, PASP, 87, 975
Mermilliod, J. C. 1982, A&A, 109, 37
Morris, P. 1961, MNRAS, 122, 325
Paunzen, E., Duffee, B., Heiter, U., Kuschnig, R., & Weiss, W. W. 2001, A&A, 373, 625
Schaller, G., Schaerer, D., Meynet, G., & Maeder, A. 1992, A&AS, 96, 269
Slettebak, A., Collins, G. W., Parkinson, T. D., Boyce, P. B., & White, N. M. 1975, ApJS, 29, 137
van Leeuwen, F. 2007, Hipparcos the New Reduction of the Raw Data (New York: Springer)

Mónica Grosso and Hugo Levato: Instituto de Ciencias Astronómicas de la Tierra y del Espacio, Casilla de Correo 49, CP 5400, San Juan, Argentina (mgrosso, hlevato@icate-conicet.gob.ar).

Revista Mexicana de Astronomía y Astrofísica, **47**, 261–275 (2011)

WIND STRUCTURE OF THE WOLF-RAYET STAR EZ CMA=HD 50896

Aaron Flores,[1] Gloria Koenigsberger,[2] Octavio Cardona,[3] and Lelio de la Cruz[1]

Received 2011 March 22; accepted 2011 May 9

RESUMEN

Presentamos los resultados del análisis de la línea de N V 4604 observada en espectros de la estrella Wolf-Rayet HD 50896 obtenidos en 1991, 1999, 2005 y 2009. Mostramos que la variabilidad de esta línea es consistente con un modelo en el que la opacidad del viento sufre cambios cíclicos con un periodo de 3.76 d o bien con un modelo de un viento con estructura cuadrupolar donde cada sector tiene una opacidad distinta.

ABSTRACT

The Wolf-Rayet star HD 50896 (EZ CMa=WR6) is well-known for the emission-line profile variability that occurs on a 3.7-day timescale. In particular, the shape of the N V 4604-21 doublet changes from a P Cygni profile to one in which no blue-shifted absorption component is present. In this paper we use spectroscopic observations obtained in 1991, 1999, 2005 and 2009 to glean physical conditions within the stellar wind that may give rise to these changes. We find that variations in the opacity at a distance $r/R_{\rm max} \sim 0.3$–0.5 of the stellar surface can produce the observed effects. Here, $R_{\rm max}$ is the extent of the N V line-forming region. The results are consistent either with a scenario in which the opacity of the inner wind region of HD 50896 undergoes cyclical variations over the 3.76 d period or with a quadrupolar wind distribution in which the sectors having different opacities rotate in and out of our line-of-sight on this periodic timescale.

Key Words: stars: individual (EZ CMa = HD 50896) — stars: winds, outflows — stars: Wolf-Rayet

1. INTRODUCTION

Classical Wolf-Rayet (WR) stars (van der Hucht et al. 1981) are the evolved remnants of massive O-type stars and are believed to be the last stable evolutionary phase of a star before it explodes as a supernova or, possibly, a "collapsar" (Crowther 2007). The WR stars are often found in binary systems in which the companion is also a massive O-type star. Van den Heuvel (1976) noted that after the more massive star in a massive binary system has become a supernova, leaving a neutron star or black hole remnant, its companion should eventually become a WR star. Hence, a number of *WR+cc* systems should be observable at any given time. The WN5-type star HD 50896 (EZ CMa=WR6; van der Hucht et al. 1981) was the first WR star to be proposed to fit this evolutionary scenario. Firmani et al. (1979, 1980) detected periodic (P = 3.76 d) emission-line profile variability which, when combined with the fact that HD 50896 is surrounded by a ring nebula (S308) and that it lies high above the galactic plane[4], led them to conclude that HD 50896 is a binary system with a low-mass companion. Shortly thereafter, linear polarization (McLean 1980) and photometric (Cherepashchuk 1981) observations confirmed the P = 3.76 day periodicity. Subsequent period determinations by Lamontange, Moffat, & Lamarre (1986) and Georgiev et al. (1999) gave, respectively $P = 3.766 \pm 0.001$ d and $P = 3.765 \pm 0.001$ d.

Two criteria were used by Firmani et al. (1979, 1980) to determine the original period: (a) the shape of the He II 4686 line profiles, particularly the lo-

[1]Facultad de Ingeniería, Universidad Autónoma del Carmen, Campeche, Mexico.

[2]Instituto de Ciencias Físicas, Universidad Nacional Autónoma de México, Mexico.

[3]Instituto Nacional de Astrofísica Óptica y Electrónica, Puebla, Mexico.

[4]Suggesting it is a "runaway" system as a consequence of the supernova "kick".

cation of superposed emission-like spikes that were either at line center, or "blueward", or "redward" of this location; and (b) the strength of the N V 4604-21 P Cygni absorptions. Georgiev et al. (1999) showed that the variations in this high ionization N V doublet retained coherence over ∼14 years of observations, with a period $P = 3.765$ d. However, although the variability in other lines and in photometric data is always consistent with the 3.76 d period, it is often not coherent over timescales of several weeks or longer (Drissen et al. 1989). Hence, the binary nature of HD 50896 has been questioned.

Another problem with the *WR+cc* scenario for HD 50896 is the absence of significant X-ray variability. Stevens & Willis (1988) and Skinner, Itoh, & Nagase (1998) showed that the observed levels of X-ray emission were far too low to be attributable to accretion onto a neutron star or black hole. On the other hand, Skinner et al. (2002) concluded that the presence of a low-mass companion upon which the WR wind collides would be consistent with the low X-ray emission levels. Hence, the binary scenario is still a viable one. However, even under the binary hypothesis, a physical mechanism by which the line-profile variability occurs is still not identified.

In this investigation we focus on one of the physical mechanisms that may produce the observed line-profile variations in HD 50896. Specifically, we will analyze the N V 4604 line profiles in order to determine the type of wind structure variations that may produce the observed variability. In § 2 we describe the observations; § 3 contains a description of the N V variability; § 4 describes the line-fitting technique; § 5 contains a discussion; and § 6 the conclusions.

2. OBSERVATIONS

The new observations were carried out during three epochs in 1999, 2005 and 2009 (hereafter referred to as OGH I, OGH II and OGH III, respectively), with the 2.1 m telescope of the Observatorio Astronómico Guillermo Haro (OGH), using a Boller & Chivens spectrograph, with a 830 grooves mm^{-1} grating in the second order, and a slit aperture of 250 μm. A Schott BG18 blocking filter was placed at the slit entrance, thus removing light at $\lambda < 4000$ Å. For the first and second epochs, we used a CCD with a 1024×1024 Tek chip and for the third epoch a CCD with 1300×1300 BestArray chip. The reciprocal dispersion for the first and second epochs was 0.31 Å/pix, and the spectral window was $\lambda\lambda$4463–4778 Å, while for the third epoch, the corresponding parameters were 0.26 Å/pix, and $\lambda\lambda$4470–4810 Å.

Data reduction was performed using standard procedures in the Image Reduction and Analysis Facility (IRAF) version 2.14.1 package[5], which included bias subtraction, flat field correction, cosmic ray deletion, and wavelength calibration. The wavelength calibration was performed using a He-Ar comparison lamp, yielding an uncertainty of 0.34 Å in wavelength measurements for the OGH II and OGH III epochs. For the OGH I epoch, due to a problem with the comparison lamp spectrum, the wavelength calibration was deficient, leading to uncertainties twice as large. Individual spectra have S/N∼110 at the continuum level, with the average spectra per night having S/N $\sim \sqrt{n}110$, where $n = 3,...,35$ is the number of spectra averaged. The individual spectra were normalized to the continuum level after interpolating a third-order Legendre polynomial function to line-free spectral regions.

One of the noteworthy features of these observations is the fact that each set was obtained over seven or eight consecutive nights, thus covering two contiguous 3.76-day cycles. On each night, between 3 and 35 spectra were obtained within time intervals ranging from one to six hours. The three sets of data are comprised of 151 spectra. Table 1 contains the journal of observations. Column 1 lists the identification number of the spectrum, Column 2 the mean Julian Date −2445000, Column 3 the date of observations, Column 4 the number of spectra obtained over the night, Column 5 the timespan (in hours) over which these spectra were collected and Column 6 the phase computed with $P = 3.7650$ d and $T_0 = 2443199.53$ from Georgiev et al. (1999).

The above data sets were complemented with a set of nightly average spectra obtained in the Observatorio Astronómico Nacional San Pedro Mártir (SPM) during 1991 January (Piceno 2003; Vázquez 2003; Morel et al. 1998; Georgiev et al. 1999). The date of observation, number of spectra averaged, and nightly timespan covered by these spectra are listed in Table 2. The SPM data set covers 13 consecutive nights. Only one spectrum was obtained on nights "a" and "d" due to bad weather; the first of these is a useful spectrum having S/N ∼ 100. On night "d" the spectrum has S/N ∼ 35 and was not used for the analysis presented in this paper. This set provides spectra for three consecutive cycles in the 3.76 d period.

[5]IRAF is distributed by the National Optical Astronomy Observatory, which is operated by the Association of Universities for Research in Astronomy, Inc., under cooperative agreement with the National Science Foundation.

TABLE 1

JOURNAL OF OBSERVATIONS FOR THE OGH SPECTRA AND LINE FIT PARAMETERS[a]

ID	JD	Day	n	Δt	ϕ	$V_{\max}$	X_0	X_1	R_1	X_2	R_2	X_3	R_3	X_4	Type
OGH I (Jan-Feb 1999)															
b24	1202.80	24	9	1.0	0.71	40	0.1	90	1.25	380	1.90	210	3.1	10.	a
b25	1203.73	25	35	6.0	0.96	34	0.1	40	1.38	370	2.10	160	2.9	10.	a
b26	1204.82	26	3	0.5	0.25	34	0.1	45	1.25	320	2.00	180	2.6	10.	a
b27	1205.71	27	25	5.0	0.48	40	0.1	45	1.45	710	2.00	60	2.7	0.1	s
b28	1206.76	28	15	2.0	0.76	34	0.1	50	1.25	310	1.90	220	2.4	70	a
b30	1208.70	30	19	2.7	0.28	38	0.1	40	1.30	410	1.88	180	2.95	60	a
b31	1209.70	31	10	2.0	0.54	42	0.1	45	1.30	640	1.90	40	2.7	0.1	s
b2	1211.70	02	35	6.0	0.07	38	0.1	46	1.40	500	2.00	70	3.0	0.1	w
OGH II (Nov 2005)															
n19	3693.84	19	8	1.0	0.37	34	20.	50	1.35	320	1.9	140	3.1	50.	a
n20	3694.96	20	10	2.7	0.64	36	0.1	55	1.30	360	1.95	75	2.7	0.1	w
n21	3695.97	21	15	2.2	0.91	35	20.	50	1.25	370	1.85	110	3.1	50.	a
n22	3696.98	22	20	5.0	0.17	40	0.1	45	1.40	650	1.85	20	2.7	0.1	s
n23	3697.96	23	7	1.0	0.44	35	0.1	50	1.25	270	1.70	140	3.8	50	a
n24	3698.95	24	5	1.0	0.70	33	0.1	60	1.35	340	1.95	33	2.9	80	w
n25	3699.98	25	10	2.7	0.97	33	0.1	40	1.40	400	2.20	93	2.9	0.8	w
n26	3700.87	26	20	5.0	0.21	40	0.1	45	1.40	700	1.85	8	2.7	0.1	s
OGH III (Feb 2009)															
d02	4864.82	02	15	1.0	0.36	33	0.1	60	1.46	400	2.05	73	2.9	0.1	w
d03	4865.74	03	20	2.7	0.60	38	0.1	43	1.40	520	2.00	40	2.7	0.1	s
d04	4866.77	04	14	2.2	0.88	34	0.1	60	1.30	280	1.90	140	2.8	40	a
d05	4867.75	05	22	5.0	0.14	38	10.	60	1.40	420	1.80	90	2.8	1	w
d06	4868.77	06	20	1.0	0.41	36	10.	60	1.39	400	2.0	60	3.0	0.1	w
d07	4869.78	07	15	1.0	0.68	35	0.1	45	1.40	400	2.00	45	2.7	0.1	s
d08	4870.71	08	6	2.7	0.92	34	0.1	60	1.38	250	1.80	110	3.0	60	a

[a]Mean Julian dates (−2450000) for the time interval (Δt) over which the data n spectra were collected. Phase (ϕ) is computed with the Georgiev et al. (1999) ephemeris. The fit parameters are described in the text. For all cases, $R_{\max} = 4.2\ R_*$, $R_a = 3.9\ R_*$ and $V_{\rm th} = 50$ km s^{-1}.

TABLE 2

JOURNAL OF OBSERVATIONS FOR THE SPM SPECTRA AND LINE FIT PARAMETERS[a]

ID	JD	n	Δt	Phase	$V_{\max}$	X_0	X_1	R_1	X_2	R_2	X_3	R_3	X_4	Type
a	280.9	1	–	0.63	36	0.1	47	1.21	410	2.02	30	2.9	0.1	s
b	281.8	22	4.5	0.87	37	0.1	59	1.40	510	2.05	18	3.0	0.1	s
c	282.8	34	6.1	0.14	34	0.1	90	1.40	250	1.95	130	3.2	9	a
e	284.8	30	5.7	0.67	31	0.1	10	1.20	330	2.2	58	2.9	1	w
f	285.8	22	5.1	0.93	37	0.1	67	1.36	460	2.02	20	2.8	0.1	s
g	286.8	32	4.9	0.20	34	0.1	90	1.27	220	1.85	130	3.2	9	a
h	287.8	35	4.5	0.47	31	0.1	30	1.30	290	2.1	78	2.9	1	w
i	288.7	7	0.6	0.70	31	0.1	30	1.40	340	2.2	58	3.0	1	w
j	289.8	34	5.5	0.00	35	20	51	1.35	390	2.12	37	2.8	0.1	s
k	290.7	7	3.4	0.24	34	0.1	90	1.35	260	1.7	120	3.5	9	a
l	291.8	40	4.4	0.53	31	0.1	30	1.40	340	2.24	60	3.0	1	w

[a]Mean JD's are −2448000. Other parameters as in Table 1.

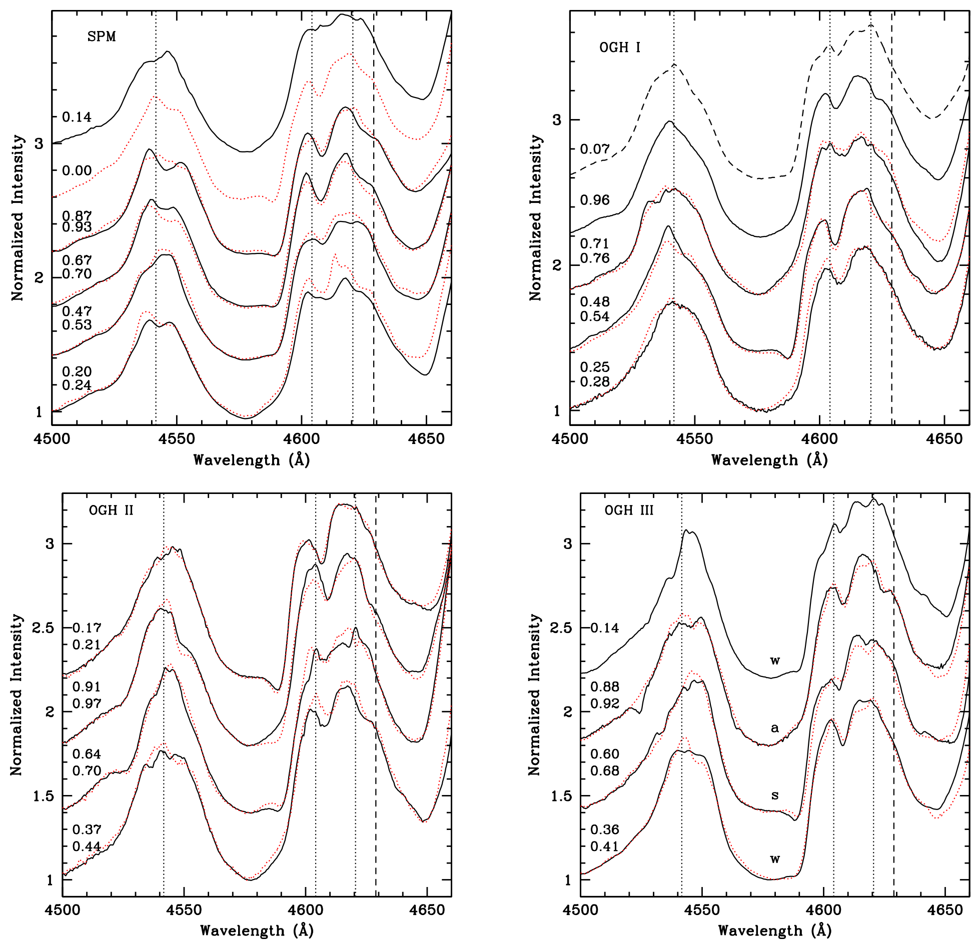

Fig. 1. Spectra from 1991 (SPM; top left), 1999 (OGH I; top right), 2005 (OGH II; bottom left) and 2009 (OGH III; bottom right). Spectra from the first 3.76 d cycle are shown with a continuous line, those from the second cycle are shown with dots, with spectra of similar orbital phases having the same vertical shift in the plot. Orbital phases with the Georgiev et al. (1999) ephemeris are listed. Vertical dotted lines indicate laboratory wavelengths of He II 4541.59, N V 4604.14 and N V 4620.50; the dashed line marks the location of O V 4628.87, a possible contributor to the blend. The letters *s*, *w* and *a* in the OGH III panel label the type of P Cygni absorption (see text). The color figure can be viewed online.

3. N V LINE-PROFILE VARIABILITY

Figure 1 shows the spectral region containing the He II 4542 and the N V 4604-21 doublet for the four epochs of observations. Spectra are displaced vertically to allow a clear view of their characteristics at different phases. Given that the observations of all four epochs were carried out over at least two 3.765 d cycles, two spectra per epoch at similar phases are generally available. The spectrum from the second cycle is plotted with dots. Phases were computed using the Georgiev et al. (1999) ephemeris and are listed.

The variations in the N V 4604-21 doublet can be described primarily in terms of the occasional presence of a prominent P Cygni absorption component which at other times is absent, and an intermediate state in which the absorption is weak. Although the same type of variability is present in all epochs, a comparison of the four panels in Figure 1 leads to the conclusion that a particular profile shape does not always appear in the same 3.76 d phase interval. For example, the P Cygni absorption component is strong at $\phi \sim 0.9 - 1.0$ in the SPM data, at $\phi \sim 0.5$ in the OGH I data; at $\phi \sim 0.2$ in the OGH II data, and $\phi \sim 0.6 - 0.7$ in the OGH III spectra. Hence, the presence of a strong P Cygni absorption does not correlate with phase for spectra separated in time by a few years, as are our data. However, on timescales of less than a couple of weeks, a phase-dependence does exist.

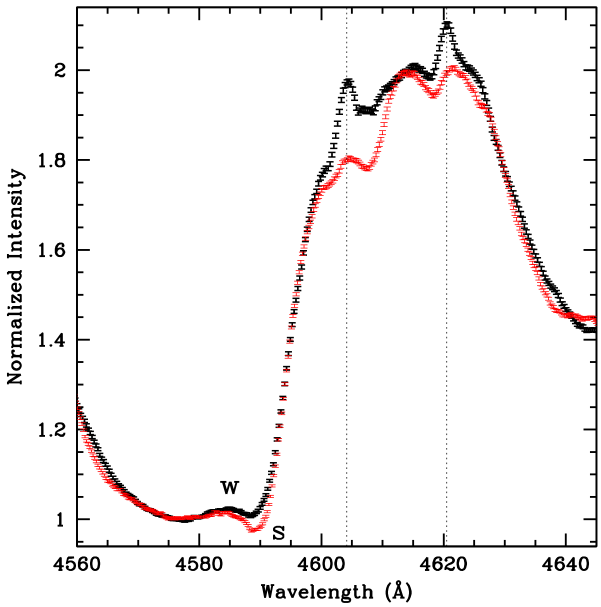

Fig. 2. Comparison between spectrum n20 and spectrum d07 illustrating the difference between the *weak* (w; black) and *strong* (s; red) types of absorption in N V 4604. Error bars indicate the uncertainties associated with each spectrum, as determined from the corresponding S/N ratios. The color figure can be viewed online.

TABLE 3

DAY-TO-DAY P CYGNI TYPE FOR EACH EPOCH[a]

Epoch	Type										
1991	s	s	a	-	w	s	a	w	w	s	a	w
1999	-	-	a	a	a	s	a	-	a	s	-	w
2005	-	-	a	w	a	s	a	w	w	s	-	-
2009	-	-	-	-	w	s	a	w	w	s	a	-

[a]Each entry of the table corresponds to one night of observations, and they are listed sequentially starting at the left with the first night of data. The letters indicate whether the N V 4604 profile has a *strong*, *weak* or *absent* P Cygni absorption component. The nights of each epoch have been aligned so that the *s* spectra all lie along the same columns. A dash indicates no data available for the given night.

We assign a classification of *strong*, *weak*, or *absent* to the type of line-profile observed. The distinction between the three types of profiles is most clearly seen at λ 4590 Å in Figure 1. The *weak* profiles have intensities that are very close to the continuum level, the *strong* profiles are below the continuum, and the *absent* profiles lie significantly above it. The continuum level lies at intensity level unity, by definition from the spectrum normalization process. Examples of the *strong* and the *weak* type profiles are shown in Figure 2. In Tables 1 and 2 each spectrum has been characterized with the letters *s*, *w* or *a* in accordance with this classification. Using this description for the N V profiles, the day-to-day variability pattern of the four epochs may be compared. Table 3 illustrates this variability pattern for each epoch individually (the different rows) and for the entire set by aligning the first *s* spectrum of the OGH data sets with the second *s* of the SPM set in the same column. Table 3 shows that the four epochs follow the same sequence that repeats with the 3.76 d period: $s \rightarrow a \rightarrow w/a \rightarrow a/w$, where a/w and w/a indicate that either a or w are present in the column.

Figure 1 also shows that part of the variability is due to the appearance of narrow emission peaks. A clear example of such features at the rest wavelength of He II 4642, N V 4604 and N V 4621 can be seen in the phase interval 0.64–0.70 of the OGH II spectra (see also Figure 2). Thus, in addition to the changing P Cyg absorption, the line-profile variability involves the presence of narrow, superposed emissions. The fact that they are located at the laboratory wavelength indicates that they originate in material that is flowing perpendicular to our line-of-sight.

Figure 3 again shows the spectral region containing He II 4542 and the N V 4604-21 doublet for the four epochs of observations. In this case, the first spectrum plotted from bottom to top is the first spectrum in the series having a *strong* N V 4604 P Cygni absorption component. In the SPM data set, we chose spectrum 'b' of the series because on night 'a' only 1 spectrum was obtained[6]. The second spectrum from bottom up, plotted with a +0.5 shift in the intensity scale, is the one obtained during the following night of observation; the third and fourth spectra correspond to the subsequent 2 nights, each with a corresponding additional +0.5 shift in the intensity scale. The fifth spectrum of the series is overlaid with the first, this time with a dotted line instead of a continuous line; similarly, with the following spectra of the series. This figure confirms the similarity between the four epochs' N V line profile variabiity, but it also shows that small changes in the line shapes are present for spectra of similar phases separated by a single 3.76 d cycle. The magnitude of these small changes may be evaluated from the ratios

[6]We do note, however, that spectrum 'a' has an *s*-type profile which apparently breaks the pattern described above.

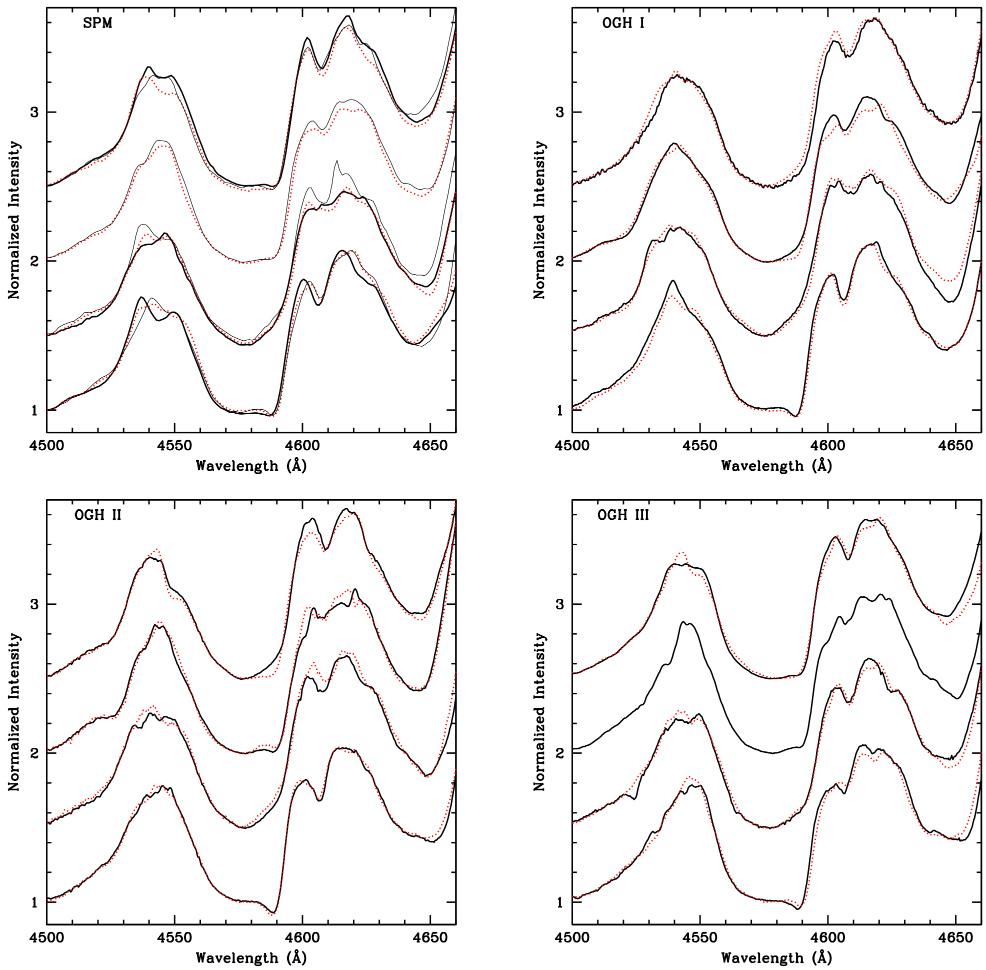

Fig. 3. Data from SPM (top left), OGH I (top right), OGH II (bottom left) and OGH III (bottom right) as in Figure 1 but here the spectra lying lowest in each plot are those in which N V 4604 has a *strong* P Cygni absorption component. Subsequent spectra stacked vertically correspond to the following nights of observation. Spectra of similar phases from contiguous cycles are superposed using different line types: the first cycle is plotted with thick lines, the second cycle with dots and the third cycle with thin lines. The *strong*-type profiles are always followed on the next night by an *absent*-type profile. The color figure can be viewed online.

of the spectra, and, for example, the changes seen in the OGH II spectra at phases 0.91 and 0.97 at 4585–4610 Å region lie in the range ∼5–8%. Given that S/N $\sim 110n^{1/2}$ in these spectra and that each of the spectra is the average of $n > 5$ individual exposures, most of these changes are well above what would be expected from random fluctuations.

4. LINE FITTING PROCEDURE

The periodic line profile variations can be interpreted within three general scenarios. The first is one in which the intrinsic wind structure of the WR star changes over the 3.76 d period; in the second scenario, it is anisotropic, for example, having quadrants with different velocity gradients or ionization fractions. In the third scenario, the inner portions of the wind have a stationary structure, but the outer regions do not, either because of some intrinsic instability or because of the perturbation from a companion. In this paper we focus on the first interpretation because it is the one that requires the smallest number of assumptions.

The line-profiles were modeled using the radiation transfer code described by Auer & Koenigsberger (1994). This is a simple code which computes the line profile produced in a wind having either a linear or a β-velocity law and an opacity distribution with arbitrary characteristics. The algorithm assumes spherical symmetry and uses the

TABLE 4

DESCRIPTION OF INPUT PARAMETERS FOR LINE FITS[a]

Parameter	Value	Description
$R_{\rm max}$	4.2	Maximum extent of line-forming region, in units of R_*
$V_{\rm max}$	–	Terminal wind speed, in units of $V_{\rm th}$
$V_{\rm th}$	50	Thermal velocity, in km s^{-1}
R_a	3.9	Extent of linear acceleration region, in units of R_*
R_i	–	Radius of the *i-th* region
X_0	–	Opacity parameter at R_*
X_i	–	Opacity parameter at R_i

[a]In Column 2 we list the values of those parameters that were held constant.

Sobolev approximation only in those portions of the wind where the approximation is valid. Where the Sobolev approximation breaks down (i.e., where the wind velocity gradient is small compared to the local Doppler velocities) it computes the radiative transfer precisely. A description of the input parameters is given in Table 4. The line is assumed to arise in a region whose maximum extent is $R_{\rm max}$. In the linear approximation, R_a is the distance over which the velocity increases; and R_i, with $i = 1,2, ...,n$ are the radii of regions within the wind having different opacities. All distances are given in units of the stellar radius, R_*, which is the hydrostatic radius. The opacity in the different regions is parametrized with the opacity factor, X, which is a nondimensional parameter that enters into the line-profile calculation through the optical depth, τ, defined as

$$\tau = \int \frac{X(r)}{[v(r)/v_{\rm th}](r/R_*)^2}\varphi[x - v_z(z)]d(z/R_*), \quad (1)$$

where $v(r)$ is the wind velocity law, $v_{\rm th}$ is the Doppler velocity, v_z is the projection of the wind velocity along the line of sight from the star to the observer in Doppler units, φ is the line profile function, x is the non-dimensional line frequency, and z is the coordinate along the line of sight. The maximum speed attained in the line-forming region is $V_{\rm max}$. It is specified in the code in units of $v_{\rm th}$.

The code allows the value of $X(r)$ to be specified for an arbitrary number of radial positions within the line-forming region. We represent its different values as X_i for the corresponding regions R_i. Note that by defining wind regions R_i with different X_i values, we are assuming that the excitation and/or ionization structure can change with distance from the stellar core.

Our analysis will be restricted to the "blue" wing of the N V 4604 line because its P Cygni absorption component is formed in the column of wind material that lies along the line of sight from the observer to the continuum emitting core. Hence, it describes the behavior of wind material whose location is constrained, thus simplifying the interpretation. In addition, it is not contaminated by other lines. This is unlike its centrally-located emission which is blended with the P Cygni absorption produced by the neighboring N V 4620 Å doublet member.

We used a linear velocity law of the form $v(r) = v_0 r$ because a standard β-velocity law failed completely to describe the observed line profiles. A β-law predicts a strong and sharp P Cygni absorption at the wind terminal speed ($\sim$1900 km s^{-1}) which is not observed. This problem can be avoided if the line opacity goes to zero in the region where the wind velocity tends asymptotically to v_∞. Hence, we opted to use a velocity law in which the wind accelerates linearly up to R_a, and then expands at a constant speed thereafter. The form of the velocity law in the code is $v(r) = V_{\rm max} r/R_a$, so the velocity at the stellar surface is $v(R_*) = V_{\rm max}/R_a$.

We chose to fix the value of $R_{\rm max} = 4.2$ based on the deduced ionization structure of HD 50896's wind from Hillier (1988; Figure 2) which shows that this is the extent of the region where the abundance of NV dominates over that of N IV. We also fixed $v_{\rm th} = 50$ km s^{-1}. This value was chosen in part because the ionization potential of NV is 98 eV which, under equilibrium conditions, corresponds to a thermal speed of 37 km s^{-1}, and in part because the code does not include turbulent broadening in the calculation and the added velocity serves to increase the Sobolev length accordingly. Since the velocities are given in units of $v_{\rm th}$, the product $V_{\rm max}\, v_{\rm th} = v_\infty$ is constrained by the observations. We also fixed the value of the acceleration radius, $R_a = 3.9\ R_*$.

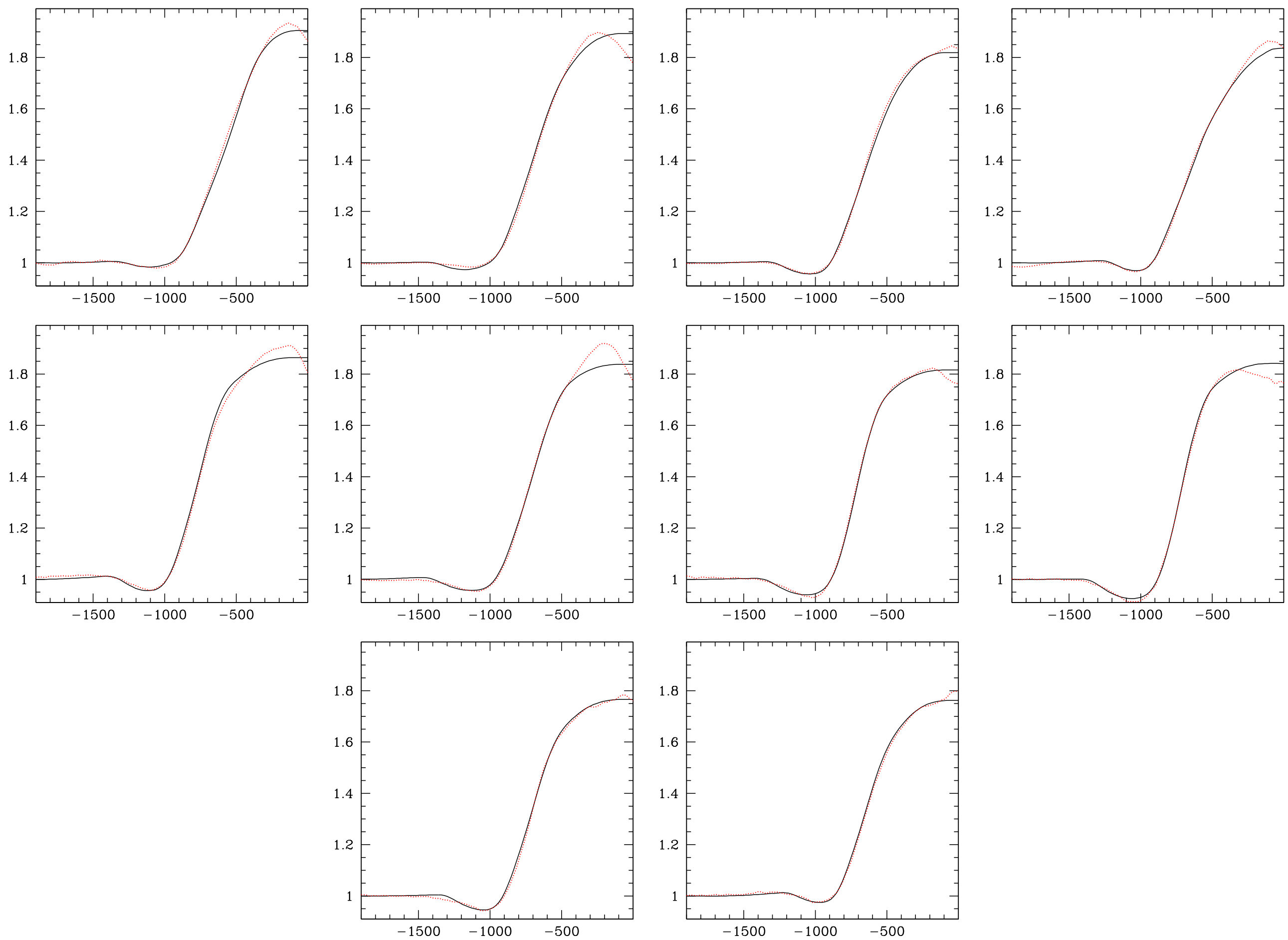

Fig. 4. Comparison of model calculations of the N V 4604 blue wing with the observations (dots) for the *strong* profiles. From left to right and from top to bottom: a, b, f, j, b27, b31, n22, n26, d03, d07. The abscissa is velocity in km s^{-1} with respect to the rest wavelength of N V 4604, the ordinate is normalized intensity. The color figure can be viewed online.

Values smaller than this lead to a sharp, blueshifted absorption component originating in the wind region that is moving at V_∞, and these absorptions are not present in the observations.

It is important to note that, with the above parameters fixed, there are different combinations of $V_{\rm max}$, X_i and R_i which lead to very similar model line profiles. Thus, the line fits of Figures 4–6 are not unique. However, once $v_{\rm th}$ is specified, $V_{\rm max}$ is constrained to values that are consistent with V_∞. Once $V_{\rm max}$ is fixed, the blue wing of the line profile is extremely sensitive to the values of X_2, X_3, R_2, and R_3 and we are unable to find different combinations of these parameters which yield the same line-profile.

The detailed shape of the P Cygni profile depends strongly on the velocity gradient and on the opacity within the accelerating region. After numerous experiments, we found it necessary to define at least three sub-regions within the accelerating region of the wind, each having different opacities. Keeping $R_{\rm max} = 4.2\ R_*$, $R_a = 3.9\ R_*$ and $v_{\rm th} = 50$ km s^{-1} constant, we fitted each line individually in an iterative manner by varying only the values of X_i, R_i and $V_{\rm max}$. As noted above, $V_{\rm max}$ is limited by the terminal wind speed, so the range of values over which it can be varied is not very broad. However, it is important to note that a small variation in $V_{\rm max}$ modifies the velocity gradient and, hence, the Sobolev optical depth. Thus, variations in $V_{\rm max}$ that are within the uncertainties of the measured V_∞ lead to noticeable differences in the line profiles.

In general, a good fit was achieved after $\sim$30 iterations. A second pass on the entire set of profiles, with $\sim$10–20 iterations each, yielded model profiles that differed from the observations within the noise

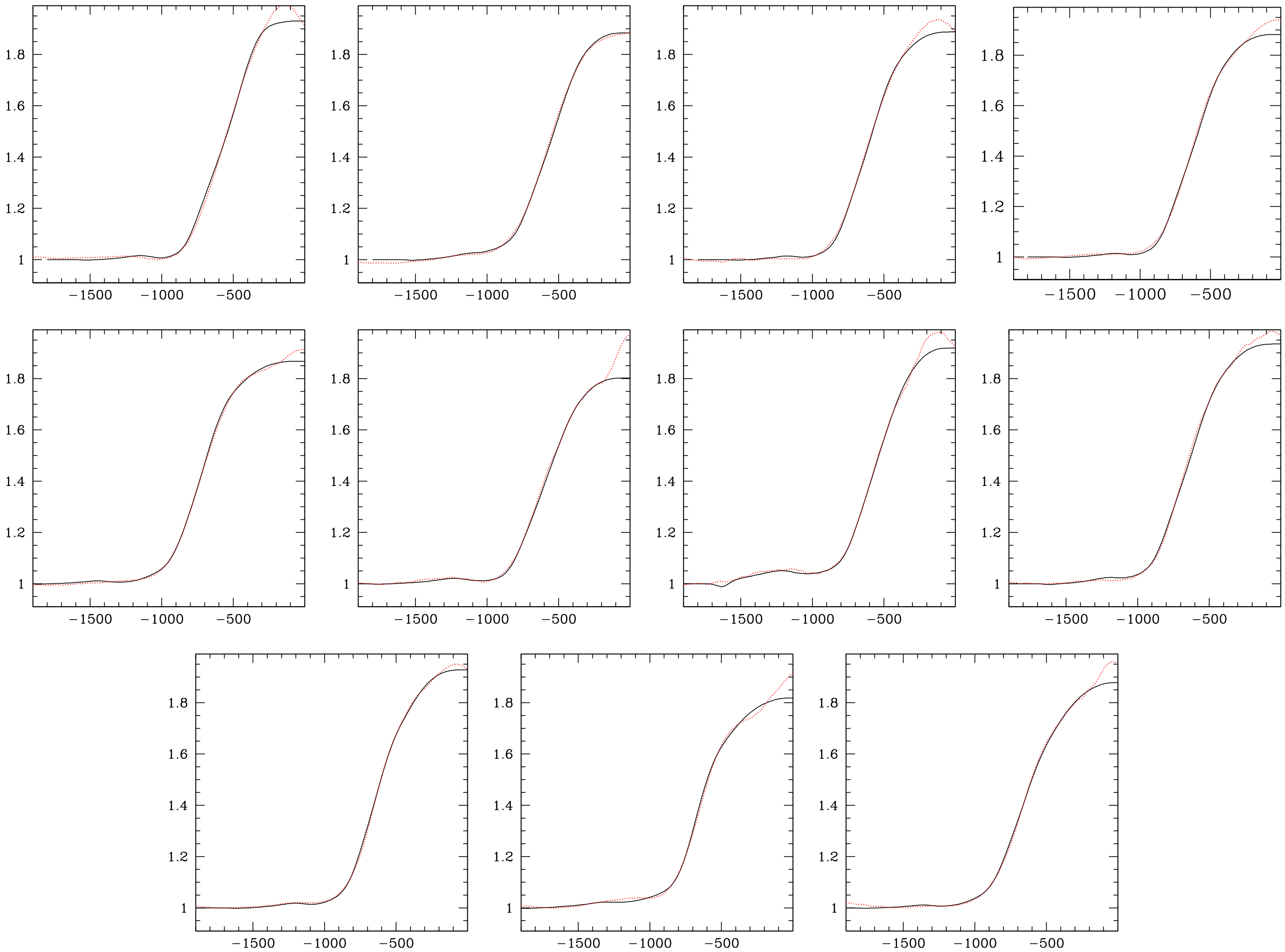

Fig. 5. Same as previous figure for the *weak* profiles. From left to right and top to bottom: e, h, i, l, b2, n20, n24, n25, d02, d05, d06. The color figure can be viewed online.

levels. The results are illustrated in Figures 4, 5, 6, where we grouped the profiles according to whether the P Cygni absorption is strong, weak or absent, respectively. In all cases, the fit to the blue wing, including the P Cyg absorption is excellent. We did not attempt to fit the centrally-located emission because it has contributions from the neighboring N V 4620, and it would be necessary to model the line transfer in the doublet. Thus, the model does not generally fit the observations around the emission maximum[7].

We examined the uncertainty in the model fits by determining the change in the input parameters needed to produce a difference of 3% in the profile with respect to the best fit model. In Figure 7 we plot the best-fit model for spectrum *n22* and the results obtained by changing the $V_{\rm max}$, X_i and R_i input parameters one at a time. The range in these parameters is $V^0_{\rm max} \pm 1.2$, $X^0_i \pm 10$, and $R^0_i \pm 0.05$, where the 0-superindex indicates the best-fit values.

The optical depth along any ray depends on both the projected velocity gradient and the opacity at each particular line-of-sight velocity component. Hence, it is *a priori* difficult to determine the effects of modifying each of the free parameters of the calculation. Within the parameter space listed in Table 4, only a a few guiding rules were found during the line-fitting process. For example, the slope of the line profile within the velocity range -800 to -200 km s^{-1} is strongly influenced by the choice of R_2. The location and strength of the P Cygni absorption component is determined to a large extent by the values of $V_{\rm max}$, X_3 and R_3. Increasing the

[7]It is interesting to note, however, that the model generally under-predicts the emission intensity, consistent with the fact that the contribution from the N V 4620 emission will add on to the λ4604 emission and approach the value of the observed intensity.

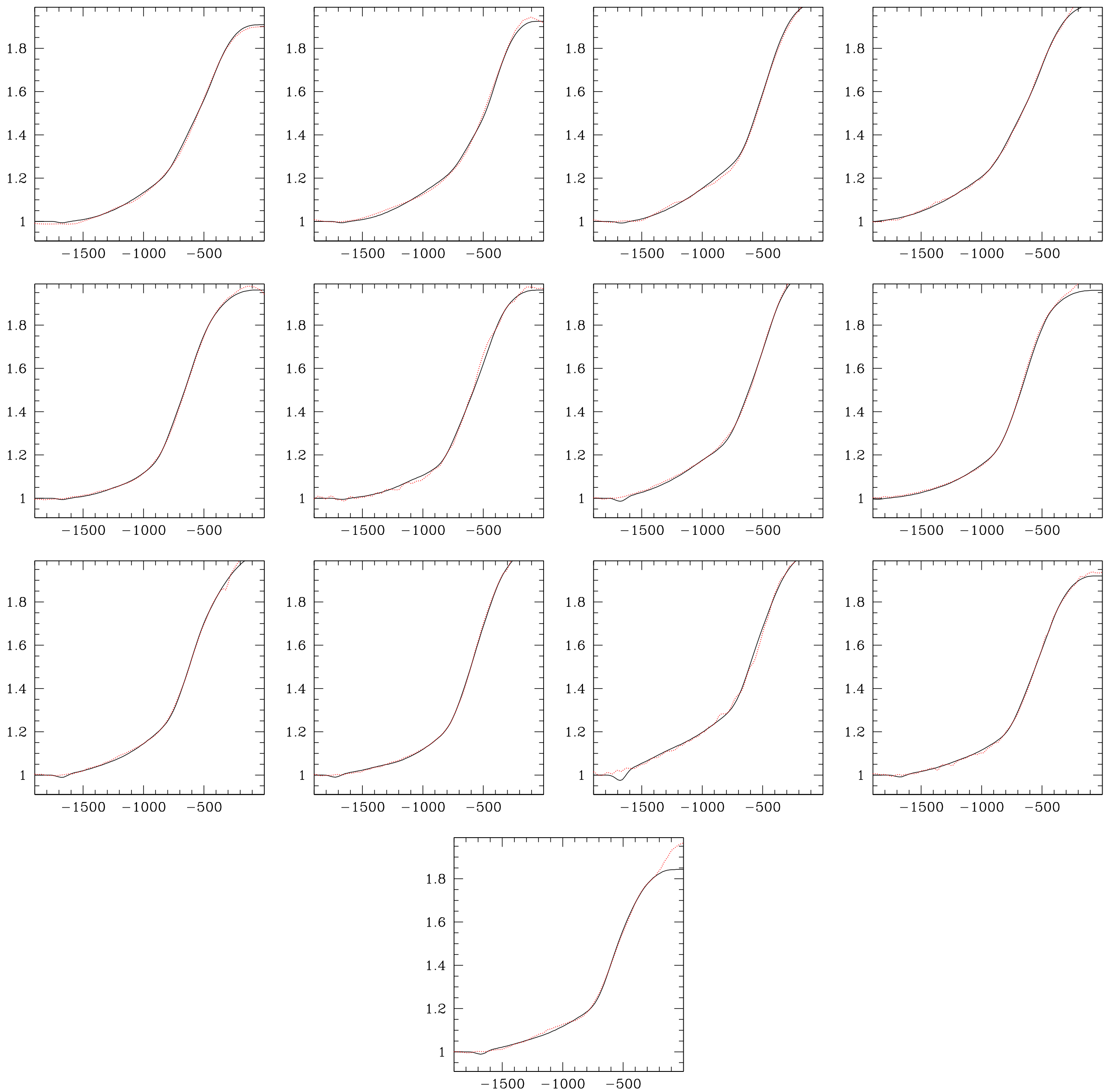

Fig. 6. Same as the previous figure for the *absent* profiles. From left to right and from top to bottom: c, g, k, b24, b25, b26, b28, b30, n19, n21, n23, d04, d08. The color figure can be viewed online.

value of X_3 and X_4 leads to an overall increase in the line strength. Changing the value of R_1 affects the strength of the emission component at small line-of-sight velocities. The values of X_0 and X_1 need to be smaller than that of X_3 to keep the line from being too strong at small velocities.

The input parameters that yielded the best fit to the P Cygni absorption of each spectrum are listed in Tables 1 and 2. The four regions into which the wind was divided are identified by their maximum extent, R_i, $i = 1,..,4$. The results of the fits provide the values of R_i and their corresponding X_i values. The first region extends from R_* to R_1, where $0.30 \leq R_1/R_{\rm max} \leq 0.35$. The second region extends to R_2, where $0.43 \leq R_2/R_{\rm max} \leq 0.52$. The third region extends to R_3, where $0.57 \leq R_3/R_{\rm max} \leq 0.74$. The fourth region extends to $R_{\rm max}$ and includes the portion of the wind that expands at a constant speed.

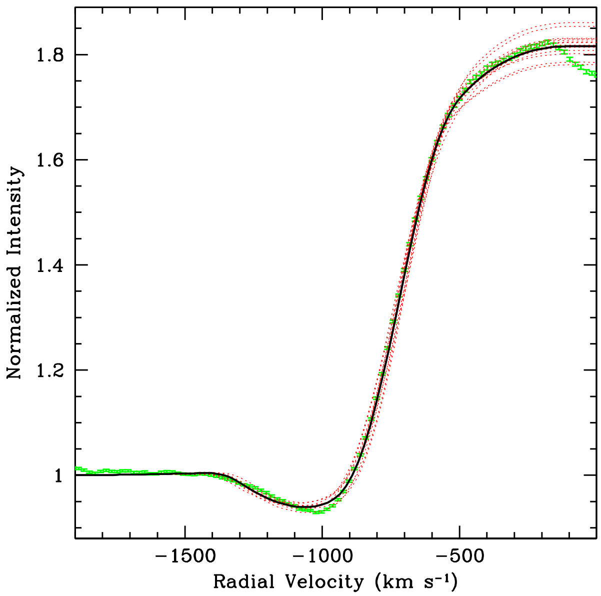

Fig. 7. Effects of changing the input parameters, one by one, on the shape of the line profile. The thick continuous line is the best-fit model. Dotted lines are the models with a different value for one of the following input parameters: $V_{\rm max}$, X_1, X_2, X_3, R_1, R_2, R_3. The observed spectrum (n22) is plotted as individual (green) points with error bars corresponding to S/N$\sim$490. The "dip" in the observed line profile at $\sim$0 km s^{-1} is the P Cyg absorption component of the neighboring N V 4620 Å line. The color figure can be viewed online.

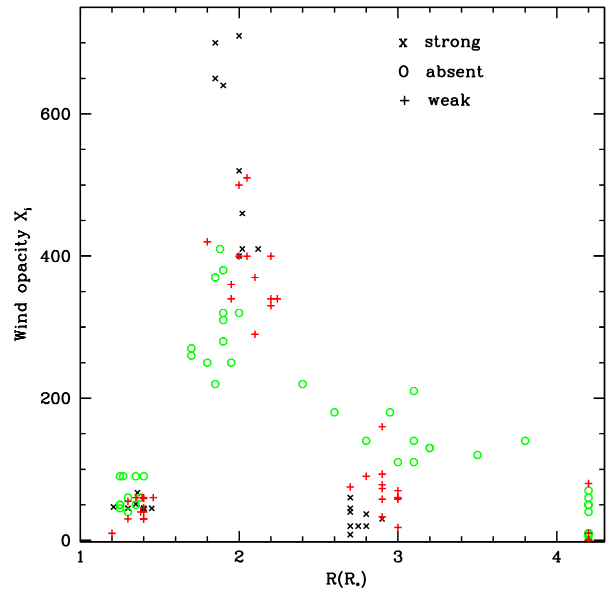

Fig. 8. Opacity parameter values (X_i, i = 1, 2, 3, 4) and their corresponding wind regions(R_i) derived from the line-profile fits. The different symbols indicate the different types of profiles: cross (s), plus sign (w) and circle (a). The color figure can be viewed online.

5. WIND STRUCTURE

Figure 8 shows the plot of the opacity parameter values, X_i, and the corresponding radial extent, R_i, derived from the line fits. The different symbols correspond to the three types of line profiles, *strong*, *weak* and *absent*, which henceforth will be referred to as s, w and a. The first noteworthy feature of this plot is that the opacity is, in general, small within the region closest to the star, $\sim$1.5 R_*. This is consistent with the NV/NVI $\ll$ 1 abundance ratio in the innermost wind region (Hillier 1988; Figure 2). The opacity then rises significantly in R_2, and then declines again in R_3 and R_4. Thus, the dominant opacity involved in the formation of the N V 4604 line is that of the wind material located in the R_2 region, but with the a profiles having a significant contribution from material in R_3. The second feature is the marked difference in the behavior of the opacity factor in the a profiles from that of the s/w profiles. The former have smaller values of X_2 and larger values of X_3 than the latter.

Given that similar profiles may be obtained with different combinations of $V_{\rm max}$, X_i and R_i, a second set of model fits was computed with $V_{\rm max}$ = const = 40, in order to illustrate the impact on the results. The fits were performed for the s and a profiles, since the w profiles are intermediate between these two. Figure 9 illustrates the difference between the results obtained above leaving $V_{\rm max}$ as a parameter to be fit (left) and holding $V_{\rm max}$ constant (right). The clear separation of the X_i, $i = 1, 2$ values for the s and a profiles persists as does the trend for a larger average value of R_3 in the a profiles.

We now examine the 3.76 d phase dependence of the model fit parameters. In Table 3 we listed the night-to-night sequence of profile types for each epoch of observations. Table 5 shows the same description as Table 3, but the letters s, a, w are here listed in sets of four, corresponding to four consecutive nights of observation (Columns 2–5). In this representation it is evident that for each epoch the profile shape cycles through the type s (day 1), a (day 2) and w/a (days 3 and 4), where w/a means either a w or an a type. Columns 6–10 and 11–14 of Table 5 list the corresponding values of the opacity parameters X_2 and X_3, respectively, in the same representation of sets of four nights. For each epoch, the column corresponding to the s profiles has the largest X_2 value and smallest X_3 value. This table clearly shows the 3.76 d cyclical pattern for

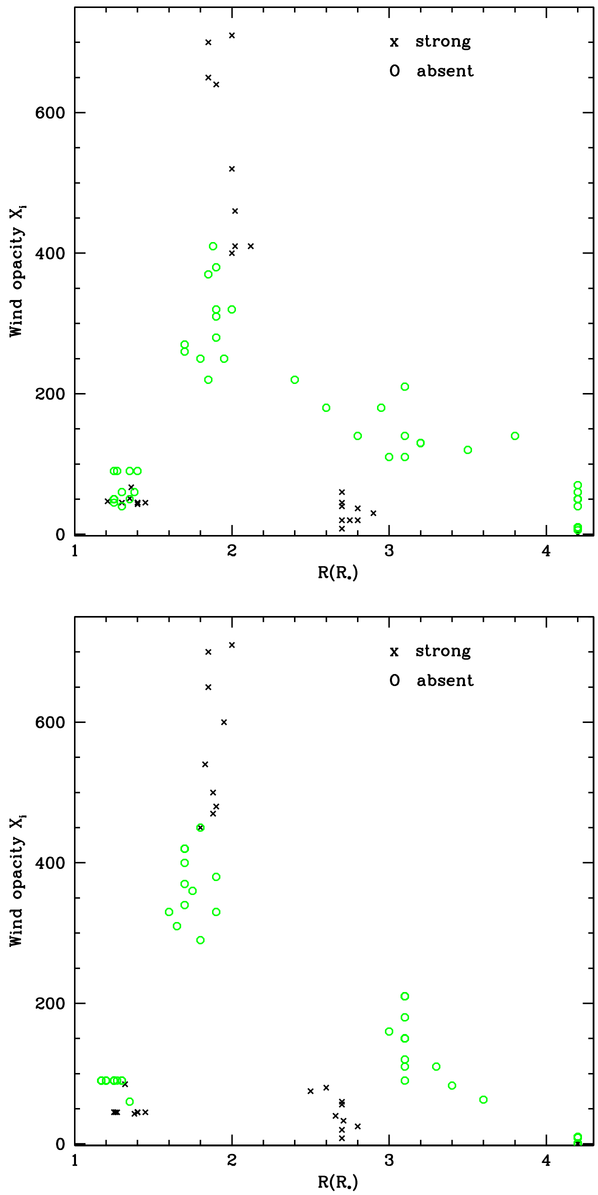

Fig. 9. Top: Same as previous figure, but showing only the values for the *s* and *a* profiles. Bottom: the same information, but this time from the model runs in which $V_{\max}$ was held constant and the fits were performed for only the X_i and R_i values. The color figure can be viewed online.

each epoch, which is also illustrated in Figure 10. Phases were all computed with the same ephemeris from Georgiev et al. (1999). This figure also shows that the phases of maximum X_2 and the amplitude of the variations differ from epoch to epoch. There is no significant difference in this figure if we plot the results obtained from the fits where $V_{\max}$ was held constant.

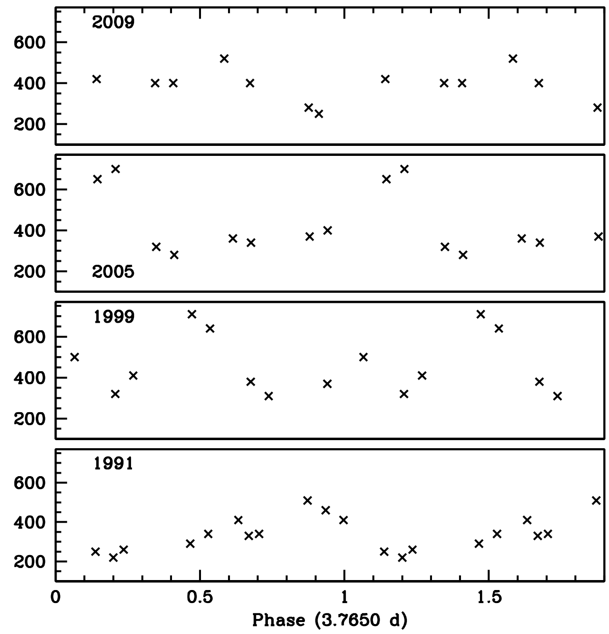

Fig. 10. Opacity parameter X_2 from the line-fits plotted as a function of 3.7650 d phase for each of the 4 observation epochs. A modulation is present in each epoch, but it is not coherent from one opoch to the next. Same data are plotted twice.

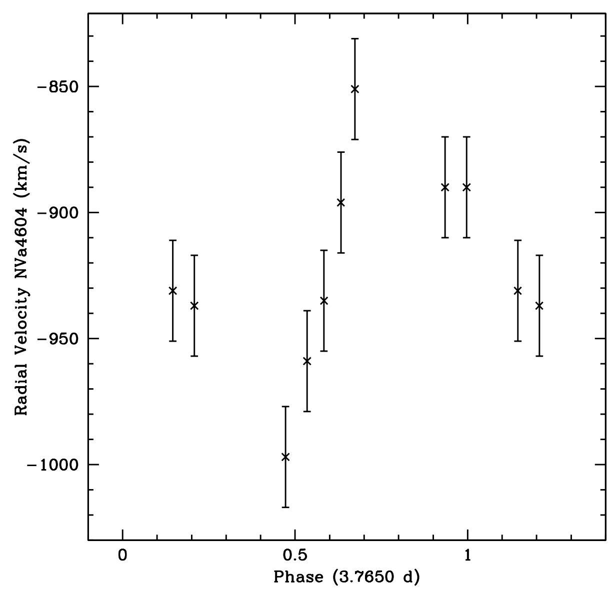

Fig. 11. Radial velocity variations of the N V 4604 P Cygni absorption component in the *strong* profiles plotted as a function of the 3.7650 d phase. A coherent variation over the 18 years of observations covered by these spectra is present.

TABLE 5

PROFILE TYPES IN GROUPS OF FOUR[a]

Epoch	Type				X_2				X_3			
	s	a	–	w	510	250	–	330	18	130	–	58
1991	s	a	w	w	460	220	290	340	20	130	78	58
	s	a	w	–	390	260	340	–	37	120	60	–
	–	a	a	a	–	380	370	320	–	210	160	180
1999	s	a	–	a	710	310	–	410	60	220	–	180
	s	–	w	–	640	–	500	–	40	–	70	–
	–	a	w	a	–	320	360	370	–	140	75	110
2005	s	a	w	w	650	270	360	400	20	140	33	93
	s	–	–	–	700	–	–	–	8	–	–	–
	–	–	–	w	–	–	—	400	–	–	–	73
2009	s	a	w	w	520	280	420	400	20	140	90	60
	s	a	–	–	400	250	–	–	45	110	–	–

[a]Columns 2–5: Same information as given in Table 3 but here organized in sets of four sequential nights per row. For all epochs there is a sequence: *s* (day 1) → *a* (day 2) → *w/a* (days 3 and 4). Second block of 4 columns: opacity parameter X_2 from the line fits; third block of 4 columns: opacity parameter X_3.

Given the above results we are led to conclude that the wind cycles through different opacity states over the 3.76 d period. These different states may be due to variations in the excitation/ionization structure or in the mass-loss rate, or a combination of the two. Such variations could be a consequence of pulsations in the underlying core. Piceno (2003) found periodic variation in the equivalent width of He II 4541 on timescales of 0.023 d, 0.044 d and 0.43 d on different nights of observation in the 1991 SPM data set, but not in the whole set of data, thus leaving an open question on the presence of possible non-radial pulsations. The precise mechanism by which the pulsations couple to the wind is still another open question (Townsend 2007).

An intriguing result concerns the radial velocity variations of the P Cygni absorption component of the *s* profiles. The centroid of these features was measured with a Gaussian fit from the location where the absorption meets the continuum level on the "blue" to the position of the emission component where the velocity is -500 km s^{-1}. In Figure 11 the derived RVs from the nine *s*-type profiles obtained over the 18 years of observation are plotted as a function of the 3.76 d phase computed with the Georgiev et al. (1999) ephemeris. The error bars correspond to the measurement uncertainties, estimated to be ± 30 km s^{-1}. This figure shows a clear modulation. Thus, although the data points are too few for a strong conclusion to be drawn, this result does suggest the presence of an underlying "clock" that retains coherence over very long timescales. It also indicates that it may be necessary to use only the *s* profiles to study the source of the "clock".

6. DISCUSSION AND CONCLUSIONS

In this paper we used the N V 4604 line observed in HD 50896 spectra obtained over 18 years to explore the possible wind structure variations that may lead to the observed changes in the shape of this line. We find that the variability in the P Cygni absorption component can be explained in terms of changes in the opacity structure of the wind. Specifically, changes in the relative opacities in regions $R_2 \sim 0.47\ R_{\rm max}$ and $R_3 \sim 0.65\ R_{\rm max}$, where $R_{\rm max}$ is the maximum extent of the N V 4604 line-forming region. Both these regions lie in the accelerating portion of the wind, according to the linear velocity law used to fit the profiles. The *strong* P Cygni absorptions are visible when the opacity in region R_2 is larger than in R_3. When this ratio is inverted, the P Cygni absorptions vanish. Evidence of opacity enhancements has previously been found in other objects, such as the O7.5-star 68 Cyg (Prinja & Howarth 1988).

The temporal sequence for the appearance of the profiles is such that a profile with a strong P Cygni absorption is followed one night later by one in which the absorption is absent. On the following two nights the profile may have either a weak or an absent absorption. On only one occasion (epoch 1991) there are *strong* profiles on two consecutive nights. Since the opacity depends on the mass-loss rate and on the ionization structure of the wind, its variation implies changes in these parameters.

The terminal velocity of HD 50896 is estimated at -1900 km s^{-1} (Prinja, Barlow, & Howarth 1990; Howarth & Schmutz 1992). However, St-Louis et al. (1993) report that the most conspicuous absorption-line variability takes place between about -1800 and -2800 km s^{-1} for the major UV P Cygni lines. This implies that most of the variability occurs at speeds exceeding the normal maximum outflow velocity of the wind. The N V 4604 line does not provide information on these very large speeds, but it does tell us that the instability appears to be present at lower speeds as well. Given that UV lines arise from atomic transitions that are more optically thick, they are able to probe lower density regions of the wind. Such low density regions having high velocities are predicted to occur as a result of radiative instabilies (Owocki, Castor, & Rybicki 1988). Thus, the *absent* type N V 4604 profiles may occur when the radiative instabilities are more prevalent. We speculate that the *strong* type profiles might correspond to a more stable state of the wind, when fewer shocks are present. St-Louis et al. (1993) also concluded that the radiative instabilities probably play an important role in governing the line-profile variations that are observed in the UV.

One intriguing aspect of these perturbations is that significant changes in the line-profiles are observed on timescales of $\sim$1 day and no shorter. St-Louis et al. (1993) show how the UV P Cygni lines undergo changes on a day-to-day timescale. This is in contrast with, for example, the opacity enhancements mentioned above for 68 Cyg, where variations on timescales as short as 1 hr were observed (Prinja & Howarth 1988). Also relevant to this discussion is the presence of relatively narrow emission-like features ("sub-peaks") superposed on the broad He II emission lines. Variable sub-peak structure in WR stars is generally associated with the presence of an inhomogeneous stellar wind. However, Drissen et al. (1989) concluded from their polarimetric data that the smaller-scale "blob" activity observed in other WRs is quite low in HD 50896. Hence, the variability of HD 50896 seems to originate in what might be described as organized episodes of unstable and stable states, rather than the random-like inhomogeneities that are present in many other WRs. Also important to note is that at least one other WN-type star, WR1 (HD 4004) displays a variability similar to that of HD 50896 (Flores et al. 2007), so HD 50896 is not unique (see, also, St-Louis et al. (2009) for a discussion of varibility in several other WR stars). Also, in the WN5 binary V444 Cygni, the N V 4603-21 doublet undergoes phase-dependent variations qualitatively similar to those of HD 50896. Specifically, the P Cygni absorptions are deepest during one orbital phase interval (primary eclipse), becoming weaker in the neighborhood of the secondary minimum, and disappearing completely at secondary eclipse (Münch 1950). This suggests that the weak P Cygni absorptions are indicative of a perturbed wind structure[8] which, in the case of V444 Cyg, probably results from a combination of irradiation and surface distortion due to tidal effects. In the case of HD 50896, the profiles with an absent P Cygni absorption are more prevalent than in V444 Cyg, indicating that the perturbation causing the absorption to vanish occurs more frequently.

The model we have applied to fit the line profiles is one based on the simplest set of assumptions; that is, we assume that the line profile variability is caused by variations in the wind properties, specifically, the opacity. Because we fit only the blue wing of the line profile, our conclusion applies, strictly speaking, primarily to the column of wind that is projected onto the continuum-emitting core. Hence, we are unable to distinguish between a cyclical (in time) variation of the entire wind structure and the variations that would be caused by different zones of the stellar wind (each with different properties) entering and leaving our line-of-sight due to stellar rotation.

Matthews et al. (1992) suggested a model consisting of two oppositely-directed jets, emerging at an angle with respect to the observer's line-of-sight. They suggested that as the star rotates, the jets would alternately come into and out of the line-of-sight, thus producing the observed variability. Although the origin of such jets remains obscure, the general concept of a quadrupole-like wind structure may have a physical basis. Koenigsberger, Moreno, & Harrington (2010) proposed that the perturbations produced by the tidal forces in the eccentric binary system HD 5980 could lead to a variable wind structure as the system goes from periastron to apastron. Furthermore, since the tidal effects are stronger in the quadrant facing the companion than in the adjacent quadrants, the tidal perturbations

[8]The absent absorptions are attributed to the physical eclipse by Marchenko et al. (1997).

could, in principle, lead to a quadrupole-like wind distribution, independently of the eccentricity of the orbit. Demonstrating that a quadrupolar wind distribution in a rotating star reproduces the observed line-profile variations requires the use of a model that allows for departures from spherical symmetry.

In conclusion, we find that the N V 4604 line-profile variability may be understood in terms of a variable wind structure which involves changes in the N V opacity. The mechanism causing this variability remains to be determined.

GK acknowledges support from PAPIIT/Universidad Nacional Autónoma de México grant and computing support from Ulises Amaya. AF acknowledges the sabbatical stay in the INAOE and support from Conacyt under the target financed project 121166 "Spectroscopy Variations of Wolf-Rayet Stars", and by the UNACAR grant 1320.

REFERENCES

Auer, L. H., & Koenigsberger, G. 1994, ApJ, 436, 859
Cherepashchuk, A. 1981, MNRAS, 194, 755
Crowther, P. 2007, ARA&A, 45, 177
Drissen, L., Robert, C., Lamontagne, R., Moffat, A. F. J., St-Louis, N., van Weeren, N., & van Genderen, A. M. 1989, ApJ, 343, 426
Firmani, C., Koenigsberger, G., Bisiacchi, G. F., Moffat, A. F. J., & Isserstedt, J. 1980, ApJ, 239, 607
Firmani, C., Koenigsberger, G., Bisiacchi, G. F., Ruiz, E., & Solar, A. 1979, in IAU Symp. 83, Mass Loss and Evolution of O-Type Stars, ed. P. S. Conti & C. W. H. de Loore (Dordrecht: Reidel), 421
Flores, A., Koenigsberger, G., Cardona, O., & de la Cruz, L. 2007, AJ, 133, 2859
Georgiev, L. N., Koenigsberger, G., Ivanov, M. M., St.-Louis, N., & Cardona, O. 1999, A&A, 347, 583
Hillier, D. J. 1988, ApJ, 327, 822
Howarth, I. D., & Schmutz, W. 1992, A&A, 261, 503
Koenigsberger, G., Moreno, E., & Harrington, D. M. 2010, in ASP Conf. Ser. 425, Hot and Cool: Bridging Gaps in Massive Star Evolution, ed. C. Lietherer, P. Bennett, & J. van Loon (San Francisco: ASP), 209
Lamontagne, R., Moffat, A. F. J., & Lamarre, A. 1986, AJ, 91, 925
Marchenko, S. V., Moffat, A. F. J., Eenens, P. R. J., Cardona, O., Echevarría, J., & Hervieux, Y. 1997, ApJ, 485, 826
Matthews, J. M., St.-Louis, N., Moffat, A. F. J., Drissen, L., Koenigsberger, G., Cardona, O., & Niemela, V. S. 1992, in ASP Conf. Ser. 22, Nonisotropic and Variable Outflows from Stars, ed. L. Drissen, C. Leitherer, & A. Nota (San Francisco: ASP), 130
McLean, I. S. 1980, ApJ, 236, L149
Morel, T., St-Louis, N., Moffat, A. F. J., Cardona, O., Koenigsberger, G., & Hill, G. M. 1998, ApJ, 498, 413
Münch, G. 1950, ApJ, 112, 266
Owocki, S. P., Castor, J. I., & Rybicki, G. B. 1988, ApJ, 335, 914
Piceno, A. 2003, M. Sc. Thesis, INAOE, Puebla, Mexico
Prinja, R. K., Barlow, M. J., & Howarth, I. D. 1990, ApJ, 361, 607
Prinja, R. K., & Howarth, I. D. 1988, MNRAS, 233, 123
Skinner, S. L., Itoh, M., & Nagase, F. 1998, New Astron., 3, 37
Skinner, S. L., Zhekov, S. A., Güdel, M., & Schmutz, W. 2002, ApJ, 579, 764
Stevens, I. R., & Willis, A. J. 1988, MNRAS, 234, 783
St-Louis, N., Chené, A.-N., Schnurr, O., & Nicol, M.-H. 2009, ApJ, 698, 1951
St-Louis, N., Howarth, I. D., Willis, A. J., Stickland, D. J., Smith, L. J., Conti, P. S., & Garmany, C. D. 1993, A&A, 267, 447
Townsend, R. 2007, in AIP Conf. Proc. 948, Unsolved Problems in Stellar Physics, ed. R. Stancliffe, G. Houdek, R. Martin, & C. Tout (Melville, NY: AIP), 345
van den Heuvel, E. P. J. 1976, in IAU Symp. 73, Structure and Evolution of Close Binary Systems, ed. P. Eggleton, S. Mitton, & J. Whelan (Dordrecht: Reidel), 35
van der Hucht, K. A., Conti, P. S., Lundstrom, I., & Stenholm, B. 1981, Space Sci. Rev., 28, 227
Vázquez, G. 2003, M. Sc. Thesis, INAOE, Puebla, Mexico

O. Cardona: Instituto Nacional de Astrofísica Óptica y Electrónica, Luis Enrique Erro 1, Tonantzintla, Puebla, Mexico (ocardona@inaoep.mx).
L. de la Cruz and A. Flores: Facultad de Ingeniería, Universidad Autónoma del Carmen, Calle 56, 4. Cd. del Carmen, Campeche, Mexico (aflores, ldelacruz@pampano.unacar.mx).
G. Koenigsberger: Instituto de Ciencias Físicas, Universidad Nacional Autónoma de México, Ave. Universidad S/N, Col. Chamilpa, Cuernavaca 62210, Mexico (gloria@fis.unam.mx).

Revista Mexicana de Astronomía y Astrofísica, **47**, 277–288 (2011)

VARIABLE JETS WITH NON-TOP HAT EJECTION CROSS SECTIONS: A MODEL FOR THE KNOTS OF THE HH 34 JET

A. C. Raga,[1] A. Noriega-Crespo,[2] P. Kajdic,[3] F. De Colle,[4] D. López-Cámara,[1] and A. Esquivel[1]

Received 2010 December 15; accepted 2011 May 9

RESUMEN

Calculamos modelos axisimétricos, con una variación sinusoidal (de un modo) y un perfil de sección recta inicial de velocidad. Encontramos que para cocientes de velocidad borde a centro decrecientes, uno obtiene superficies de trabajo con choques de proa con alas progresivamente más extendidas. Estas alas producen emisión de [S II] que parcialmente llena las regiones entre los nudos en los mapas de emisión predichos. Luego calculamos modelos de 3 modos (con parámetros apropiados para el chorro HH 34), y comparamos los mapas de emisión predichos con imágenes del archivo del HST de HH 34. Encontramos que un modelo con cociente de velocidades borde a centro moderado produce estructuras de nudos con morfologías y variabilidades temporales muy parecidas a las observadas en HH 34.

ABSTRACT

We compute axisymmetric, single-sinusoidal mode variable ejection models with a non-top hat ejection velocity cross section. We find that for decreasing edge-to-center velocity ratios one obtains internal working surfaces with progressively more extended bow shock wings. These wings produce [S II] emission which partially fills in the inter-knot regions in predicted intensity maps. We then compute 3-mode models (with parameters appropriate for the HH 34 jet), and compare predicted intensity maps with archival HST images of HH 34. We find that a model with a moderate edge-to-center velocity ratio produces knot structures with morphologies and time-variabilites with clear similarities to the observations of HH 34.

Key Words: ISM: jets and outflows — ISM: kinematics and dynamics — stars: mass-loss — stars: pre-main sequence

1. INTRODUCTION

Rees (1978) first suggested that a variability in the ejection might be responsible for the structure observed in extragalactic jets. This idea was then pursued numerically by Wilson (1984), who modeled extragalactic jets with "twin-lobe" structures.

Raga et al. (1990) proposed an ejection variability as a mechanism for explaining the chains of knots observed along HH jets such as HH 34 (Reipurth et al. 1986) and HH 111 (Reipurth 1989). This proposed model was strengthened by the fact that later ground-based (Reipurth & Heathcote 1992; Reipurth, Raga, & Heathcote 1992) and HST images (Reipurth et al. 2002, 1997) showed that some of the knots along the HH 34 and HH 111 jets have bow-like morphologies.

This model has been explored analytically (e.g., Cantó, Raga, & D'Alessio 2000) and numerically (e.g., De Colle, Raga, & Esquivel 2008). Different effects in variable ejection jets have been studied, such as:

- different forms of the ejection variability (Hartigan & Raymond 1993; Tesileanu et al. 2009),
- the added presence of a precession (Raga & Biro 1993; Smith & Rosen 2005),
- variable jets with magnetic fields (Gardiner & Frank 2000; De Colle et al. 2008),
- variable jets in a sidewind (Esquivel et al. 2009).

[1]Instituto de Ciencias Nucleares, Universidad Nacional Autónoma de México, Mexico.

[2]Spitzer Science Center, California Institute of Technology, CA, USA.

[3]Instituto de Geofísica, Universidad Nacional Autónoma de México, Mexico.

[4]Astronomy and Astrophysics Department, University of California, Santa Cruz, CA, USA.

In the present paper, we focus on the effect on a variable ejection jet of a non-top hat ejection velocity cross section. An analytic model for the effect of a centrally peaked ejection velocity cross section was presented by Raga, Cantó, & Cabrit (1998). These authors show that for decreasing edge-to-center ejection velocity ratios the internal working surfaces (resulting from the ejection time-variability) become progressively more curved. This effect might produce emitting knots with a closer resemblance to some of the bow-shaped knots observed in HH jets.

Some numerical simulations of variable ejection jets have incorporated a non-top hat ejection velocity cross section. For example, Völker et al. (1999) used a quadratic ejection velocity cross section with a factor of 1/2 edge-to-center velocity ratio in variable ejection models. Some of the more recent papers of this group also describe models which incorporate a (presumably quadratic) non-top hat ejection velocity cross section (Rosen & Smith 2003, 2004; Smith & Rosen 2005) with a edge-to-center velocity ratio of 0.7 or 0.8. Dennis et al. (2008) present constant ejection jet models with a quadratic ejection velocity cross section with an edge-to-center ratio of 0.9. Raga et al. (1998) describe an analytic model for leading and internal working surfaces in jets with arbitrary ejection (density and velocity) cross sections, but only present a single numerical simulation of the leading head of a jet with a quadratic velocity cross section with an edge-to-center velocity ratio of 0.8. Raga et al. (2009) also computed variable jet models with a quadratic velocity cross section, and find that even jets with an edge-to-center velocity ratio of 0.8 differ substantially from initially top hat jets. Finally, the paper of Frank et al. (2000) appears to be the only study of a jet with a non-quadratic radial dependence of the ejection velocity. Somewhat surprisingly, a systematic numerical study of the effect on variable jets of different edge-to-center ejection velocity ratios has not yet been made.

In this paper, we present a set of eight axisymmetric, variable jet models (with a sinusoidal ejection variability) in which we explore the effect of varying the edge-to-center ejection velocity ratio. In order to illustrate the possible relevance of non-top hat cross sections for modelling HH jets, we then present a comparison between intensity maps predicted from the models and red [S II] images of the HH 34 jet.

For this purpose, we compute non-top hat, ejection models with the three-mode sinusoidal variability empirically determined for HH 34 by Raga et al. (2002). We explore a set of different edge-to-center ejection velocity ratios, and compare the predicted intensity maps with archival HST images of the HH 34 jet.

The paper is organized as follows. In § 2, we give a short description of the archival HST images of HH 34. In § 3, we describe the single-mode, non-top hat jet models. In § 4, we compare the intensity maps predicted from non-top hat, three-mode models with the HST images of HH 34. Finally, the results are summarized in § 5.

2. THE ARCHIVAL HST IMAGES OF HH 34

The *Hubble Space Telescope* (HST) Wide Field Planetary Camera 2 (WFPC2) data of HH 34 have been retrieved from the *Hubble Legacy Archive* (HLA), for two epochs (1998 & 2007). The processing of the HLA data uses a new calibration pipeline that includes an improved handling of the UV contamination, bias variations and other artifacts[5]. Furthermore, the WFPC2 HLA data have been resampled onto a uniform grid to correct for geometric distorsions, an essential step to determine, for instance, the proper motions of knots along the jet between the two epochs.

The 1998 images were described in detail by Reipurth et al. (2002). The HH 34 archival images from 2007 to our knowledge have not been presented anywhere, and we therefore describe them briefly. The data were obtained during the HST Cycle 16 (October 30, 2007) and belong to program 11179 (PI. P. Hartigan) on the dynamics of clumpy supersonic flows in stellar jets. Like in the 1998 observations (Reipurth et al. 2002) the data were obtained using the standard WFPC2 narrow band filters of Hα (F656N) and [S II]λ 6716+30 (F673N). The final images are the result of multiple co-added exposures (eight for both Hα & [S II]) which are used to mitigate the effects of cosmic rays, and with a total integration time of 9600 sec for each filter.

3. NON-TOP HAT, SINGLE MODE JETS

We have computed a set of models with a time-dependent ejection velocity of the form:

$$v_j(r,t) = \left[v_0 + v_1 \sin\left(\frac{2\pi t}{\tau}\right)\right]\left[1-(1-\sigma)\left(\frac{r}{r_j}\right)^2\right], \tag{1}$$

where t is the time, r is the cylindrical radius (measured across the initial cross secion of the jet), v_0 is the mean axial velocity of the jet, v_1 is the half-amplitude of the axial velocity variability and $\sigma = v_{\rm edge}/v_{\rm axis}$ is the ratio between the ejection velocity at the edge of the jet ($v_{\rm edge}$, at $r = r_j$) and

[5]See e.g. `http://hla.stsci.edu/hla_faq.html#WFPC2`.

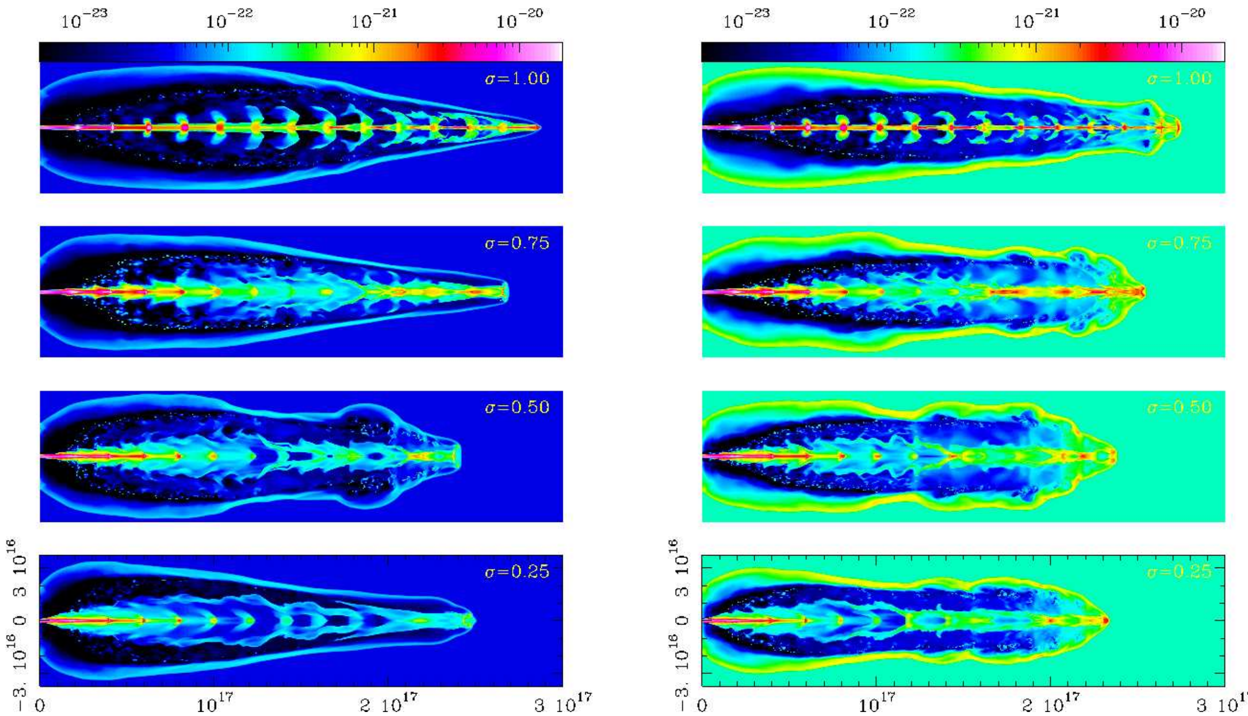

Fig. 1. Density stratifications obtained from the single-sinusoidal mode variable jet models (see § 3). The models of jets moving into an environment with $n_a = 15$ cm^{-3} are shown at $t = 350$ yr integration time (left column) and the models with $n_a = 100$ cm^{-3} are shown at $t = 400$ yr (right column). The results are labeled with the value of σ (the edge-to-center ejection velocity ratio) of each model. The full computational domain is shown on both sides of the symmetry axis (the axes are labeled in cm). The densities are depicted with the logarithmic color scheme given (in g cm^{-3}) by the top bar. The color figure can be viewed online.

the velocity along the jet axis ($v_{\rm axis}$, at $r = 0$). In other words, the ejection velocity has a single-mode, sinusoidal ejection velocity variability, and a center-to-edge, quadratic radial dependence.

When calculating variable ejection jet models, it is of course possible to include a time-variability in the initial density and/or temperature of the jet. Such variabilities, however, lead to the production of shocks with velocities of the order of the initial sound speed (typically of $\approx$ a few km s^{-1} for HH jets). Because of this, if one wants to model the emission along HH jets (which is formed in shocks with velocities $\sim$10 $\rightarrow$ 100 km s^{-1}), it is clear that an ejection velocity variability with a highly supersonic amplitude has to be included.

We have run two sets of four models (each set corresponding to environments with different densities, see below) with edge-to-center ejection velocity ratios $\sigma = 1.0$ (top hat), 0.75, 0.5 and 0.25. The models have the same ejection variability, with $v_0 = 250$ km s^{-1}, $v_1 = 30$ km s^{-1} and $\tau = 30$ yr. The ejection density and temperature have top-hat profiles with $n_j = 5000$ cm^{-3} and $T_j = 1000$ K (respectively). For the surrounding, homogeneous environment, we have considered a $T_a = 1000$ K temperature, and two possible densities: $n_a = 15$ and 100 cm^{-3}. It is assumed that both the jet and the environment are initially neutral except for C and S, which are assumed to be singly ionized. The jets have a $r_j = 10^{15}$ cm initial radius.

The gas-dynamic equations are integrated together with a set of rate equations for H, He, C, N, O and S ions, with an axisymmetric version of the "yguazú-a" adaptive grid code. The resulting, non-equilibrium ionization has been used to compute the energy loss term (included in the energy equation). The version of the code used is identical to the one described in detail by Kajdic, Velázquez, & Raga (2006) and by Raga et al. (2007). For the present calculations, we use a 6-level, binary adaptive grid which would fill the domain with 4096×512 (axial $\times$ radial) points at the highest grid resolution. The cylindrical domain has an on-axis reflection condition, an inflow condition for $r \leq r_j$ and a reflection condition for $r > r_j$ on the injection ($x = 0$) plane, and outflow conditions at the remaining two bound-

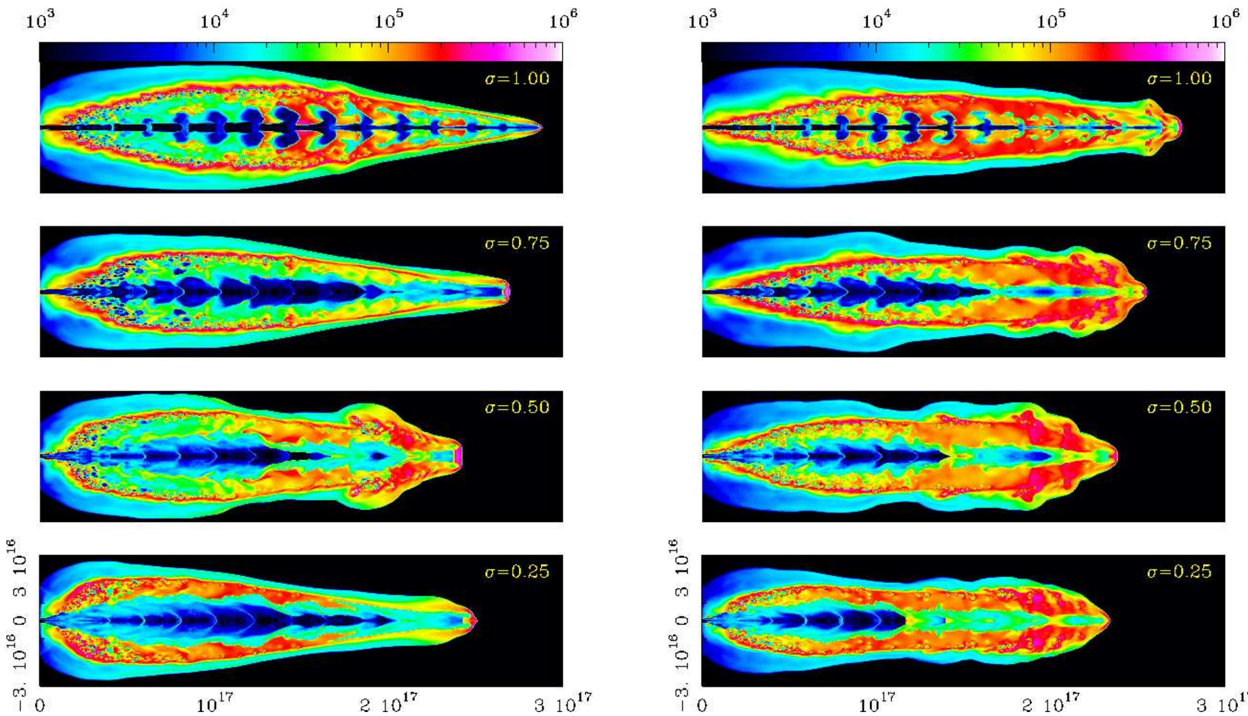

Fig. 2. Temperature stratifications obtained from the single-sinusoidal mode variable jet models (see § 3). The models of jets moving into an environment with $n_a = 15$ cm^{-3} are shown at a $t = 350$ yr integration time (left column) and the models with $n_a = 100$ cm^{-3} are shown at $t = 400$ yr (right column). The results are labeled with the value of σ (the edge-to-center ejection velocity ratio) of each model. The temperatures are depicted with the logarithmic color scheme given (in K) by the top bar. The color figure can be viewed online.

aries of the $(30, 3.75) \times 10^{16}$ cm (axial × radial) computational domain.

The density and temperature stratifications obtained from the four $n_a = 15$ cm^{-3} models after a $t = 350$ yr time-integration and the four $n_a = 100$ cm^{-3} models at $t = 400$ yr are shown in Figures 1 and 2. The models show a leading jet head and a series of travelling "internal working surfaces" (IWS) which are formed as a result of the ejection time-variability.

We first note that the knots within $\approx 10^{17}$ cm from the source have very similar structures in the $n_a = 15$ and 100 cm^{-3} models. From this, we conclude that the precise value of the environmental density does not have a strong effect on the sequence of knots close to the outflow source (see Figures 1 and 2). It is clear, however, that the value of n_a does have (as expected) an important effect on the structure and propagation of the leading head of the jet.

On the other hand, it is clear from Figures 1 and 2 that the value chosen for the edge-to-center ejection velocity ratio σ does have a strong effect on the structure of the IWS. For $\sigma = 1$, the working surfaces have compact, dense regions within the jet beam, which eject low density material out into the cocoon of the jet. For lower values of σ, the IWS have clear, bow-shaped morphologies, with densities that fall away from the symmetry axis (see Figure 1).

The value of σ also has a strong effect on the resulting temperature stratifications. For $\sigma = 1$, a relatively hot cocoon (with $T \sim 3 \rightarrow 20 \times 10^4$ K) is in contact with the jet beam. For lower values of σ, a lower temperature region (with $T \sim 10^4$ K) buffers the jet beam from the hot cocoon (this cool region is most clearly seen in the $\sigma = 0.25$ model, see Figure 2).

In Figure 3, we show the [S II] 6716+6730 emission maps predicted from the four $n_a = 15$ cm^{-3} models for $t = 350$ yr. These maps have been computed solving the appropriate 5-level atom problem, and integrating the resulting emission coefficient along lines of sight. It has been assumed that the outflow axis lies on the plane of the sky.

The maps shown in Figure 3 display the region close to the outflow source. It is clear that for $\sigma = 1$ the emission from the IWS is concentrated in compact "knots", with only very faint "wings" seen in

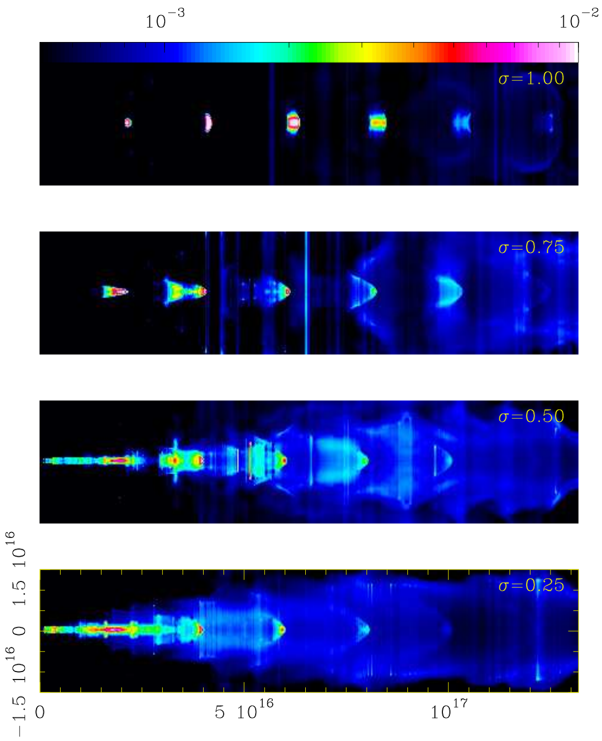

Fig. 3. [S II] 6716+30 intensity maps predicted from the four single-mode jet models with $n_a = 15$ cm^{-3} (see § 3) for a $t = 350$ yr integration time. The maps have been computed assuming that the outflow axis lies on the plane of the sky. Only a region close to the jet source is shown (compare with the full computational domain shown in Figures 1 and 2). The intensities are shown with a logarithmic color scheme given (in erg s^{-1} cm^{-2} sterad^{-1}) by the top bar. The color figure can be viewed online.

the knots with $x > 10^{17}$ cm. For lower values of σ, the emission knots have bow-wings of increasing intensity. The emission from these bow-wings partially fills in the gaps corresponding to the inter-knot regions (these gaps are clearly seen in the $\sigma = 1$ model, see Figure 3).

With these models we therefore show that the edge-to-center ejection velocity ratio σ has a strong effect on the morphology of the IWS (which results from the ejection velocity time-variability). For $\sigma = 1$ (i.e., for a top-hat jet, see equation 1), the [S II] emission of the IWS has a morphology of compact clumps, with low-emission gaps between the clumps. For lower values of σ, the emission from the IWS develops progressively more extended bow wings, which partially fill in the gaps between the successive knots. Therefore, by tuning the value of σ it is possible to produce knots with different morphologies, which could then be compared with the emission observed in specific HH jets. An attempt to do this is presented in the following section.

4. THREE-MODE MODEL FOR HH 34

Raga & Noriega-Crespo (1998) and Raga et al. (2002) proposed a three-mode ejection velocity variability for modelling the structure of the southern lobe of the HH 34 outflow. In particular, Raga et al. (2002) used radial velocity and proper motion observations of HH 34 to derive a variability of the form:

$$v_c(t) = v_0 + v_1 \sin\left(\frac{2\pi t}{\tau_1} + \phi_1\right) + v_2 \sin\left(\frac{2\pi t}{\tau_2} + \phi_2\right) + v_3 \sin\left(\frac{2\pi t}{\tau_3}\right) , \qquad (2)$$

with $v_0 = 270$ km s^{-1}, $v_1 = 70$ km s^{-1}, $\tau_1 = 1400$ yr, $\phi_1 = -0.80$ rad, $v_2 = 25$ km s^{-1}, $\tau_2 = 270$ yr, $\phi_2 = -0.85$ rad, $v_3 = 10$ km s^{-1} and $\tau_3 = 27$ yr. This function represents the past time-variability of the ejection of HH 34, with $t = 0$ representing the present time. Negative values of t represent the times at which the material presently observed along the HH 34 jet was ejected from the source.

We then choose an ejection velocity v_j with this three-mode variability, modulated with a quadratic center-to-edge profile:

$$v_j(r,t) = v_c(t)\left[1 - (1-\sigma)\left(\frac{r}{r_j}\right)^2\right] , \qquad (3)$$

where $v_c(t)$ is given by equation (2) and σ is the center-to-edge ejection velocity ratio (see equation 1).

Following Raga et al. (2002), we choose time-independent, top-hat ejection density and temperature cross sections with $n_j = 5000$ cm^{-3} and $T_j = 1000$ K (respectively), and a $r_j = 5 \times 10^{15}$ cm jet radius. The jet moves into a homogeneous environment with $n_a = 15$ cm^{-3} and $T_a = 1000$ K.

The computational domain has an (axial × radial) extent of $(16.8, 2.1) \times 10^{17}$ cm, resolved with 4096×512 grid points at the highest resolution of the 6-level, binary adaptive grid. The setup of the three-mode models is otherwise identical to the one of the single-mode models described in § 3.

We have then computed three models, with center-to-edge ejection velocity cross sections with $\sigma = 1$, 0.75 and 0.5. The simulations were all started at $t = -3000$ yr, and allowed to evolve until $t = 300$ yr.

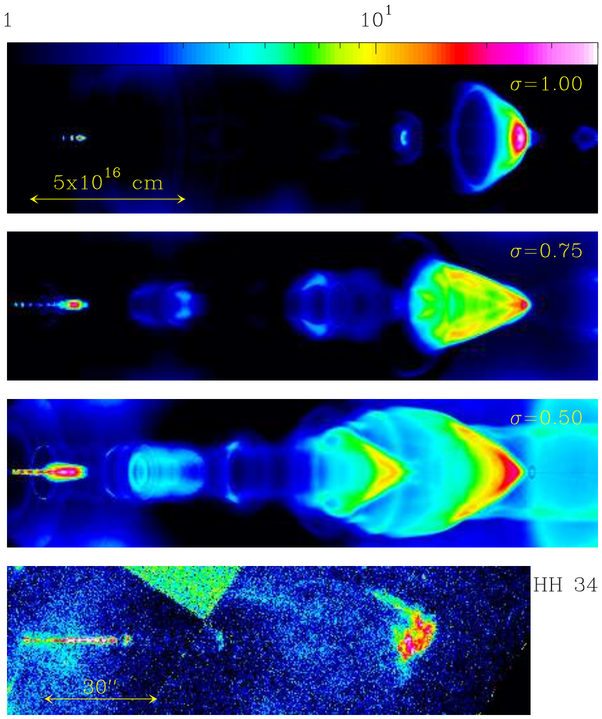

Fig. 4. [S II] 6716+30 intensity maps predicted from the three 3-mode jet models for a time $t = 0$ (the integration was started at $t = -3000$ yr, see § 4). The bottom frame shows the [S II] image obtained with the HST in 1998 (see § 2). The predicted maps have been computed assuming that the outflow axis lies at a 30° angle with respect to the plane of the sky (as appropriate for HH 34), and show a $(10.69, 2.67) \times 10^{17}$ cm domain. The HH 34 [S II] map has been scaled to the same scale as the predicted maps, assuming a distance of 450 pc (the displayed region has a vertical size of $39''.6$). The source of HH 34 is on the left of the chain of aligned knots. The intensities are shown with a logarithmic color scheme covering a dynamic range of 40 (see the top bar), scaled so that in the four maps the brighter regions start to saturate at the highest depicted intensity. The color figure can be viewed online.

In Figure 4, we present the [S II] 6716+30 intensity maps predicted from these three models for $t = 0$ (i.e., for years ∼1990–1994 at which the data analyzed by Raga et al. 2002 were obtained). These maps were computed assuming a 30° angle between the jet axis and the plane of the sky, corresponding to the approximate orientation of the HH 34 outflow (see Heathcote & Reipurth 1992). Together with the predicted maps, we show an archival [S II] HST image of the southern lobe of the HH 34 outflow, rotated so that the outflow axis is parallel to the abscissa. The physical size of the domains of the synthetic and observed maps are identical (assuming a 450 pc distance to HH 34).

For all of the computed models, emission structures with a qualitative resemblance to HH 34 are obtained. The four models show a large bow shock at a distance from the source comparable to HH 34S, a chain of knots close to the source, and a few broader, faint condensations between the chain of knots and the large bow shock. These three main features are in qualitative agreement with the observed structure of the HH 34 jet.

It is clear from Figure 4 that the shape of the large bow shock is more flat-topped in the $\sigma = 1$ model than in the $\sigma = 0.75$ and 0.5 models, in which the bow shock has a more conical morphology. Also, in the $\sigma = 1$ model (presented previously by Raga et al. 2002), the [S II] emission from the chain of knots is fainter than the emission from the large bow shock. The $\sigma = 0.75$ and 0.5 models show a comparable peak [S II] emission in the main bow shock and in the brighter knots in the chain, in better qualitative agreement with the [S II] image of HH 34.

Figures 5, 6 and 7 show the time-evolution of the [S II] emission of the chain of knots for the $\sigma = 1$, 0.75 and 0.5 models (respectively), at 100 yr intervals. In the 300 yr time-sequence obtained from the $\sigma = 1$ model (Figure 5), we see either one or two groups of compact knots. The predicted emission is qualitatively different from the emission from the HH 34 jet (bottom panel), in which the inter-knot regions show considerably brighter emission. Also, some of the observed knots have bow shapes which are not seen in the maps predicted from the $\sigma = 1$ model.

The time-sequence of [S II] intensity maps obtained from the $\sigma = 0.75$ model (Figure 6) does show bow-shaped knots. The inter-knot regions show brighter emission, in better qualitative agreement with the HH 34 jet observation.

The emission maps obtained from the $\sigma = 0.5$ model show groups of knots having less contrast between the knot and inter-knot emission than the HH 34 jet. Because of this, we conclude that the $\sigma = 0.75$ model produces the best qualitative agreement with the structure of knots along the HH 34 jet. In the following, we therefore focus on the $\sigma = 0.75$ model.

In Figures 8 and 9 we show a sequence of intensity maps with a time-interval of 10 yr, together with the 1998 and 2007 HST [S II] images (see § 2). From these figures, it is clear that the knots along the HH 34 jets have changed quite strongly over a

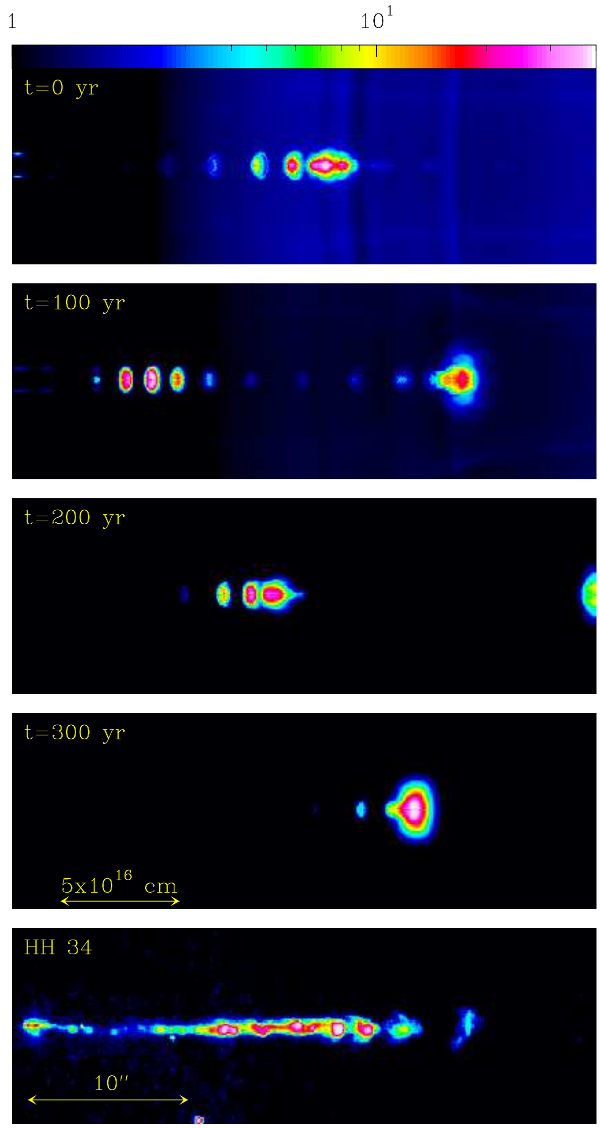

Fig. 5. [S II] 6716+30 intensity maps predicted from the $\sigma = 1$, 3-mode jet model for times $t = 0$, 100, 200 and 300 yr (the integration was started at $t = -3000$ yr, see § 4). The bottom frame shows the [S II] image obtained with the HST in 1998 (see § 2). The predicted maps have been computed assuming that the outflow axis lies at a 30° angle with respect to the plane of the sky (as appropriate for HH 34), and show a region with the source on the left and an axial extent of 2.46×10^{17} cm. The HH 34 [S II] map has been scaled to the same scale as the predicted maps, assuming a distance of 450 pc (the displayed region has a horizontal size of 36″.5). The intensities are shown with a logarithmic color scheme covering a dynamic range of 40 (see the top bar), scaled so that in the four maps the brighter regions start to saturate at the highest depicted intensity. The color figure can be viewed online.

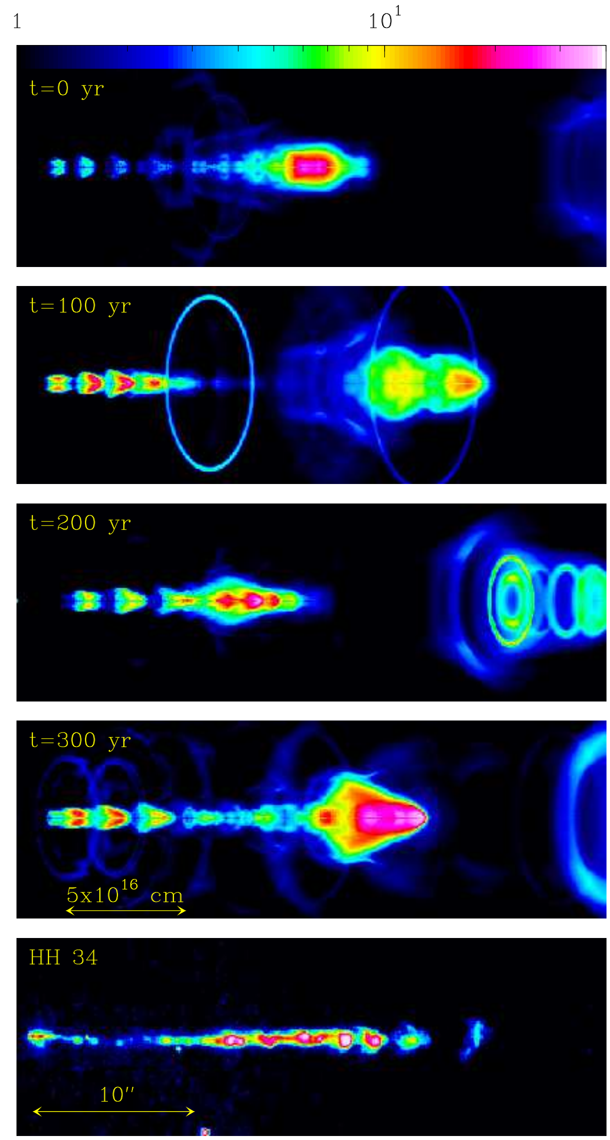

Fig. 6. The same as Figure 5 but for the $\sigma = 0.75$, 3-mode jet model (see § 4). The color figure can be viewed online.

13 yr time-span, with some of the knots becoming relatively fainter and other knots becoming brighter.

These changes are clearly seen in Figure 10, which shows intensity vs. position traces (obtained by integrating across the HH 34 jet and subtracting the adjacent background). It is clear that the $x < 2''$ region (where x is the distance from the source) has become considerably brighter, that the knots in the $10'' < x < 30''$ region have had clear variations (several of the knots having become fainter and others brighter).

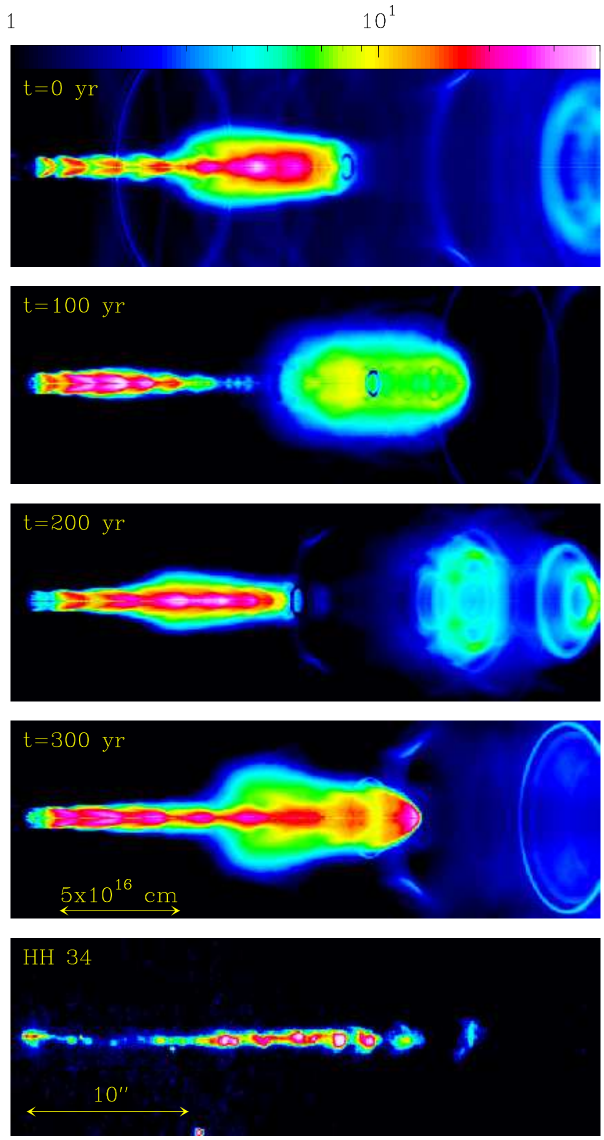

Fig. 7. The same as Figures 5 and 6 but for the σ = 0.5, 3-mode jet model (see § 4). The color figure can be viewed online.

In order to quantify these variations, we have defined segments along the [S II] tracings, incorporating the emission of the better defined knots. The positions and lengths of these segments were defined on the 1998 image (top frame of Figure 10), and were displaced $0''.7$ in the $+x$ direction for calculating the knot intensities in the 2007 frame (except for the segment incorporating the emission around the outflow source, which was not displaced). This displacement corresponds to the average motion of the knots along the HH 34 axis between the two epochs (corresponding to a proper motion of ≈170 km s^{-1}, consistent with previous measurements of proper motions in this outflow). In the bottom frame of Figure 10, we plot the 2007/1998 intensity ratios for the successive knots (defined above), showing that some of the knots have had intensity variations of up to a factor of ∼2.

From Figures 8 and 9 we notice that intensity variabilities similar to the observed ones are also seen in the predicted intensity maps over 10–20 yr time-intervals. For example, from $t = -60$ to $t = -50$ yr and $t = -40$ yr we see that the main knots have intensity changes (with the brightest knot becoming fainter, and some of the other knots brighter). Also, a systematic brightening of the region close to the source is seen from the $t = 0$ to the $t = 60$ yr time-frames, with clear changes over each decade.

None of the predicted intensity maps show [S II] emission structures that one could even attempt to compare quantitavely with the HH 34 knots. However, it is clear that several of the time-frames from the model do show structures which resemble the observed knots (see Figures 8 and 9).

5. CONCLUSIONS

We have presented a systematic study of the effect of having a non-top hat velocity cross section in the ejection of a variable jet. We have chosen a parabolic velocity cross section, with an edge-to-center velocity ratio $\sigma = 0.25 \to 1.0$.

For a jet with a single-mode, sinusoidal ejection velocity variability (see equation 1), we find that for larger edge-to-center velocity contrasts (i.e., for lower σ values) the internal working surfaces develop bow shapes with progressively more extended wings. These bow wings appear as extensions to the [S II] emission from the knots, filling in the gaps between the knots (see Figure 3).

We then compute a model with the three sinusoidal modes deduced from observations of the HH 34 jet by Raga et al. (2002). We find that a model with $\sigma = 0.75$ produces a chain of knots close to the source which better resembles the HH 34 [S II] emission than models with $\sigma = 1$ (i.e., with a top-hat ejection cross section) and with $\sigma = 0.5$ (this model producing a chain of knots with a too low intensity contrast between the knots and the inter-knot regions).

Finally, we present a time-sequence of the [S II] emission of the knots predicted from the $\sigma = 0.75$, three-mode model, and compare the maps with two epochs of HST images of HH 34 (with a ≈10 yr time interval). We find that the model predicts knot structures with reasonable qualitative similarity to

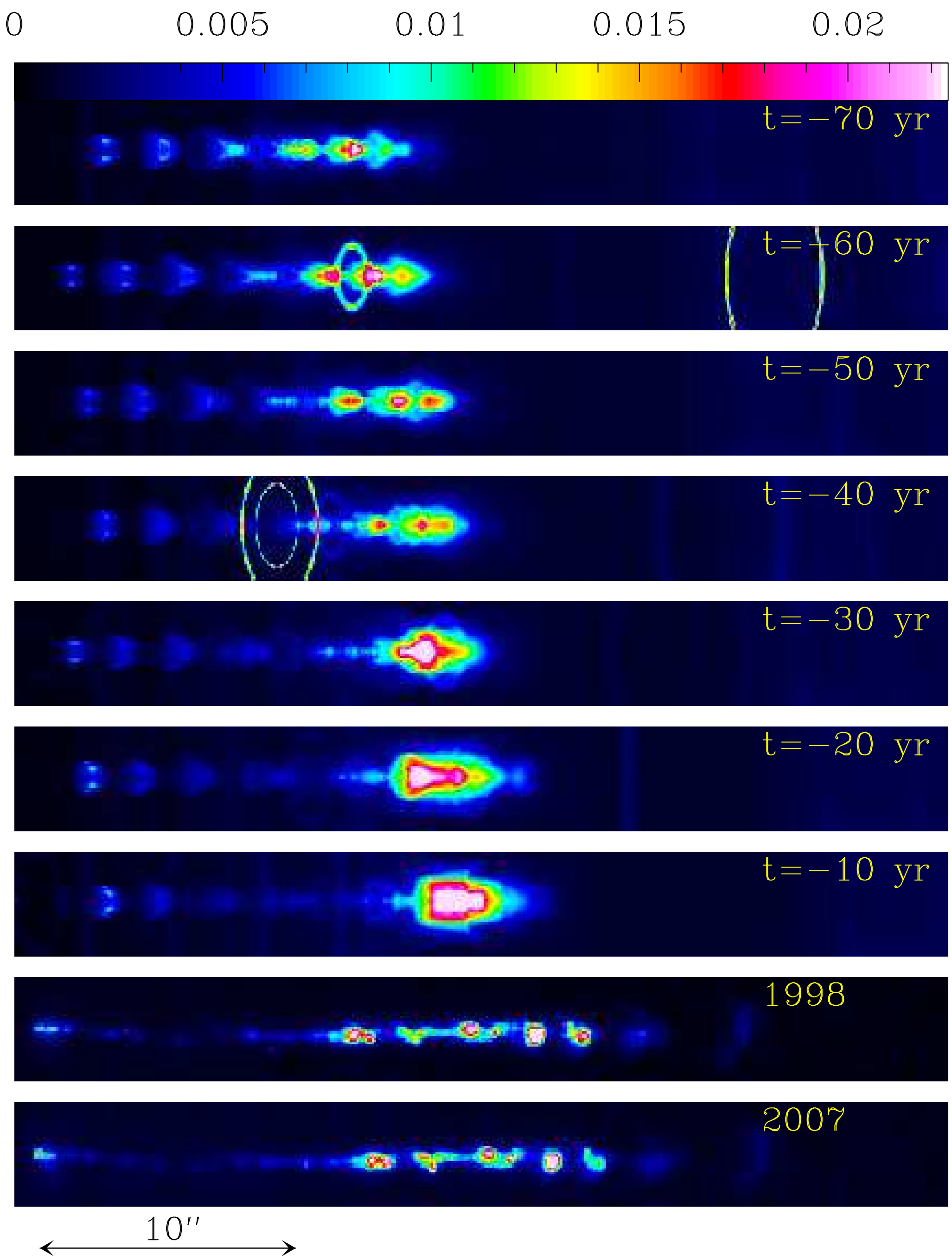

Fig. 8. [S II] 6716+30 intensity maps predicted from the $\sigma = 0.75$, 3-mode jet model for times $t = -70$ to -10 yr, at 10 yr intervals (the integration was started at $t = -3000$ yr, see § 4). The two bottom frames show the [S II] images obtained with the HST in 1998 and 2007 (see § 2). The predicted maps have been computed assuming that the outflow axis lies at a 30° angle with respect to the plane of the sky (as appropriate for HH 34), and show a region with the source on the left and an axial extent of 2.46×10^{17} cm. The HH 34 [S II] maps has been scaled to the same scale as the predicted maps, assuming a distance of 450 pc (the displayed region has a horizontal size of 36″.5). The intensities of the predicted maps are shown with a linear color scheme (given in erg s^{-1} cm^{-2} sterad^{-1} by the top bar), and the HH 34 maps are shown with a linear color scheme with a maximum value corresponding to 0.2 counts per second per pixel. The color figure can be viewed online.

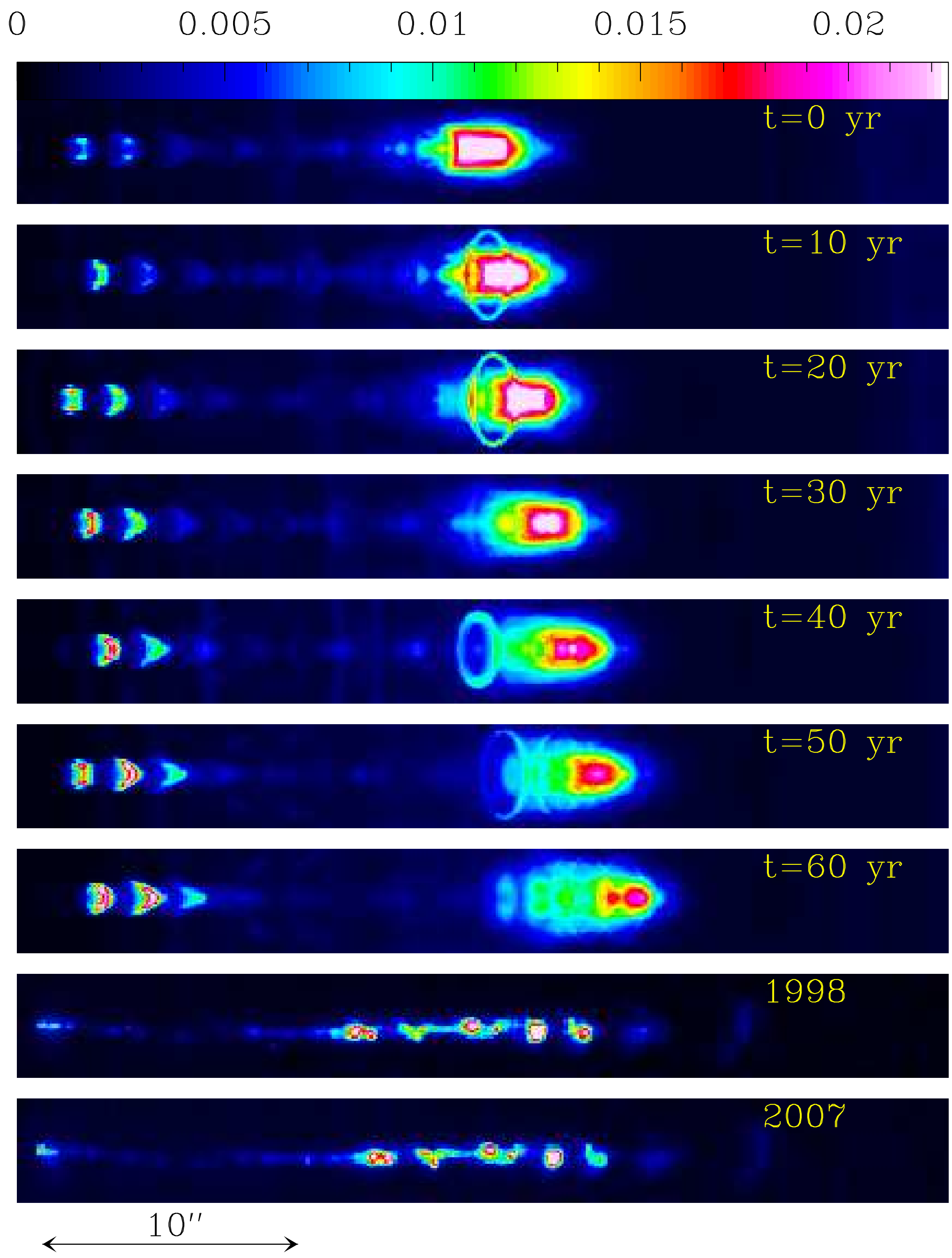

Fig. 9. The same as Figure 9, but with the intensity maps predicted from the $\sigma = 0.75$, 3-mode jet model for the times $t = 0$ to 60 yr, at 10 yr intervals (see § 4). The color figure can be viewed online.

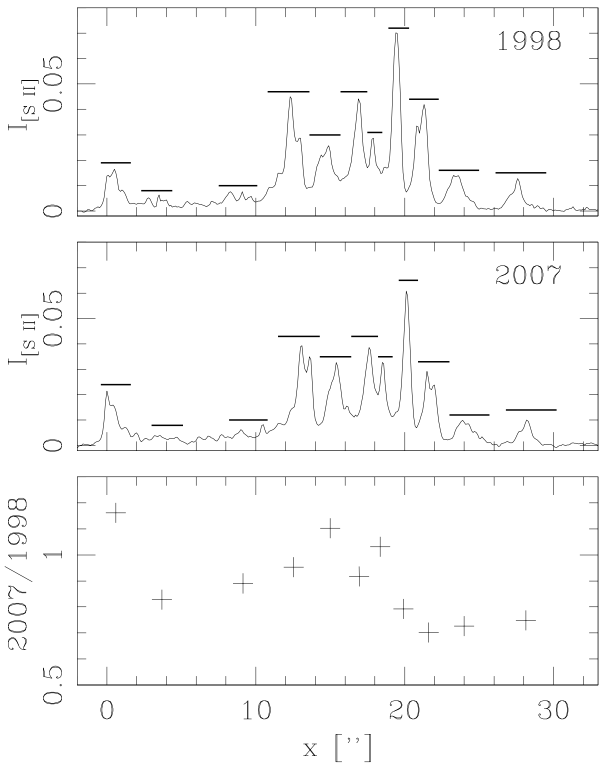

Fig. 10. [S II] tracings along the HH 34 jet for the 1998 (top) and 2007 (center) epochs, obtained by averaging over 3″ across the jet axis. The adjacent background emission has been subtracted. We have integrated the intensity over segments along the tracings. The lenghts and positions of the segments are shown on the two intensity tracings, with a displacement of $+0''.7$ along the x-axis for the 2007 epoch, (except for the segment incorporating the source, which was not displaced). The ratios between the integrated intensities (in the segments defined above) in the two epochs are shown in the bottom plot. The x-axis is the distance (in arcseconds) from the HH 34 source.

the HH 34 jet, and that the predicted structures show variabilities over ≈10 yr intervals which are consistent with the observed variability of the knots in HH 34.

The success we have obtained in reproducing the chain of knots within the first ∼1′ of the HH 34 jet is limited, as we are clearly not yet able to even attempt to carry out a quantitative comparison between the predicted and the observed emission structures. Nevertheless, the results are reasonably encouraging, because the predicted knot structures do show general morphologies and time-variabilities which appear to be consistent with the properties of the HH 34 knots. Also, the simulations approximately reproduce the shape of the HH 34S bow shock, and the intensity contrast between this bow shock and the chain of aligned knots. In particular, we find that including a non-top hat ejection velocity cross section (with a moderate edge-to-center velocity ratio) improves the qualitative similarity between predicted and observed knot structures. If this result is to be taken at face value, it would imply that the HH 34 jet has a centrally peaked velocity profile, with a drop of ∼25% towards the edge of the jet (this outer edge representing a sharp boundary at which the jet beam is interrupted).

This result, however, is uncertain. It has been shown that the presence of a toroidal magnetic field (De Colle et al. 2008), and/or the presence of a multi-mode (possibly chaotic) ejection variability can lead to the formation of elongated IWS (De Colle 2011). In future work, it will be necessary to explore whether or not these possibilities produce knot morphologies and time-variations similar to the ones observed in the HH 34 jet.

This work is part of an ongoing effort to attempt to reproduce the observational chatacteristics of a set of specific HH jets with variable jet models. We have previously presented models for HH 34 (Raga & Noriega-Crespo 1998; Raga et al. 2002; Masciadri et al. 2002a), HH 111 (Masciadri et al. 2002b), HH 32 (Raga et al. 2004), HH 30 (Esquivel, Raga, & De Colle 2007), the DG Tau microjet (Raga et al. 2001) and the photoionized jet HH 444 (López Martín et al. 2001; Raga, Riera, & González-Gómez 2010). This kind of comparison between predictions from numerical simulations and observations should eventually provide the grounds for deciding which HH objects have emitting structures that are definitely the result of an ejection time-variability. It should also provide constraints on models for the ejection of HH jets and at the same time give us an understanding of the mechanisms by which the emitting structures are formed.

As a final point, we should note that our study of non-top hat ejection velocity jets is limited to quadratic cross sections. The choice of a quadratic velocity cross section is to some extent natural, because it can be thought of as a second order Taylor series of an arbitrary, flat-topped function. For this reason, most of the previous papers on HH jet models with non-top hat velocity cross sections have considered quadratic profiles (for example, Völker et al. 1999; Rosen & Smith 2003, 2004). Another natural choice for the functional form of the ejection velocity cross section would be a Gaussian, as this is the form of the velocity cross section of turbulent laboratory jets. However, for the edge-to-center velocity ratios σ used in the present paper, the deviations between a Gaussian and a quadratic cross section are not very large (they are smaller than 6, 14 and 21% for $\sigma = 0.75$, 0.5 and 0.25, respectively). We would therefore not expect to obtain significantly different results for Gaussian cross sections.

This work was supported by the Conacyt grants 61547, 101356 and 101975. We acknowledge the support of E. Palacios of the ICN-Universidad Nacional Autónoma de México computing staff. We also thank an anonymous referee for helpful comments.

REFERENCES

Cantó, J., Raga, A. C., & D'Alessio, P. 2000, MNRAS, 313, 656
De Colle, F. 2011, in IAU Symp. 275, Jets at all Scales, ed. G. A. Romero, R. A. Sunyaev, & T. Belloni (Cambridge: Cambridge Univ. Press), 392
De Colle, F., Raga, A. C., & Esquivel, A. 2008, ApJ, 689, 302
Dennis, T. J., Cunningham, A. J., Frank, A., Balick, B., Blackman, E. G., & Mitran, S. 2008, ApJ, 679, 1327
Esquivel, A., Raga, A. C., Cantó, J., & Rodríguez-González, A. 2009, A&A, 507, 855
Esquivel, A., Raga, A. C., & De Colle, F. 2007, A&A, 468, 613
Frank, A., Lery, T., Gardiner, T. A., Jones, T. W., & Ryu, D. 2000, ApJ, 540, 342
Gardiner, T. A., & Frank, A. 2000, ApJ, 545, L153
Hartigan, P., & Raymond, J. C. 1993, ApJ, 409, 705
Heathcote, S., & Reipurth, B. 1992, AJ, 104, 2193
Kajdic, P., Velázquez, P. F., & Raga, A. C. 2006, RevMexAA, 42, 217
López-Martín, L., Raga, A. C., López, J. A., & Meaburn, J. 2001, A&A, 371, 1118
Masciadri, E., de Gouveia Dal Pino, E. M., Raga, A. C., & Noriega-Crespo, A. 2002a, ApJ, 580, 950
Masciadri, E., Velázquez, P. F., Raga, A. C., Cantó, J., & Noriega-Crespo, A. 2002b, ApJ, 573, 260
Raga, A. C., & Biro, S. 1993, MNRAS, 264, 758
Raga, A. C., Cabrit, S., Dougados, C., & Lavalley, C. 2001, A&A, 367, 959
Raga, A. C., Cantó, J., Binette, L., & Calvet, N. 1990, ApJ, 364, 601
Raga, A. C., Cantó, J., & Cabrit, S. 1998, A&A, 332, 714
Raga, A. C., Cantó, J., De Colle, F., Esquivel, A., Kajdic, P., Rodríguez-González, A., & Velázquez, P. F. 2009, in Protostellar Jets in Context, ed. K. Tsinganos, T. Ray, & M. Stute (Berlin: Springer), 295
Raga, A. C., De Colle, F., Kajdic, P., Esquivel, A., & Cantó, J. 2007, A&A, 465, 879
Raga, A. C., & Noriega-Crespo, A. 1998, AJ, 116, 2943
Raga, A. C., Riera, A., & González-Gómez, D. I. 2010, A&A, 517, 20
Raga, A. C., Riera, A., Masciadri, E., Beck, T., Böhm, K. H., & Binette, L. 2004, AJ, 127, 1081
Raga, A. C., Velázquez, P. F., Cantó, J., & Masciadri, E. 2002, A&A, 395, 647
Rees, M. J. 1978, MNRAS, 184, 61
Reipurth, B. 1989, Nature, 340, 42
Reipurth, B., Bally, J., Graham, J. A., Lane, A. P., & Zealy, W. J. 1986, A&A, 164, 51
Reipurth, B., Hartigan, P., Heathcote, S., Morse, J. A., & Bally, J. 1997, AJ, 114, 757
Reipurth, B., & Heathcote, S. 1992, A&A, 257, 693
Reipurth, B., Heathcote, S., Morse, J., Hartigan, P., & Bally, J. 2002, AJ, 123, 362
Reipurth, B., Raga, A. C., & Heathcote, S. 1992, ApJ, 392, 145
Rosen, A., & Smith, M. D. 2003, MNRAS, 343, 181
__________. 2004, MNRAS, 347, 1097
Smith, M. D., & Rosen, A. 2005, MNRAS, 357, 579
Tesileanu, O., Massaglia, S., Mignone, A., Bodo, G., & Bacciotti, F. 2009, A&A, 507, 581
Völker, R., Smith, M. D., Suttner, G., & Yorke, H. W. 1999, A&A, 343, 953
Wilson, M. J. 1984, MNRAS, 209, 923

F. De Colle: Astronomy and Astrophysics Department, University of California, Santa Cruz, CA 95064, USA (fabio@ucolick.org).
P. Kajdic: Instituto de Geofísica, Universidad Nacional Autónoma de México, 04510 D.F., Mexico (primoz@geofisica.unam.mx)
D. López-Cámara and A. C. Raga: Instituto de Ciencias Nucleares, Universidad Nacional Autónoma de México, Apdo. Postal 70-543, 04510 D.F., Mexico (raga@nucleares.unam.mx, diegorretas@gmail.com.)
A. Noriega-Crespo: Spitzer Science Center, California Institute of Technology, Pasadena, CA 91125, USA (alberto@ipac.caltech.edu).

Revista Mexicana de Astronomía y Astrofísica, **47**, 289–295 (2011)

AN INTEPRETIVE BALLISTIC MODEL FOR QUASI-SYMMETRIC BIPOLAR JET SYSTEMS

A. C. Raga,[1] A. Noriega-Crespo,[2] J. C. Rodríguez-Ramírez,[1] V. Lora,[3] K. R. Stapelfeldt,[4] and S. J. Carey[2]

Received 2011 April 10; accepted 2011 June 6

RESUMEN

Presentamos un modelo analítico, balístico para sistemas de chorros/contra-chorros cuasi-simétricos, considerando tanto el caso no relativista como el relativista. El modelo considera la presencia de asimetrías en el tiempo y en la velocidad de eyección, las cuales producen diferencias entre las posiciones de los nudos a lo largo del chorro y del contra-chorro. Un ajuste de las predicciones del modelo no relativista a observaciones de dos flujos HH cuasi-simétricos (HH 34 y HH 111) nos permite obtener las magnitudes de las asimetrías de tiempo y velocidad de eyección de estos sistemas.

ABSTRACT

We present an analytic, ballistic model for quasi-symmetric jet/counterjet systems, considering both the non-relativistic and the relativistic cases. The model considers the presence of ejection time and velocity asymmetries, which produce offsets between the positions of the knots in jet/counterjet pairs. A fit of the non-relativistic model predictions to observations of two quasi-symmetric HH outflows (HH 34 and HH 111) allows us to obtain the magnitudes of the ejection time and velocity asymmetries of these systems.

Key Words: Herbig-Haro objects — infrared: ISM — ISM: individual objects (HH 34, HH 111) — ISM: jets and outflows — stars: formation

1. INTRODUCTION

Many HH outflows do not have well defined symmetries between the red- and blue-shifted lobes. Examples of this are HH 32 (in which the red-shifted lobe is not well developed, see e.g., Curiel et al. 1997) and HH 262 (the outflow from the L1551 IRS5 source, which shows a very complex structure at all wavelengths, see e.g., López et al. 2008).

Other HH objects show at least some degree of similarity between the two outflow lobes. Gyul'budagyan (1984) presents a discussion of the partially symmetric bipolar structure of the HH 1/2 outflow. The deviations from perfect symmetry in bipolar HH outflows were discussed by Bally & Reipurth (2001) and Woitas et al. (2002), who studied the asymmetries in the ejection density and velocity between the two outflow lobes.

Some IR bipolar outflows from young stellar objects (YSOs) show a surprising degree of "knot by knot" symmetry between the two outflow lobes. Examples of this are HH 212 (see, e.g., Smith, O'Connell, & Davis 2007; Cabrit et al. 2007) and HH 211 (e.g., Lee et al. 2010). In the well studied HH 34 and HH 111 optical outflows, it has been noted that good jet/counterjet knot symmetries are also present, particularly when one combines optical with IR observations (in which the highly obscured counterjets are detected). This was seen in HH 111 by Gredel & Reipurth (1994) and in HH 34 by García López et al. (2008).

Recent IR images obtained with the IRAC camera of *Spitzer* of HH 34 (Raga et al. 2011) and HH 111 (Noriega-Crespo et al. 2011) give us the possibility of directly measuring the positions of the knots (relative to the source) along the jet and counterjet in a single image, and to carry out a quantitative analysis of the degree of symmetry in the

[1]Instituto de Ciencias Nucleares, Universidad Nacional Autónoma de México, Mexico.

[2]SPITZER Science Center, California Institute of Technology, CA, USA.

[3]Astronomisches Rechen-Institut Zentrum für Astronomie der Universität Heidelberg, Germany.

[4]Jet propulsion Laboratory, California Institute of Technology, CA, USA.

outflows. Such an analysis was not possible before because the HH 34 and 111 jets, counterjets, and outflow sources were not simultaneously detected in previous optical and/or near-IR images. Therefore, the *Spitzer* images open up a new possible analysis of HH outflows, because even though they have somewhat lower angular resolution than previous optical/IR images, they simultaneously show the source and the knots along the two outflow lobes.

Motivated by these new observations, in the present paper we develop a model of a jet with quasi-symmetric ejections of ballistic knots. The model predicts the behavior of the spatial offsets between jet/counterjet knot pairs as a function of increasing distance from the outflow source. The predicted dependence can then be compared with the knot positions measured in observed HH outflows in order to constrain the model parameters. A simpler model of this kind was described by Raga et al. (2011).

The paper is organized as follows. The ballistic, binary ejection model is described in § 2 (both the non-relativistic and the relativistic cases are considered). An application of the non-relativistic model to the observed positions of the jet/counterjet knots in HH 34 and 111 is described in § 3. Finally, the implications of the results are discussed in § 4.

2. A BALLISTIC, QUASI-SYMMETRIC BINARY EJECTION MODEL

2.1. *Non-relativistic flows*

Let us consider a non-relativistic, bipolar ejection with imperfect symmetry. In one direction (along the "jet"), a clump is ejected at a time τ with a velocity v_j (projected on the plane of the sky). In the opposite direction (along the "counterjet"), a clump is ejected at a time $\tau + \Delta\tau$, with a velocity $v_j - \Delta v$. If the parcels are ballistic, at a later time t they will be at distances x_j and x_{cj} (on the plane of the sky, along the jet and the counterjet, respectively) given by:

$$x_j = (t-\tau)v_j\,; \quad x_{cj} = (t-\tau-\Delta\tau)(v_j-\Delta v)\,. \tag{1}$$

From this equation, one obtains that the offset $\Delta x = x_j - x_{cj}$ (between the positions of the jet and counterjet knots) grows with distance from the source, following

$$\Delta x = x_j - x_{cj} = \Delta\tau v_j + \frac{\Delta v}{v_j}x_j\,, \tag{2}$$

where we have neglected the term $\Delta\tau\,\Delta v$ (which involves the product of the two perturbations).

Now, let us assume that we have an ensemble of knot pairs, with $\Delta\tau$ and Δv values uniformly distributed in intervals $[\tau_0 - \Delta\tau_0, \tau_0 + \Delta\tau_0]$ and $[v_0 - \Delta v_0, v_0 + \Delta v_0]$, respectively. In other words, we allow for an intrinsic asymmetry in the ejection velocity Δv and in the time-delay $\Delta\tau$ between the jet/counterjet ejections.

The ensemble average of equation (2) is:

$$\begin{aligned} <\Delta x> &= \int_{v_0-\Delta v_0}^{v_0+\Delta v_0}\int_{\tau_0-\Delta\tau_0}^{\tau_0+\Delta\tau_0} \Delta x\;\frac{d\Delta\tau\, d\Delta v}{4\Delta\tau_0\Delta v_0} \\ &= \tau_0 v_j + \left(\frac{v_0}{v_j}\right)x_j\,. \end{aligned} \tag{3}$$

Therefore, the ensemble average of Δx as a function of x_j (where x_j is the distance to the successive knots measured along the jet) is a straight line with intercept a_1 and slope b_1 such that:

$$a_1 = \tau_0 v_j\,; \qquad b_1 = \frac{v_0}{v_j}\,. \tag{4}$$

We should note that if we have an error of magnitude Δx_s in the estimated position of the source, we will obtain $a_1 = \tau_0 v_j \pm \Delta x_s$.

Also of interest is the quadratic average:

$$\begin{aligned} <(\Delta x)^2> =& \int_{v_0-\Delta v_0}^{v_0+\Delta v_0}\int_{\tau_0-\Delta\tau_0}^{\tau_0+\Delta\tau_0}\Bigg[(\Delta\tau)^2 v_j^2 + \left(\frac{\Delta v x_j}{v_j}\right)^2 \\ & + 2\Delta\tau\Delta v x_j\Bigg]\frac{d\Delta\tau\, d\Delta v}{4\Delta\tau_0\Delta v_0} \\ =& \, v_j^2\left(\tau_0^2 + \frac{\Delta\tau_0^2}{3}\right) + \left(\frac{x_j}{v_j}\right)^2\left(v_0^2 + \frac{\Delta v_0^2}{3}\right) + \tau_0 v_0 x_j\,. \end{aligned} \tag{5}$$

Therefore, the ensemble average of $(\Delta x)^2$ has a quadratic, $<(\Delta x)^2> = a_2 + b_2 x_j + c_2 x_j^2$ dependence with:

$$a_2 = v_j^2\left(\tau_0^2 + \frac{\Delta\tau_0^2}{3}\right)\;; \quad c_2 = \left(\frac{v_0}{v_j}\right)^2 + \frac{1}{3}\left(\frac{\Delta v_0}{v_j}\right)^2\,, \tag{6}$$

and with $b_2 = a_1 b_1$ given by the results of the fit to the $<\Delta x>$ vs. x_j dependence (see equations 4 and 5).

To summarize, if one observes an outflow in which pairs of jet/counterjet knots can be identified, one has to make fits to the Δx vs. x_j and $(\Delta x)^2$ vs. x_j dependencies (where $\Delta x = x_j - x_{cj}$, the observed positional asymmetry between the jet/counterjet knot pairs). If one has an independent estimate of the spatial velocity v_j of the knots, the coefficients of the fits (see equations 4 and 6) directly give us the mean and half width of the ejection time (τ_0 and $\Delta\tau_0$) and velocity (v_0 and Δv_0) distributions.

2.2. *Relativistic flows*

Let us now consider the problem of quasi-symmetric, binary ejections at relativistic velocities. In § 2.1 (in which we considered a non-relativistic flow), we did not introduce the effect of projection onto the plane of the sky because the distances from the source and the jet velocity have the same plane-of-the-sky projection (and therefore, one can work with the projected distances and velocities).

In the case of a relativistic binary ejection, the clump ejected along the jet at a time τ with an intrinsic velocity v_j will be at a time t at a projected distance (from the source):

$$x_j = \frac{(t-\tau)v_j \cos\phi}{1 - v_j \sin(\phi/c)}\,, \tag{7}$$

where ϕ is the angle (towards the observer) between the jet axis and the plane of the sky, and c is the speed of light.

The clump ejected along the counterjet at a time $t + \Delta\tau$ with a velocity $v_j - \Delta v$ will be at a time t at a projected distance:

$$x_{cj} = \frac{(t-\tau-\Delta\tau)(v_j - \Delta v)\cos\phi}{1 + (v_j - \Delta v)\sin(\phi/c)}\,. \tag{8}$$

Combining equations (7-8) and expanding in a Taylor series up to first order in $\Delta\tau$ and Δv we obtain:

$$\Delta x = x_j - x_{cj} = \frac{\Delta\tau v_j \cos\phi}{1 + v_j \sin(\phi/c)}$$
$$+\left[\frac{2v_j \sin(\phi/c)}{(1+v_j\sin(\phi/c))} + \frac{(1-v_j\sin(\phi/c))(\Delta v/v_j)}{(1+v_j\sin(\phi/c))^2}\right] x_j\,. \tag{9}$$

Carrying out the ensemble averages described in § 2.1, we then derive:

$$<\Delta x> = A_1 + B_1 x_j\,;\ \ <(\Delta x)^2> = A_2 + B_2 x_j + C_2 x_j^2\,, \tag{10}$$

with

$$A_1 = \tau_0 v_j A\,, \qquad B_1 = B + C\frac{v_0}{v_j}\,,$$

$$A_2 = A^2\left(\tau_0^2 + \frac{\Delta\tau_0^2}{3}\right)v_j^2\,,\ \ B_2 = 2A(Bv_j + Cv_0)\tau_0\,,$$

$$C_2 = \frac{C^2}{v_j^2}\left(v_0^2 + \frac{\Delta v_0^2}{3}\right) + B^2 + 2BC\frac{v_0}{v_j}\,, \tag{11}$$

where A, B and C are the dimensionless functions

$$A = \frac{\cos\phi}{1+v_j\sin(\phi/c)}\,,\quad B = \frac{2v_j\sin(\phi/c)}{(1+v_j\sin(\phi/c))}\,,$$

$$C = \frac{1 - v_j\sin(\phi/c)}{(1+v_j\sin(\phi/c))^2}\,. \tag{12}$$

A, B and C are functions of order unity (except when $1 + v_j \sin(\phi/c) \ll 1$) for relativistic jets, with $v_j \sim c$. For $v_j \ll c$, they have limits $A = C = 1$ and $B = 0$. Inserting these values in equation (11) it is clear that we recover the non-relativistic equations (3–5) (considering that the velocities used in equation 11 correspond to the full spatial motion and not the projection on the plane of the sky considered in equations 3–5).

3. AN APPLICATION OF THE MODEL TO TWO HH JETS

3.1. *Results of the model fit*

We now apply the non-relativistic ballistic ejection model described in § 2.1 to two HH jets: HH 34 and HH 111. We first calculate least squares fits of the jet/counterjet knot offsets $\Delta x = x_j - x_{cj}$ and of $(\Delta x)^2$ as a function of distance x_j from the source. We then use the coefficients from the fits (together with an estimate of the knot velocities v_j) to constrain the ejection time ($\tau_0 \pm \Delta\tau_0$) and ejection velocity ($v_0 \pm \Delta v_0$) distributions resulting in the observed jet/counterjet asymmetries.

Given the fact that the distances and velocities along the jet/counterjet have identical projections onto the plane of the sky, we carry out the fitting procedure using the angular distances and proper motion velocities measured for the knot pairs. To obtain physical values from the angular distances and velocities, we assume a distance of 417 pc to HH 34 and 111 (see Menten et al. 2007).

3.2. *The observations*

The observations of HH 34 and HH 111 were downloaded from the *Spitzer* Heritage Archive[5]. They are part of our original General Observer (GO) program 3315 (PI Noriega-Crespo) obtained with the infared camera IRAC (Fazio et al. 2004) and the infrared photometer MIPS (Rieke et al. 2004) in March 28, 2005. The high quality of the archival images (Post Basic Calibrated Data or Post-BCD; S18.7 products) was enough for our purposes and no further processing was required. The HH 34 and HH 111 observations with IRAC were taken in its four channels (1, 2, 3, 4) = (3.6, 4.5, 5.8 & 8.0 μm) and with a total integration time per pixel of 360 sec, using 30 sec High Dynamic Range (HDR) exposures. The final images are sampled with 0.6″ per pixel,

[5] `http://sha.ipac.caltech.edu/applications/Spitzer/SHA`.

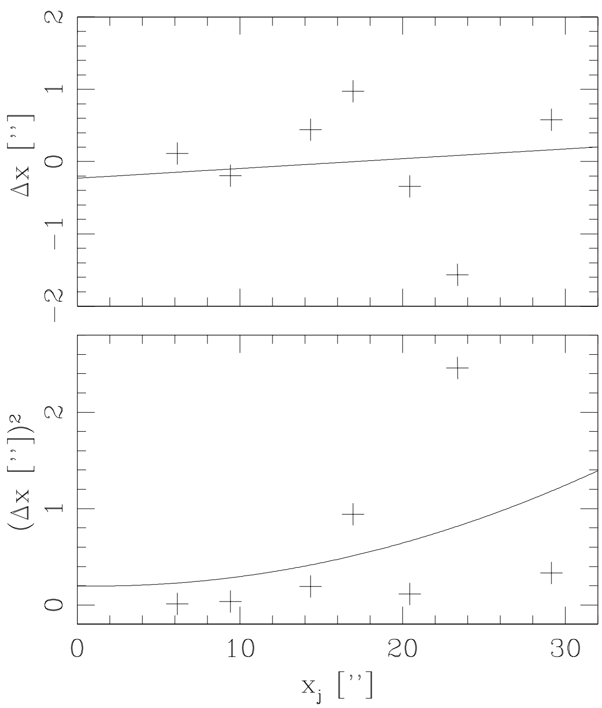

Fig. 1. Model fit to the HH 34 jet/counterjet knot pairs. We take the positions of the knots within 30″ from the outflow source (from Raga et al. 2011) and plot $\Delta x = x_j - x_{cj}$ (the jet/counterjet knot position offset, top graph) and $(\Delta x)^2$ (bottom graph) as a function of x_j. The straight line in the top graph and the curve in the bottom graph show the model fits, which result in the parameters given in Table 1.

nearly one third of the standard ∼2″ IRAC angular resolution.

As described in Raga et al. (2011) and Noriega-Crespo et al. (2011), given the collisional excitation characteristics of young stellar outflows like HH 34 and 111, the emission in the IRAC bandpasses is likely to be dominated by the pure rotational H_2 lines (e.g., Noriega-Crespo et al. 2004a,b; Looney, Tobin & Kwon 2007; Tobin et al. 2007; Ybarra & Lada 2009; De Buizer & Vacca 2010). Finally, in the HH 111 image we carried out astrometry of several field stars in order to correctly locate the position of the VLA 1 source (the source of the HH 111 outflow, see, e.g., Rodríguez et al. 2008).

3.3. *The HH 34 knots*

For the HH 34 outflow, we consider the 7 quasi-symmetric knot pairs detected in the *Spitzer* image of Raga et al. (2011). These knots lie at angular distances <30″ from the source, and have a clear correspondence between the jet and the counterjet.

TABLE 1

FITS TO THE HH 34/111 KNOTS

	HH 34	HH 111
a_1	$(-0.23 \pm 0.72)''$	$(2.19 \pm 0.85)''$
b_1	0.024 ± 0.039	0.027 ± 0.011
a_2	$(0.20 \pm 0.48)['']^2$	$(8.5 \pm 4.1)['']^2$
c_2	$(1.26 \pm 1.10) \times 10^{-3}$	$(0.93 \pm 0.42) \times 10^{-3}$
v_j	150 km s^{-1}	240 km s^{-1}
τ_0	(-3.0 ± 9.5) yr	(18.1 ± 7.0) yr
v_0	(2.0 ± 5.9) km s^{-1}	(6.5 ± 2.6) km s^{-1}
$\Delta\tau_0$	(8.8 ± 17.4) yr	(27.7 ± 20.5) yr
Δv_0	(9.0 ± 5.6) km s^{-1}	(10.9 ± 5.8) km s^{-1}

The results of the least squares fits to the Δx vs. x_j and $(\Delta x)^2$ vs. x_j dependencies are shown in Figure 1. The coefficients of the (linear Δx vs. x_j and quadratic $(\Delta x)^2$ vs. x_j) fits, together with the errors estimated through the fitting procedure, are given in Table 1.

Proper motion measurements (see, e.g., Reipurth et al. 2002) indicate that the knots close to the source of the HH 34 system have plane of the sky velocities $v_j \approx 150$ km s^{-1}. Using this velocity and the parameters derived from the fits, from equations (4–6) we obtain the mean values of the widths of the ejection time (τ_0 and Δv_0) and of the ejection velocity (v_0 and Δv_0) distributions. The resulting values (together with their uncertainties) are given in Table 1.

3.4. *The HH 111 knots*

Noriega-Crespo et al. (2011) present a *Spitzer* image of the HH 111 system. This system does not show such a clearly symmetric structure as the HH 4 outflow. This fact is illustrated in Figure 2.

From the observed jet and counterjet structures, we choose a set of 5 well defined knot pairs which appear to have clear jet/counterjet correspondences (see Figure 2). We then use these 5 knot pairs to obtain the Δx vs. x_j and $(\Delta x)^2$ vs. x_j dependencies. The fits to these dependencies are shown in Figure 3, and the resulting coefficients are given in Table 1.

From the values of the coefficients from the fits and a $v_j \approx 240$ km s^{-1} plane of the sky velocity (see, e.g., Hartigan et al. 2001), we obtain the parameters of the ejection time and velocity distributions (τ_0, $\Delta\tau_0$ and v_0, Δv_0, respectively). These parameters are given in Table 1.

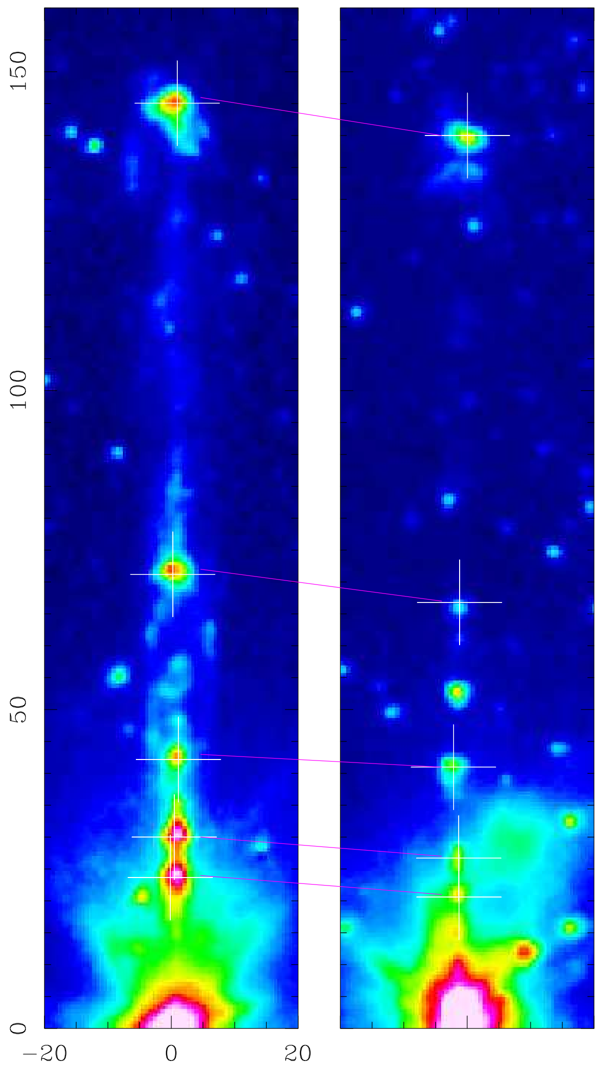

Fig. 2. The HH 111 *Spitzer* IRAC I2 band image of Noriega-Crespo et al. (2011), displayed in two frames. The left frame shows the E lobe, and the right frame the W lobe of HH 111. In both cases, the outflow axis has been rotated so that the outflow is parallel to the ordinate. In both frames, the source is placed at the origin of the reference system. The arrows indicate the chosen jet/counterjet knot pairs, and the crosses show the positions determined from parabolic fits to the emission peaks of the knots. The axes are labeled in arcseconds. The color figure can be viewed online.

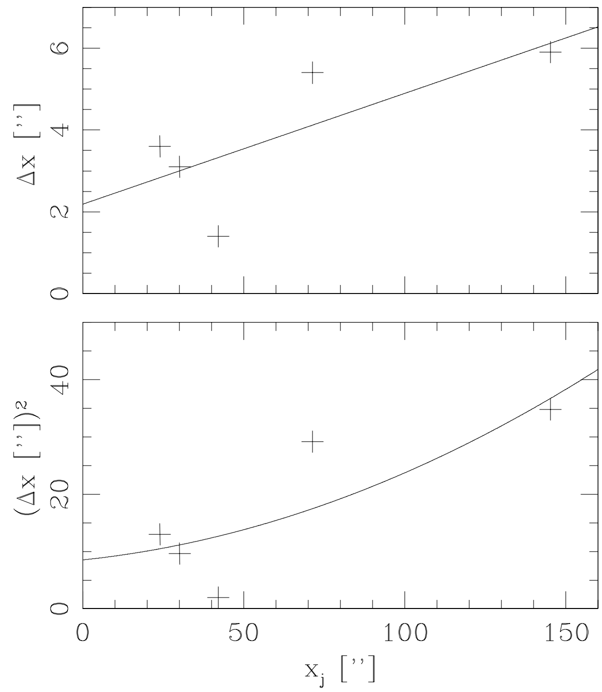

Fig. 3. Model fit to the HH 111 jet/counterjet knot pairs. We take the positions of the knot pairs shown in Figure 2 and plot Δx (top graph) and $(\Delta x)^2$ (bottom graph) as a function of x_j. The straight line in the top graph and the curve in the bottom graph show the model fits, which result in the parameters given in Table 1.

3.5. *Discussion*

From Table 1, we see that the ejection asymmetries deduced for the HH 34 and HH 111 outflows differ from each other in a significant way. If we look at the average values τ_0 and v_0 of the ejection time and velocity offsets (respectively), we find that:

- the knot structure of HH 34 implies ejection asymmetries with average time [$\tau_0 = (-3.0 \pm 9.5)$ yr] and velocity [$v_0 = (2.0 \pm 5.9)$ km s^{-1}] offsets which are not significantly different from zero,

- the positions of the knots of HH 111 imply non-zero average time [$\tau_0 = (18.2 \pm 7.1)$ yr] and velocity [$v_0 = (6.5 \pm 2.6)$ km s^{-1}] offsets.

As it is explained after equation (4), the non-zero value of τ_0 determined for HH 111 could be due to an error in the estimated position for the outflow source. For HH 111 the required offset would be $\Delta x_s = \tau_0 v_j \approx 2''.2$. Given the fact that we have located the source of HH 111 with an accuracy of better than one pixel ($\approx 0''.6$), it is clear that the average time offset that we find for the HH 111 ejections is not dominated by a possible error in the position of the outflow source. The $v_0 = (6.5 \pm 2.6)$ km s^{-1} average velocity offset also is undoubtedly a real effect.

For the widths of the ejection time and velocity offset distributions (see Table 1) we obtain that:

- HH 34 has a time offset distribution with a $\Delta\tau_0 = (8.9 \pm 17.3)$ yr width, which is not significantly different from zero. The velocity offset distribution has a $\Delta v_0 = (9.0 \pm 5.6)$ km s^{-1} width,
- HH 111 implies a time offset distribution with $\Delta\tau_0 = (27.7 \pm 20.5)$ yr and $\Delta v_0 = (10.9 \pm 5.8)$ km s^{-1}.

4. CONCLUSIONS

We have presented a simple, ballistic binary ejection model for interpreting the observed knot structures of quasi-symmetric bipolar outflows. In this model it is assumed that knots are ejected with small time ($\Delta\tau$) and velocity (Δv) offsets, which result in a slightly asymmetric propagation as the knots move away from the source. It is also assumed that these offsets have uniform distributions with mean values τ_0 and v_0 and half-widths $\Delta\tau_0$ and Δv_0 (for the time and velocity offsets, respectively). Under these assumptions, we show that the values of τ_0, v_0, $\Delta\tau_0$ and Δv_0 can be recovered from observations of the spatial jet/counterjet knot offsets $\Delta x = x_j - x_{cj}$ for a system of identifiable knot pairs.

We then apply this method to recent *Spitzer* observations of the HH 34 (Raga et al. 2011) and HH 111 (Noriega-Crespo et al. 2011) jet/counterjet systems. We find that the knots of the HH 34 outflow imply binary ejections with basically zero systematic jet/counterjet ejection times or velocities. The dispersion of the ejection times also lies below the errors due to small number statistics. However, the observed spatial distribution of the jet/counterjet knot offsets does imply a non-zero value for the width of the ejection velocity distribution [$\Delta v_0 = (9.0 \pm 5.6)$ km s^{-1}, see Table 1].

As noted by Raga et al. (2011), the good time coordination of the binary ejections of HH 34 imply that the triggering of the ejection events occurs in a compact region. Even though we are not able to obtain a well constrained value for the time-offsets between the jet and counterjet knots, we can take as an estimate either the value of τ_0 or of $\Delta\tau_0$ (both $\sim$5 yr, see Table 1). If we assume a (sound or Alfvén) wave propagation velocity $v_s \sim 3$ km s^{-1} for the jet formation region, this coordination timescale then implies a size $d \sim 3$ AU.

A clearly different result is obtained for HH 111. The jet/counterjet knot pairs of this system imply a clear bias towards one side, with the clumps in the W lobe being ejected on average a time $\tau_0 = (18.2 \pm 7.1)$ yr later and $v_0 = (6.5 \pm 2.6)$ km s^{-1} slower than the corresponding knots in the E lobe. The observations also imply non-zero widths for the ejection time and velocity distributions ($\Delta\tau_0 = (27.7 \pm 20.5)$ yr and $\Delta v_0 = (10.9 \pm 5.8)$ km s^{-1}, respectively, see Table 1).

For HH 111 we then conclude that an intrinsically asymmetric ejection is taking place, with one side producing faster and earlier ejections than the other. Such an effect is seen at least in one other YSO outflow: Curiel et al. (2006) present high resolution radio continuum maps at many epochs of the Cepheus A HW2 outflow, and they find that the knots are ejected $\sim$2 yr earlier in one of the two lobes. It appears that in HH 111 we are seeing a similar effect, but with a time-delay that is larger by one order of magnitude.

The systematic velocity offset ($v_0 \approx 6.5$ km s^{-1}, see Table 1) of the HH 111 jet/counterjet knots could actually be the result of a non-ballistic behavior of the motion. For example, if the knots along one of the outflow lobes were interacting directly with a denser medium, this interaction could lead to a lower velocity knot propagation velocity. However, as the knots are traveling into the wake of previous ejection episodes, such a direct knot/environment interaction seems unlikely. Also, the different velocities could in principle be the result of different orientations of the lobes with respect to the plane of the sky. However, the very small deviations from a straight path on the plane of the sky observed in HH 111 (see Noriega-Crespo et al. 2011) do not favor this scenario.

The asymmetries in the ejections of the HH 34 and 111 knots in principle provide constraints on the jet production model. However, in many cases it is not yet possible to apply these constraints because the present models for the production of outflows from young stars are either stationary (e.g., Salmeron, Königl, & Wardle 2011) or do not appear to incorporate the mechanism(s) that produce the knots observed along HH jets (e.g., Ramsey & Clarke 2011; Stute et al. 2010; Yamada et al. 2009). A recent analysis of models producing asymmetric ejections (as the result of the presence of a time-independent magnetospheric magnetic field with both a dipole and a quadrupole component) is given by Lovelace et al. (2010), who for some parameters obtain outflows that "flip-flop" with a period of $\sim$30 days. Given the fact that this predicted timescale is a factor of 10–100 times too small for explaining the asymmetries observed for the HH 34 and 111 knots, it is clear that if one is to rescue the ideas of Lovelace et al. (2010) it will be necessary to introduce other elements. A possibility would be the presence of a time-variability in the magnetospheric magnetic field, as explored by De Colle, García, &

Murphy (2008). The magnetospheric magnetic field could have time-dependencies on timescales similar to the solar cycle (i.e., with periods $\sim$20 yr).

From the observational point of view, significant progress will be possible through the analysis of other bipolar HH jets. Such studies should include both objects with good jet/counterjet symmetries (such as HH 211, see, e.g., Lee et al. 2010) and objects with evident asymmetries (such as HH 228, see Wang & Henning 2009).

Finally, in § 2.2 we have described a model for relativistic, quasi-symmetric binary ejections. An application of this model to observations of relativistic jets is left for a future paper.

This work was supported by the Conacyt grants 61547, 101356 and 101975.

REFERENCES

Bally, J., & Reipurth, B. 2001, ApJ, 546, 299
Cabrit, S., Codella, C., Gueth, F., Nisini, B., Gusdorf, A., Dougados, C., & Bacciotti, F. 2007, A&A, 468, L29
Curiel, S., Raga, A. C., Raymond, J. C., Noriega-Crespo, A., & Cantó, J. 1997, AJ, 114, 2736
Curiel, S., et al. 2006, ApJ, 638, 878
De Buizer, J. M., & Vacca, W. D. 2010, AJ, 140, 196
De Colle, F., Gracía, J., & Murphy, G. 2008, ApJ, 688, 1137
Fazio, G., et al. 2004, ApJS, 154, 10
García López, R., Nisini, B., Giannini, T., Eislöffel, J., Bacciotti, F., & Podio, L. 2008, A&A, 487, 1019
Gredel, R., & Reipurth, B. 1994, A&A, 289, L19
Gyul'budagyan, A. L. 1984, Astrophysics, 20, 75
Hartigan, P., Morse, J. A., Reipurth, B., Heathcote, S., & Bally, J. 2001, ApJ, 559, L157
Lee, C.-F., Hasegawa, T. I., Hirano, N., Palau, A., Shang, H., Ho, P. T. P., & Zhang, Q. 2010, ApJ, 713, 731
Looney, L. W., Tobin, J. J., & Kwon, W. 2007, ApJ, 670, L131
López, R., García-Lorenzo, B., Sánchez, S. F., Gómez, G., Estalella, R., & Riera, A. 2008, MNRAS, 391, 1107
Lovelace, R. V. E., Romanova, M. M., Ustyugova, G. V., & Koldoba, A. V. 2010, MNRAS, 408, 2083
Menten, K. M., Reid, M. J., Forbrich, J., & Brunthaler, A. 2007, A&A, 474, 515
Noriega-Crespo, A., et al. 2004a, ApJS, 154, 352
Noriega-Crespo, A., et al. 2004b, ApJS, 154, 402
Raga, A. C., Noriega-Crespo, A., Lora, V., Stapelfeldt, K. R., & Carey, S. J. 2011, ApJ, 730, L17
Ramsey, J. P., & Clarke, D. A. 2011, ApJ, 728, L11
Reipurth, B., Heathcote, S., Morse, J., Hartigan, P., & Bally, J. 2002, AJ, 123, 362
Rieke, G. H., et al. 2004, ApJS, 154, 25
Rodríguez, L. F., Torrelles, J. M., Anglada, G., & Reipurth, B. 2008, AJ, 136, 1852
Salmeron, R., Königl, A., & Wardle, M. 2011, MNRAS, 412, 1162
Smith, M. D., O'Connell, B., & Davis, C. J. 2007, A&A, 466, 565
Stute, M., Gracía, J., Tsinganos, K., & Vlahakis, N. 2010, A&A, 516, A6
Tobin, J. J., Looney, L. W., Mundy, L. G., Kwon, W., & Hamidouche, M. 2007, ApJ, 659, 1404
Wang, H., & Henning, T. 2009, AJ, 138, 1072
Woitas, J., Ray, T. P., Bacciotti, F., Davis, C. J., & Eislöffel, J. 2002, ApJ, 580, 336
Yamada, M., Machida, M. N., Inutsuka, S., & Tomisaka, K. 2009, ApJ, 703, 1141
Ybarra, J. E., & Lada, E. A. 2009, ApJ, 695, 120

S. J. Carey and A. Noriega-Crespo: Spitzer Science Center, California Institute of Technology, Pasadena, CA 91125, USA (carey, alberto@ipac.caltech.edu).
V. Lora: Astronomisches Rechen-Institut Zentrum für Astronomie der Universität Heidelberg, Mönchhofstr. 12-14 69120 Heidelberg, Germany (vlora@ari.uni-heidelberg.de).
A. C. Raga and J. C. Rodríguez-Ramírez: Instituto de Ciencias Nucleares, Universidad Nacional Autónoma de México, Apdo. Postal 70-543, 04510 D.F., Mexico (raga, juan.rodriguez@nucleares.unam.mx).
K. R. Stapelfeldt: Jet propulsion Laboratory, California Institute of Technology, MS 183-900, 4800 Oak Grove Drive, Pasadena, CA 91109, USA (krs@exoplanet.jpl.nasa.gov).

Revista Mexicana de Astronomía y Astrofísica, **47**, 297–307 (2011)

V1898 CYGNI: AN INTERACTING ECLIPSING BINARY IN THE VICINITY OF NORTH AMERICA NEBULA[1]

A. Dervişoğlu,[2] Ö. Çakırlı,[2,3] C. İbanoğlu,[2] and E. Sipahi[2]

Received 2011 April 12; accepted 2011 June 12

RESUMEN

Presentamos observaciones espectroscópicas de la binaria eclipsante tipo Algol, de doble línea, V1898 Cygni. El análisis de las curvas de luz en las bandas BV nos lleva a una determinación de los parámetros fundamentales de las componentes de V1898 Cygni. Los parámetros absolutos son: $M_1 = 6.054 \pm 0.037\ M_\odot$, $M_2 = 1.162 \pm 0.011\ M_\odot$, $R_1 = 3.526 \pm 0.009\ R_\odot$, $R_2 = 2.640 \pm 0.010\ R_\odot$, $T_{\rm eff_1} = 18000 \pm 600$ K, y $T_{\rm eff_2} = 6200 \pm 200$ K. Analizamos los residuos entre los tiempos observados y calculados para el eclipse medio y obtenemos una tasa de cambio del período de $\dot{P}/P = 6.68 \times 10^{-7}$ yr^{-1}. Estimamos una tasa de transferencia de masa de $1.88 \times 10^{-7}\ M_\odot$ por año. Utilizando las magnitudes infrarojas JHK y las correcciones bolométricas para la estrella primaria, calculamos la distancia al sistema V1898 Cyg como 501 ± 5 pc. Las componentes de los movimientos propios del sistema presentan alguna información sobre su pertenencia a la Nebulosa de Norteamérica.

ABSTRACT

We present spectroscopic observations of the double-lined Algol type eclipsing binary V1898 Cyg. Analyses of the BV light curves and RVs led to determination of the fundamental stellar parameters of the V1898 Cyg's components. The absolute parameters for the stars are derived as: $M_1 = 6.054 \pm 0.037\ M_\odot$, $M_2 = 1.162 \pm 0.011\ M_\odot$, $R_1 = 3.526 \pm 0.009\ R_\odot$, $R_2 = 2.640 \pm 0.010\ R_\odot$, $T_{\rm eff_1} = 18000 \pm 600$ K, and $T_{\rm eff_2} = 6200 \pm 200$ K. The residuals between the observed and computed times of mid-eclipses were analysed and a rate of the period change $\dot{P}/P = 6.68 \times 10^{-7}$ yr^{-1} was obtained; a mass transfer rate of $1.88 \times 10^{-7}\ M_\odot$ in a year is estimated. We have calculated the distance to the system V1898 Cyg as 501 ± 5 pc using the infrared JHK magnitudes and bolometric corrections for the primary star. The components of the system's proper motions present some indications about membership to the North America nebula.

Key Words: binaries: close — binaries: eclipsing — binaries: general — binaries: spectroscopic — stars: individual (V1898 Cyg)

1. INTRODUCTION

V1898 Cyg (HD 200776, BD +45° 3384, 2MASS J21035377+4619499, HIP 103968, $V = 7^m.81$, $(B-V) = +0^m.01$) was discovered to be a single-lined spectroscopic binary by Abt, Levy, & Gandet (1972). HD 200776 was included in the list of bright OB stars to be observed for the determination of galactic rotation constants and other galactic parameters. Their spectroscopic observations yield that HD 200776 is a spectroscopic binary with an orbital period of 2.9258 days. They also calculated the preliminary elements and mass function for the system. McCrosky & Whitney (1982) searched for photometric variations in some short-period spectroscopic binaries (including HD 200776) given in the Seventh Catalogue of the Orbital Elements of Spectroscopic Binary System (Batten, Fletcher, & Mann 1978). They observed abrupt drops, amounting to

[1]Based on observations collected at Catania Astrophysical Observatory (Italy) and TÜBİTAK National Observatory (Antalya, Turkey).

[2]Department of Astronomy and Space Sciences, Science Faculty, Ege University, Turkey.

[3]TÜBİTAK National Observatory, Akdeniz University Campus, Turkey.

$0^m.2 - 0^m.4$, in the brightness of the system which were inconsistent with the orbital period proposed by Abt et al. (1972). Photometric observations in the B and V-bandpass made by Halbedel (1985) revealed that HD 200776 is an eclipsing binary with both eclipses nearly identical, in contrast to the spectroscopic observations. He proposed a new orbital period of 3.0239 days, 3 percent longer than that given by Abt et al. (1972). Caton & Smith (2005, hereafter CS) published a new light curve and new times of mid-eclipses as well as a new orbital period of 1.5131273 days, nearly half that of given by Halbedel (1985). Later, Dallaporta & Munari (2006, hereafter DM) presented complete and accurate BV light curves of HD 200776 as well as three times for the mid-primary eclipse. Fortunately the same comparison star was used in the photometric observations of Halbedel (1985) and DM. No further spectroscopic observations were made for this eclipsing-spectroscopic binary after Abt et al. (1972).

The main aims of this study are: (1) to detect some lines of the secondary component; (2) to reveal radial velocities for both components; (3) to solve the radial velocity curves for the primary and secondary components on the basis of new observations in order to obtain accurate masses and radii; and (4) to determine the rotational velocities of the components and compare them with those expected for orbital synchronization.

2. SPECTROSCOPIC OBSERVATIONS

The spectra were obtained with several telescopes over the course of three years, beginning in 2007. Table 1 lists the full set of observations. The first set was observed with the Échelle spectrograph (FRESCO) at the 91 cm telescope of Catania Astrophysical Observatory. Spectroscopic observations were performed with the spectrograph fed by the telescope through an optical fibre (UV-NIR, 100 μm core diameter) and located, in a stable position, in the room below the dome level. Spectra were recorded on a CCD camera equipped with a thinned back-illuminated SITe CCD of 1k×1k pixels (size 24×24 μm). The cross-dispersed échelle configuration yields a resolution of about 22000, as deduced from the full width at half maximum of the lines of the Th-Ar calibration lamp. The spectra cover the wavelength range from 4300 to 6650 Å, split into 19 orders. In this spectral region, and in particular in the blue portion of the spectrum, there are several lines useful for measuring the radial velocity, as well as for spectral classification of the stars.

The system was also observed with the Turkish Faint Object Spectrograph Camera (TFOSC) attached to the 1.5 m RTT150 telescope on August 07–20, 2010 under good seeing conditions[4]. The wavelength coverage of each spectrum was 4100–9000 Å in 11 orders, with a resolving power of $\lambda/\delta\lambda$ 7000 at 6563 Å.

The electronic bias was removed from all spectra and we used the CRREJECT task of IRAF[5] for cosmic ray removal. The échelle spectra were extracted and wavelength calibrated by using a Fe-Ar and Th-Ar lamp source with help of the IRAF echelle package. The stability of the instruments was checked by cross-correlating the spectra of the standard star against each other using the FXCOR task in IRAF. The standard deviation of the differences between the velocities measured using FXCOR and the velocities in Nidever et al. (2002) was about 1.1 km s^{-1}.

Twenty-eight spectra of V1898 Cyg were collected during the two different seasons. Typical exposure times for the V1898 Cyg spectroscopic observations were between 2400 and 2600 s for the Catania telescope and 1200 s for the RTT150 telescope. The signal-to-noise ratio (S/N) achieved was between 70 and 115, and ∼150 depending on atmospheric condition. α Lyr (A0V), 59 Her (A3IV), ι Psc (F7V), HD 27962 (A2IV), and τ Her (B5IV) were observed during each run as radial velocity and/or rotational velocity templates. The average S/N at the continuum in the spectral region of interest was 150–200 for the standard stars.

3. SPECTROSCOPIC ANALYSIS

Double-lined spectroscopic binaries reveal two peaks in the cross-correlation function (CCF) between variable and the radial velocity template spectrum, which displace back and forth, as seen in Figure 1. The location of the peaks allows to measure the radial velocity of each component at the time of observation. The cross-correlation technique applied to digitized spectra is now one of the standard tools for the measurement of radial velocities in close binary systems.

The radial velocities of V1898 Cyg were obtained by cross-correlating échelle orders of the V1898 Cyg spectra with the spectra of the bright radial velocity standard stars α Lyr (A0V), 59 Her (A3IV) and ι Psc (F7V) (Nordström et al. 2004). For this purpose the IRAF task FXCOR was used.

[4]Further details on the telescope and the spectrograph can be found at `http://www.tug.tubitak.gov.tr`.

[5]IRAF is distributed by the National Optical Observatory, which is operated by the Association of the Universities for Research in Astronomy, inc. (AURA) under cooperative agreement with the National Science Foundation.

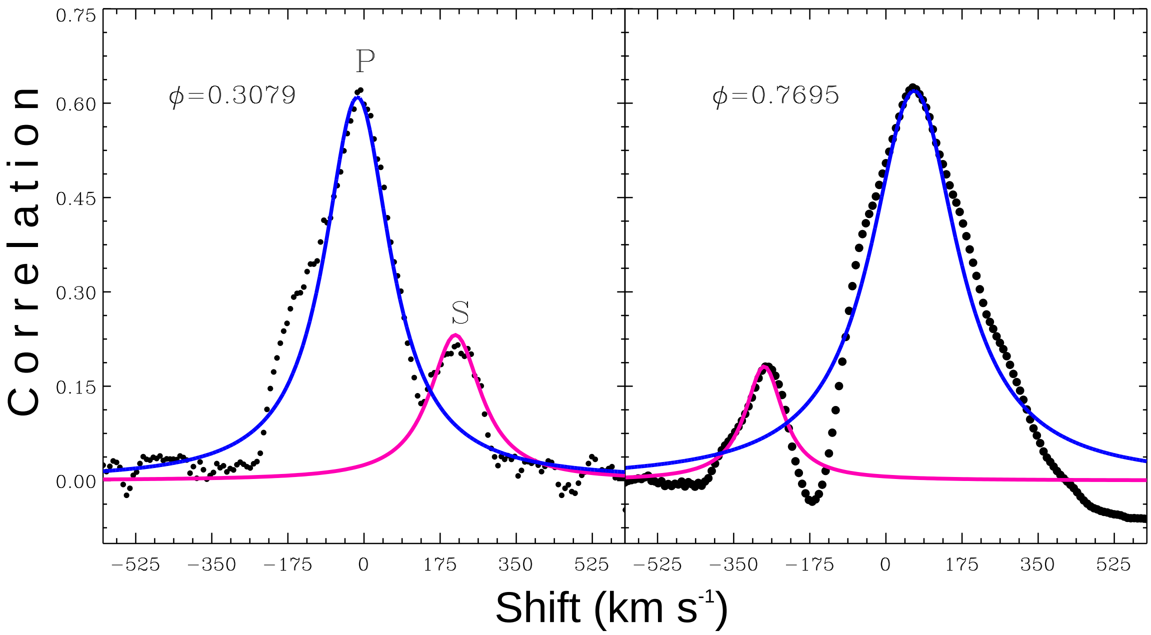

Fig. 1. Sample of Cross Correlation Functions (CCFs) between V1898 Cyg and the radial velocity template spectrum (Vega) at four different orbital phases. The color figure can be viewed online.

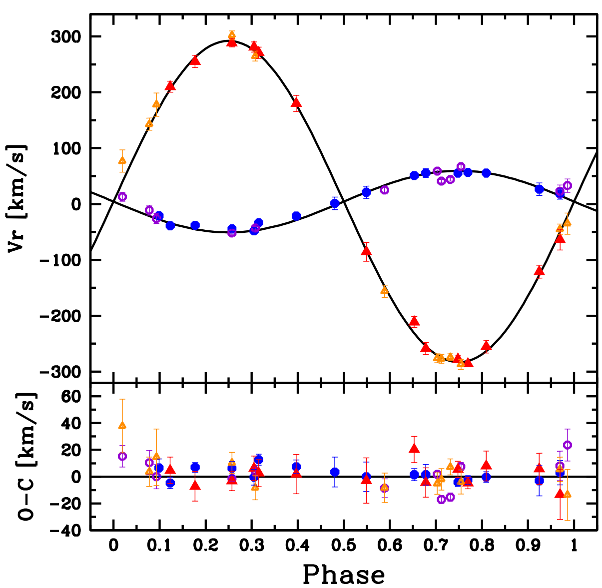

Fig. 2. Radial velocities of the primary (dots) and secondary stars (triangles) folded on an orbital period of 1.513126 days. The velocities obtained at the Catania observatory are indicated by filled symbols while those obtained at the National Observatory of Turkey by open symbols. The vertical lines show error bars of each radial velocity. The residuals between the observed and computed RVs are plotted in the lower panel. The color figure can be viewed online.

Figure 1 shows examples of CCFs of V1898 Cyg near the first and second quadrature. The two non-blended peaks correspond to each component of V1898 Cyg. We applied the cross-correlation technique to five wavelength regions with well-defined absorption lines of the primary and secondary components. These regions include the following lines: Si III 4568 Å, Mg II 4481 Å, He I 5016 Å, He I 4917 Å, He I 5876 Å. The stronger CCF peak corresponds to the more massive component that also has a larger contribution to the observed spectrum. To better evaluate the centroids of the peaks (i.e. the radial velocity difference between the target and the template), we adopted two separate Gaussian fits for the case of significant peak separation.

The radial velocity measurements, listed in Table 1 together with their standard errors, are weighted means of the individual values deduced from each order. The observational points and their error bars are displayed in Figure 2 as a function of orbital phase as calculated by means of the linear part of the ephemeris given in equation (2). The radial velocities of the secondary component of V1898 Cyg are presented for the first time in this study. The simultaneous analysis of both curves shows the semi-amplitude of the more massive, more luminous component to be $K_1 = 55.2 \pm 0.8$ km s^{-1} and $K_2 = 287.6 \pm 2.1$ km s^{-1} for the secondary component, with a systemic velocity of 4.4 ± 0.8 km $^{-1}$.

TABLE 1

RADIAL VELOCITIES OF THE V1898 CYG'S COMPONENTS[1]

HJD 2400000+	Phase	Star 1 $\mathbf{V}_p$	σ	O-C	Star 2 $\mathbf{V}_s$	σ	O-C	Remarks
54327.55412	0.5489	21.1	10.9	0.0	−85.5	16.9	−3.0	a
54328.50480	0.1772	−38.1	3.6	6.9	255.3	11.1	−7.2	a
54329.46135	0.8093	55.5	3.9	−0.3	−255.5	11.1	8.0	a
54330.47685	0.4805	1.2	11.1	3.5	···	···	···	a
54331.44914	0.1231	−38.8	4.2	−4.7	210.1	9.9	4.7	a
54335.45358	0.7695	56.7	3.3	−2.5	−285.8	4.3	−4.8	a
54336.40281	0.3969	−21.5	5.1	7.3	179.9	14.6	1.9	a
54337.46485	0.0988	−21.1	6.6	6.5	···	···	···	a
54338.44704	0.7479	55.5	3.1	−4.1	−277.7	6.1	5.5	a
54360.40110	0.2571	−44.4	5.1	6.3	288.6	7.2	−3.2	a
54361.41090	0.9245	16.6	11.2	−3.0	−121.1	11.6	5.8	a
54362.55110	0.6780	55.5	7.7	1.4	−258.6	10.9	−4.3	a
54363.50010	0.3052	−47.9	5.9	−0.5	281.1	9.2	6.1	a
54364.50527	0.9695	18.0	9.1	3.1	−63.7	18.5	−13.4	a
54365.53939	0.6530	51.1	4.5	1.4	−211.1	9.8	20.3	a
54366.54137	0.3152	−33.5	4.1	12.6	270.9	10.1	2.6	a
55387.53130	0.0777	−11.0	9.0	10.4	143.0	11.0	3.6	b
55390.46920	0.0193	13.0	8.0	15.2	77.0	20.0	37.8	b
55390.58090	0.0932	−26.0	9.0	0.0	178.0	21.0	14.6	b
55391.50380	0.7031	59.0	2.0	1.8	−276.0	8.0	−5.2	b
55391.58150	0.7544	67.0	3.0	7.4	−287.0	9.0	−3.9	b
55392.41900	0.3079	−43.0	3.0	4.1	265.0	9.0	−8.3	b
55393.41980	0.9694	23.0	11.0	8.0	−45.0	9.0	5.5	b
55394.57290	0.7314	44.0	3.0	−15.2	−274.0	6.0	7.2	b
55396.47080	0.9857	33.0	12.0	23.6	−35.0	19.0	−13.6	b
55397.38320	0.5887	25.0	7.0	−8.6	−156.0	11.0	−8.3	b
55397.56950	0.7119	41.0	3.0	−17.0	−277.0	8.0	−2.0	b
55398.39480	0.2573	−52.0	2.0	−1.4	302.0	8.0	10.2	b

[1]The columns give the heliocentric Julian date, the orbital phase, the radial velocities of the two components with the corresponding errors and residuals.

Remarks: (a) Based on Catania and (b) on TUG observations.

3.1. *Spectral classification*

The spectral types of the stars can be found either from photometry or from spectroscopy or from both. The apparent visual magnitude and colors of V1898 Cyg were estimated by Hiltner (1956) as $V = 7^m.81$, $B-V = 0^m.01$, $U-B = -0^m.82$. However the apparent magnitudes are given by Reed (2003) as $7^m.0$, $7^m.80$ and $7^m.82$ in the U, B and V passbands, respectively. On the other hand, the $B-V$ color of the system out of eclipse was determined as $0^m.01$ by Halbedel (1985). We computed the $B-V$ color of the system at the maxima as $0^m.036$ using the data given by Dallaporta & Munari (2006). The combined spectral types are given as B1 IVp by Abt et al. (1972) and B2 III by Kennedy & Buscombe (1974). The infrared magnitudes of the system are given by Cutri et al. (2003) as $J = 7^m.697$, $H = 7^m.718$ and $K = 7^m.757$. Unfortunately, intermediate- and narrow-band photometric measurements are not available. Bessell, Castelli, & Plez (1998) derive reddening-independent Q-parameter from theoretical colors as $Q = (U-B) - 0.71\,(B-V)$. They also predict an interstellar reddening for the main-sequence OB stars as $E(B-V) = (B-V) - ((U-B) - 0.71(B-V))/3$. Using the observed $(U-B)$ and $(B-V)$ colors by Hiltner (1956) we find $E(B-V) = 0^m.28$, while Dallaporta & Munari (2006) estimate the reddening as $0^m.31$.

We computed the intrinsic colors of the primary component using the JHK magnitudes as $J-H=-0^m.021\pm0^m.044$ and $H-K=-0^m.039\pm0^m.033$. V1898 Cyg is located between supergiants and dwarfs in the infrared $(J-H)-(H-K)$ diagram (Tokunaga 2000). Using the the equations given by Straižys, Corbally, & Laugalys (2008) we estimated the interstellar reddening as $E(J-H)=0^m.106\pm0^m.060$ and $E(H-K)=0^m.052\pm0^m.060$. Using the transformation equation given by Bessell et al. (1998) we find $E(B-V)=0^m.286$, in very good agreement with that found from the UBV colors. Since the observed common color index is $0^m.036$ one obtains an intrinsic $B-V$ color of $-0^m.25$ which corresponds to a B1V star in the calibrations of Papaj, Krelowski, & Wegner (1993).

We used our spectra to determine the spectral type of the primary component of V1898 Cyg. We followed the procedures of Hernández et al. (2004), choosing helium lines in the blue-wavelength region, where the contribution of the secondary component to the observed spectrum is almost negligible. From several spectra we measured EWs of HeI $\lambda\,4026, 4144, 4387, 4922$ as 0.867 ± 0.044, 0554 ± 0.062, 0.497 ± 0.090, 0.768 ± 0.028 Å, respectively. Then we used the EW-spectral type diagrams given by Hernández et al. (2004). The EWs of the helium lines indicate that the spectral type of the primary component is $B1.8\pm0.6$ which is in a agreement with that obtained from infrared photometry. The calibration of Papaj et al. (1993) gives an effective temperature of 18700 K and $B-V$ of $-0^m.21$ for a B2V star, 16800 K and $-0^m.19$ for the same spectral type but for a giant star. Therefore, we estimated an effective temperature of 18000 ± 600 K for the primary component of V1898 Cyg.

3.2. *Reddening*

The measurement of reddening is a key step in determining the distance of stars. V1898 Cyg is located in the direction of the NAP, where reddening varies from one place to other. We estimated the reddening in the $B-V$ color as $0^m.29$ using the infrared colors. On the other hand we find $E(B-V)=0^m.25$ for a star of type B2V and $E(B-V)=0^m.23$ for a B2III star. The photometric and spectroscopic determinations of the interstellar reddening seem to be in a good agreement within a 3σ error. Our spectra cover the interstellar Na I (5890 and 5896 Å) doublet, which is an excellent estimator of the reddening as demonstrated by Munari & Zwitter (1997). They calibrated a tight relation linking the Na I D1 (5890 Å) equivalent widths with the $E(B-V)$ reddening. On spectra obtained at quadratures, lines from both components are un-blended with the interstellar ones, and they can therefore be accurately measured. We derive an equivalent width of 0.52 ± 0.06 Å for the Na I D1 line, which corresponds to $E(B-V)=0^m.33\pm0.09$. Since the star is located nearly on the galactic plane ($l=87°.60$, $b=-0°.34$) and near the edge of North America nebula (NAN) such a reddening at optical wavelengths is expected.

3.3. *Rotational velocity*

The width of the cross-correlation profile is a good tool for the measurement of $v\sin i$ (see, e.g., Queloz et al. 1998). The rotational velocities ($v\sin i$) of the two components were obtained by measuring the FWHM of the CCF peaks in nine high-S/N spectra of V1898 Cyg acquired close to the quadratures, where the spectral lines have the largest Doppler-shifts. In order to construct a calibration curve FWHM-$v\sin i$, we have used an average spectrum of HD 27962, acquired with the same instrumentation. Since the rotational velocity of HD 27962 is very low but not zero ($v\sin i\simeq 11$ km s^{-1}, e.g., Royer et al. (2002) and references therein), it could be considered as a useful template for A-type stars rotating faster than $v\sin i\simeq10$ km s^{-1}. The spectrum of HD 27962 was synthetically broadened by convolution with rotational profiles of increasing $v\sin i$ in steps of 5 km s^{-1} and the cross-correlation with the original one was performed at each step. The FWHM of the CCF peak was measured and the FWHM-$v\sin i$ calibration was established. The $v\sin i$ values of the two components of V1898 Cyg were derived from the FWHM of their CCF peak and the aforementioned calibration relations, for a few wavelength regions and for the best spectra. This gave values of 110 ± 5 km s^{-1} for the primary star and 90 ± 9 km s^{-1} for the secondary star.

4. TIMES OF MINIMA AND THE ORBITAL PERIOD

Times of mid-eclipses were published by Halbedal (1985), CS, DM and Brát et al. (2008). These times of eclipses are presented in Table 2. The O-C(I) residuals are computed using the light curve elements given below,

$$\mathrm{MinI(HJD)} = 2\,450\,690.6948 + 1^d.51311\times E\,, \quad (1)$$

where the orbital period is adopted from DM. The behavior of the deviations from the linear light curve

TABLE 2

TIMES OF MID-ECLIPSES FOR V1898 CYG AND THE O-C RESIDUALS (SEE TEXT)

Minimum time (HJD-2400000)	Epoch	O-C(I)	O-C(II)	O-C(III)	Ref.
45960.6758	−3126	−0.0371	0 .0139	0.0004	1
45963.6986	−3124	−0.0406	0.0105	−0.0030	1
46010.6101	−3093	−0.0355	0.0151	0.0018	1
46013.6351	−3091	−0.0367	0.0138	0.0006	1
50690.6948	0	0.0000	0.0010	0.0010	3
52169.7772	977.5	0.0174	0.0027	0.0014	3
52185.6636	988	0.0161	0.0013	0.0000	3
52895.3220	1457	0.0259	0.0036	0.0007	2
52901.3740	1461	0.0255	0.0031	0.0002	2
52928.6107	1479	0.0262	0.0035	0.0005	3
53207.7802	1663.5	0.0269	0.0013	−0.0025	3
53226.6966	1676	0.0294	0.0036	−0.0003	3
53246.3663	1689	0.0287	0.0027	−0.0013	2
53270.5757	1705	0.0284	0.0021	−0.0020	3
54443.2559	2480	0.0483	0.0096	0.0011	4
54443.2565	2480	0.0489	0.0102	0.0017	4
54691.4070	2644	0.0494	0.0080	−0.0016	4
54691.4089	2644	0.0513	0.0099	0.0003	4
54691.4097	2644	0.0521	0.0107	0.0011	4

References: (1) Halbedel (1985), (2) Dallaporta & Munari (2006), (3) Caton & Smith (2005), (4) Brát et al. (2008).

elements O-C(II) with respect to the epoch numbers suggests an upward curved parabola. Therefore, a parabolic fit to the data was adopted, which gives,

$$\mathrm{MinI(HJD)} = 2\,450\,690.6938(8) + 1^{d}.5131260(2) \times E + 1.38(13)10^{-9} \times E^{2}\,. \qquad (2)$$

The standard mean errors in the last digits are given in parentheses. The coefficient of the quadratic term is positive, which indicates that the orbital period of the system is increasing with the epoch number. Such a quadratic ephemeris appears to a very good representation of the orbital period change of V1898 Cyg, as well as other interacting Algols. This quadratic behaviour of the O-C(II) residuals, plotted in the upper panel of Figure 3, is an indication of the secular period increase for the system. In the bottom panel of Figure 3 the O-C(III) residuals with respect to ephemeris (2) are plotted, which illustrates a good agreement between the timings and the new ephemeris. It is known that the classical Algols have an evolved less massive component which fills its Roche lobe and transfers its mass to the more massive primary star through the Lagrangian L_1 point of the system. The orbital period of the system is increasing at an average rate of $\dot{P}/P = 6.68(\pm 0.63) \times 10^{-7}$ yr^{-1} which means that the orbital period has increased by about $0.38(\pm 0.04)$ seconds in the last 24 years. The sum of the squares of residuals for the parabolic fit is 3.672×10^{-5} d^2. We limited times of mid-eclipses covering about 24 yrs. The time span of the observations is too short to reveal any abrupt period change caused by the fast mass transfer phenomenon. Of course, observations to be obtained in the coming years could indicate some hints about the nature of the orbital period change. Assuming a conservative mass transfer from the less massive component to the more massive primary star we estimate a transfer of $1.88(\pm 0.17) \times 10^{-7}$ $M_\odot$ in a year.

5. ANALYSIS OF THE LIGHT CURVES

Three light curves V1898 Cyg have been obtained and published. The first photometric observations were obtained by Halbedel (1985) between July and November, 1985. The second photometric observations were made by CS from August 22, 2001 to Oc-

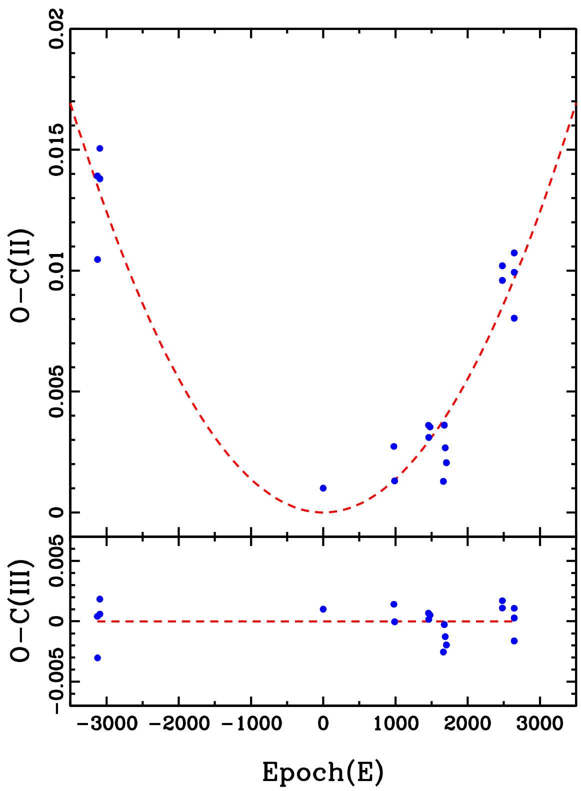

Fig. 3. The O-C(II) residuals plotted versus the epoch number for V1898 Cyg. A least-squares quadratic fit to the residuals is shown by the dashed line (upper panel). In the lower panel the O-C(III) residuals, the deviations from the quadratic fit, are also plotted. The color figure can be viewed online.

tober 26, 2004. The star was observed by DM from July 22, 2003 to September 17, 2004. Only the V-band light curve and observational data of CS were published. However, DM published the B and V light curves. The V light curves obtained in these studies are asymmetric in shape, and they differ from each other. The brightness of the system shows a fast decrease from phase 0.75 up to external contact. However, the increase in brightness following the primary eclipse is no steeper. The distortion of the light curve preceding the primary eclipse is larger in the CS light curve. A remarkable change in the light curve is seen at the phase interval between 0.09 and 0.42. The total brightness of the system in the V-bandpass at this phase interval is greater by about $0^m.03$ in the CS light curve than in DM's. However, CS report that the brightness of their primary comparison star showed light variations during the observations. Moreover the depth of the secondary eclipse is larger by about $0^m.007$ in the light curve of CS than in that of DM. We should note that there is also a slight asymmetry in both the DM's B- and V-passband light curves. This feature is attributed to the transfer of material from the cool secondary to the high temperature primary star which occults a small area of the primary star just before the deeper eclipse.

Acerbi & Barani (2007) analysed the DM's light curves. Since the spectroscopic mass-ratio was not available at that time, they started the analysis by deriving the photometric mass-ratio. Their preliminary analysis indicated that the mass-ratio for the system was about 0.30. Assuming an effective temperature of 20183 K for the primary component and that the secondary, less massive, star fills its corresponding Roche-lobe, i.e. a semi-detached configuration, they arrived at preliminary elements for the system. Their orbital parameters were: $i = 70°$, $r_1 = 0.3196$ and $r_2 = 0.2795$ and $T_2 = 7500$ K. Since the light curves were asymmetric they reported that the agreement between the computed and observed light curves was not very satisfactory: the sum of the squares of the residuals was about 0.814.

In order to analyse the light curves we choose the Wilson-Devinney (W-D) code implemented into the PHOEBE package tool by Prsa & Zwitter (2005). A preliminary analysis indicates that the system is a classical Algol, the secondary component filling its corresponding Roche lobe. Therefore Mode-5 is applied. The WD code is based on Roche geometry which is sensitive to the mass ratio which is taken from RV analysis as 0.192 ± 0.002. Gravity-darkening exponents $g_1 = 1$, $g_2 = 0.32$ and bolometric albedos $\mathrm{Alb}_1 = 1$, $\mathrm{Alb}_2 = 0.5$ were set, i.e. the more massive star has a radiative envelope while the less massive secondary has a convective atmosphere. We used the non-linear square-root limb-darkening and the bolometric limb-darkening coefficients from the tables of Díaz-Cordovés, Claret, & Giménez (1995) and van Hamme (1993).

The orbital inclination (i), effective temperature of the secondary star (T_2), surface potential of the primary (Ω_1), phase shift ($\Delta\phi$), and fractional luminosity of the primary (L_1) were taken as adjustable parameters. The other parameters were fixed. The iterations were carried out automatically until convergence was achieved, and a solution was defined as the set of parameters for which the differential corrections were smaller than the probable errors. The final results obtained by separate analysis of three light curves are listed in Table 3 and the computed light curves are shown as continuous lines in Figure 4. The uncertainties assigned to the adjusted parameters are the internal errors provided directly

TABLE 3

RESULTS OF INDIVIDUAL LIGHT CURVE ANALYSES FOR V1898 CYG

Parameter	CS V	DM B	DM V
$i(^\circ)$	74.20±0.02	73.05±0.03	73.03±0.03
T_1 (K)		18000[Fix]	
T_2 (K)	6582±65	6205±76	6109±50
Ω_1	3.0887±0.0085	3.2885±0.0116	3.2784±0.0103
Ω_2		2.2122[Fix]	
$q_{\rm spec}$		0.1918[Fix]	
$L_1/(L_{1+2})$	0.9563±0.0013	0.9801±0.0017	0.9490±0.0016
r_1	0.3513±0.0013	0.3296±0.0013	0.3286±0.0012
r_2	0.2464±0.0012	0.2464±0.0012	0.2464±0.0012
$\Delta\phi$	0.0022±0.0001	0.0008±0.0001	0.0008±0.0001
$\Sigma(\rm res)^2$	0.1196	0.0109	0.0123

Ref: r_1, r_2: Relative volume radii, CS V: Caton & Smith's (2005) V-band light curve, DM B and DM V: The B- and V-band light curves of Dallaporta & Munari (2006). The errors quoted for the adjustable parameters are the formal errors determined by the WD-code.

TABLE 4

FUNDAMENTAL PARAMETERS OF V1898 CYG

Parameter	Primary	Secondary
Mass ($M_\odot$)	6.054±0.037	1.162±0.011
Radius ($R_\odot$)	3.526±0.009	2.640±0.010
$T_{\rm eff}$ (K)	18 000± 600	6 200±200
log ($L/L_\odot$)	3.071±0.029	0.957±0.085
log g (cgs)	4.125±0.002	3.660±0.004
Spectral type	B2IV±1	G2III±1
a ($R_\odot$)	10.714±0.022	
i ($^\circ$)	73.05±0.03	
d (pc)	501±5	
$(v \sin i)_{\rm obs}$ (km s^{-1})	110±5	90±9
$(v \sin i)_{\rm calc}$ (km s^{-1})	112.8±0.3	84.5±0.4
J, H, K_s (mag)*	7.697±0.035, 7.718±0.026, 7.757±0.020	
$\mu_\alpha \cos\delta$, μ_δ (mas yr^{-1})**	2.07±0.62, 0.81±0.53	

* *2MASS* All-Sky Point Source Catalogue (Cutri et al. 2003).

**Newly Reduced Hipparcos Catalogue (van Leeuwen 2007).

by the WD code. As seen in Table 3 the sum of the squares of the residuals is 0.0109 and 0.0123 for the B- and V-bandpass light curves, being 75-times smaller than those of the analysis made by Acerbi & Barani (2007) of the same data. In the bottom panel of Figure 4 the residuals between observed and computed intensities are also plotted. The residuals reveal that the binary model may represent the observed DM's light curves successfully. However, the computed light curve differs mostly from fourth contact to beginning of secondary eclipse in the CS light curve.